NUMERICAL MODELLING OF TRANSIENT AND DROPLET TRANSPORT FOR PULSED PRESSURE - CHEMICAL VAPOUR DEPOSITION (PP-CVD) PROCESS

A thesis submitted in partial fulfilment of the requirements for

the Degree

of

Doctor of Philosophy in Mechanical Engineering

at the

University of Canterbury

Christchurch, New Zealand

by

Chin Wai Lim

2012

Table of Contents

List of Figures

List of Tables

List of Nomenclatures

λ	molecular mean free path
μ	dynamic viscosity
ν	kinematic viscosity
τ	time constant
ϕ	molecular incidence rate
∇	gradient operator
κ	second coefficient of viscosity
δ_{ij}	Kronecker delta function
$\vec{\xi}$	microscopic velocity of a particle
Ω_{col}	collision term
η	conserved properties
δ	perturbations from the equilibrium phase space distribution
σ_T	total collision cross section
χ	deflection angle after collision
ω	temperature exponent of the viscosity coefficient
Γ	gamma function
α	VSS molecular parameter
γ	ratio of specific heats
σ^2	variance of the velocity distribution
Ω	number of simulated translational degrees of freedom
σ_s	surface tension
ε	emissivity
τ_{scheme}	effective shear stress of the QDS scheme
μ_{scheme}	effective dynamic viscosity of the QDS scheme
ν_{scheme}	effective kinematic viscosity of the QDS scheme

$\nu_{physical}$	physical kinematic viscosity of a gas
σ_{ij}	collision cross section
ϕ_i	number of collision
$\vec{V}$	flow velocity vector
$\vec{g}$	vector for gravitational field
$\vec{u}$	macroscopic velocity of a particle
$\vec{x}$	position of a particle
$\vec{F}$	external force acting on the particles
f^{eq}	Maxwell-Boltzmann equilibrium distribution function
N_{pair}	number of simulated particle pairs
d_{VHS}	VHS molecular diameter
v_j	associated velocity of each velocity bin in QDS
$\dot{N}_{coll\ gas-drop}$	molecular collision rate
$\bar{c}$	average thermal speed of the gas molecules
$\overline{Nu}$	average Nusselt number
q'_{conv}	convection heat transfer per unit temperature change
$\bar{u}$	mean velocity of the cell
$v_{i,post,\phi_i}$	speed of molecules in i velocity bin after ϕ_i collisions
A	surface of area
Bi	Biot number
C	conductance
C_D	drag coefficient
c_p	specific heat for constant pressure
c_v	specific heat for constant volume
d	effective molecular diameter
D	dimension of the space

D_{12}	effective diffusion coefficient
d_{ref}	reference diameter at reference temperature
d_{VSS}	VSS molecular diameter
e	internal energy
E_{cond}	conduction energy
$E_{condensate}$	condensation energy
$E_{evaporate}$	evaporated energy
E_K	kinetic energy of the flow above the substrate
E_{rad}	radiative energy from surrounding
E_t	relative translational energy
f	gas distribution function
$F_{gas\text{-}drop}$	drag force exerted by the surrounding gas molecules to the droplet
F_η	net flux of η
g	equilibrium state of f
h	enthalpy of the fluid
h	the convection heat transfer coefficient
J^*_P	dimensionless total molecular flux
J_P	total molecular flux
k	Boltzmann constant
k_{cond}	thermal conductivity
k_f	thermal conductivity of fluid
Kn	Knudsen number
Kn_{GLL}	gradient length local Knudsen number
L	length
L_c	characteristic length
M	molecular mass
m	mass
m_r	reduced mass of the collision partners

n	number density
N_A	Avogadro's number
P	pressure
p	momentum
P_r	Prandlt number
q_{conv}	convection heat transfer
q_j	abscissas of the Gaussian quadrature
Q_P	evacuation rate
R	gas constant
r	radius
Re	Reynolds number
R_f	uniform distributed random number between 0 and 1
R_u	universal gas constant
s	Stefan-Boltzmann constant
S_P	volume displacement rate
T	temperature
$t_{col,avg}$	average time between particle collisions
t_P	process cycle time
$u_{i,pre}$	speed of molecules in i velocity bin before the collision
V	volume
v	velocity of a gas molecule
V_{ave}	average flow velocity
v_r	relative velocity of the collision partners
$v_{th,avg}$	average translational thermal speed
We	Weber number
w_j	weights of the Gaussian quadrature
W_α	weight coefficient
Z_{rot}	rotational relaxation collision number
Δt_{col}	mean collision time

AMOS	accumulated mass of gas molecules that strike onto substrate
APCVD	Atmospheric pressure CVD
BGK	Bhatnagar-Gross-Krook
BL	Borgnakke-Larsen
CER	collision en route
CFD	Computational Fluid Dynamics
CFL	Courant–Friedrichs–Lewy
CVD	Chemical Vapour Deposition
DD-QDS	directional decoupled QDS
DREAM	DSMC Rapid Ensemble Averaging Method
DSMC	Direct Simulation Monte Carlo
EFM	Equilibrium Flux Method
EIM	Equilibrium Interface Method
EPSM	Equilibrium Particle Simulation Method
HS	hard sphere
LBM	Lattice Boltzmann method
LPCVD	Low pressure CVD
MAPE	Mean Absolute Percentage Error
MBE	Model Boltzmann Equation
MC	Monotonized Central Difference
MINMOD	Minimum Modulus
NTC	No Time Counter
PDSC	parallelised DSMC code
PP-CVD	Pulsed Pressure CVD
QDS	Quiet Direct Simulation
TDEFM	True Directional Equilibrium Flux Method
TD-QDS	true-directional QDS
UHV-CVD	ultra high vacuum CVD
VHS	variable hard sphere
VSS	variable soft sphere

Acknowledgement

There is a Chinese proverb that says jade can only become a useful tool if it undergoes fine craftsmanship. I am very lucky to be in the good hands of a master craftsman. He is knowledgeable, resourceful and systematic. However, what defines him most is his patient devotion in supervising his apprentices. From the bottom of my heart, I thank my supervisor, Dr. Mark C. Jermy, for all the fruitful discussion, advice, clear direction on the research work, and understanding and support, in both academically and financially. He is undoubtedly a role model to me, professionally and personally.

I would also like to thank my co-supervisor, Dr. Susan P. Krumdieck, who is practically the "guru" in the Pulsed Pressure Chemical Vapour Deposition technique. Her insightful advice and explanations enriched my knowledge on this novel deposition technique. I am also thankful to Prof. Chong-sin Wu, who is my associate supervisor. Through his research group, I have had a chance to learn and work on this fascinatingly fast modelling technique for my PhD research. His hospitality during our visit to Taiwan was also greatly appreciated.

A very important person who helped me tremendously on this work was Dr. Hadley M. Cave. He is effectively the originator of the computational coding in my thesis work. His guidance and friendship gave me a wonderful start to my research work.

Another key person in helping to complete my thesis research was Dr. Matthew R. Smith who owns a brilliant mind. He always gave me the best

solution in the midst of my frustrations over debugging and running the computational codes, and saved my day.

To my friends in the Advanced Energy and Material Systems Laboratory, Dr. Vilailuck Sirwongrungson and Darryl Lee, I thank them for all the useful discussions and explanations on the experimental work. I also owe enormous appreciation to Luke Sinclair, Vivian How and Wen Eng Ong for their generous help in proof reading this thesis. Their devotions of time and friendships I will cherish in my memory for my whole lifetime.

To my late father and my mother, I thank them for their unconditional love and support. Both of them have only the educational level of primary school. However, they knew the importance of education for their children and have given me all the support they could and the opportunity to endeavour to higher education.

Finally, I am grateful to my beloved wife, Kerrie Wan. Her endless love, understanding and support are indescribable in words. She completes me. To my lovely boy, Zhong Han Lim, he may not aware of it at his current toddler age but my limited time spent with him during these busy years on thesis research work was a way of great support from him. Also, the arrival of my little baby girl, Wan Rou Lim, who is still in her mommy's tummy during the production of this thesis is certainly a great motivation to me in completing this thesis.

Abstract

The objective of this thesis is to develop an easy-to-use and computationally economical numerical tool to investigate the flow field in the Pulsed Pressure Chemical Vapour Deposition (PP-CVD) reactor. The PP-CVD process is a novel thin film deposition technique with some advantages over traditional CVD methods. In the PP-CVD process, a controlled volume of the precursor solution is injected into the continuously evacuated reactor in timed pulses. The precursor solution can be in either liquid or gas phase. The large, time-varying density gradient drives a complex flow field in the reactor.

In this thesis, a method to perform rapid approximations of the PP-CVD flow field is presented. The numerical modelling of the PP-CVD flow field is carried out using the Quiet Direct Simulation (QDS) method, which is a flux-based kinetic-theory approach. The QDS method calculates fluxes of conserved properties between cells by enforcing a Maxwell-Boltzmann velocity distribution locally within the computational cell at every time step. Fluxes are determined by the discretisation of the Maxwell-Boltzmann velocity distribution into a small number of velocity groups. Two approaches are considered for the flux reconstruction, which are the true directional manner and the directional splitting method.

Both the true directional and the directional decoupled QDS codes are validated against various numerical methods which include EFM, direct simulation, Riemann solver and the Godunov method. Both two dimensional and

axisymmetric test problems are considered. Good agreements are obtained between the results of the QDS method and that of the other numerical methods for all simulated test cases.

Simulations are conducted to investigate the PP-CVD reactor flow field at 1 Pa and 1 kPa reactor base pressures. The simulations reveal that an under-expanded jet develops during the injection phase of the PP-CVD process and dissipates soon after the end of the injection phase. The uniformity of the flow field in the reactor restores after the jet dissipates. The time required to establish the quasi-steady under-expanded jet is found to be about 3-5 ms, and the jet dissipates within 1 ms after the end of injection. The directional flux splitting QDS scheme is found to be slightly more accurate compared to the true directional QDS scheme.

The assumption of the local Maxwell-Boltzmann equilibrium distribution used in the QDS scheme is verified by examining the gradient length local Knudsen number based on the density, and by estimating the average number of particles collisions within each computational cell in one time step. The validity of the local equilibrium assumption is found to be satisfactory at 1 kPa reactor base pressure but not at 1 Pa. The limitation of the QDS scheme in PP-CVD flow simulation is also investigated. The limit of the rarefaction level in the flow that allows the assumption of the local equilibrium in the QDS schemes to be made is identified. It is found that the directional decoupled QDS scheme is able to

simulate PP-CVD flow field with reactor pressure higher than 400 Pa at reasonable accuracy. The numerical dissipation of the scheme is also quantified.

A droplet flash evaporation model is presented to model the evaporation and transport of the liquid droplets injected. The solution of the droplet flash evaporation model is used as the inlet conditions for the QDS gas phase solver. The droplet model is found to be able to provide pressure rise in the reactor at the predicted rate. All the droplets are found to be fully evaporated within 5 cm of the inlet nozzle, which agree with visual observations during the experiments.

A series of parametric studies are conducted for the PP-CVD process. The numerical study confirms the hypothesis that the flow field uniformity is insensitive to the reactor geometry. However, a sufficient distance from the injection inlet is required to allow the injected precursor solution to diffuse uniformly before reaching the substrate. It is also recommended that placement of the substrate at the reactor's centre axis should be avoided.

The second order directional decoupled axisymmetric QDS solver is used to perform parametric study of the flow field for the PP-CVD process to deposit thin film coating on two concentric cylinders. The simulations conducted focus on the injection phase of the PP-CVD process in the 2nd generation PP-CVD reactor with two concentric cylinders as the substrate. Overall, the simulation results show that good flow field uniformity can be achieved near the substrate surfaces. The flow field uniformity is found to decrease when the total mass of precursor solution injected is increased. This is as expected from the theoretical prediction.

The future work required for the development of the QDS scheme is proposed. A hybrid scheme is proposed to improve the accuracy of the simulation. Future extension of the scheme with cut cells will allow PP-CVD reactor modelling with more complex reactor geometries.

List of Publications

Journal Publications:

Lim, C.W., Smith, M.R., Jermy, M.C., Wu, J.-S. & Krumdieck, S.P., The direction decoupled Quiet Direct Simulation method for rapid simulation of axisymmetric inviscid unsteady flow in Pulsed Pressure Chemical Vapour Deposition, *Computers and Fluids* (submitted).

Conference Papers:

Lim, C. W., Cave, H., Jermy, M., & Krumdieck, S., (2009). Liquid droplet evaporation in simulations of the flow in Pulsed-Pressure MOCVD, *ECS Transactions*, **25**(8), 1251-1258.

Lim, C. W., Cave, H. M., Jermy, M. C., Krumdieck, S. P., & Wu, J.-S., (2011). An approximate method for solving unsteady transitional and rarefied flow regimes in Pulsed Pressure Chemical Vapor Deposition process using the Quiet Direct Simulation method, *AIP Conference Proceedings*, **1333**(1), 1039-1044.

Lim, C.W., Jermy, M.C., Wu, J.-S. & Krumdieck, S.P., Simulation of unsteady low pressure flow in Pulsed Pressure Chemical Vapour Deposition process using the Quiet Direct Simulation method, 17th Australasian Fluid Mechanics Conference, Auckland, New Zealand, 5 - 9 December 2010.

Lim, C.W., Zainol Abidin, Z., Cave, H.M., Jermy, M.C., Wu, J.-S., Smith, M.R. & Krumdieck, S.P., Numerical simulations of unsteady inviscid flow using the Quiet Direct Simulation method", in Proc. of the 7th Pacific Symp. on Flow Visualization and Image Processing, Kaohsiung, Taiwan (2009).

Lim, C.W., Cave, H.M., Jermy, M.C., Wu, J.-S. & Krumdieck, S.P., Numerical simulation of low pressure flows in PP-CVD using Quiet Direct Simulation (QDS) method", in Proc. of the 22nd Int. Conf. on Parallel CFD, Kaohsiung, Taiwan (2010).

Cave, H., Lim, C. W., Jermy, M., Wu, J. S., Smith, M., & Krumdieck, S. (2009). CVD flow field modelling using the Quiet Direct Simulation (QDS) method, *ECS Transactions*, **25**(8), 389-396.

Jermy, M. C., Lim, C. W., & Cave, H. M. (2010). Validity and inherent viscosity of the Quiet Direct Simulation method, *AIP Conference Proceedings*, 1333(1), 902-909.

Cave, H. M., Lim, C. W., Jermy, M. C., Krumdieck, S. P., Smith, M. R., Lin, Y. J., & Wu, J. S. (2011). Multi-species fluxes for the parallel Quiet Direct Simulation (QDS) method, *AIP Conference Proceedings*, 1333(1), 878-883.

1 Introduction

1.1 Thin Film Deposition Technologies and Applications

Thin film deposition is an industrial technique for forming thin layers of solid material on a target surface. The coating formed is considered a thin film when the thickness is between a few nanometres and about ten micrometres (Seshan, 2002). When formed by chemical reaction, the source material which is used to form the thin film is called the precursor. The target surface where the thin film is deposited is termed the substrate. In general, the purpose of the thin film coating is to enhance or add some material properties to the substrate surface. For example, the enhanced or added material properties may include: surface hardness, wear resistance, thermal insulation, corrosion protection, conduction pathways, biocompatibility or antireflection. Thin film deposition techniques can be classified into four basic types of process: vacuum evaporation, glow-discharge processes, liquid phase chemical processes and gas phase chemical processes (Seshan, 2002).

The vacuum evaporation technique is used to deposit thin films with no chemical reaction involved throughout the process. The material is vaporised by boiling or subliming through various ways which include: resistive heating, exposure to electron beams, radiation, crucible heated by conduction and lasers. The evaporated precursor is transported through the vacuum chamber and condenses to form a solid film on the substrate surface.

The glow-discharge technique is basically a sputtering method to eject surface atoms from an electrode surface into the gas phase. The ejected atoms are in thermodynamic non-equilibrium. Consequently, the atoms will not only form a thin film on the substrate but also onto any surface within the reactor such the reactor walls or reactor components. Hence, reactor cleaning becomes one of the problems in the glow-discharge technique.

Liquid phase chemical processes are thin film depositions from the liquid phase through chemical reactions. This method is usually used to form inorganic thin films. The substrate is commonly immersed, sprayed or flow coated in a liquid media. The growth of the thin film is accomplished via electrochemical or chemical plating processes.

Gas phase chemical processes involve thin film formation from a gas or vapour phase via chemical vapour deposition and thermal oxidation. These processes are generally referred to as Chemical Vapour Deposition (CVD). The source materials are injected into the reactor in the gas or liquid phase. In the case of liquid materials, vaporisation occurs to transform the source materials into the vapour phase upon reaching the substrate. The substrate is usually heated in order to activate the chemical reaction of the source materials on the substrate surface for thin film formation.

1.2 Pulsed Pressure Chemical Vapour Deposition

Pulsed Pressure CVD (PP-CVD) is an innovative CVD technique developed by Versteeg *et al.* (Versteeg, Avedisian, & Raj, 1995a). It has shown improved performance over conventional CVD methods including high precursor conversion efficiency, film quality and substrate conformity (Krumdieck, Kristinsdottir, Ramirez, Lebedev, & Long, 2007; Krumdieck, Lee, & Raatz, 2003; Krumdieck & Raj, 1999; Siriwongrungson, Alkaisi, & Krumdieck, 2007). Krumdieck *et al.* continue in developing the PP-CVD technique at the University of Canterbury in Christchurch, New Zealand to the present date.

The operating cycle of the PP-CVD process consists of an injection and pump-down phase. During the injection phase, a controlled volume of precursor solution at high supply pressure is injected into a continuously evacuated reactor volume. The injection of precursor mixture is carried out within a short period via an ultrasonic atomizer or choked orifice. This causes the reactor pressure to increase to a maximum value rapidly. The process is followed by a pump-down phase when the reactor inlet valve is closed. The reactor volume is continuously evacuated by a vacuum pump to return to its initial pressure before the next pulse cycle begins.

The rapid injection of precursor solution leads to a high vapour concentration near the reactor inlet during the injection phase. The continuous evacuation of the reactor chamber causes the fluid density to reduce significantly along the distance from the inlet to the outlet. The fluid density also reduces

significantly with time after the end of the injection phase. This pulsed process cycle results in a highly unsteady flow field with large density gradients throughout the reactor volume.

Experimental results conducted on laboratory scale PP-CVD reactors have demonstrated several advantages of this deposition technique. The thin film produced by the PP-CVD process is highly uniform and conformal. The PP-CVD process has high deposition rates and high precursor conversion efficiency. It has also been shown experimentally that the deposition performance of the PP-CVD process is relatively less sensitive to the change of the reactor geometry than steady flow CVD process (Krumdieck, Baluti, Marcus, & Peled, 2005). Therefore, the PP-CVD reactor can be easily scaled up to industrial applications and may be readily adapted to new coatings and substrates.

1.3 Conventional Computational Fluid Dynamics Method

Computational Fluid Dynamics (CFD) is a numerical approach to study the phenomena and problems related to fluid dynamics. The conventional CFD methods were developed in order to solve the theoretical governing equations of fluid dynamics numerically in discrete time and space. The three basic ways of discretising time and space are finite difference, finite volume, and finite element.

The theoretical governing equations of fluid dynamics, which are the Navier-Stokes equations, are formulated based on the concept of continuum. The continuum assumption treats a fluid as a continuous medium in which the fluid

macroscopic properties are considered to be continuous functions of position and time. The Navier-Stokes equations are differential equations that describe the physics of a viscous flow. In some flow conditions, where the viscous effect becomes negligible, the Navier-Stokes equations can be simplified to the Euler equations. Hence, in the conventional CFD approach, the Navier-Stokes solver is used to provide a solution for viscous flows while the Euler solver is employed for handling inviscid flows.

In CFD, the time marching technique is implemented to solve either the Euler or Navier-Stokes equations with a time derivative. There are two different schemes in the time marching technique, namely the explicit and implicit scheme. The explicit scheme determines the spatial difference equations from the values obtained in the previous time step. This scheme is simple and easy to implement but generally has poor stability and convergence efficiency. In the implicit scheme, the spatial unknowns are solved by the means of a simultaneously solving the difference equations applied at all the grid points arrayed at a given time step (Anderson, 1995). The implicit scheme has greater stability and convergence efficiency than the explicit scheme. However, it is more costly in time and computing resources. It is also more complicated for implementation. Both the explicit and implicit time marching schemes have been well developed as useful CFD tools.

1.4 Kinetic Theory Based Methods

An alternative approach in CFD is to take into account kinetic theory and the particle-based nature of gases in simulating the flow field. In general, instead of solving the continuum based governing equations, these methods describe the fluid as a large collection of particles analogous to molecules. The fluid particles are grouped according to their properties at the molecular level, which are the microscopic properties. The macroscopic properties of these particle groups are calculated from the microscopic properties. The motion and collision between the particles are tracked to determine the change in the state of the flow. Some examples of kinetic theory based methods include: Direct Simulation Monte Carlo (DSMC) method, Lattice Boltzmann method (LBM), the Bhatnagar-Gross-Krook (BGK) scheme, the Equilibrium Particle Simulation Method (EPSM), the Equilibrium Flux Method (EFM), the True Directional Equilibrium Flux Method (TDEFM) and the Quiet Direct Simulation (QDS) method, the Chapman-Enskog method and the kinetic method that solves the Grad's 13 moment equations.

The Direct Simulation Monte Carlo (DSMC) method has earned the reputation as a successful kinetic theory based method that provides accurate solutions of fluid flows. The DSMC method is developed by Bird and has attracted many researcher’s interest since the 1960s (Bird, 1963). In the DSMC method, simulated particles are used to represent a collection of the physical gas particles. The simulated particles are allowed to undergo a free movement phase without any intermolecular interaction. At the end of the free flight phase,

simulated particles that have reached the destination computational cells are assembled and undergo probabilistic intermolecular collisions. Post-collision velocity of each simulated particle is updated to represent the change of the flow field after one computational time step. The free flight and collision phase are then repeated iteratively until the simulation is completed.

Another branch of kinetic theory based methods is to solve the Boltzmann distribution function, which represent the time evolution of the particle distribution within a defined phase space. The LBM is a common example of a kinetic theory based solver that solves the Boltzmann equation. In the LBM, the Boltzmann equation is solved by discretising the Boltzmann distribution function into discrete velocities, space and time. A finite velocity set is used to represent the velocity distribution of the particles. The changes of the locations and velocities of the particles are due to the movement of the particles in a discrete space with the associated discrete velocities and the collision between the particles in a discrete time.

The BGK scheme simplifies the Boltzmann equation by replacing the collision term with Bhatnagar-Gross-Krook (BGK) simplified collision model (Bhatnagar, Gross, & Krook, 1954). The BGK scheme solves the time-dependent gas evolution equation by the construction of numerical fluxes at the computational cell interfaces. The relaxation of the gas particles is then performed in the computational cell within each time step to update the change in the state of

the flow field. The BGK scheme is capable of simulating non-equilibrium flow in order to provide more realistic solutions.

The EPSM (Pullin, 1980) is regarded as a continuum flow solver to provide a DSMC solution with infinite intermolecular collisions. Similarly to the DSMC method, simulated particles are used to represent the collections of physical gas molecules. The simulated particles undergo a free movement phase as in the DSMC. However, the EPSM does not perform the selection of random collision partners as in the DSMC during the collision phase. Instead, the simulated particles are assigned new velocities from the local Maxwell-Boltzmann velocity distribution based on the state of the cell.

The EFM was proposed by Pullin (Pullin, 1980) and uses directional splitting method to compute fluxes analytically across the interface of two computational cells. The EFM fluxes are constructed by assuming a Maxwell-Boltzmann equilibrium distribution of the molecular velocities locally in the computational cells. This means the EFM fluxes are derived with no density gradient locally within the cell during a small time step, approaching the limit of an infinite number of particles within each computational cell. Hence, the EFM is considered as a method that provides the Euler solution of a flow field.

The TDEFM (Smith, 2008; Smith, Macrossan, & Abdel-jawad, 2008) also computes molecular fluxes based on the Maxwell Boltzmann equilibrium distribution function as in the EFM. However, the TDEFM considers multiple moments over both velocity and physical space to provide a more general form of

the distribution compared to the EFM. In the TDEFM, the analytical solution to the molecular fluxes, based on the Maxwell-Boltzmann equilibrium distribution, is computed. During the free flight phase of the gas molecules, the TDEFM fluxes are allowed to move to an arbitrary destination cell whether or not the cells have a shared interface. This means that the TDEFM fluxes can travel to a diagonal cell which shares only a vertex with the source cell. Such fluxing methods are termed true directional methods (Smith, et al., 2008).

The QDS (Smith, Cave, Wu, Jermy, & Chen, 2009) method calculates molecular fluxes between cells by enforcing a Maxwell-Boltzmann equilibrium distribution of velocities throughout the flow field at every time step. The QDS fluxes are determined by carrying mass, momentum and energy between cells via the discretisation of the Maxwell-Boltzmann velocity distribution into a small number of masses and velocities determined from the weights and abscissas of a Gauss-Hermite quadrature. This allows the QDS to be a fast and accurate method since the error functions involved in evaluating the moments of the equilibrium distribution are avoided. The QDS method is discussed in detail in Chapters 5 and 6.

1.5 Motivation of Present Work

The potential for industrial scale-up directly from process parameters determined through laboratory research appears possible in the PP-CVD process. This initiates the research in controlling the PP-CVD process, the reactor design and

materials to be deposited. In optimising the design of a PP-CVD reactor, a thorough understanding of the flow dynamics in the time-variant reactor pressure region is required. The difficulties of experimental measurement and flow field visualisation in the low density reactor volume are hurdles for experimental investigation of the PP-CVD flow field. A more feasible way to study the flow dynamics in the reactor is through numerical simulation. Thus, it is necessary to identify simulation tools in order to simulate the flow in the reactor numerically.

Previously, the DSMC method has been adopted for the numerical investigation of the PP-CVD flow field. The simulation solver used in the previous study is called the parallelised DSMC code (PDSC). With the recent developments in PDSC, Cave has performed a remarkable first attempt to simulate a gas flow field in PP-CVD reactor at realistic pressures during the injection phase (Cave, 2008; Cave et al., 2007). However, being a pure DSMC solver, the computational expense of simulation with the PDSC is remarkably high especially when the density of the simulated gas is increased and when unsteady simulations are conducted. The results obtained have also shown a large amount of statistical scatter. Moreover, PP-CVD reactors are usually equipped with liquid-injection delivery systems where a liquid precursor solution is injected directly into the reactor. Hence, the numerical modelling and simulation of the PP-CVD reactor with liquid-injection delivery system is yet to be developed.

Difficulties also arise in simulating the PP-CVD flow using conventional CFD solvers. Due to the highly complex flow throughout the reactor, it would be

difficult to obtain converged solutions with a Navier-Stokes equations solver. The computational expenses are also high to simulate such complex and unsteady flow using the Navier-Stokes solver (Lin, 2008). However, it should also be noted that it is sometimes possible to model PP-CVD flow with conventional CFD solvers at a cost of slow convergence and extra effort in simulation setup.

For the purpose of industrial scale-up and commercialisation the PP-CVD reactor, the ease of use and computational speed of the numerical tool are the main concerns. A computationally economic solver is important to provide a rapid simulation tool for PP-CVD reactor design and operating condition selection. A simulation tool that requires relatively less CFD expertise is also essential to allow its usage by industrial engineers.

1.6 Research Objectives

The objective of this research is to develop a rapid simulation tool to obtain an approximated solution of the liquid and gaseous flow in the PP-CVD reactor volume. The numerical solution is used to understand the PP-CVD flow field phenomena in order to optimise the design parameters of the reactor. Therefore, the scope of this research focuses mainly on the transport phenomena of the flow field in the PP-CVD reactor including:

1. further development of the existing PDSC to simulate numerically the transport phenomena of precursor with polyatomic molecular structure in

the PP-CVD reactor flow regime with inelastic collisions between precursor molecules

2. development of a rapid simulation tool to model the PP-CVD flow field during the injection and pump down phase
3. modelling of the fast evaporation and transport phenomena of liquid precursor solution in the pulse pressure flow regime
4. numerically investigate the PP-CVD flow field
5. parametric simulation of new reactor design concepts in preparation for commercialising the PP-CVD reactor for industrial purposes

1.7 Thesis Organisation

This thesis is organized in the following order:

- Chapter 1, an introduction of the thesis is given.
- Chapter 2, the background of the Chemical Vapour Deposition (CVD) process, various techniques in CVD and detailed introduction of the PP-CVD process are described.
- Chapter 3, the characterisation of fluid flow and various fluid flow simulation tools are discussed.
- Chapter 4 the PP-CVD flow field, modelling considerations and method are presented.
- Chapter 5, the development and the detail of true directional QDS method are first described. It follows with the preliminary PP-CVD

flow field simulation using the true directional QDS solver. Then, a validity check of the assumptions used in the QDS method are performed and discussed.

- Chapter 6, a simple analysis of the numerical dissipation inherent in QDS method is carried out. Next, the directional decoupled QDS method is presented to improve the simulation results of PP-CVD flow field modelling. Validity checks on the assumptions used in the QDS method are again performed and discussed. Lastly, the limitation of the QDS method in simulating PP-CVD flow is discussed.
- Chapter 7, the modelling of the liquid droplet flash evaporation in PP-CVD reactor volume is presented.
- Chapter 8, parametric simulations of the existing and new reactor design concepts are conducted and discussed.
- Chapter 9, the conclusion of the present work is given.
- Chapter 10, suggested future work is presented in order to improve the existing QDS solver as well as to extend the QDS solver in modelling objects with complex geometries.
- The Gauss-Hermite parameters are given in Appendix.

2 Background

2.1 Chemical Vapour Deposition Process Overview

In general, there are three elementary phases in Chemical Vapour Deposition (CVD) of thin films. These three phases include the transport of reactants from the supply source to the substrate, the adsorption and decomposition of the reactants near or on the substrate surface, and the nucleation and crystal growth on the substrate surface (Taga, 2001). The CVD reactor is considered cold wall reactor when only the substrate is heated. The overall physical and chemical processes involved in a cold wall CVD reactor with liquid precursor solution delivery system can be demonstrated in Figure 2.1.

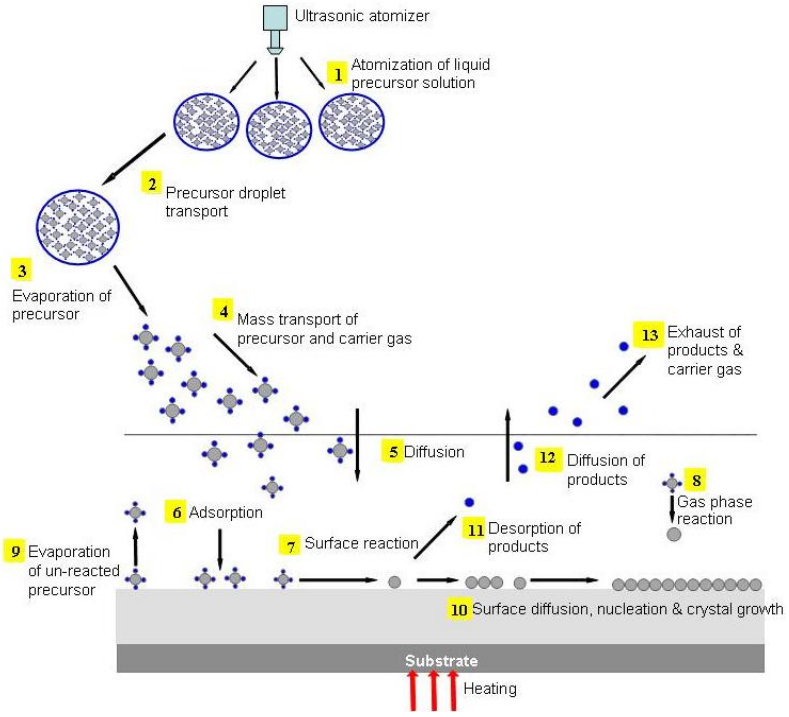

Figure 2.1 Schematic of mass transport and surface kinetics in a typical CVD process [diagram courtesy of Krumdieck, S.P.].

Each step in the deposition process can be summarised as followings:

1. Atomization of liquid precursor solution through an ultrasonic atomizer
2. Transport of the liquid precursor solution droplets in the reactor
3. Evaporation of liquid precursor solution droplets
4. Mass transport of the precursor solution into the reactor and near the substrate surface
5. Diffusion of the precursor solution to the substrate surface through concentration gradient
6. Adsorption of precursor solution onto the substrate surface
7. Thermal decomposition of the precursor solution molecules
8. Possible gas phase reactions rather than surface reaction on substrate surface
9. Evaporation of un-reacted precursor solution from substrate surface
10. Nucleation of precursor followed by surface diffusion and crystal lattice incorporation
11. Desorption of reaction products from the substrate surface
12. Diffusion of the reaction products away from the substrate
13. Transport of the reaction products out of the reactor in exhaust

The precursor solution is also referred as reactant.

Throughout the entire CVD process, in general, there are three growth rate limiting steps, the slowest of which controls the overall deposition rate. The three possible growth rate limiting steps are mass transport of the first kind, mass

transport of the second kind and surface kinetics control (Choy, 2003; Morosanu, 1990):

1. Mass Transport of the First Kind - the rate limiting step where the main gas flow in the process controls the deposition rate. The main gas flow includes the reactant feed to, and the product removal from, the deposition zone. This type of process control occurs for high to ultra-high deposition temperatures e.g. $\geq$ 1450°C (Choy, 2003).
2. Mass Transport of the Second Kind - the growth rate limiting step depends on the reactant transfer between the main gas flow and the substrate surface. The mass transfer between the main gas flow and the substrate surface is by diffusion or convection. As the diffusion coefficients vary only weakly with temperature, the growth rate depends weakly on temperature. Hence, the film growth rate is almost constant for this type of process control.
3. Surface Kinetic Control - the surface kinetics or reaction rate becomes the limiting step of the process. Surface kinetics include chemical reactions, reactant adsorption, product desorption, surface migration and lattice incorporation. The deposition temperature is low at this type of process control. The growth rate depends strongly on the deposition temperature which activates the surface chemical reactions.

The flow field modelling of the steps in Figure 2.1 is vital in order to understand and, hence, control the growth rate limiting step in the CVD process.

This allows CVD reactor design and optimization for required deposition applications to be performed efficiently. In the current research project, steps 1, 2, 3, 4, 5, 12, and 13 are the main focus of interest.

2.2 Characterisation of CVD Flow

The reactions, and hence the deposition, throughout the CVD process are closely related to the mass transport phenomena of the precursor. Therefore, a thorough understanding and modelling of the mass flow through the reactor is an important step in reactor design and optimization. As there are wide varieties of CVD reactor configurations and operating pressures, the flow inside the reactor can be in a viscous flow, a free molecular flow, or in a transition state which is intermediate between viscous and molecular flow. For the fluid in a viscous state, the flow can be laminar or turbulent. In a CVD system, two dimensionless numbers are commonly used to characterise the fluid flow in the reactor. The two numbers are the Knudsen number, *Kn*, and the Reynolds number, *Re*.

The Knudsen number expresses the ratio of the molecular mean free path to the characteristic length perpendicular to the flow direction. The molecular mean free path, λ, is defined as the average distance travelled by a molecule before colliding with another molecule, which is given in Equation (2.1) as:

$$\lambda = \frac{kT}{\sqrt{2}\pi d^2 P} \tag{2.1}$$

where k is the Boltzmann constant, T is the fluid temperature, d is the effective molecular diameter and P is the pressure. The Knudsen number is used to identify the state of the gas flow among the viscous, transition and molecular regimes. Hence, it is an expression of the relative level of the fluid flow rarefaction.

In a flow with a low Knudsen number, typically $Kn < 0.01$, the gas is considered to be in a state of viscous flow (Roth, 1990). The gas density is sufficiently high that intermolecular collisions dominate the effect at the molecular level and the flow can be modelled in terms of the continuum flow properties (Bird, 1994). The Navier-Stokes equations provide the conventional mathematical model of continuum gas dynamics. The mass transport in continuum flow CVD reactors are highly dependent on: the bulk gas flow velocity, the fluid physical properties, the pressure gradient between the inlet and outlet of the reactor and the solid surfaces geometry that interact with the flow. This continuum flow pattern determines the precursor arrival rate to the substrate surface (Jones & Hitchman, 2009).

However, when the Knudsen number is greater than 1, the gas in the flow is in the molecular state. The mean free path of the fluid molecules is large which causes the molecules to move in random motion. Hence, the molecular effect has a significant influence on the flow pattern and the continuum model of the flow properties becomes invalid. In this case, a discrete particle or molecular model is needed to express the flow phenomena.

Generally, an overall characteristic dimension based on the flow geometry, such as diameter of the pipe for an internal flow through a circular pipe, is chosen in determining a single overall Knudsen number for the complete flow. However, this can be misleading. For some flows with significant macroscopic property changes in certain regions or throughout the flow, such as the presence of strong shock structure, the local continuum flow condition may be invalid. Hence, the limit of continuum flow model can be specified more appropriately if a local Knudsen number which is defined based on a scale length of the macroscopic gradient (Bird, 1994; Oran, Oh, & Cybyk, 1998), given in Equation (2.2) as:

$$Kn_Q = \frac{\lambda}{L} = \frac{\lambda}{\left[\frac{Q}{\partial Q / \partial x}\right]} \tag{2.2}$$

where Q can be any of the macroscopic properties (i.e. density, velocity, or temperature).

The Reynolds number measures the ratio of inertia to viscous forces, which is given in Equation (2.3) as:

$$\mathrm{Re} = \frac{\rho UL}{\mu} = \frac{UL}{\nu} \tag{2.3}$$

where ρ is the fluid density, U is the flow velocity, L is a characteristic length μ is the dynamic viscosity and ν is the kinematic viscosity. The Reynolds number is used to characterise the different flow regimes of a fluid in motion such as laminar or turbulent flow. Considering a fluid flow inside a circular pipe, the flow is in

laminar flow regime when the *Re* is less than 2000. The viscous forces are dominant in laminar flow where the flow field is rather smooth with constant fluid motion. The turbulent flow occurs when the *Re* is more than 4000. The inertial forces become dominant. This results small disturbance in the flow causes eddies. The flow is in the transition regime when the *Re* is between 2000 and 4000 with the presence of both laminar and turbulent flow (Potter, Wiggert, Hondzo, & Shih, 2002). Because of the low precursor flow rate, most conventional CVD systems operate in the laminar flow regime.

2.3 Chemical Vapour Deposition Techniques

CVD process requires a heating system with temperature control to activate the chemical reaction of the precursor molecules on substrate surface at an elevated temperature. CVD reactors can be classified by the heating strategy adopted in the reactor system (Seshan, 2002). The two types of heating approaches used in CVD reactors are the hot-wall and cold-wall reactor systems.

For the hot-wall reactor system, the entire reactor is heated in an isothermal oven. This provides a uniform thermal field on the substrate to allow uniform thin film growth. However, due to the whole reactor being heated, the reaction of the precursor molecules occur not only on the substrate but also on the reactor wall and other heated components in the reactor. This could become a source of particle contamination which reduces the deposition quality and causes a poor

precursor conversion efficiency. It also increases the operating cost due to cleaning and maintenance problems (Choy, 2003).

In the cold-wall reactor system, only the substrate is heated and, hence, the thermally activated precursor reactions occur only on the heated substrate. The substrate is usually heated by a heater through conduction heat transfer. This improves significantly on the particle contamination and high cost problems faced by the hot-wall reactors. However, it proposes challenges in controlling the heating system for uniform substrate heating.

Regardless of the different type of heating strategy, CVD reactors are categorised depending on the operating pressure range. Atmospheric pressure CVD (APCVD) reactors operate within the viscous flow regime at atmospheric pressure. Low pressure CVD (LPCVD) operates at below atmospheric pressure whereas ultra high vacuum CVD (UHV-CVD) operates at pressure typically below 0.1 Pa (Ohring, 2002; Schuegraf, 1988).

APCVD reactors are continuum flow CVD reactors where the reactant vapours are convected through the reactor from inlet to outlet by the bulk gas flow. A boundary layer which is the solid-fluid interaction zone is formed near the substrate. The precursor molecules in the bulk flow diffuse to the deposition surface due to the concentration gradient and being consumed across the boundary layer. Hence, the thin film growth rate in APCVD reactors is limited by the mass transport of the second kind as discussed in section 2.1. APCVD reactors are able to provide high film growth rate but obtaining film uniformity is challenging due

to the diffusion limited growth regime (Jones & Hitchman, 2009). Since the deposition depends on the diffusion of the precursor vapour to the substrate surface and the diffusivity decreases with increasing pressure, it is important to ensure reactant depletion does not occur anywhere on the substrate surface with consequent poor film uniformity (Ohring, 2002). Several methods such as showerhead and planetary reactors are used to improve the uniformity of the film growth in APCVD reactors.

LPCVD process was introduced into the CVD marketplace in 1976 (Schuegraf, 1988) to improve the diffusion limiting problem encountered in the APCVD process by reducing the operating pressure. Since the gas diffusivity increases at lower pressure, a better film uniformity can be achieved. This allows a simpler reactor design compared to APCVD reactors. However, the challenge in LPCVD approach is to increase the concentration of the reactant vapour in the reduced pressure environment in order to maintain film growth rate and hence the throughput of thin film production.

UHV-CVD reactors operate at very low pressure where the Knudsen number of the flow is generally greater than 1. The reactant vapour flow in the reactor is in the free molecular regime where the gas molecules are in random motion. Hence, the reactant vapour in a UHV-CVD reactor is considered to be in a “well-mixed” condition due to the random molecular movement that encourages uniform film deposition. The film quality can be controlled by controlling the reactant product cleanup through a good vacuum exhaust system. The deposition

rate in the UHV-CVD process, however, is usually low because of the necessity in keeping the mass flow rate of the reactant vapour low enough for maintaining the low operating pressure range.

2.4 Pulsed Pressure Chemical Vapour Deposition

The innovative Pulsed Pressure Chemical Vapour Deposition (PP-CVD) was developed by Versteeg *et al*. at Cornell University in Ithaca, New York, U.S.A. as a promising technique for producing high uniformity thin films efficiently (Versteeg, Avedisian, & Raj, 1995b). A research scale PP-CVD reactor was then built in 2000 by Krumdieck at the Advanced Energy and Material System, Laboratory (AEMS Lab) at the University of Canterbury, Christchurch, New Zealand. The development of the PP-CVD process has been actively carried out by the research group led by Krumdieck (Cave, Krumdieck, & Jermy, 2008; Krumdieck, Cave, Baluti, Jermy, & Peled, 2007; Krumdieck, Kristinsdottir, et al., 2007; Krumdieck, Siriwongrungson, Reyngoud, & Barnett, 2010; Siriwongrungson, et al., 2007).

PP-CVD reactor is a cold-wall low pressure CVD reactor in which only the substrate is heated to activate the chemical reaction of the precursor molecules. The unique feature of PP-CVD reactor is to deliver a controlled volume of reactant solution into the reactor in a timed pulse manner. In PP-CVD unlike the conventional CVD technique, the reactant solution is injected into the continuously evacuated reactor volume without the use of carrier gas. Figure 2.2

shows the schematic diagram of a PP-CVD reactor. In general, the PP-CVD reactor can be broken down into three subsystems: injection, reactor and exhaust. The injected precursor solution can either be gas which is injected through an orifice on top of the reactor or liquid which is supplied using an ultrasonic nozzle. Liquid precursor solution supplied to the low pressure reactor chamber is flash evaporated. The rapidly injected precursor solution diffuses uniformly to the vicinity of a heated substrate and reacts at the surface to form a solid thin film. The outlet of the reactor chamber is fitted to a vacuum pump for continuous evacuation of the reactor chamber as well as reaction product removal.

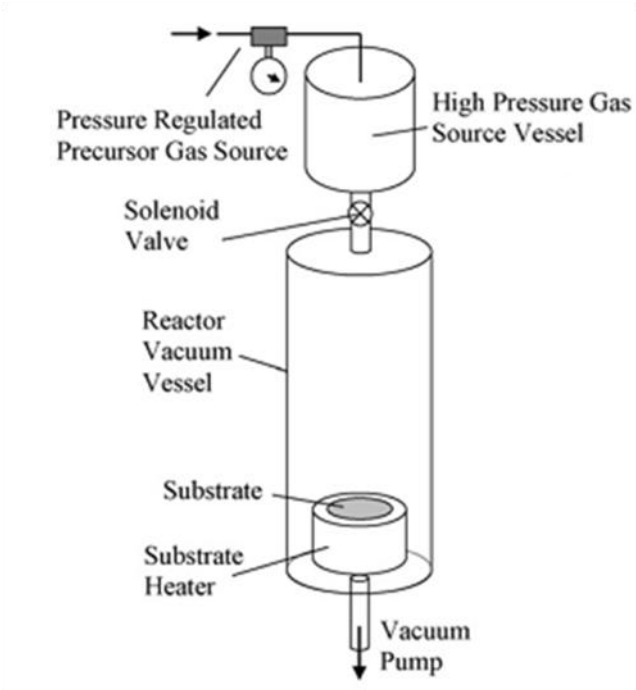

Figure 2.2 Schematic of Pulsed Pressure Chemical Vapour Deposition (PP-CVD) reactor. [diagram courtesy of Krumdieck, S.P.].

The operating cycle of the PP-CVD process consists of an injection and pump-down phase. During the injection phase, a metered quantity of precursor

solution at high supply pressure is injected into a continuously evacuated reactor volume, increasing reactor pressure to a maximum rapidly. The timed injection of the precursor solution causes the reactor pressure to be time-variant. The pressure of an operating cycle inside the PP-CVD reactor chamber can be illustrated in Figure 2.3. The rapid injection of precursor solution during the injection phase ($0 < t < t_i$) causes a sudden increase of the reactor pressure from its base pressure P_{min} to peak pressure P_{max}. At process time $t = t_i$, the injection valve is closed. The process is then followed by a pump-down phase ($t_i < t < t_p$) when the reactor pressure decreases back to the base pressure before the next pulse cycle begins. The period after the pressure returns to the minimum but before the next injection phase is called relaxation time. This cycle is repeated continuously throughout the whole deposition process.

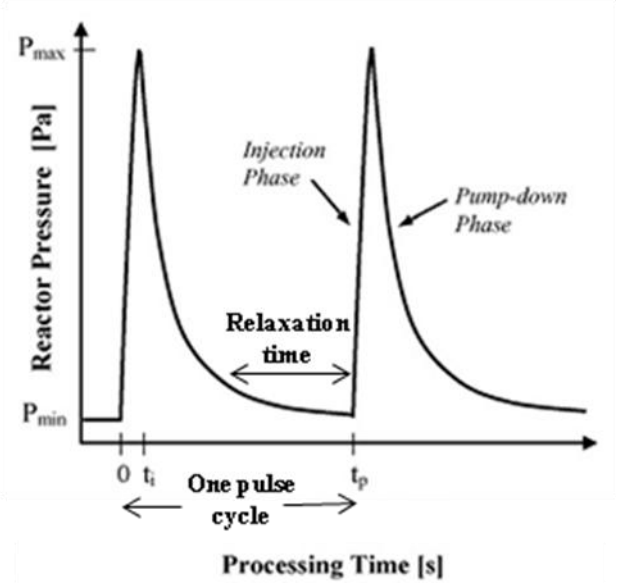

Figure 2.3 Schematic of Pulsed Pressure Chemical Vapour Deposition (PP-CVD) reactor.

The rapid injection of precursor solution leads to a high vapour concentration near the reactor inlet during the injection phase while the continuously evacuated reactor chamber causes the fluid density to reduce significantly with time after the end of the injection phase, and with the distance from the inlet. This pulsed process cycle produces a highly unsteady flow field with large density gradient throughout the reactor volume.

2.4.1 Mass Transport Model of PP-CVD Process

The novelty of the pulsed injection in PP-CVD is to control the molecular flux in the reactor to be as uniform as possible before arriving to the substrate surface. Under uniformly distributed precursor vapour, it is then expected that the film growth rate depends solely on the precursor molecules arrival rate and deposition temperature. Experimental results have demonstrated the expected behaviour of film growth rate where the growth rate is limited by the reaction kinetic at low temperature while limited by the precursor supply rate at high temperature (Krumdieck & Raj, 2001a). In the same paper, a growth rate model based on the simple Langmuir surface mass balance describes the arrival rate of precursor to the surface by the gas kinetics and depends only on the precursor partial pressure. Good agreement was obtained between the model derived and the experimental results. This shows the potential of pulsing, which yields non-steady state flow field, in PP-CVD technique allows the deposition rate to not be limited by diffusion as in the conventional steady flow CVD technique.

The precursor injection time and the pulsed cycle time are important in controlling the uniformity of the flow field in PP-CVD. Due to the sudden increase in the reactor pressure when the precursor solution is pulse injected into the low pressure PP-CVD reactor, the precursor solution undergoes a rapid expansion. When the pressure inside the reaction chamber is increasing at a sufficiently fast rate, the expansion forces will be dominant over the viscous forces, causing an expansion mass transport regime to occur (Krumdieck, Cave, et al., 2007). It has been demonstrated experimentally that the mass transport field remains uniform throughout the reactor volume for the maximum pressure up to 16 kPa. In the experiment, the injection time and pulse cycle time was maintained at certain ranges. These time ranges are determined based on the reactor design variables which are the reactor geometry and exhaust pump rate (Krumdieck, et al., 2005).

A study has been carried out to model the molecular flux within the PP-CVD reactor (Krumdieck, Lee, et al., 2003). Considering the ideal gas law and assuming a constant reactor temperature, T_R, the number of molecules, n, inside the reactor with volume, V_R, at any time, t, can be expressed in Equation (2.4) as:

$$n(t) = \frac{P(t)V_R N_A}{R_u T_R} \tag{2.4}$$

where N_A is the Avogadro's number and R_u is the universal gas constant. The vacuum pump used to evacuate the reactor continuously with volume displacement rate, S_P, and conductance, C, operates at evacuation rate, Q_P, which is given in Equation (2.5) as:

$$Q_P = \frac{S_P C}{S_P + C} \tag{2.5}$$

The molecular balance inside the reactor chamber during one pulse cycle can then be expressed in Equation (2.6) as:

$$n_L dt - \frac{Q_P}{V_R}\left[n(t) - n_{\min}\right]dt = d\left[n(t) - n_{\min}\right] \tag{2.6}$$

where n_L is the molecular leak rate, which is negligible compared to the vacuum pump speed and n_{min} is the number of molecules in the reactor at the minimum pressure. By integrating Equation (2.6) from t = 0 to any time t during the pulse cycle, the dimensionless reactor pressure, $P^*(t)$, is defined in Equation (2.7) as:

$$P^*(t) \equiv \frac{P(t) - P_{\min}}{P_{\max} - P_{\min}} = \exp\left(-\frac{t}{\tau}\right) \tag{2.7}$$

where τ is the time constant of the reactor, P_{max} and P_{min} are the peak and base pulse pressure, respectively, given in Equation (2.8) as:

$$\tau = \frac{V_R}{Q_P} \qquad P_{\max} = P_S\left(\frac{V_S}{V_R}\right)\left(\frac{T_R}{T_S}\right) + P_{\min} \tag{2.8}$$

P_S, V_S and T_S are the pressure, volume and temperature of the precursor supply volume, respectively. It should be noted that the processing time of a pulse cycle needs to be at least 4 times that of the reactor time constant for the maximum and minimum pressure to be repeated continuously throughout the entire deposition process (Baluti, 2005).

The molecular incidence rate, ϕ, striking on a unit area of the reactor internal surface, which is termed the molecular flux, is expressed using the gas dynamics relation given in Equation (2.9) as:

$$\phi(t) = \frac{N_A P(t)}{\sqrt{2\pi M R_u T_R}} \tag{2.9}$$

where M is the molecular mass. Since the PP-CVD process is an unsteady process, the molecular flux is a time-variant function. By combining Equations (2.7) and (2.9) and integrating the molecular flux over the process cycle time, t_P, the total molecular flux per unit area per pulse cycle is given in Equation (2.10) as:

$$J_P = \left(\frac{N_A}{\sqrt{2\pi M R_u T_R}} \right) \left[P_{\min} t_P + \tau \left(P_{\max} - P_{\min} \right) \left(1 - \exp\left(-\frac{t_P}{\tau} \right) \right) \right] \tag{2.10}$$

By defining $J = \phi t_P$, the dimensionless total molecular flux, J^*_P, can then be expressed in Equation (2.11) as:

$$J_P^* \equiv \frac{J_P - J_{\min}}{J_{\max} - J_{\min}} = \frac{\tau}{t_P} \left[1 - \exp\left(-\frac{t_P}{\tau} \right) \right] \tag{2.11}$$

2.4.2 Development and Deposition by PP-CVD

PP-CVD reactors have been developed and investigated in various deposition experiments with a wide variety of materials. An early deposition experiment was to deposit lithium tantalite ($LiTaO_3$), which is a useful optical film, on sapphire from a liquid metalorganic precursor of lithium hexa-t-butoxide (Xie & Raj, 1993). Another liquid metalorganic precursor, titanium dioxide or titania (TiO_2), was

then deposited on sapphire from titanium tetra isoproxide (TTIP) (Versteeg, et al., 1995a). Titania films have broad range of applications such as semiconductors and thermal barrier coatings.

The recent investigations and depositions using PP-CVD technique are mainly from Krumdieck *et al*. Some of the studies on deposition of TiO_2 from TTIP conducted by Krumdieck *et al*. include: the investigation of conversion efficiency and growth rate over temperature range of 400 to 700ºC (Krumdieck & Raj, 1999), the effect of temperature and precursor injection rate on the growth rate and morphology of TiO_2 film deposition (Krumdieck & Raj, 2001b), and conversion efficiency, crystallographic orientation and microstructure of TiO_2 films (Krumdieck & Raj, 2001a). A kinetic model and experimental characterisation of the PP-CVD reactor using TTIP as the precursor to deposit TiO_2 films has also been conducted (Krumdieck, 2001). TiO_2 film deposition has been further studied for conformal step coverage over a range of deposition temperatures (Siriwongrungson, et al., 2007). Other than TiO_2 films, deposition of solid yttria-stabilised zirconia (YSZ) films from a metalorganic precursor has also been studied (Krumdieck, Sbaizero, Bullert, & Raj, 2002). A deposition of yttria-stabilised zirconia (YSZ) films onto solid oxide fuel cell electrodes to act as an electrolyte layer has also been conducted (Krumdieck, Sbaizero, Bullert, & Raj, 2003).

3 Numerical Modelling of Fluid Dynamics

3.1 Fluid Flow Characterisation

Fluid mechanics is the branch of physics that deals with the behaviour of liquids and gases in relation to the corresponding properties in the presence of various forces. It can be divided into fluid statics and dynamics. Fluid statics is the study of fluids with no relative motion. Conversely, fluid dynamics is the study of fluid in motion and in most practical examples shearing stresses exist between fluid particles which cause a velocity gradient in the flow field.

In the presence of a force, transmitted through the fluid by pressure, the fluid is deformed. Deformation, through compression or dilation, may be a change in volume without a change in shape. Or, this may include a change in aspect ratio, a shear deformation, or a combination of the two. The fluid is compressed if subjected to an increase in pressure which consequently results an increase in the fluid density. In general, the fluid is considered incompressible if the changes in density are less than 3%, throughout the flow field (Potter, et al., 2002). This corresponds to a low speed flow, in general. At a Mach number less than 0.3, the fluid flow may be treated as incompressible flow. On the other hand, the flow is regarded as a compressible flow if the changes in the density are significant anywhere in the flow where the Mach number is greater than 0.3.

A fluid flow may also be classified as either viscous or inviscid. Viscosity can be defined as the internal resistance to shearing deformation. Hence, viscosity is related to the shear stress which results in deformation and energy dissipation of

the fluid in motion. Viscous flow is considered to be when the effects of viscosity are important and cannot be neglected. However, when the viscous effects do not influence the flow significantly, an approximated flow condition is used which is called inviscid flow. The viscous effect becomes negligible if the shear stresses in the flow are small or act over a small area since the viscous effects require substantial surface area in order to affect the flow significantly. Thus, the inviscid flow condition may be assumed for flow over a short distance. What is more, as discussed in section 2.2, the Reynolds number is a measure of inertial forces over the viscous forces present in the flow. For a flow where the inertial forces are strongly dominant, the flow may also be treated as inviscid flow.

In solving a fluid dynamics problem, the choice of the flow modelling technique depends on the classification of the flow. As defined and discussed in section 2.2, the Knudsen number may be used to identify the flow regime of a flow problem. Figure (3.1) shows the Knudsen number limits of various mathematical models developed in the study of fluid dynamics. At $Kn \leq 0.01$, the mean free path of the gas molecules is small enough to allow sufficient collisions between molecules to exchange energy and attain near-equilibrium condition. An inviscid continuum flow model such as the Euler equation solver will be able to provide an accurate solution of the flow. For $0.01 \leq Kn \leq 0.1$, there are relatively fewer collisions between gas molecules. The viscous effect is significant in influencing the flow and cannot be neglected. Hence, a continuum model which takes viscous effect into account is needed to model the flow. When the *Kn* grows

larger than 0.1, the flow becomes rarefied. The collisions between gas molecules are rare. At this condition, continuum breakdown occurs which prohibit the use of continuum techniques to model the flow.

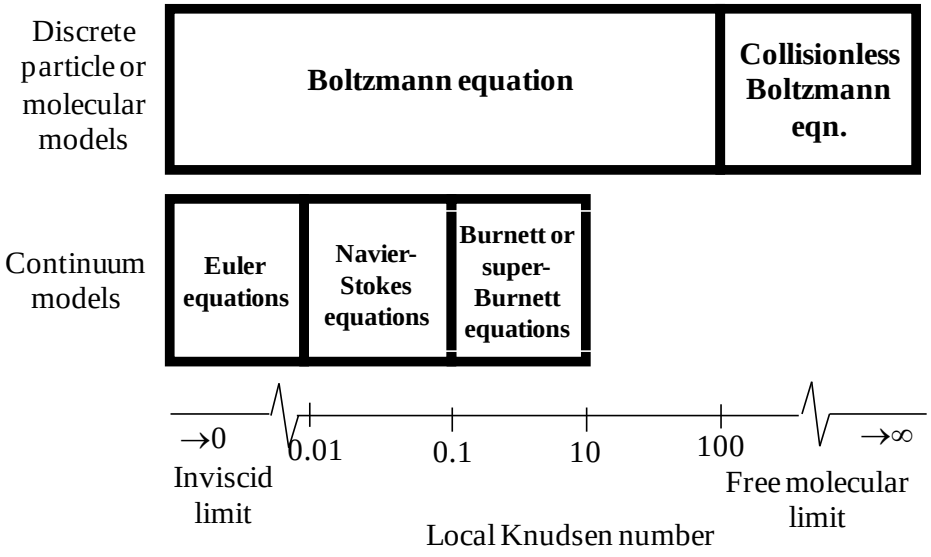

Figure 3.1 Knudsen number limits of various mathematical models, based on (Agarwal, Yun, & Balakrishnan, 2001; Bird, 1994).

Another branch of modelling techniques is to represent the flow by discrete particles based on the kinetic theory. The flow field is described mathematically by the famous Boltzmann equation, which will be discussed in detail in section 3.4. As the Boltzmann equation is a mathematically complex model to solve, various methods have been developed to approximate the solution to the Boltzmann equation. Some of these methods are discussed in this chapter.

3.2 Computational Fluid Dynamics

There are three approaches in the philosophical study of fluid flow phenomena which are the experimental, theoretical and computational fluid dynamics. Among these three, computational fluid dynamics (CFD) is the relatively newly developed approach. The foundations of experimental fluid dynamics were established in the 17^{th} century in France and England. Theoretical fluid dynamics was then developed in the 18^{th} and 19^{th} century primarily in Europe (Anderson, 1995). It was only in the latter half of the 20^{th} century that the numerical approach of studying fluid dynamics began to bloom after the advent of high speed digital computer facilities. CFD is robust in solving complex flow fields expeditiously with reliable accuracy. This has made CFD to be a partner of equal importance to both pure theoretical and pure experimental approaches. The three approaches often complement one another.

In the CFD approach, numerical methods and computational algorithms are developed to solve the governing equations of fluid flow in order to predict the flow field phenomena. The governing equations are usually discretised into discrete equations and computed by advancing them in space and time. The appropriate representation of the flow field is obtained with a collection of numbers.

Although the various CFD methods are often significantly different from each other, the CFD procedures consist of three general stages: pre-processing, simulation and post-processing. The pre-processing is a stage to generate a

computational mesh on the flow field over or within a defined geometry of interest. The flow field volume is divided into discrete computational cells. This is often the most important stage. The choice of mesh size and structure usually has a significant influence on the simulated solution, especially in the conventional CFD methods. The boundary and initial conditions are also defined in the pre-processing stage. In the simulation stage, the flow field is first initialised based on the initial conditions specified. Then the discrete governing equations, which usually represent the conservation of the fluid properties in respective computational cells, are solved in the manner of advancing in space throughout the whole flow field. The boundary conditions are applied to the inlet, outlet and interfaces between the flow field and any solid object within the flow field or wall boundaries that define the computational domain. In some instances, other equations are solved alongside the conservation equations, such as chemical reactions or heat transfer. The computed solution is then advanced in time to update the changes in the flow field over space and time until a satisfactory solution has been reached. In the post-processing stage, the computed solution is analysed and presented either in graphical or merely numerical form using appropriate post-processing software or techniques.

3.3 Conventional Computational Fluid Dynamics Method

The fundamental principles in fluid dynamics are that energy, momentum and mass are conserved. These principles are commonly expressed in partial

differential form to represent the state of the fluid in a defined control volume. This is the basis of all governing equations derived in the study of fluid dynamics. The well accepted governing equations of fluid dynamics are the famous Navier-Stokes equations for viscous flow or Euler equations when inviscid flow is considered. The Navier-Stokes, Euler, and Burnett equations are formulated assuming the concept of a continuum. The continuum assumption treats a fluid as a continuous medium with the fluid macroscopic properties, which are considered to be continuous functions of position and time (Fox, McDonald, & Pritchard, 2003). Hence, the conventional CFD methods are based on macroscopic continuum equations.

When the fluid in a flow is treated as inviscid condition, the behaviour of such a gas is governed by the Euler equations. The continuity equation given in Equation (3.1) as:

$$\frac{\partial \rho}{\partial t} + \nabla \cdot \left(\rho \vec{V} \right) = 0 \tag{3.1}$$

where ρ is the fluid density, t is the time, $\vec{V}$ is the flow velocity vector and ∇ is the gradient operator given in Equation (3.2) as:

$$\nabla = \vec{i} \frac{\partial}{\partial x} + \vec{j} \frac{\partial}{\partial y} + \vec{k} \frac{\partial}{\partial z} \tag{3.2}$$

The conservation of momentum equation is given in Equation (3.3) as:

$$\rho \frac{D\vec{V}}{Dt} = \rho \vec{g} - \nabla P \tag{3.3}$$

where $\vec{g}$ is the vector for gravitational field, P is the pressure and the substantial or material derivative is defined in Equation (3.4) as:

$$\frac{DQ}{Dt} = \frac{\partial Q}{\partial t} + \left(\vec{V} \cdot \nabla\right)Q \tag{3.4}$$

where Q represents any fluid property. Lastly, the energy equation is given in Equation (3.5) as:

$$\rho \frac{Dh}{Dt} = \frac{DP}{Dt} + \nabla \cdot \left(k \nabla T\right) \tag{3.5}$$

where $h = e + P/\rho$ is the enthalpy of the fluid with internal energy e, k is the thermal conductivity and T is the fluid temperature. In the conventional CFD methods, the Euler equations are solved when the viscous effect in the flow is negligible such as in the flow with infinitely high Reynolds number.

The Navier-Stokes equations are the equations used in the conventional CFD methods to solve for flow when the viscous effect is not negligible. The continuity equation has the same form as in Equation (3.1). The conservation of momentum equation is given in Equation (3.6) as:

$$\rho \frac{D\vec{V}}{Dt} = \rho \vec{g} - \nabla P \tag{3.6}$$

where μ is the first coefficient of viscosity which can be taken from measurements or the Sutherland's law, κ is second coefficient of viscosity in which Stokes' hypothesis can be used to assume $\kappa = -2/3\mu$ (White, 1991), δ_{ij} is the Kronecker delta function where $\delta_{ij} = 1$ if $i = j$ while $\delta_{ij} = 0$ if $i \neq j$ where the subscripts i and j

denote the three coordinate directions. The energy equation is given in Equation (3.7) as:

$$\rho \frac{Dh}{Dt} = \frac{DP}{Dt} + \nabla \cdot (k \nabla T) + \frac{\partial u_i}{\partial x_j} \left[\mu \left(\frac{\partial u_i}{\partial x_j} + \frac{\partial u_j}{\partial x_i} \right) + \delta_{ij} \kappa \nabla \cdot \vec{V} \right] \qquad (3.7)$$

Due to the mathematical complexity of solving the governing equations in their partial differential form, the conventional CFD method was built up in order to solve these theoretical governing equations numerically in discrete time intervals and spatial locations. The three basic ways of discretising time and space are finite difference, finite volume, and finite element.

In the conventional CFD methods, extra care is needed in meshing of the computational domain in order to ensure accurate results, convergence and stability of the simulation. There are generally three different types of meshes: structured, unstructured and hybrid meshes. Both structured and unstructured meshes have their own benefits and disadvantages while the hybrid meshes attempts to combine the advantages of both. Structured meshes usually require less computational resources to solve and the algorithm is more efficient for simple problems. For complex flow problems, unstructured meshes tend to have better performance than structured meshes due to better mesh alignment to the flow field. However, it requires extra effort and computational resources to generate and store the connectivity information between the cells. Whether structured or unstructured meshes are used, it is important to ensure that proper continuity exists across the interfaces between computational cells so that the

discrete solutions can be assembled to represent the complete solution of the flow field. Hence, the conventional CFD methods suffer from the major disadvantage that poor alignment of the grid with the flow field may result in significant errors because flux can only occur between elements which share an interface.

What is more, in unsteady flow simulations, it would be difficult to fit the constantly changing flow field into a fixed computational mesh. In such instance, an adaptive mesh may be used where the computational mesh changes according to the instantaneous solution of the flow field in order to ensure the gird aligns well with the flow. This will cost extra computational resources which may reduce the computational efficiency.

The need to solve the complete set of the governing equations for every computational cell is the main reason for high computational cost requirement. Due to the complexity of the governing equations, the computational cost is already high in the conventional CFD methods. This is made worse when a time dependent turbulent model is required in the simulation, for which extra equations must be solved.

3.4 Boltzmann Equation and Lattice Boltzmann Method (LBM)

Lim has done a review of the Boltzmann equation and used a lattice Boltzmann model for simulating compressible flows. The discussion of the distribution function, the derivations of the Boltzmann equation and LBM in this section are adapted from Lim's master thesis (Lim, 2004).

3.4.1 Distribution Function

In classical statistical mechanics, the goal is to derive all the equilibrium properties of a macroscopic molecular system from the laws of molecular dynamics. Thus, statistical mechanics predicts the equilibrium state of a given system (Huang, 1987). Unlike the continuum assumption used in traditional fluid dynamics, statistical mechanics is concerned with the collection of particles and determines the macroscopic properties of a fluid system by averaging across all the particles. Each particle carries an individual mass, *m*, and microscopic velocity, $\vec{\xi}$. The macroscopic properties such as the density, ρ, macroscopic velocity, $\vec{u}$, and internal energy, *e*, are then determined by averaging the respective values of the particles in the collection of particles around a given position.

A distribution function $f(\vec{x},\vec{\xi},t)d^3xd^3\xi$ is defined to represent the number of particles which have an individual position lying within a volume element d^3x about $\vec{x}$ and velocity lying within the velocity-space element $d^3\xi$ about $\vec{\xi}$ at time *t*. The volume elements d^3x and $d^3\xi$ are not the same as the infinitesimal quantities used in differential mathematics. Instead, they are finite volume elements which are large enough to contain a very large number of particles. On the other hand, they are also small enough to be considered as a point when compared to the macroscopic dimensions.

A phase space spanned by the position $\vec{x}$ and the velocity $\vec{\xi}$ of a particle is introduced to define the distribution function of $f\left(\vec{x},\vec{\xi},t\right)$ more precisely. The

schematic of a six-dimensional phase space is shown in Figure (3.2). A point $\left(\vec{x},\vec{\xi}\right)$ in the phase space, such as the point *A* in Figure (3.2), represents the state of a particle at the position of $\vec{x}$ with the velocity of $\vec{\xi}$. The state of the entire collection of *N* particles is represented by *N* points in this phase space.

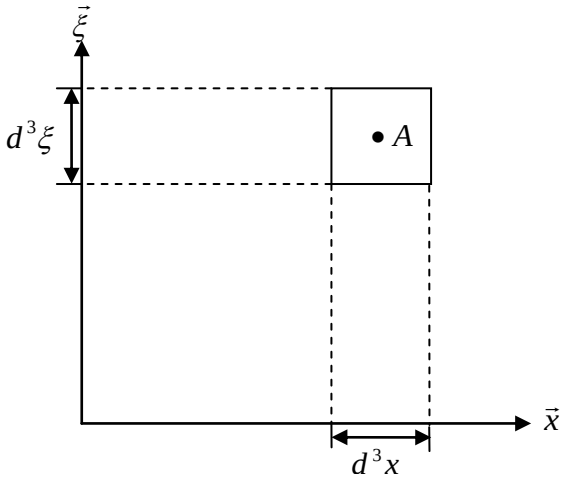

Figure 3.2 Schematic of the six-dimensional phase space.

The total number of particles within a volume element can be found by constructing a volume element about a point in the phase space. For example, a volume element $d^3x\ d^3\xi$ is constructed about point *A* in Figure (3.2). The distribution function $f(\vec{x},\vec{\xi},t)d^3xd^3\xi$ is, by definition, the number of points contained in each volume element. The distribution function $f\left(\vec{x},\vec{\xi},t\right)$ is considered continuous by assuming each volume element consists of a large number of points and the density gradient between these points is small. Hence, an approximation can be made for the entire phase as given in Equation (3.8):

$$\sum f(\vec{x},\vec{\xi},t)d^3xd^3\xi \approx \int f(\vec{x},\vec{\xi},t)d^3xd^3\xi \qquad (3.8)$$

Consequently, the total number of particles in the phase space can be determined from Equation (3.9) as:

$$N = \int f(\vec{x}, \vec{\xi}, t) d^3x d^3\xi \tag{3.9}$$

3.4.2 Boltzmann Equation

The Boltzmann equation is a time evolution function of the particle distribution function. The particle distribution function changes with time due to the fact that the particles constantly travel in and out the volume element in the phase space. The motion of the particles is due to the particles' translation with their original velocity. When the particles are subjected to an external force field the particles' velocities change. Eventually, collisions occur between particles which further change the particles' velocities.

The Boltzmann equation can be derived by tracking the changes of positions and velocities of the particles in a volume element $d^3x d^3\xi$ constructed about point *A* in the phase space with the coordinates of $(\vec{x}, \vec{\xi})$ as shown in Figure (3.3). After a small time step of Δt, the coordinates of point *A*, $(\vec{x}, \vec{\xi})$ shifts to the new phase at point A' with the coordinates changed to $(\vec{x} + \vec{\xi}\Delta t, \vec{\xi} + (\vec{F}/m)\Delta t)$. The parameter $\vec{F}$ in the new coordinates is the external force acting on the particles.

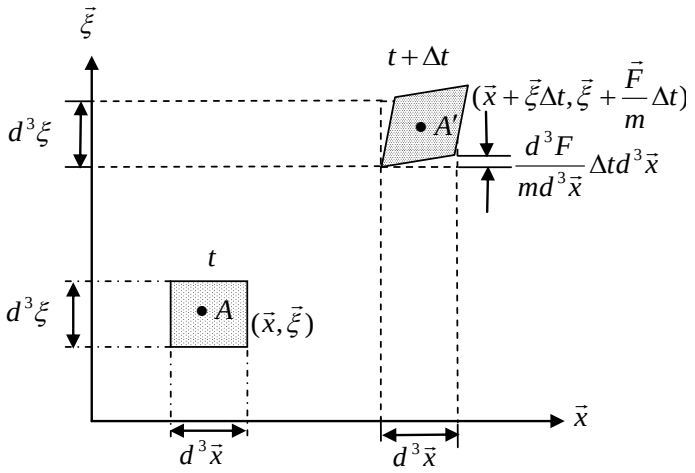

Figure 3.3 Schematic of time evolution of a volume element in phase space (Huang, 1987) .

In the absence of collisions, the number of particles within the volume element will be conserved. There are no particles entering or leaving the volume element. All the particles within the volume element will travel to new location without the collisions between the particles. The evolution equation for the particle distribution function can then be expressed in Equation (3.10) as

$$f(\vec{x}+\vec{\xi}\Delta t, \vec{\xi}+\frac{\vec{F}}{m}\Delta t, t+\Delta t)d^3xd^3\xi = f(\vec{x},\vec{\xi},t)d^3xd^3\xi \qquad (3.10)$$

By cancelling the $d^3xd^3\xi$ term on both sides of the equation, Equation (3.10) is then reduced to Equation (3.11):

$$f(\vec{x}+\vec{\xi}\Delta t, \vec{\xi}+\frac{\vec{F}}{m}\Delta t, t+\Delta t) = f(\vec{x},\vec{\xi},t) \qquad (3.11)$$

When the collisions between particles are considered, Equation (3.11) has to be modified. The collisions between particles will change the particles' velocities. As a result, some of the particles will enter or leave the control volume. Therefore

the number of particles within the volume element will no longer be conserved. Thus, the collision term, Ω, is introduced and added into Equation (3.11) to describe the change in the particle distribution due to the effects of collisions between particles. The collision term is added into the distribution function and expressed in Equation (3.12) as:

$$f(\vec{x}+\vec{\xi}\Delta t, \vec{\xi}+\frac{\vec{F}}{m}\Delta t, t+\Delta t) = f(\vec{x},\vec{\xi},t)+\Omega_{col}\Delta t \qquad (3.12)$$

In order to express the Boltzmann equation in the differential form rather than the difference form as in Equation (3.12), the Taylor expansion is applied to the left-hand side of Equation (3.12) to the first order in Δt to form Equation (3.13) as:

$$\begin{aligned} & f(\vec{x}+\vec{\xi}\Delta t, \vec{\xi}+\frac{\vec{F}}{m}\Delta t, t+\Delta t) \\ &= f(\vec{x},\vec{\xi},t)+\frac{\partial f}{\partial t}\Delta t+\vec{\xi}\Delta t\cdot\nabla_{\vec{x}} f+\frac{\vec{F}}{m}\Delta t\cdot\nabla_{\vec{\xi}} f+O(\Delta t^2) \end{aligned} \qquad (3.13)$$

By substituting Equation (3.13) into Equation (3.12), the Boltzmann equation is expressed as a partial differential equation given in Equation (3.14) as:

$$\frac{\partial f}{\partial t}+\vec{\xi}\cdot\vec{\nabla}_{\vec{x}} f+\frac{\vec{F}}{m}\cdot\vec{\nabla}_{\vec{\xi}} f+O(\Delta t)=\Omega_{col} \qquad (3.14)$$

By letting $\Delta t \to 0$, the first order error term in Equation (3.14) $O(\Delta t)$ can be neglected and the Boltzmann equation in the differential form is given in Equation (3.15) as:

$$\frac{\partial f}{\partial t}+\vec{\xi}\cdot\vec{\nabla}_{\vec{x}} f+\frac{\vec{F}}{m}\cdot\vec{\nabla}_{\vec{\xi}} f=\Omega_{col} \qquad (3.15)$$

For flow fields with an absence of external forces, such as in the case of a non-rotating rotor or stationary flow channel, the external force term in the Boltzmann equation is normally neglected. Hence, the Boltzmann equation without considering external force acting on the flow field can be written in Equation (3.16) as:

$$\frac{\partial f}{\partial t} + \vec{\xi} \cdot \vec{\nabla}_{\vec{x}} f = \Omega_{col} \tag{3.16}$$

One of the important terms in the Boltzmann equation is the collision term, Ω_{col}. As mentioned above, the velocities of the particles within a volume element change due to the collisions between particles and the particles will be able to travel in and out of the volume element. Thus, the total number of particles inside a volume element will vary. In other words, the collision term is the rate of change in the density of the particle distribution function.

Due to the mathematical difficulty in solving the Boltzmann equation analytically, numerical approaches are adopted to solve the Boltzmann equation. However, it is very computationally expensive to evaluate the collision term in the Boltzmann equation as given in Equation (3.16). One of the important considerations in modelling the collision term is that the basic conservation laws of physics (conservation of mass, momentum, and energy) have to be satisfied. By letting η denote any of these conservative properties, either mass, momentum, or energy of the particles, the restriction of a collision model can be written in the following integral form given in Equation (3.17) as:

$$\int \Omega_{col} \eta d^3\xi = 0 \qquad (3.17)$$

It is common to approximate the collision term using various simplified collision models. This allows the simplified Boltzmann equation to be modelled which is generally named as the Model Boltzmann Equation (MBE). A variety of MBEs have been proposed such as the higher order Chapman-Enskog expansions, the Fokker-Planck approximation (Risken, 1989) and the ellipsoidal model by Holway (Holway, 1966). One of the simplest models, which is commonly adopted in the majority of MBEs reported recently, is the Bhatnagar-Gross-Krook (BGK) simplified collision model (Bhatnagar, et al., 1954), which was also developed independently by Welander at about the same time (Welander, 1954). In the BGK model, the rate of change in the density of the particle distribution function is assumed to be proportional to the difference between the present distribution function and the equilibrium distribution function. The BGK collision model is called single-relaxation-time model and is given in Equation (3.18) as:

$$\Omega_{col} = -\frac{1}{\tau}(f - f^{eq}) \qquad (3.18)$$

where τ is the relaxation time and f^{eq} is the Maxwell-Boltzmann distribution function.

3.4.3 Equilibrium Boltzmann Equation

The equilibrium distribution function is the solution to the Boltzmann equation as shown in Equation (3.16). It describes the state where the Boltzmann equation

achieves the equilibrium condition and no longer depends explicitly on time. The equilibrium distribution function is called the Maxwellian-Boltzmann equilibrium distribution function. It can be derived from the Boltzmann *H*-theorem (Huang, 1987), and is given in Equation (3.19) as:

$$f^{eq} = n\left(\frac{m}{2\pi k_B T}\right)^{\frac{D}{2}} \exp\left[-\frac{m(\vec{\xi}-\vec{u})^2}{2k_B T}\right] \tag{3.19}$$

where n is the number density of particles within the volume element, m is the molecular mass, k_B is the Boltzmann constant, T is the macroscopic temperature, D is the dimension of the space, $\vec{\xi}$ is the microscopic velocity and $\vec{u}$ is the macroscopic velocity.

3.4.4 Chapman-Enskog Expansion and Recovery of the Navier-Stokes Equation

Although the Boltzmann equation is derived with a different approach compared to the derivation of the governing equations used in traditional fluid dynamics, it describes the fluid flow phenomena in the same manner as traditional fluid dynamics. In fact, the governing equations of fluid dynamics, which are formulated based on the concept of a continuum, can be recovered from the Boltzmann equation by applying the Chapman-Enskog expansion.

The Chapman-Enskog expansion uses an asymptotic expansion of the distribution function near the equilibrium distribution to approximate the

Boltzmann equation (Huang, 1987). It is assumed that the distribution function can be expanded into a series form as given in Equation (3.20):

$$f = f^{(0)} + \delta f^{(1)} + \delta^2 f^{(2)} + \cdots = \sum_{n=0}^{\infty} \delta^n f^{(n)} \qquad (3.20)$$

with $f^{(n)}$ getting smaller as n increases. The first term in Equation (3.20) is the equilibrium distribution function which says that $f^{(0)} = f^{eq}$ where δ is a parameter representing the perturbations from the equilibrium phase space distribution.

The Euler equation, which describes an inviscid flow in traditional fluid dynamics, can be represented by the zeroth-order terms of the Chapman-Enskog expansion. The Navier-Stokes equation, which governs a viscous flow, can be viewed as the first-order terms of the Chapman-Enskog expansion (Huang, 1987). In recent years, the Burnett equations have been developed as the second-order terms of the Chapman-Enskog expansion to provide solution for a flow with $0.1 < Kn < 10$ as shown in Figure 3.1.

3.4.5 Lattice Boltzmann Method

The Lattice Boltzmann method (LBM) is a MBE method that utilizes a finite set of discrete molecular velocities to discretise the Boltzmann distribution function. Hence, a discrete velocity, space and time on lattice grid is used to solve the Boltzmann equation. In LBM, the velocity in the phase space is discretised into a

velocity set. The number of velocities $\vec{\xi}_\alpha$ in a velocity set is finite. The subscript α denotes the α^{th} module of the velocity set in the discrete phase space with α = 1…M where M is the total number of velocities in the velocity set. Each one of the velocities in the velocity set represents a microscopic velocity of a particle. Besides, the position space is also discretised in such a manner to allow the particles that travel with velocity $\vec{\xi}_\alpha$ to arrive at a corresponding node after a given time step. In other words, a particle with the velocity of $\vec{\xi}_\alpha$ will travel from a given grid node of $\vec{x}$ to a destination grid node of $\vec{x}+\vec{\xi}_\alpha \Delta t$. Figure (3.4) illustrates two common examples of the velocity sets and grid models.

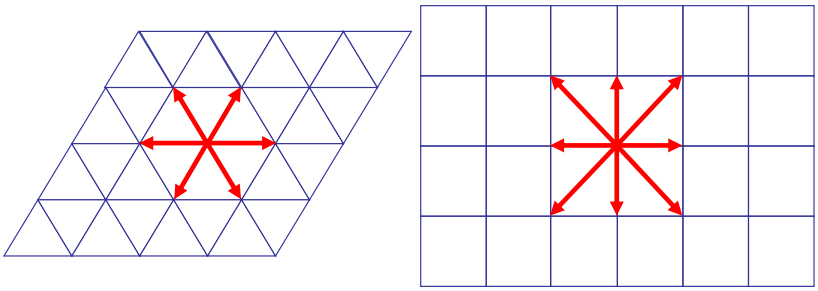

Figure 3.4 Schematic of velocity set of a 7-velocities LB model on a hexagonal grid (left) and velocity set of a 9-velocities LB model on a square grid (right).

The evolution equation for the LBM is the difference form of the Boltzmann equation and is given in Equation (3.21) as:

$$f(\vec{x}+\vec{\xi}_\alpha \Delta t, \vec{\xi}_\alpha, t+\Delta t) - f(\vec{x}, \vec{\xi}_\alpha, t) = \Omega_\alpha \qquad (3.21)$$

where the collision term is the BGK simplified collision term (Bhatnagar, et al., 1954) and is given in Equation (3.22) as:

$$\Omega_\alpha = -\frac{1}{\tau}\left[f(\vec{x},\vec{\xi}_\alpha,t) - f^{eq}(\vec{x},\vec{\xi}_\alpha,t)\right] \tag{3.22}$$

The macroscopic quantities can be evaluated by employing the Chapman-Enskog assumption. The macroscopic quantities are determined from the microscopic quantities and the equilibrium distribution function. Hence, the macroscopic quantities are defined in Equation (3.23) as:

$$Y \equiv \int \eta f^{eq}\left(\vec{x},\vec{\xi},t\right)d\vec{\xi} \tag{3.23}$$

where η is any of the microscopic conservative quantities of a particle such as mass, density, momentum, and energy. Y is the corresponding macroscopic quantity.

After discretising the phase space, Equation (3.23) is then approximated by Equation (3.24) as:

$$Y = \int \eta\left(\vec{\xi}\right) f^{eq}\left(\vec{x},\vec{\xi},t\right)d\vec{\xi} = \sum_\alpha W_\alpha \eta\left(\vec{\xi}_\alpha\right) f^{eq}\left(\vec{x},\vec{\xi}_\alpha,t\right) \tag{3.24}$$

where W_α is a weight coefficient. Equation (3.24) is then rewritten in Equation (3.25) as:

$$Y = \sum_\alpha \eta\left(\vec{\xi}_\alpha\right) f_\alpha^{eq}\left(\vec{x},\vec{\xi}_\alpha,t\right) \tag{3.25}$$

where the equilibrium distribution function for α^{th} velocity module is given in Equation (3.26) as:

$$f_\alpha^{eq}\left(\vec{x},\vec{\xi}_\alpha,t\right)d\vec{\xi} = W_\alpha f^{eq}\left(\vec{x},\vec{\xi}_\alpha,t\right) \tag{3.26}$$

One of the important limitations inherent in most of the MBE methods such as LBM is that finite limits must be constrained on the velocity space which is

theoretically limitless in extent. These limits are chosen in order to ensure the scheme has a negligible number of particle velocities that lie outside the range of the discretised velocity space. Consequently, the macroscopic velocity is limited. Therefore, the basic LBM has great difficulty in simulating compressible flows at high Mach numbers (Alexander, Chen, Chen, & Doolen, 1992; Sun, 1998; Sun & Hsu, 2004).

Moreover, the LBM is well known to have instability problems that arise frequently when solving non-isothermal flows with large temperature variants. This may be due to the equilibrium distribution function used in the basic LBM not being equivalent to the Maxwell-Boltzmann equilibrium distribution function (Xu & Luo, 1998). Hence, the equilibrium distribution obtained in solving non-isothermal flows cannot simultaneously guarantee the fulfilment of Boltzmann's *H*-theorem which ensures the equilibrium velocity distribution function is at the maximum entropy state (Sterling & Chen, 1996; Succi, 2001). This limits the basic LBM to the simulation of isothermal flows.

3.5 Direct Simulation Monte Carlo Method

The Direct Simulation Monte Carlo (DSMC) method is a particle-based technique developed in the 1960s which takes into account kinetic theory when simulating the flow field. It was first developed by Bird for investigating the translational relaxation of a monatomic gas (Bird, 1963). Since it was introduced, the DSMC technique has become a notable kinetic theory based simulation method

particularly for near continuum and rarefied flows. It has been implemented in a variety of applications including CVD reactor modelling (Cave, 2008; Coronell & Jensen, 1992), supersonic jet simulations (Teshima & Usami, 2001), hypersonic flows in astronautic studies (LeBeau & Lumpkin III, 2001) and microfluid flow modelling (Karniadakis & Beşkök, 2002).

In the DSMC method, a number of simulated particles are chosen to represent a very large number of actual gas particles within a computational cell. The DSMC method models the macroscopic behaviour of the gas by decoupling the ballistic motion of the gas particles and their intermolecular collisions over a time step which is smaller than their mean collision time. The computational grid is chosen to be a size that is less than the mean free path of the gas. The intermolecular collisions are simulated in a probabilistic manner.

It has been shown that the DSMC method solves the Boltzmann equation statistically (Bird, 1970b). The DSMC method has also been proven mathematically to provide a solution to the Boltzmann equation if the number of simulated particles used is close to the actual amount of gas particles (Wagner, 1992).

3.5.1 Typical DSMC Implementation Procedures

The implementation of the DSMC method is much relatively simpler than that of both conventional CFD methods and the LBM. It is, however, strongly based on the assumption that the flow can be split into free flight phase and collision phase.

Hence, the accuracy of DSMC method depends heavily on the choices of the simulation time step and the computational grid size. The accuracy also depends upon the methods used to model the physical processes during the simulation. In particular, the molecular collisions process and the sampling technique to obtain the flow properties from the limited number of simulated particles used.

After setting up the simulation domain with boundary conditions and initialising the simulated particle velocities and positions, the simulated particles are moved in free flight without collision. The simulated particles are allowed to move in a true directional manner. This means they are able to move not only to adjacent cells sharing an interface but to diagonally adjacent cells as well within one time step. The simulated particles are moved and indexed to a new position x' in the grid which is given in Equation (3.27) as:

$$x' = x + v\Delta t \tag{3.27}$$

where x is the vector of the original locations, v is the vector of particle velocities and Δt is the time step used. Typically, no external forces are involved during the free flight phase. Thus, the particle velocities remain unchanged. To allow such a free flight condition, the time step chosen which separates the free flight phase and collision phase needs to be less than the mean collision time Δt_{col}. Generally, $\Delta t \leq \Delta t_{col}/5$ is recommended (Bird, 2006).

During the free flight phase, the interaction of the simulated particles with the flow boundaries is also enforced. The inflow and outflow boundaries can be implemented through a constant free stream or periodic boundary conditions. The

interaction of simulated particles with the solid surfaces can be implemented as either specular or diffuse reflection. The specular reflection considers a complete elastic collision with the surface where the velocity component normal to the surface is reversed while maintaining the same tangential component. The diffuse reflection, however, destroys all incident velocities on the surface. Simulated particles are assumed to reach thermal equilibrium with the solid surface and assigned a velocity sampled from the Maxwell-Boltzmann equilibrium distribution function using the wall temperature and zero bulk velocity. The simulated particles are then released from the surface in random directions.

At the end of the free flight phase, the simulated particles are indexed to the computational grid to sample the local flow properties within the computational cell prior to collision. The size of the sampling cell is important as the sampled cell properties dictate the collision rate of the simulated particles. In general, the collision partners are chosen within the sampling cell, or sometimes within a sub-cell, to allow collisions within a time step Δt. Thus, the cell size used needs to be smaller than the mean free path of the physical gas molecules λ, and is commonly chosen to be in the order of $\lambda/3$. Besides, having sufficient simulated particles within the sampling cell is also required in order to calculate the macroscopic flow properties in the cell with an acceptable level of statistical scatter. Generally, the amount of simulated particles is chosen to ensure the number of particles per computational cell is maintained at about 20 throughout the simulation (Bird, 2006).

Lastly, the collisions of the simulated particles are simulated during the collision phase which changes the particles velocities and internal energies. During the collision phase, the simulated particles undergo probabilistic collisions. The efficient No Time Counter (NTC) scheme (Bird, 1994) is commonly used in many DSMC codes. In the NTC scheme, the number of simulated particle pairs to be selected for collision is given in Equation (3.28) as:

$$N_{pair} = \frac{nN_c\left(\sigma_T v_r\right)_{\max} \Delta t}{2} \tag{3.28}$$

where n is the number density of the physical gas, N_c is the number of simulated particles within the sampling cell, σ_T is the total collision cross section and v_r is the relative velocity of the collision partners. The collision partners are chosen randomly using an acceptance-rejection method with the condition given in Equation (3.29) as:

$$R_f < \frac{\sigma_T v_r}{\left(\sigma_T v_r\right)_{\max}} \tag{3.29}$$

where R_f is an uniform distributed random number between 0 and 1. Post-collision velocities of each simulated particle are updated accordingly at the end of the collision phase.

The free flight and collision phase are then repeated iteratively until the simulation is completed. Due to the stochastic particle collision treatment in the DSMC method, there is usually statistical scatter in the results especially for flows approaching the continuum regime. An ensemble average of a number of runs is usually made to reduce the statistical scatter in the result. For steady flow, an

ensemble average is made of several runs after the steady state is reached whereas an ensemble average of separate runs is carried out for unsteady flow.

3.5.2 Collision Models Adopted in DSMC Method

Referring to Equation (3.28), the total collision cross section σ_T is determined depending on the collision model being used. There are various collision models developed. The three common collision models are the hard sphere (HS) model, variable hard sphere (VHS) model and variable soft sphere (VSS) model. The total collision cross section for these three models depends on the deflection angle after collision χ, the relative velocity v_r of the collision partners, and the distance of closest approach b. These parameters are illustrated in Figure (3.5). The details of each collision model can be found in the text by Bird (Bird, 1994).

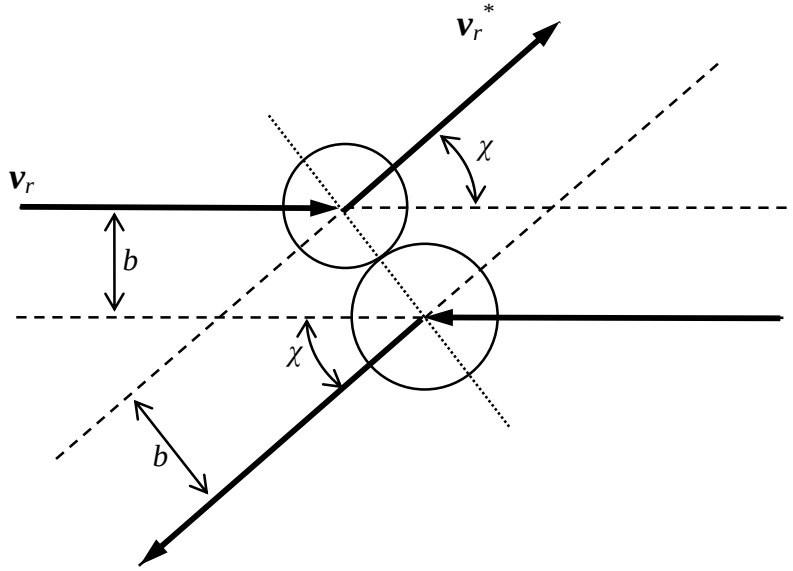

Figure 3.5 Collision parameters of a binary collision.

The simplest collision model is the hard sphere model in which the collision is fully elastic. The hard sphere collision partners will collide if $b \leq d_{12}$ where d_{12} is the mean molecular diameter of the two molecules. The total collision cross section is independent of the deflection angle χ and is given in Equation (3.30) as:

$$\sigma_T = \pi d_{12}^2 \tag{3.30}$$

The HS model is advantageous in that it is easily calculated. However, the total cross section is independent of the relative translational energy in the collision so the HS model provides an erroneous relationship between the viscosity coefficient and temperature.

The variable hard sphere (VHS) molecular model was introduced to overcome the error encountered in the HS model (Bird, 1994). In the VHS model, the molecular diameter is expressed as a function of the relative velocity of the collision partners. This function usually takes the form of simple inverse power law. Hence, the total collision cross section of the VHS model is given in Equation (3.31) as:

$$\sigma_T = \pi d_{VHS}^2 \tag{3.31}$$

where the molecular diameter, d_{VHS}, is given in Equation (3.32) as (Bird, 1994):

$$d_{VHS} = \left[\frac{(15/8)(m/\pi)^{1/2}(kT_{ref})^{\omega}}{\Gamma(9/2-\omega)\mu_{ref} E_t^{\omega-1/2}} \right]^{1/2} \tag{3.32}$$

where m is the mass of the gas molecule, k is the Boltzmann constant, μ_{ref} is the viscosity coefficient at reference temperature T_{ref}, ω is the temperature exponent

of the viscosity coefficient (commonly known as the viscosity index), Γ represents the gamma function and E_t is the relative translational energy given in Equation (3.33) as:

$$E_t = \frac{1}{2}\frac{m_1 m_2}{m_1 + m_2} v_r^2 \tag{3.33}$$

The deflection angle of VHS model is given in Equation (3.34) as:

$$\chi = 2\cos^{-1}\left(\frac{b}{d}\right) \tag{3.34}$$

In the VHS model, the momentum transfer cross section is equivalent to the total collision cross section. This results in discrepancies between the VHS and the inverse power law model when the molecular diffusion is important in the flow field (Koura, Matsumoto, & Shimada, 1991). Following the discovery of this problem, a variable soft sphere (VSS) model was introduced (Koura & Matsumoto, 1991). The molecular diameter in the VSS model varies as a function of the relative velocity in a similar manner to the VHS model but the deflection angle is determined by Equation (3.35) as:

$$\chi = 2\cos^{-1}\left[\left(\frac{b}{d_{VSS}}\right)^{1/\alpha}\right] \tag{3.35}$$

where α is a VSS molecular parameter which is the exponent of the cosine of the deflection angle. The total collision cross section in the VSS model can be calculated using Equation (3.31) by replacing with the VSS molecular diameter d_{VSS} given in Equation (3.36) as (Bird, 1994):

$$d_{VSS} = d_{ref}\sqrt{\frac{\left(\frac{2kT_{ref}}{m_r v_r^2}\right)^{\varpi-1/2}}{\Gamma(5/2-\omega)}} \tag{3.36}$$

where d_{ref} is the reference diameter at temperature T_{ref} and m_r is the reduced mass of the collision partners given in Equation (3.37) as:

$$m_r = \frac{m_1 m_2}{m_1 + m_2} \tag{3.37}$$

For polyatomic molecules, there are internal degrees of freedom in the rotational and vibrational modes, in addition to the translational degree of freedom. During the collision of polyatomic molecules, the internal energy of the molecule is exchangeable with the translational energy. This is defined as an inelastic collision. A variety of phenomenological approaches have been proposed to model the energy exchange between the translational and internal degrees of freedom with the DSMC method. The Borgnakke-Larsen (BL) model is a widely accepted phenomenological collision model that gives adequate accuracy at low computational expenses (Borgnakke & Larsen, 1975). The BL model, using a statistical method, considers a fraction of the total number of collisions to be inelastic and subjected to internal energy exchange. More detail of the BL model will be discussed in section 4.3.

3.5.3 Advantages and disadvantages of DSMC method

The DSMC method is always numerically stable and does not suffer from convergence problems. Due to the nature of the technique in simulating the behaviour of the real gas directly, the DSMC simulated particles can carry and transfer mass, momentum and energy between any two locations in the flow field, not just between elements with a shared interface. Such flow property transport methods are termed true directional fluxing. Therefore, setting up a mesh that is aligned with the flow is not a requirement for the DSMC method. This saves significant pre-processing effort and time in setting up a simulation. In addition, the stochastic collision between selected collision partners carried out in DSMC method allows gradual and selective transfer of momentum and energy. This enables the DSMC method to be capable of handling non-equilibrium effects accurately.

However, due to the nature of particle tracking, DSMC method imposes an expensive computational cost especially in solving near continuum or continuum flows. The requirements for time step, sampling cell size, and the number of particles per cell set the limiting conditions for the applicability of DSMC method. For high density flows, the mean collision time and mean free path of the molecules are significantly smaller. This results in longer computational time in the DSMC method due to the restriction of having small time steps and higher memory requirements for smaller sampling cells while a larger amount of simulated particles are needed.

Furthermore, the DSMC algorithm requires the use of random numbers and is thus subject to statistical scatter. Hence, it requires an averaging of the results over a large number of time steps to reduce the scatter in the sampled macroscopic properties. This further increases the computational cost of the simulation especially for unsteady flows. In raising the computational speed to extend the applicability of DSMC method, various studies have been performed in either parallelising or hybridising the basic DSMC algorithm.

In parallelising the DSMC method, the computations of the simulation are carried out over multiple computer processors. The DSMC method is well suited for parallelisation since the coupling of the simulated particles occurs only during the collision phase while the collisions between particles are purely local and independent of the information in the other cells. A large number of studies in parallelizing DSMC computation have been conducted by various research groups including Boyd's (Dietrich & Boyd, 1996), LeBeau's (LeBeau, 1999) and Wu's (Wu & Lian, 2003).

In hybridising the DSMC method, the basic DSMC algorithm is usually coupled to a continuum solver. Such hybrid methods will enable non-continuum regions to be detected through the use of a continuum breakdown parameter and the flow field in these regions is simulated by DSMC method, while continuum flow regions are computed using an appropriate numerical continuum method such as the Navier-Stokes equations solver. The major challenge for the hybridisation of the DSMC and the continuum solver is the detection of the flow

regime for the respective solver and the information coupling between the solvers. Examples of the study on the hybridisation of DSMC-continuum method include the hybrid continuum/particle approach for modelling subsonic rarefied flows by Sun *et al.* (Sun, Boyd, & Candler, 2004) and the coupled DSMC-NS scheme using unstructured meshes by Wu *et al.* (Wu, Lian, Cheng, Koomullil, & Tseng, 2006).

3.6 Other Kinetic Theory Solvers

The main reason that DSMC method is not widely used in all fluid flow problems is the computational expense and statistical scatter apparent in the results. Many efforts have been made to make the computation process of the DSMC method faster for use in near continuum flows including Macrossan's υ-DSMC scheme (Macrossan, 2001) and collision limited DSMC schemes (Sharma & Long, 2004; Titov & Levin, 2007). Despite these advances, direct simulations used as continuum solvers are still very expensive solutions compared to finite volume solvers solving the Euler equations. A continuum method, derived from kinetic theory with the conceptual strengths of direct simulations and the speed of continuum solvers would be extremely useful in situations where a quicker result yet with accuracy in an acceptable range is desired. For example, in the PP-CVD reactor flow field simulations for the design of reactor and operational conditions, a fast approximated solution is needed. For this reason, several kinetic theory based solvers are studied and briefly described.

3.6.1 Equilibrium Particle Simulation Method

In the high collision rate limit of the DSMC method, the particle velocity distributions approach that of the Maxwell-Boltzmann equilibrium distribution and moments of the Boltzmann equation reduce to the Euler equations (Gombosi, 1994). For this, Pullin has proposed the Equilibrium Particle Simulation Method (EPSM) as a continuum flow solver to provide a DSMC solution at the infinite collision limit (Pullin, 1980). Hence, technically, EPSM represents a solution to the Euler equations.

In EPSM, the standard collision phase in the DSMC is replaced by a different method. The collision phase is arguably the most computational expensive phase in the DSMC procedure. During collision phase in EPSM, the simulated particles are assigned new velocities from the local Maxwell-Boltzmann velocity distribution based on the state of the cell. Similar to the DSMC, these particle locations remain unchanged during this "collision" phase. The new velocities are generated randomly in each cell for each time step. However, since the velocities are generated randomly from the equilibrium distribution, EPSM also exhibits statistical scatter in the results and as such requires averaging over a large number of time steps in the same way as the DSMC method.

3.6.2 Equilibrium Flux Method

Pullin also proposed the Equilibrium Flux Method (EFM) in which fluxes are calculated analytically across the interface of two cells by taking the moments of the equilibrium function at the location of the shared interface (Pullin, 1980). The EFM fluxes are derived by assuming an equilibrium distribution of the molecular velocities locally in the computational cells. This equilibrium, molecular velocity distribution is the Maxwell-Boltzmann velocity probability distribution function given in Equation (3.19).

Consider a typical one dimensional cell surface with the conserved macroscopic properties η given in Equation (3.38) as:

$$\eta = \begin{bmatrix} \rho \\ \rho u \\ \rho\left(\frac{1}{2}u^2 + c_p T\right) \end{bmatrix} \tag{3.38}$$

where ρ is the density, and c_p is the specific heat for constant pressure. By using the velocity distribution function and the conserved properties on either side of the surface, the net flux of η, F_η, across the cell surface can be expressed as:

$$F_\eta = F^+_{\eta,EFM} + F^-_{\eta,EFM} \tag{3.39}$$

where the superscripts + and – denote conditions on the left and right of the surface, respectively. The flux due to the gas molecules transporting from the left to the right of the surface can be determined by evaluating the integral given in Equation (3.40) as:

$$F^+_{\eta,EFM} = \int_0^\infty v\eta^+ f(v)dv \tag{3.40}$$

while the flux due to the gas molecules transporting from the right to the left of the surface is computed by evaluating the integral given in Equation (3.41) as:

$$F_{\eta,EFM}^{-} = \int_{-\infty}^{0} v\eta^{-} f(v)dv \tag{3.41}$$

Using the equilibrium molecular velocity distribution on either side of the surface, the integral in Equation (3.40) can then be expanded to the form given in Equation (3.42) as:

$$\begin{aligned} F_{\eta,EFM}^{+} = W^{+}\begin{bmatrix} \rho u \\ \rho u^2 + \rho RT \\ \rho u\left(\frac{1}{2}u^2 + c_p T\right) \end{bmatrix}^{+} \\ + D^{+}\begin{bmatrix} \rho\sigma \\ \rho\sigma u \\ \rho\sigma\left(\frac{1}{2}u^2 + \frac{1}{2}(\gamma+1)c_v T\right) \end{bmatrix}^{+} \end{aligned} \tag{3.42}$$

where c_v is the specific heat for constant volume, γ is the ratio of specific heats and the variables W^+ and D^+ are given in Equation (3.43) as:

$$W^{+} = \frac{1}{2}\left\{1 + erf\left[\left(\frac{u}{\sigma}\right)^{+}\right]\right\} \qquad D^{+} = \frac{1}{2\sqrt{\pi}} exp\left[-\left(\frac{u}{\sigma}\right)^{2+}\right] \tag{3.43}$$

Similarly, Equation (3.41) can be expanded to the form given in Equation (3.44) as:

$$F^{-}_{\eta,EFM} = W^{-}\begin{bmatrix} \rho u \\ \rho u^2 + \rho RT \\ \rho u\left(\frac{1}{2}u^2 + c_p T\right) \end{bmatrix} + D^{-}\begin{bmatrix} \rho\sigma \\ \rho\sigma u \\ \rho\sigma\left(\frac{1}{2}u^2 + \frac{1}{2}(\gamma+1)c_v T\right) \end{bmatrix} \tag{3.44}$$

where the variables W^{-} and D^{-} are given in Equation (3.45) as:

$$W^{-} = \frac{1}{2}\left\{1 - \mathrm{erf}\left[\left(\frac{u}{\sigma}\right)^{-}\right]\right\} \qquad D^{-} = -\frac{1}{2\sqrt{\pi}}\exp\left[-\left(\frac{u}{\sigma}\right)^{2-}\right] \tag{3.45}$$

EFM is not subject to the statistical scatter inherent in the DSMC or the EPSM methods. However, the extension of the EFM to two or higher spatial dimensions is performed by calculating a series of one dimensional fluxes across the shared interfaces between cells. This is called the direction decoupled method which is commonly adopted in conventional CFD methods. The EFM method has been implemented in various studies, for example, Macrossan applied the EFM in computing the non-equilibrium chemical reaction in a flow (Macrossan, 1989).

3.6.3 True Direction Equilibrium Flux Method

Smith (Smith, 2008) has developed the True Direction Equilibrium Flux Method (TDEFM) which represents the more general form of the EFM and takes multiple moments over both velocity and physical space. The TDEFM is the analytical solution to molecular fluxes selected from the Maxwell-Boltzmann equilibrium distribution of any source cell to an arbitrary destination region during the free flight phase of the gas molecules. This allows fluxes to be exchanged between all cell locations and is not restricted to only the shared interface.

The true directional nature of the scheme has the advantage of providing more accurate solutions. It has been shown that directional decoupled methods may produce non-physical results such as negative temperatures or densities at strong shocks interaction region when the cell structure is not well aligned with the physical structure in the flow (Cook, 1998). The directional decoupled solvers may also produce asymmetrical solutions for flow problems in which symmetrical results are expected. Figure (3.6) shows the comparison of the solution between directional decoupled solvers (i.e. EFM and Van Leer (van Leer, 1982)) and the TDEFM for radially imploding or exploding flows on rectangular meshes. For this problem, there is a low pressure cylindrical region initially enclosed in a high pressure surrounding. It is expected that a cylindrically symmetric shock wave will propagate toward the centre, causing an increase in temperature and density as the shock travels inwards. The comparison shows that the directional decoupled solvers produce asymmetrical solutions.

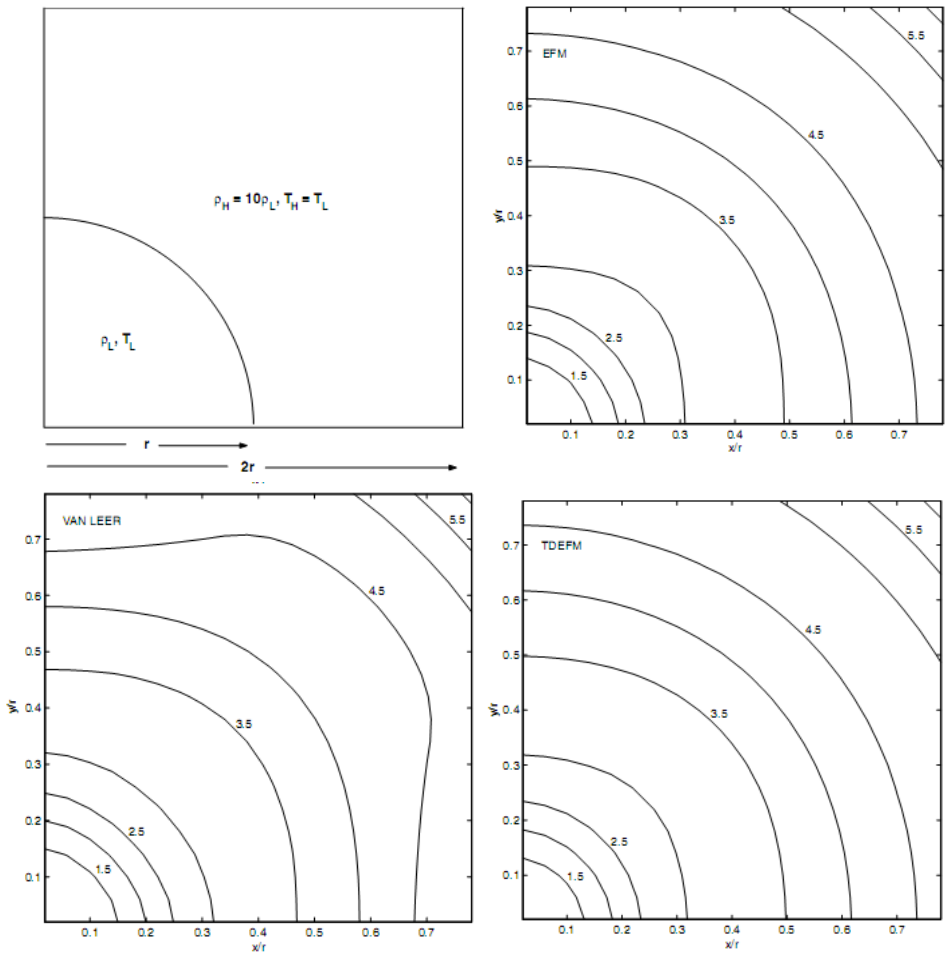

Figure 3.6 Comparison of solutions to the implosion problem using a 50 × 50 mesh: (top left) initial condition where γ = 9/7, T_H/T_L = 1.0, ρ_H/ρ_L = 10; (top right) EFM; (lower left) Van Leer (Van Leer, 1977) and TDEFM (lower right) Contours are of density (ρ/ρ_L) at t = 0.098 (Smith, *et al.*, 2008).

Although the true directional approach produces more accurate results, the directional decoupled method is often used for its simplicity in implementation. Complexity may arise when implementing true directional computation in a flow field across an object. For example, extra precaution is needed in the wall boundary treatment for flows over the corners of a solid object. Gas particles should not be allowed to flow diagonally across the corners. The geometrical

simplicity of the directional decoupled approach also enables simpler implementation of higher order reconstruction schemes in order to limit numerical diffusivity.

The TDEFM and EFM fluxes are equivalent when the kinetic Courant–Friedrichs–Lewy (*CFL*) number approaches zero (Smith, *et al.*, 2008). Hence, by considering the time step $\Delta t \to 0$, the differences between TDEFM and EFM exist only in higher spatial dimensions when flux computation in the EFM is direction decoupled while the TDEFM is true directional.

The TDEFM fluxes are also derived by assuming the Maxwell-Boltzmann equilibrium distribution of the molecular velocities, (given in Equation (3.19)), exists locally in the computational cells. The following equations of the TDEFM fluxes are summarized from the PhD thesis of Smith where the detail of the derivation is shown (Smith, 2008). Consider a gas particle located at position x in the source cell with uniform flow properties within the computational cell. The mass flux of the gas particle as shown in Figure (3.7) moves to a destination cell at a location between $x_{D,L}$ and $x_{D,R}$ during a time step, t, is given in Equation (3.46) as:

$$
\begin{aligned}
f_m = {} & M_c \exp\left[\frac{-\left(u\Delta t + x_{S,R} - x_{D,L}\right)^2}{2RT\Delta t^2}\right] + M_1 erf\left[\frac{u\Delta t + x_{S,R} - x_{D,L}}{\sqrt{2RT}\,\Delta t}\right] \\
& - M_c \exp\left[\frac{-\left(u\Delta t + x_{S,R} - x_{D,R}\right)^2}{2RT\Delta t^2}\right] + M_2 erf\left[\frac{u\Delta t + x_{S,R} - x_{D,R}}{\sqrt{2RT}\,\Delta t}\right] \\
& - M_c \exp\left[\frac{-\left(u\Delta t + x_{S,L} - x_{D,L}\right)^2}{2RT\Delta t^2}\right] + M_3 erf\left[\frac{u\Delta t + x_{S,L} - x_{D,L}}{\sqrt{2RT}\,\Delta t}\right] \\
& + M_c \exp\left[\frac{-\left(u\Delta t + x_{S,L} - x_{D,R}\right)^2}{2RT\Delta t^2}\right] + M_4 erf\left[\frac{u\Delta t + x_{S,L} - x_{D,R}}{\sqrt{2RT}\,\Delta t}\right]
\end{aligned}
\tag{3.46}
$$

where u is the bulk velocity, T is the temperature and R is the gas constant.

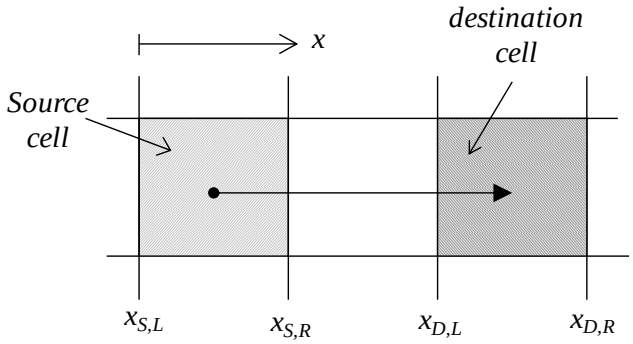

Figure 3.7 Schematic of TDEFM flux moving from source to destination cell.

The momentum flux of a gas particle that moves from the source cell to the destination cell during a time step, t, is given in Equation (3.47) as:

$$
\begin{aligned}
f_p = {} & P_c \exp\left[\frac{-\left(u\Delta t + x_{S,R} - x_{D,L}\right)^2}{2RT\Delta t^2}\right] + P_1 erf\left[\frac{u\Delta t + x_{S,R} - x_{D,L}}{\sqrt{2RT}\,\Delta t}\right] \\
& - P_c \exp\left[\frac{-\left(u\Delta t + x_{S,R} - x_{D,R}\right)^2}{2RT\Delta t^2}\right] + P_2 erf\left[\frac{u\Delta t + x_{S,R} - x_{D,R}}{\sqrt{2RT}\,\Delta t}\right] \\
& - P_c \exp\left[\frac{-\left(u\Delta t + x_{S,L} - x_{D,L}\right)^2}{2RT\Delta t^2}\right] + P_3 erf\left[\frac{u\Delta t + x_{S,L} - x_{D,L}}{\sqrt{2RT}\,\Delta t}\right] \\
& + P_c \exp\left[\frac{-\left(u\Delta t + x_{S,L} - x_{D,R}\right)^2}{2RT\Delta t^2}\right] + P_4 erf\left[\frac{u\Delta t + x_{S,L} - x_{D,R}}{\sqrt{2RT}\,\Delta t}\right]
\end{aligned}
\tag{3.47}
$$

The energy flux of gas particle that moves from the source cell to the destination cell during a time step, *t*, is calculated using Equation (3.48) as:

$$
\begin{aligned}
f_E = {} & E_c \exp\left[\frac{-\left(u\Delta t + x_{S,R} - x_{D,L}\right)^2}{2RT\Delta t^2}\right] + E_1 erf\left[\frac{u\Delta t + x_{S,R} - x_{D,L}}{\sqrt{2RT}\,\Delta t}\right] \\
& - E_c \exp\left[\frac{-\left(u\Delta t + x_{S,R} - x_{D,R}\right)^2}{2RT\Delta t^2}\right] + E_2 erf\left[\frac{u\Delta t + x_{S,R} - x_{D,R}}{\sqrt{2RT}\,\Delta t}\right] \\
& - E_c \exp\left[\frac{-\left(u\Delta t + x_{S,L} - x_{D,L}\right)^2}{2RT\Delta t^2}\right] + E_3 erf\left[\frac{u\Delta t + x_{S,L} - x_{D,L}}{\sqrt{2RT}\,\Delta t}\right] \\
& + E_c \exp\left[\frac{-\left(u\Delta t + x_{S,L} - x_{D,R}\right)^2}{2RT\Delta t^2}\right] + E_4 erf\left[\frac{u\Delta t + x_{S,L} - x_{D,R}\right)}{\sqrt{2RT}\,\Delta t}\right]
\end{aligned}
\qquad (3.48)
$$

The corresponding TDEFM coefficients M_c, M_1 to M_5, P_c, P_1 to P_5, E_c, and E_1 to E_5, are given in the appendix of Smith's PhD thesis (Smith, 2008).

As the TDEFM considers the transfer of particle fluxes in a true directional manner, it eliminates the direction decoupling induced errors that are encountered in the EFM and other conventional CFD solvers. The TDEFM algorithm is unconditionally stable. The calculated fluxes are theoretically valid for any value of the time step although the time step is usually determined in a manner that keeps the *CFL* number below unity to ensure physical correctness. However, the major disadvantage of the TDEFM is the expensive computational resources required due to the need of evaluating the numerous error functions in the particle fluxes calculations.

3.6.4 Quiet Direct Simulation Method

The Quiet Direct Simulation (QDS) method is a kinetic-based flux scheme that computes true-direction fluxes of mass, momentum and energy with high computational efficiency. In QDS, the space of the flow field is discretised into a uniform Cartesian grid. In each computational cell the molecular velocity is represented by the Maxwell-Boltzmann equilibrium distribution approximated by a Gauss-Hermite quadrature. A list of the Gauss-Hermite quadrature is given in Appendix A. This molecular velocities distribution is usually discretised into N (typically 3 or 4) molecular speeds in each coordinate direction. The speeds are chosen according to the local bulk velocity and temperature. In other words, the physical gas molecules are represented by N molecular groups in each coordinate direction.

The computation of the flow in each time step is divided into streaming and collision phases. In the streaming phase, the flux of molecules from a source cell to its nearest neighbouring cells are calculated by assuming collisionless flight. The fraction of molecules that move from a source cell to each neighbouring destination cell is calculated and stored. The remainder are retained in the source cell. A global kinetic CFL criterion is used to adjust the time step as the simulation progresses. This prevents molecules streaming beyond neighbouring cells and maintains the physical realism of the flow. The time step is chosen such that the fastest discretised molecular group moves within a distance no more than a set fraction of the grid spacing, typically set to be ≤ 0.5. The mass, momentum

and energy carried by these fluxes are then determined and added to each destination cell.

At the end of the streaming phase the fluxes of mass, momentum and energy to each cell are summed with the quantities remaining in the cell from molecules which did not leave. In the collision phase, an infinite collision rate was assumed and forcing the molecular velocity distribution in the cell takes the form of the Maxwell-Boltzmann equilibrium distribution function. Hence, it is fair to consider that the solution provided by QDS is essentially an Euler solution of the flows.

There are several advantages in the QDS scheme for flow simulation. In its original form, QDS fluxes are streamed in the true directional manner (Smith, et al., 2009). It was recently extended to axisymmetric flow field computation in the directional decoupled manner for convenient formulations (Lim, Smith, Jermy, Wu, & Krumdieck, submitted). Because the calculation of the property fluxes is deterministic, QDS exhibits no statistical scatter. The QDS formulations do not involve complex mathematical functions such as the error functions which are important function for flux computation in many kinetic theory based schemes. This enables QDS solvers to be computationally inexpensive and exceptionally well-suited as a rapid flow simulation tool. The QDS algorithm is also suitable for parallelization with its highly local nature in the flux computation. Furthermore, QDS has a large dynamic range, is easily extendable to multiple dimensions and species. The major disadvantage with the original scheme was its diffusivity. However, this problem was partially alleviated by extending the QDS scheme to

the second order which resulted in a reduction in the numerical diffusion with no effect on the high stability of the scheme (Lin, Smith, Cave, Huang, & Wu, 2011; Smith, et al., 2009) .

Within the scope of this thesis work is the exploration of the applicability of the QDS method as a rapid simulation tool in the study of the PP-CVD flow simulation. A fast approximation of the reactor flow field during a PP-CVD process, with acceptable accuracy, is desired. A speedy solution is important particularly for the customization of the PP-CVD reactor design and the selection of operational conditions that allow a specific application of the thin film deposition technique to be performed.

4 PP-CVD Reactor Flow Field Modelling

4.1 PP-CVD Flow Field dynamics

As discussed in Chapter 2, the PP-CVD process consists of a series of pulse cycles. Each pulse cycle is made up of an injection phase followed by a pump down phase. During the injection phase, a controlled volume of precursor solution (also known as reactant) is injected into the continuously evacuated reactor at high supply pressure, P_S. The supply pressure is usually controlled by a gas pressure regulator which is used to adjust the pressure from a highly pressurised source vessel. The injection is carried out at a discrete time interval. At the end of the injection phase, the supply system stops and the reactor inlet is closed. At this stage, the pressure in the reactor volume is at its peak pressure, P_{max}. The pulse cycle continues with the pump down phase where the reactor is evacuated by a vacuum pump to reduce the pressure in the reactor volume to its initial base pressure, P_{min}. The pump down phase is relatively much longer, in the order of more than 10 times, compared to the injection phase. In fact, in an experimental study of deposition uniformity in two different reactor sizes, it has been found that good flow field uniformity was obtained for the ratio of pump down time to the injection time $t_P/t_i \geq 20$ for a small reactor and $t_P/t_i \geq 40$ for a large reactor (Krumdieck, Cave, et al., 2007). A PP-CVD pulse cycle ends when the reactor pressure is restored to its base pressure and the PP-CVD process continues with another pulse cycle.

In general, the reactant in the PP-CVD reactor experiences continuous expansion during both injection and pump down phases. Convective flow from inlet towards outlet and from the reactor centre to the outer radius of the reactor occurs throughout the pulse cycle. However, the flow field dynamics are physically different between the phases. The PP-CVD flow field undergoes a rapid change especially during the injection phase. The PP-CVD flow field dynamics also depend significantly on the reactant delivery system, which can be categorised by the chemical phase of the supplied reactant delivery system: as gas or liquid.

4.1.1 PP-CVD reactor with gas delivery system

In the PP-CVD process where the precursor solution is introduced into the reactor in gaseous form, the reactant vapour is injected from a high pressure source volume into the reactor through an orifice during the injection phase. As the pressure ratio of the source volume to the considerable quiescent reactor volume is greater than 10, the flow will develop into a highly under-expanded jet (Woodmansee, Iyer, Dutton, & Lucht, 2004). In fact, due to the rapid injection of the reactant vapour into the continuously evacuated reactor chamber, the flow field in the PP-CVD reactor develops into an unsteady under-expanded jet during the injection phase. This jet dissipates soon after the end of the injection phase when the inlet orifice is closed.

Figure 4.1 shows the schematic of a steady, under-expanded jet structure. When a choked flow condition occurs at the orifice and the high-pressure gas is exhausted to a much lower pressure environment, a rapidly expanding jet is created in the low pressure region. An expansion fan is formed at the exit of the orifice. These expansion waves diverge rapidly and reflect at the jet boundary as compression waves. The interaction of these expansion and compression waves results in a barrel-shaped intersecting shock inside the jet boundary. A normal shock, which is called Mach disc, is formed at the end of the intersecting shock and separates a highly supersonic region upstream at the jet core from a subsonic region downstream. This shock structure is repeated to form a series of Mach diamonds which usually decrease in size in the downstream direction (Crist, Sherman, & Glass, 1966).

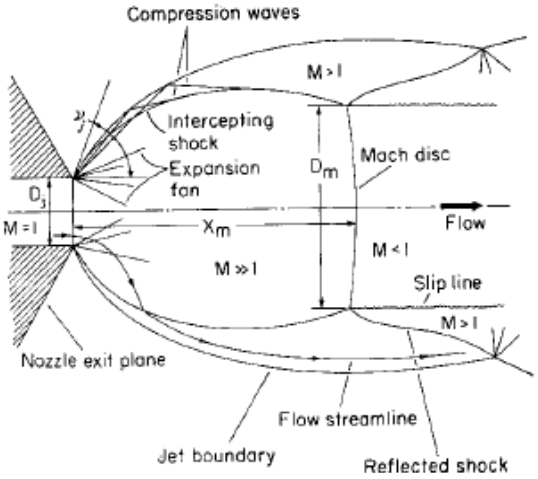

Figure 4.1 Schematic of a steady under-expanded jet structure (Crist, et al., 1966).

During the pump down phase, the under-expanded jet structure dissipates quickly. The flow field becomes highly uniform as soon as the jet structure

dissipates completely. Due to the only driving force for the flow field during the pump down phase being the evacuation at a relatively slow rate at the reactor outlet, the reactor flow field is mainly driven by the pressure gradient within the reactor volume. The flow rate throughout the reactor is relatively slow at this stage. The flow field is considered to be in a quasi-equilibrium state which will be examined and discussed in section 5.8 and 6.5.

4.1.2 PP-CVD reactor with liquid reactant delivery system

In this PP-CVD process, a metered quantity of liquid precursor solution is injected into the continuously evacuated reactor chamber through an ultrasonic atomiser. The injection of the precursor solution is done over a discrete timed interval. A dilute gas called a push gas, aid the injection of the liquid reactant from the supply sample loop. Usually, a noble gas or relatively inert diatomic gas, at high supply pressure is used as the push gas. The ultrasonic atomiser is used to generate micrometer scale liquid droplets of the reactant when entering the reactor chamber. A detailed description of the PP-CVD reactor with liquid reactant delivery system can be found in the PhD thesis by Siriwongrungson (Siriwongrungson, 2010).

When the liquid precursor solution droplets enter the low pressure PP-CVD reactor chamber, the droplets flash evaporate. Flash evaporation is an instant boiling process when a liquid (usually slightly pre-heated) is exposed to a sudden pressure drop below its saturation pressure. The sudden reduction of pressure results in the energy of the fluid being unable to be contained in the liquid as

sensible heat. Hence, the surplus heat is transformed into the latent heat of vaporization causing the subcooled liquid to turn into superheated fluid. When there is an absence of dissolved gas inside the liquid, the flash evaporation process occurs only at the surface level of the liquid (Billet, 1989; Saury, Harmand, & Siroux, 2002).

In this study, the experimental conditions of Siriwongrungson's PhD research work are considered. In Siriwongrungson's experimental study, the precursor solvent, toluene, is used with titanium tetraisopropoxide (TTIP) which is completely dispersed in the solvent with a precursor concentration of 0.15 mol%. As the precursor is very dilute in the injected solution, only the solvent is modelled for simplicity. A numerical study of PP-CVD reactor flow using QDS method with multiple species, it was found that the precursor concentration distribution shows a similar flow phenomena to that of the solvent (Cave et al., 2011). The injected precursor solution is generally at a pressure of 50 - 70 kPa and at a temperature of about 310 K. The reactor initial (base) pressure and temperature are about 100 Pa and 293 K, respectively. Hence, the operating pressure and temperature of the PP-CVD process is far below the critical state of Toluene, of which the critical temperature is 591.75 K and critical pressure is 4.126 MPa (Lemmon, McLinden, & Friend, retrieved July 19, 2011).

As an approximation of the phase change of the precursor solution in the reactor chamber, the phase diagram of Toluene as shown in Figure 4.2 is used. To estimate the instantaneous pressure inside the spherical droplet, the Young–

Laplace equation is utilised to estimate the pressure difference between the liquid enclosed in the droplet and the surrounding gas vapour, ΔP, which is shown in Equation (4.1) as (Frohn & Roth, 2000):

$$\Delta P = \frac{2\sigma_s}{r} \tag{4.1}$$

where r is the radius of the spherical droplet and σ_s is the surface tension of the droplet as a function of temperature. The ultrasonic atomiser used in Siriwongrungson's experimental study was SONO-TEK 8700-120 cone shape micro spray. This atomiser generates droplet with median diameter of 18 μm (Sono-TekCorporation, 1997). As an example, the surface tension of Toluene at 310 K is about 0.0264 N/m (Lemmon, et al., retrieved July 19, 2011) while the reactor base pressure, P_{min}, is at 100 Pa. Hence, the pressure of the liquid enclosed in the droplet of the precursor solution, P_d, when entering into the reactor can be estimated by Equation (4.2) as:

$$P_d = P_{\min} + \Delta P = 100Pa + \frac{2 \times 0.0264 \, N/m}{18 \times 10^{-6} m} \approx 3033.33Pa \tag{4.2}$$

As shown in Figure 4.2, Toluene at the PP-CVD supply conditions when enters into the reactor is expected to become superheated at the much lower pressure inside the reactor. Therefore, it is assumed that "instant" boiling of the liquid droplets occurs on the droplet surface; hence the evaporation is considered to be flash evaporation.

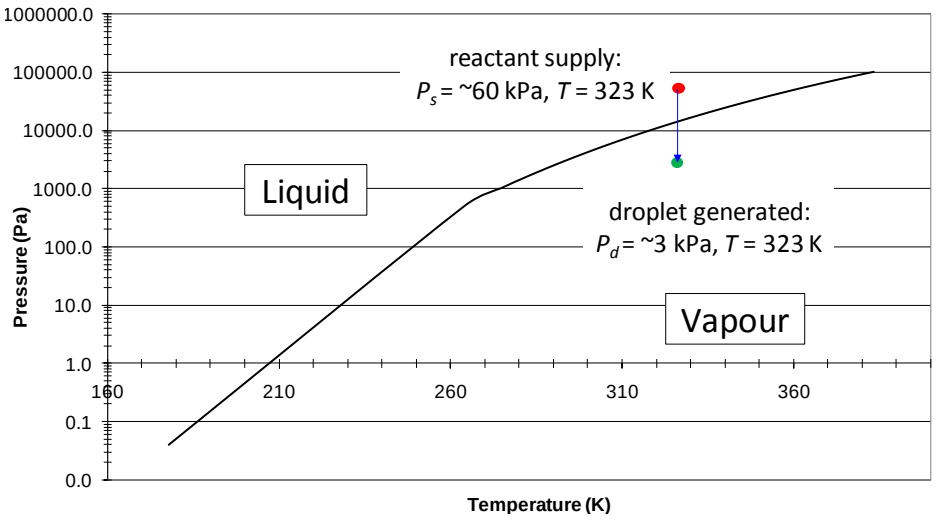

Figure 4.2 Saturation phase diagram of Toluene (Lemmon, et al., retrieved July 19, 2011).

The pressure inside the reactor chamber increases rapidly due to the flash evaporation of the precursor solution. At the end of the injection phase, when the ultrasonic atomiser is stopped, the liquid droplets are expected to be fully evaporated. During the pump down phase, the evaporated vapour is driven by the pressure gradient within the reactor volume caused by the vacuum pump. The flow field becomes highly uniform at this stage. The pressure of the reactor decreases back to the base pressure before the next pulse cycle. The modelling of the PP-CVD process with liquid droplet injection will be discussed in detail in chapter 7.

4.2 PP-CVD Processes Modelling

4.2.1 Modelling of PP-CVD Reactor Flow Field

As discussed in section 2.1, there are several steps involved in the PP-CVD deposition process. The scope of this research work covers the modelling of the flow dynamics inside the PP-CVD reactor chamber during both injection and pump down phases for PP-CVD reactor with a gas or liquid reactant delivery system. The scope of this modelling work includes:

1. Choked flow inlet condition and the unsteady development of the quasi-steady under-expanded jet for gas-fed reactor.
2. Droplet injection via ultrasonic atomizer, flash evaporation and mass transport of the liquid reactant droplets for liquid-fed reactor.
3. Mass transport of the precursor solution vapour during the flow expansion from the reactor nozzle inlet to the substrate region throughout the initially quiescent reactor condition.
4. The continuous evacuation of vacuum pump at the reactor outlet.
5. The dissipation of the jet structure in the gas-fed reactor and the pressure gradient driven flow of the precursor solution vapour during the pump down phase.

It has been shown experimentally that the film growth rate in the PP-CVD process depends mainly on the activation energy of the reaction, the local substrate temperature, the absorption and reaction rate of the precursor on the substrate surface and the precursor solution vapour arrival rate onto the substrate

surface (Krumdieck, 2001; Krumdieck & Raj, 2001b). The modelling of the substrate surface temperature distribution, precursor absorption and reaction on the substrate are not within the scope of this modelling work. Hence, it is assumed that the substrate surface temperature is uniform and no depletion of the gas molecules occurs on the substrate surface. The precursor solution vapour arrival rate, however, is included in the scope of this project. In the following subsections, some of the aspects related to modelling the PP-CVD reactor flow field will be discussed.

4.2.1.1 Substrate surface temperature distribution

The substrate surface temperature distribution is mainly affected by the heat conduction from the heater to the substrate. A very simple approximation was carried out based on Helium gas to compare the convection heat transfer on the substrate surface due to the gas flow to the conduction heat transfer across the substrate surface. The substrate radius and thermal properties of idea Helium gas at an initial reactor temperature of 300 K are tabulated in Table 4.1.

Table 4.1 Substrate radius and thermal properties of idea Helium gas at 300 K (Incropera & DeWitt, 2001).

Substrate radius, r [m]	0.0375
Dynamic viscosity, μ [N·s/m^2]	2×10^5
Prandlt number, Pr	0.682
Thermal conductivity, k_f [W/m·K]	0.152

The empirical correlation for the average Nusselt number, $\overline{Nu}$, for an external flow over flat plate is given in Equation (4.3) as (Incropera & DeWitt, 2001):

$$\overline{Nu} = 0.664 Re^{1/2} Pr^{1/3} \tag{4.3}$$

where *Re* is the Reynolds number given in Equation (4.4) as:

$$Re = \frac{\rho U r}{\mu} \tag{4.4}$$

Note that the substrate radius is used as the length of the flat plate in this approximation analysis. The convection heat transfer coefficient, *h*, can be calculated using Equation (4.5) as:

$$h = \frac{\overline{Nu} \cdot k_f}{r} \tag{4.5}$$

The convection heat transfer per unit temperature change, q'_{conv}, can then be estimated by Equation (4.6) as:

$$q'_{conv} = h \cdot A \tag{4.6}$$

where $A = \pi r^2$ is the area of the substrate surface. Based on the simulation results of the PP-CVD flow field at two operating conditions, the convection heat transfer on the substrate surface can be roughly estimated and is given in Table 4.2. The two operating conditions simulated are with reactor base pressure of 1 Pa and 1 kPa, respectively, which will be discussed in detail in Chapter 5. The data considered in this estimation is based on the flow condition during the injection

phase, 4 ms after the start of injection when the flow has developed into a quasi-steady state.

Table 4.2 Estimation of convection heat transfer on substrate surface for PP-CVD flow field at 2 different reactor base pressures.

Reactor base pressure, Pmin [Pa]	1	1000
Density near substrate [kg/m^3]	1.5×10^{-5}	2.0×10^{-3}
Maximum velocity near substrate [m/s]	784.563	152.978
Nusselt number	3.245	13.223
Convection heat transfer coefficient [W/m^2·K]	13.154	53.598
Convection heat per unit temperature [W/K]	0.058	0.237

The estimated convection heat transfer per unit temperature is compared to the approximated conduction heat transfer from the heater which is placed beneath the substrate. The conduction heat transfer per unit temperature can be estimated using Fourier's law given in Equation (4.7) as:

$$q'_{cond} = \frac{k \cdot A}{L} \tag{4.7}$$

where L is the substrate thickness which is about 5 mm. The stainless steel substrate used has the thermal conductivity, k_{cond}, of about 15 W/m·K (Incropera & DeWitt, 2001). Hence, the conduction heat transfer from the heater to the substrate surface is estimated to be 13.25 W/K, which is much higher compared to the convection heat transfer estimated above. Hence, the convection heat transfer due to the gas flow on the surface is considered to have a negligible effect on the temperature distribution on the substrate surface. Therefore, the heat transfer and temperature distribution on substrate surface is dominated by the material conduction instead of the fluid flow convection.

4.2.1.2 Reactant arrival rate onto the substrate surface and deposition uniformity

The precursor solution vapour arrival rate onto the substrate surface is to be modelled and is used to determine the surface deposition uniformity. The accumulated mass of gas molecules that strike onto the substrate surface (AMOS) was computed. In the present work, AMOS is used primarily to determine the uniformity of the reactant arrival rate onto the substrate surface. It is also thought that AMOS is directly related to the uniformity in the gas flow field within the PP-CVD reactor.

As shown in Figure 4.3 below, the total mass of the gas molecules that strikes onto the substrate surface within a computational grid with the size of Δr at a time t_1 is computed. Furthermore, such total mass of the gas molecules that strikes onto the substrate surface is accumulated between the computational times of t_1 to t_2. This accumulation of the mass of the gas molecules that strikes onto the substrate surface is used to define AMOS between the computational times of t_1 to t_2. For uniform surface deposition, a uniform value in AMOS is expected along the substrate radius R.

Moreover, to justify the uniformity of the total mass on the substrate surface, AMOS over the annular area of the substrate surface was computed and used as the key parameter to investigate the uniformity of the particles arriving at the substrate surface. The detail of the uniformity calculation will be discussed in Chapter 8.

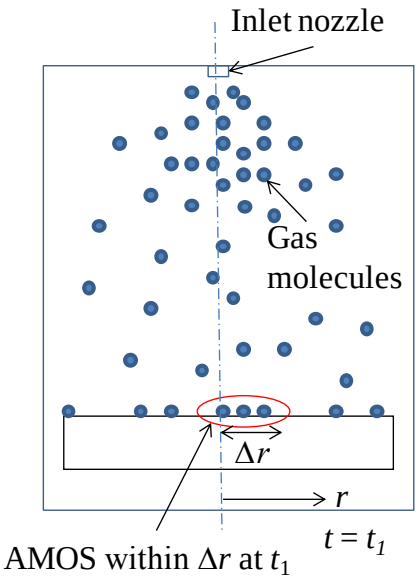

Figure 4.3 Illustration of the accumulated mass of gas molecules strikes onto the substrate surface (AMOS).

4.2.1.3 Boundary Conditions

For the inflow boundaries in the PP-CVD simulation, choked flow conditions are used for PP-CVD reactor with a gaseous precursor solution delivery system. A choked flow condition occurs at the inlet orifice if the pressure ratio of the gas supply pressure, P_S, to the reactor pressure, P_R, satisfies the condition given in Equation (4.8) as (Anderson, 1990):

$$\frac{P_S}{P_R} \geq \left(\frac{\gamma+1}{2}\right)^{\frac{\gamma}{\gamma-1}} \tag{4.8}$$

In the present gas injected simulations, Helium gas with $\gamma = 5/3$ is used. Hence the pressure ratio of P_S / $P_R \geq 2.053$ is required. Consider two cases in which the reactor base pressure of P_{min} = 1 Pa and 1 kPa, respectively. For the first case with

P_{min} = 1 Pa, the supply pressures P_S = 10 kPa and the maximum reactor pressure P_R = 100 Pa. For the second case, the supply pressures P_S = 40 kPa while the maximum reactor pressure P_R = 5 kPa. Thus, the pressure ratio of P_S / $P_R \geq 100$ and 8 for the first and second case, respective, are obtained. For this, the choked flow condition at inlet can be assumed at all times. For the PP-CVD reactor with a liquid precursor solution delivery system, a droplet flash evaporation model is used to provide the inflow condition for the gas phase simulation. The droplet flash evaporation model will be described in detail in Chapter 7.

For the outflow boundary, a constant volumetric flow rate is used to represent the constant vacuum pump evacuation of the PP-CVD reactor. The outflow rate can be approximated based on the vacuum pump evacuation rate by calculating the number flux to the outlet surface under equilibrium conditions. The number of molecules crossing the outlet cross section, N', can be determined by Equation (4.9) as (Roth, 1990):

$$N' = Av_{av}n \tag{4.9}$$

where A is the area of the cross section, n is the number of molecules per unit volume (also known as the number density), and v_{av} is the average velocity in the Maxwell-Boltzmann equilibrium distribution which can be calculated by Equation (4.10) as:

$$v_{av} = \sqrt{\frac{8kT}{\pi m}} \tag{4.10}$$

where k is the Boltzmann constant, T is the gas temperature and m is the molecular mass. The mass flux of molecules m′ to be removed from the reactor can be determined by Equation (4.11) as:

$$m' = \rho Q_P = nmQ_P \tag{4.11}$$

where Q_P is the evacuation rate of the vacuum pump. The fraction of molecules to be removed from the reactor, x, can then be calculated by Equation (4.12) as:

$$x = \frac{nmQ_P}{mN'} = \frac{Q_P}{v_{av}A} \tag{4.12}$$

Therefore, in implementing the evacuation outflow boundary conditions for PP-CVD flow simulations, a fraction x of the QDS mass fluxes which strike on the outlet boundary are removed from the flow.

The validation of this outflow boundary condition is assessed by comparing the average reactor pressure calculated in the QDS simulations during the pump-down phase and the experimental result (Siriwongrungson, 2010). In the experimental work, the process time for a single pulse cycle is about 10 s with a 1 s injection phase. The total precursor solution injected within a pulse cycle is about 43 μg. For a feasible simulation time, the pulse cycle time was scaled down to 1 s with 0.1 s injection phase in this comparison. The total amount of 4.2 μg Toluene, the precursor solvent used in the experiment, was injected as droplets into the reactor in the simulation. The droplet flash evaporation model described in Chapter 7 is used to model the vaporisation of the liquid droplet. The vaporised Toluene is used as the inlet condition. Figure 4.4 shows the computational

geometry used for the simulation conducted in order to assess the outflow boundary treatment.

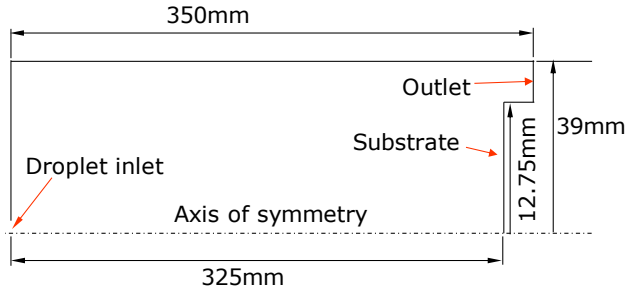

Figure 4.4 Schematic of PP-CVD reactor geometry.

Table 4.3 lists the key parameters used in the simulation.

Table 4.3 Simulation conditions for PP-CVD flow field simulations.

Initial Pressure, P_i	100 Pa
Initial Temperature, T_i	293 K
Injection time, t_i	0.1 s
Reactor evacuation rate, Q_P	0.46 L/s
Median droplet diameter	18 μm
Mean droplet velocity	8 m/s
Droplet spray angle	6°
QDS velocity bin, N	4 per coordinate direction
Simulation time step, Δt	variable time step with maximum CFL < 0.5
Slope limiter	MINMOD

Figure 4.5 shows the comparison of measured pressure in the experimental and average reactor pressure profiles in the PP-CVD process with liquid reactant delivery system during one pulse cycle.

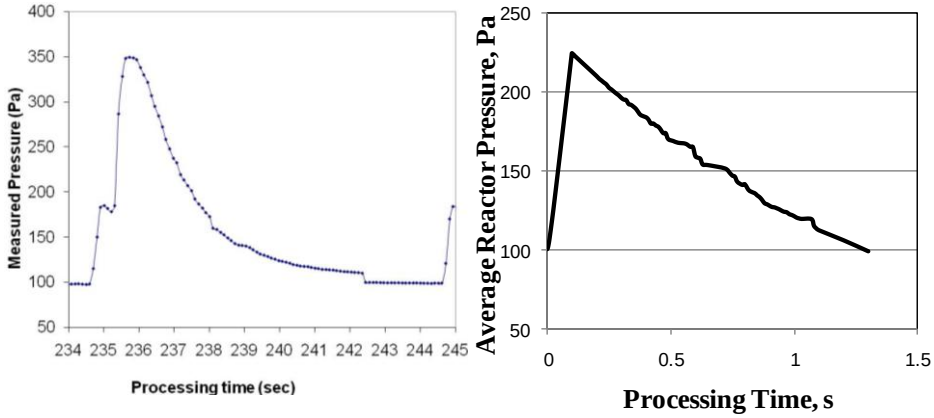

Figure 4.5 Comparison of experimental (left) and simulated (right) pressure of the PP-CVD reactor during one pulse cycle. Note: simulation and experiment used different injection pulse lengths and cycle periods.

From Figure 4.5, although the process times used in the experiment and simulation are different, similar pressure profiles are seen. The simulated pressure profile also agrees well to the predicted reactor pressure profile as shown in Figure 2.3. The pressure was recorded for a continuous PP-CVD process over a series of pulses but only one pulse cycle is shown in Figure 4.5 for this comparison. Hence, the processing time at 235 s for the experimental result shown in Figure 4.5 should be interpreted as the start of an injection phase. The injection phase was stopped at 236 s. During the pump down phase in the experiment, the reactor pressure returns to the initial pressure about 10 s after the start of a pulse cycle. This means a pulse cycle is completed after t/t_i = 10. From the simulated results, the average reactor pressure restored to the initial pressure at t/t_i = 12.5, which is close to that of the experimental value. This justifies the use of the outlet boundary condition for the simulation, expressed in Equation 4.12, to provide a good approximation of the actual reactor exhaust conditions by the vacuum pump.

It is also noted that the experimental decrease of reactor pressure is slightly faster than the average reactor pressure calculated in the simulation. This is due to precursor depletion on the substrate surface, which accelerates the pressure drop within the reactor, but was not modelled in the simulation. It is also noted that the experimental data shows a shoulder at the beginning of the injection phase. The origin of this feature is not yet understood. It may be due to two distinct phases in the development of the spray, for example a period of coarse atomisation as the spray establishes, which is not modelled in the simulation.

Figure 4.5 can also be used to partly assess the validity of the droplet evaporation rate model which is described in detail in Chapter 7. In the simulation, the reactor pressure reached the peak value at the end of the injection phase. This agrees to that of the theoretical prediction for the PP-CVD process, as shown in Figure 2.3. This shows that the droplet flash evaporation model described in Chapter 7 is capable of providing a good approximation for the droplet vaporisation rate, which provides an inlet condition for the gas phase simulation. Note that the peak pressure from the simulation result is lower than that of the experimental measurement due to a smaller amount of precursor solution being injected.

For the wall boundary conditions, specular reflected wall treatment is used which will simulate the slip wall boundary condition. This is justified in two ways. First, the time scale for the gas molecule flow across the substrate surface was calculated and compared to the simulation time step. Second, a linear gradient in

velocity from the jet core to the wall was assumed. The shear stress was then calculated and compared to the dynamic pressure within the reactor at a chosen time.

Table 4.4 shows the comparison between the estimated time for the flow to travel across substrate surface and the instantaneous time step used at 4 ms in the two cases simulated in Chapter 5. This comparison is made using the data from the simulation time at 4 ms because the quasi-steady jet structure that impinges on the substrate surface was developed by this time. When the jet impinges on the substrate surface, the flow speed across the substrate surface is high enough that a boundary layer may be formed due to the wall shear stress. Also, the velocity gradient between the centreline of the reactor (i.e. the jet core) and reactor wall is strong at this time.

Table 4.4 Comparison between the estimated time for the flow to travel across substrate surface and the instantaneous time step used at 4 ms.

	Case I	**Case II**
Substrate radius	0.0375 m	
Average bulk velocity above substrate	784.563 m/s	152.978 m/s
Estimated time for the flow to travel across substrate	4.78×10^{-5} s	2.451×10^{-4} s
Instantaneous time step	5×10^{-8} s	6×10^{-8} s

From Table 4.4, it shows that the time step used is much smaller than the time for the gas molecules flow across the substrate. Thus, there is insufficient time for boundary layer development within each time step. Because both simulations were unsteady flow, the flow field changes in every time step.

Therefore, it can be assumed that boundary layer formation is negligible and slip wall treatment is justified.

By assuming a linear gradient in velocity from the jet core to the reactor wall, the shear stress, τ, at 4 ms of the flow time was then estimated using Equation (4.13) as:

$$\tau = \mu \frac{du}{dr} = \mu \frac{u_{centreline,t} - u_{wall,t}}{R_{reactor}} \tag{4.13}$$

where $u_{centreline,t}$ is the axial velocity at the centre of the reactor (i.e. at the jet core), $u_{wall,t}$ is the axial velocity at the reactor wall and $R_{reactor}$ is the reactor radius. The dynamic pressure, P_{dyn}, within the reactor was also estimated using Equation (4.14) as:

$$P_{dyn} = \frac{1}{2} \rho_{ave} V_{ave}^2 \tag{4.14}$$

where ρ_{ave} is the flow density and V_{ave} is the average flow velocity. Table 4.5 shows the comparison between the shear stress and the dynamic pressure within the reactor at flow time of 4 ms in the two cases simulated in Chapter 5.

Table 4.5 Comparison between the shear stress and dynamic pressure at 4 ms.

	Case I	**Case II**
Dynamics viscosity	2×10^{-5} Pa·s	
Reactor radius	0.059 m	
$u_{centreline,t}$	1166.3 m/s	622.76 m/s
$u_{wall,t}$	457.74m/s	47.79 m/s
$\boldsymbol{\tau}$	**0.24 Pa**	**0.19 Pa**
ρ_{ave}	8.67×10^{-6} kg/m^3	0.0017 kg/m^3
V_{ave}	543.695 m/s	112.16 m/s
$\boldsymbol{P_{dyn}}$	**1.282 Pa**	**10.693 Pa**

From Table 4.5, it shows that the dynamic pressure is much higher than the wall shear stress estimated in both cases. Hence, it can be concluded that the wall shear stress can be neglected and this justifies the use of the slip wall condition in the simulation.

4.2.2 Continuum breakdown parameter

The continuum approach in fluid mechanics assumes that the change of fluid properties in a flow occurs gradually without discontinuities i.e. the flow property gradients are continuous and smooth. This is valid when the perturbation of the molecular velocity distribution from the Maxwell-Boltzmann equilibrium distribution is small. Also, the number of molecules within the region of interest needs to be sufficiently large in order to define the macroscopic properties by averaging the microscopic properties of the molecules. What is more, there should be a sufficient number of intermolecular collisions for the molecules to relax and re-establish the equilibrium condition.

In certain flow conditions such as highly rarefied or hypersonic flow, the continuum assumptions may become invalid. The failure of the continuum assumption is commonly termed continuum breakdown. There are two main reasons for continuum breakdown to occur. First, the scale length of macroscopic properties gradients are small enough to causes the fluid molecules to flow downstream before the local equilibrium condition is established. Second, the number of intermolecular collisions between the fluid molecules is insufficient for

the molecules to exchange properties and relax to the equilibrium molecular velocity distribution. Due to the considerably low operating pressure in PP-CVD process and the rapid expansion of the flow, especially during the injection phase, continuum breakdown may take place.

The transition of continuum to molecular flow is usually characterised by the operating pressure in vacuum system (Roth, 1990). As discussed in section 2.2, the Knudsen number, *Kn*, is commonly used to characterise the rarefaction of the flow. However, the *Kn* is independent of local flow conditions. In a flow where the *Kn* is considerably low, the thermal equilibrium condition is usually expected. In a flow with sufficiently high speed or with a significant macroscopic property gradient in certain regions, the fluid molecules may travel downstream before the local continuum flow condition is established. Hence, Bird (Bird, 1970a) proposed a breakdown parameter that predicts the continuum breakdown in an expanding gas flow, which is given in Equation (4.15) as:

$$P_B = \frac{1}{\nu}\left|\frac{D(\ln \rho)}{Dt}\right| \tag{4.15}$$

where ν is the collision rate and D/Dt is the substantial derivative. It has been found that continuum breakdown occurs for $P_B > 0.02$ in both steady and unsteady flow.

This idea was then extended by Boyd's research group (Boyd, Chen, & Candler, 1995; Wang & Boyd, 2003) to allow simpler calculation of the

breakdown parameter based on gradients of other fluid properties. The gradient-length local Knudsen number was proposed and is given in Equation (4.16) as:

$$Kn_{GLL} = \frac{\lambda}{\eta}\left|\nabla \eta\right| \tag{4.16}$$

where λ is the local mean free path, η is the flow property (e.g. density, translational temperature or velocity) and $\nabla \eta$ is the spatial gradient of the flow property. Studies found that continuum breakdown occurs when $Kn_{GLL} > 0.05$ (Boyd, et al., 1995).

Krumdieck *et al.* also proposed an alternative breakdown parameter based on the time dependent mean free path evolution in a rapidly expanding gas (Krumdieck, Cave, et al., 2007). This breakdown parameter takes into account the spatio-temporal change of the mean free path compared to the local average molecular velocity, which is given in Equation (4.17) as:

$$B = \frac{1}{v_{av}}\left|\frac{D\lambda}{Dt}\right| \tag{4.17}$$

where v_{av} is the average molecular velocity. This breakdown parameter is developed based on the observation that the rate of mass transport due to sufficiently rapid flow expansion through a control volume will be greater than the intermolecular collision rate. This leads to the establishment of the equilibrium condition. Equation (4.17) can also be broken into spatial and temporal components given in Equation (4.18) as:

$$B = B_{spat} + B_{temp} \qquad where \quad B_{spat} = \frac{1}{v_{av}}\left|\bar{u}\cdot\nabla\lambda\right|; \quad B_{temp} = \frac{1}{v_{av}}\left|\frac{d\lambda}{dt}\right| \tag{4.18}$$

where $\bar{u}$ is the bulk velocity within the control volume.

4.3 PP-CVD Reactor Flow Field Modelling Method

4.3.1 Numerical modelling of CVD flow field

There have been significant numbers of work published in CVD flow field modelling. In the conventional CVD technique, the deposition occurs mainly after the flow field within the reactor has reached steady flow condition. Hence, most of the literatures reported on numerical modelling of CVD flow concentrate on steady flow field simulations. Coronell and Jensen conducted an analysis of transition regime flows in a horizontal, multiple-wafer Low Pressure Chemical Vapour Deposition (LPCVD) reactors using DSMC method. Average sampling of the steady flow results were performed to study the effect of various number of wafers, wafer spacing, wafer radii, molecular mass and inlet flow rate. The simulations were conducted on dedicated workstations while the reactor pressures were limited in the mTorr range (Coronell & Jensen, 1992).

Kotecki *et al.* has employed a two-dimensional CFD model to examine the heat and mass transport in two metalorganic CVD (MOCVD) reactors (Kotecki et al., 1994). In their model, the steady state Navier-Stokes equations were solved using a finite element method based on the Galerkin procedure. However, the modelled bulk fluid velocity was very low and no shock waves present in the reactor flow field. In their investigation of fine particle transport in a low-pressure parallel plate CVD reactor, Setyawan *et al.* has used commercial CFD code Fluent to perform the numerical simulation of the reactor flow field (Setyawan, Shimada, Ohtsuka, & Okuyama, 2002). The reactor operating pressures considered in their

study are at 2.0 and 4.0 Torr. Two millions computational nodes with unstructured triangular/tetrahedral meshes were used in the numerical simulation while viscous dissipation was neglected. Vanka *et al.* also employed the conventional finite volume based numerical method to study the mixed convection flow in an atmospheric pressure CVD (APCVD) with an impinging jet at the reactor inlet (Vanka, Luo, & Glumac, 2004). The reactor pressure range considered was between 0.5 to 1.0 atm and steady state solution was simulated.

4.3.2 Previous attempts of modelling the PP-CVD reactor flow field

In the conventional steady state CVD techniques, the pressure variation within the reactor throughout the deposition process is minor. Hence, in the numerical study of CVD flow, most of the reported works used either conventional CFD methods for deposition flow in low Knudsen number regime or DSMC method for CVD process at low operating pressure. There has been hardly literature documenting the unsteady expansion of an under-expanded jet into a confined volume in which the pressure constantly rises, as is the case in PP-CVD, could be found. Therefore, few modelling techniques were explored within the research group members in simulating the PP-CVD reactor flow field.

By considering the sublimation rate of naphthalene at different location within the PP-CVD reactor, Baluti has studied the relation of the injection time to the processing time of a pulse cycle in both experimental and numerical approaches using Navier-Stokes solver (Baluti, 2005). The sublimation uniformity

was defined and compared between PP-CVD process and steady condition. The modelling of the PP-CVD flow field has also been conducted preliminarily by Lin (Lin, 2008) using the parallelized UNIC-UNS Navier-Stokes solver. Lin's simulations indicate that at initial reactor pressures above approximately 1000Pa, the Navier-Stokes equations are able to capture the flow field accurately. However, the results have unrealistic values for the gas temperature (on the order of 10,000 K) at lower pressures.

Cave (Cave, 2008) then developed a kinetic theory based approach for modelling unsteady non-continuum flows, centred on the particle-based Direct Simulation Monte Carlo (DSMC) method. Due to the computational limitation of the DSMC technique in relatively dense and unsteady PP-CVD flow fields, Cave attempted the simulation of the PP-CVD reactor flow field through parallel computation based on the parallel DSMC (PDSC) code developed by Wu *et al.* (Wu, Chou, Lee, Shao, & Lian, 2005; Wu & Lian, 2003). An unsteady sampling routine for a general PDSC was developed to allow the simulation of time-dependent flow problems in the near continuum range encountered in PP-CVD flow fields.

In PDSC, the computational mesh of the flow domain is first generated using appropriate commercial meshing software. The DSMC technique as discussed in section 3.5 is implemented on the computational mesh using a particle ray-tracing technique. This utilises the cell connectivity information provided by the meshing data and allows boundary treatment of complex

geometries. Important features of PDSC include parallel processing with dynamic domain decomposition (Wu & Tseng, 2005), combination of variable time-step scheme with solution-based adaptive mesh refinement (Wu, Tseng, & Wu, 2004), and conservative weighting schemes for treating trace species and chemical reaction functions for hypersonic air flows (Wu, Hsiao, Lian, & Tseng, 2003).

PDSC uses the multilevel graph partitioning tool ParMETIS (Karypis, Schloegel, & Kumar, 2011) to decompose the computational domain and distribute the computational cells amongst the processors. The communication between processors is optimized by transferring flow particle data between processors only for particles that strike the inter-processor boundaries after all other particles on each processor have been moved. This allows maximization of the parallel speed-up. A post-processing procedure called DSMC Rapid Ensemble Averaging Method (DREAM) is utilised in PDSC to improve the statistical scatter in the results (Cave et al., 2008). By using DREAM, a combination of time and ensemble-averaged data was built up by repeating runs over small number of sampling intervals prior to sampling the point of interest. The repeated runs are restarted using Maxwell-Boltzmann distributions based on macroscopic properties obtained by the original unsteady sampling of the PDSC.

4.3.3 Importance of inelastic collision in PP-CVD modelling

In the previous modelling attempts, the PP-CVD flow field was modelled using mainly monatomic molecules as an initial modelling approach. The intermolecular

collisions were treated as purely elastic where the kinetic energy is conserved after the collision in the simulations. However, most of the thin film manufacturing processes involve both precursors and solvents with large molecules in polyatomic molecular structures. Besides molecular translational energy, for polyatomic molecules, there exists an internal energy exchange in the molecular rotational (or vibrational) mode during the collisions exists which is considered as an inelastic collision. The effect of inelastic collisions on the PP-CVD reactor flow field, particularly the mass and momentum distributions on the substrate surface, is uncertain. Hence, it is necessary to first investigate the effect of inelastic collisions between diatomic or polyatomic molecules to the PP-CVD reactor flow field, especially in the region near the substrate.

4.3.3.1 Molecular structure and internal energy

A molecule may consist of a single atom (monatomic) or as a collection of atoms bound together by intermolecular forces (Anderson, 1990). A molecule which consists of two atoms is termed as diatomic molecule while polyatomic molecule has more than two atoms. The amount of macroscopic energy of a gas is calculated by adding up the different modes of energy held within the molecules. In general, the modes of energy of a molecule can be divided into translational, rotational, vibrational and electronic energy. Figure 4.6 shows examples of each mode of molecular energy.

The translational energy is also termed as the kinetic energy of a molecule and exists due to the movement of the centre of mass of the molecule. This is the only form of molecular energy that is possessed by a monatomic molecule. Since the space has 3 geometrical components (such as *x*, *y* and *z* in a Cartesian space), the movement of the molecule on each coordinate direction can contribute to the total kinetic energy. Hence, the molecule is considered to have 3 thermal degrees of freedom in the translational mode of energy.

The rotational energy is associated with the rotational movement of the molecule about the three orthogonal axes. The amount of rotational energy is proportional to the rotational moment of inertia around each axis. For diatomic and linear polyatomic molecules, the moment of inertia about the intermolecular axis is very small and hence is usually neglected. Therefore, diatomic or linear polyatomic molecules are considered to have 2 thermal degrees of freedom in the rotational mode. However, for non-linear polyatomic molecules, there are 3 thermal degrees of freedom in rotational mode.

The vibrational energy is related to the vibration of each individual atom with respect to an equilibrium location within the molecule. Such vibration can be modelled by the connection between the atoms with a spring. The sources of this mode of internal energy are the linear motion of the atoms along the springs and the potential energy contained within the springs. Thus, there are 2 thermal degrees of freedom in vibrational mode for diatomic molecules while larger molecules possess a larger number of thermal degrees of freedom.

The electronic energy is associated with the motion of the electrons orbiting the nucleus of each atom and the potential energy of the electrons in the orbit. Due to the complexity in modelling the motion of electrons, the concept of thermal degrees of freedom is usually not useful in describing the electronic energy. The electronic energy is also usually neglected in the modelling of the macroscopic energy of a gas.

(a) Diatomic molecule 

(b) Translational energy

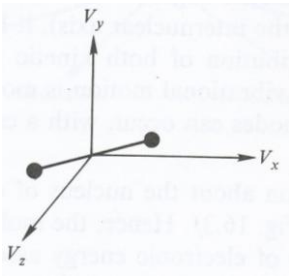

Energy source:
Translational kinetic energy of the centre of mass (thermal degrees of freedom – 3)

(c) Rotational energy

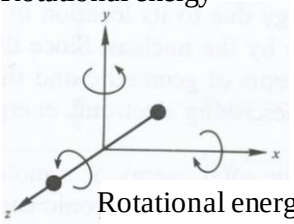

Energy source:
Rotational kinetic energy; (thermal degrees of freedom – 2 for diatomic; 2 for linear polyatomic; and 3 for nonlinear polyatomic)

Rotational energy about the internuclear axis for a diatomic molecule is negligibly small.

(d) Diatomic molecule

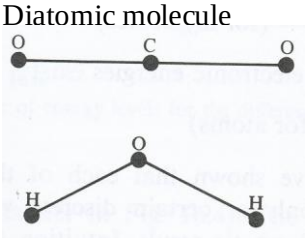

CO_2; linear polyatomic molecule

H_2O; nonlinear polyatomic molecule

(e) Vibrational energy

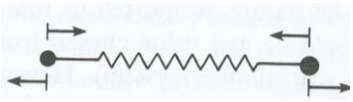

Energy source:
1. Kinetic energy
2. Potential energy

(thermal degrees of freedom – 2)

(a) Diatomic molecule

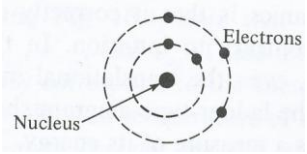

Energy source:
1. Kinetic energy of electrons in orbit
2. Potential energy of electrons in orbit

Figure 4.6 Modes of molecular energy (Anderson, 1990).

4.3.3.2 PDSC modelling with internal energy exchange

For diatomic and polyatomic molecules, the characteristic temperature is the key to determine whether the rotational or vibrational mode of the molecules is activated. In general, the characteristic temperature of rotation is small while the characteristic temperature of vibration is significantly high. Bird shows examples of the characteristic temperatures of some common diatomic molecules. The characteristic temperatures of rotation are in the order of 2 - 80 K whereas the characteristic temperatures of vibration are in the order of 800 - 6000 K (Bird, 1994). Hence, it may be assumed that the rotational energy mode is fully excited in the typical operating temperature range of the PP-CVD process while the vibrational energy mode can be neglected.

In modelling inelastic molecular collisions in DSMC method, the energy exchange method of Borgnakke and Larsen (BL) (Borgnakke & Larsen, 1975) is commonly applied. The BL method is a phenomenological approach that gives adequate accuracy with low computational expenses in modelling the internal energy exchange. In the BL method, a statistical collision model is used to determine the amount of energy exchange between the translational mode and other internal modes stochastically. The post-collision energies for relaxing collisions are sampled from equilibrium energy distributions for the collision. A detailed description on selecting particles for BL internal energy exchange and the procedure for computing the rotational energy exchange has been outlined by Lilley (Lilley, 2005). The BL inelastic collision model was used to calculate the

rotational energy exchange in the PDSC simulations to study the effect of inelastic molecular collisions in the PP-CVD flow.

4.3.3.3 Requirement of inelastic molecular collisions in PP-CVD flow simulation

Simulations of the PP-CVD flow regime were conducted to examine the necessity of modelling inelastic molecular collisions, which involve translational and rotational energy exchange during the molecular collisions. A quasi-steady jet flow in a PP-CVD reactor was simulated using the PDSC, and comparisons made between flow simulations with and without the BL inelastic collision model. Diatomic VHS nitrogen gas with a supply pressure of 10 kPa and temperature of 293 K at choked flow conditions was injected into the PP-CVD reactor at initial pressure of 1 Pa and a temperature of 293 K. An absorbing wall was used as the outflow condition where a fraction of particles that collide on the outlet were destroyed at the reactor exit to allow a quasi-steady jet flow to be developed in the reactor. The simulations were performed on the University of Canterbury's IBM System p5™ 575 node utilizing 64 processors. Each simulation took approximately two days to develop the quasi-steady jet in the flow domain.

Figure 4.7 shows the computational geometry of the PP-CVD reactor used for the simulation investigating the effect of inelastic collisions on the reactor flow field using PDSC. The inelastic collision model parameters such as the rotational relaxation collision number, Z_{rot}, and the characteristic temperature of rotation are taken from Bird's textbook (Bird, 1994).

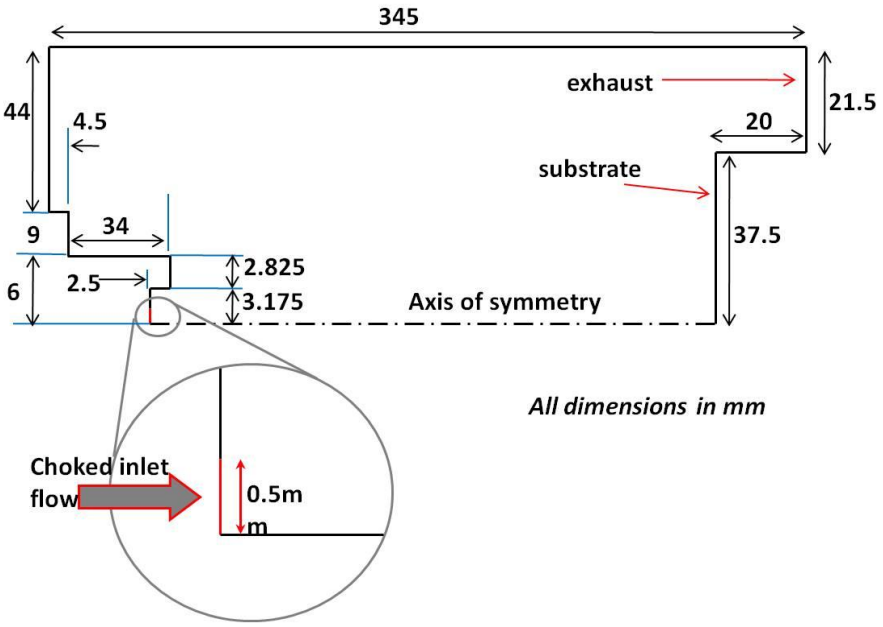

Figure 4.7 Schematic of PP-CVD reactor geometry for PDSC simulation.

Figure 4.8 shows the comparison of the density contour of the steady jet simulated in PP-CVD reactor between the PDSC simulations with and without the BL inelastic collision model. Figure 4.9 shows the comparison of the Mach number contour of the same simulation results.

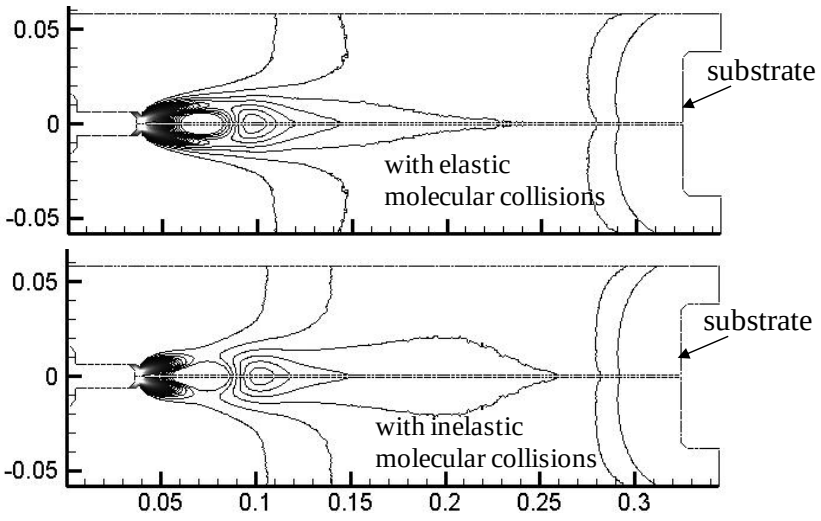

Figure 4.8 Comparison of density contour of PP-CVD flow simulations with elastic (top) and BL inelastic (bottom) collision model.

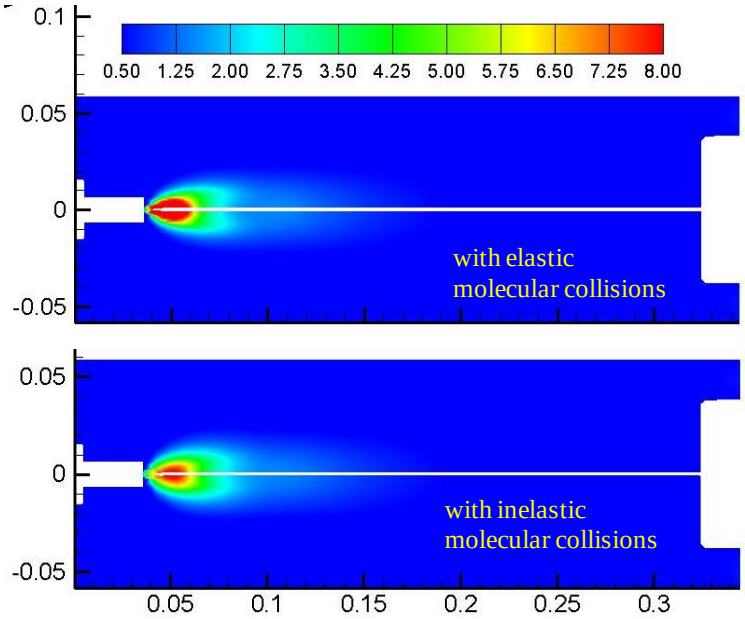

Figure 4.9 Comparison of Mach number contour of PP-CVD flow simulations with elastic (top) and BL inelastic (bottom) collision model.

It should be noted that the BL inelastic collision model used considers only the exchange of translational and rotational energy during the inelastic molecular collision. From the simulation results, flow simulation with inelastic molecular collisions provides a thicker shock pattern with that is slightly lesser in density distribution near the inlet nozzle. This was due to some molecular energy being distributed to the extra rotational energy mode. This causes less translational energy to be held by the molecules and results in slower molecular movement near the inlet nozzle. However, both simulations with or without inelastic molecular collisions produced similar flow patterns and uniformity in the region near the substrate in the reactor. Therefore, it was concluded that internal energy

exchange during molecular collisions in PP-CVD flow simulation can be ignored for simpler simulation setups.

4.3.4 Selection of modelling techniques for PP-CVD flow

It is within the scope of this research work to develop a rapid and easy-to-use simulation method for modelling the reactor flow field during a PP-CVD process with acceptable accuracy. A fast numerical solution is of particular interest for the purpose of customization of the PP-CVD reactor design, operational conditions selection, as well as the scaling up of the PP-CVD process to be a practical industrial tool for thin film deposition.

Although the previous attempt to simulate PP-CVD flow field during the injection phase using PDSC (Cave, 2008) produced constructive results in modelling the PP-CVD flow field, the computational expense was high. Besides, despite much effort being made, the simulations show statistical scatter in the results. What is more, it requires a high level of expert skill and time for the manual creation of the computational grid during the pre-processing stage and the sampling of the results during the post-processing stage.

The modelling of the PP-CVD flow field is also possible to be carried out using continuum-based CFD solvers. However, this also involves much expert skill and time to manually create a computational grid and post process the results. The unstructured meshes used require prior knowledge of the flow in order to obtain meaningful and converged solutions. Due to the complexity of the

governing equation in the Navier-Stokes solver, the computational speed is slow. It also requires the use of high power computational facilities. In order to scale up the PP-CVD reactor design for industrial applications, a rapid modelling method is desired. It is important that the chosen modelling method be feasible for the alternation of the reactor design and operational conditions in order to suit various industrial deposition purposes. Moreover, a simulation tool that requires relatively less CFD expertise in the industrial or chemical engineers from the thin film production plants is also preferred.

Modelling techniques that are based on the kinetic theory provide alternatives for PP-CVD fluid flow simulations. One of the kinetic theory based modelling techniques is the model Boltzmann equation (MBE) which discretises the Boltzmann distribution equation as discussed in section 3.4. One of the popular MBEs, to date, is the Lattice Boltzmann Method (LBM) (Succi, 2001). In LBM, a finite molecular velocity set is used and stored at lattice nodes to represent the molecular velocity distribution of the flow. The discretised Boltzmann equation is evolved in time explicitly. LBM uses simple structured Cartesian computational meshes which enables easy simulation setup. Other advantages of the LBM include fast computation, applicability to mesoscopic physical processes modelling and efficient parallel computing. However, the LBM is limited to model incompressible or weakly compressible flow. The modelling errors in LBM grow with Mach number. LBM is also well known to have instabilities in non-isothermal flow. Many efforts have been spent to

accommodate compressibility effects in LBM but at the cost of increased complexity.

Another alternative technique for flow modelling that is based on kinetic theory is the Quiet Direct Simulation (QDS) method as discussed in section 3.6.4. The Quiet Direct Simulation (QDS) method is a relatively new kinetic theory based numerical simulation tool that computes fluxes of mass, momentum and energy with extremely high computational efficiency. The QDS solver requires very little input from the user to specify the geometry of the flow domain, initial and supply conditions of the flow field and choices of boundary conditions in order to set up a simulation. There is no pre-processing step required to generate the computational grid as the space of the flow field is discretised into a simple uniform Cartesian grid. The formulation of the QDS scheme is simple and straight forward which allows easy extension and development of the scheme by expert users. Therefore, for the purpose of rapid approximation of the PP-CVD flow field in designing the reactor and operation conditions, QDS is a method worthy of investigation to be a feasible numerical simulation tool.

4.3.5 Assumptions in PP-CVD flow field simulations

There are some assumptions commonly made in all the PP-CVD flow field simulations presently worked on. This section outlines the assumptions made in this modelling process.

The ideal gas condition is considered in the gas phase simulations. As discussed above, the precursor is considered to be very dilute in the solvent, hence only the solvent species is simulated to study the flow field uniformity throughout the PP-CVD process.

The heat transfer from the heated substrate surface to the flow field is neglected due to the insignificant amount of convection heat transfer based on the convection heat transfer coefficient estimated in section 4.2.1 above. In practice, the substrate temperature, T_s, is usually maintained at about 400 - 600°C while the average temperature of the gas flow, T_{ave}, is about 300 K in the reactor. The amount of convection heat transfer q_{conv} from the heated substrate to the gas flow can be estimated by Equation (4.19) as:

$$q_{conv} = h \cdot A \cdot (T_s - T_{ave}) \tag{4.19}$$

Using Equation (4.19), the convection heat transfer is estimated to be about 13.25 W and 56.0 W for the PP-CVD flow field with base pressure of 1 Pa and 1 kPa, respectively, and is simulated in Chapter 5. The dynamic simulation time step used in a typical PP-CVD flow simulation using QDS is in the order of 10^{-8} s. Thus, the convection heat transfer on the substrate surface can be estimated to be about 1.3×10^{-7} J to 5.4×10^{-7} J, respectively. Based on the flow velocity listed in Table 4.2, the kinetic energy of the flow above the substrate, E_K, can be estimated by Equation (4.20) as:

$$E_K = \frac{1}{2} m V^2 \tag{4.20}$$

where m is the mass of the gas molecule within the cells adjacent to the substrate surface. Using Equation (4.20), the kinetic energy of the flow above the substrate surface can be approximated to be about 7.1×10^{-6} J to 2.3×10^{-5} J for the PP-CVD flow field with base pressure of 1 Pa and 1 kPa, respectively, and is simulated in Chapter 5. The convection heat transfer is in one order, or lower, less than that of the kinetic energy of the flow on the substrate surface. This indicates that negligible heat energy is transferred from the heated substrate to the gas flow and has an insignificant influence on the flow phenomena. Therefore, the substrate surface temperature was not included in the flow field modelling by the PP-CVD reactor volume being assumed to be initially isothermal at the gas temperature.

Another crucial assumption in the QDS method is that thermal equilibrium is established locally within each computational cell by the end of the time step, allowing the molecular velocity distribution to be approximated with the Maxwell-Boltzmann distribution. In investigating the validity of the local equilibrium assumption, the gradient length local Knudsen number, Kn_{GLL}, is adapted. In general, for an expanding flow, thermal equilibrium among the particles' energy modes cannot be maintained when the particle collision rate becomes so low that continuum breakdown occurs. Hence, the Kn_{GLL} discussed in section 4.2.3 and given in Equation 4.9 is used as one of the parameters to check the validity of local thermal equilibrium in QDS. As studied by Boyd, the criterion for continuum breakdown occurs when $Kn_{GLL} > 0.05$ (Boyd, et al., 1995). When Boyd's continuum assumption condition is satisfied, it signifies that the

local density gradient within the computational cell is not high enough to transport the particles downstream before thermal equilibrium condition is re-established in each time step.

The validity of the thermal equilibrium assumption may also be tested by considering the average time between particle collisions $t_{col,avg}$ estimated by Equation (4.13) as:

$$t_{col,avg} = \frac{\lambda}{v_{th,avg}} \tag{4.21}$$

where λ is the molecular mean free path and $v_{th,avg}$ is the average translational thermal speed given in Equation (4.14) as:

$$v_{th,avg} = \sqrt{\frac{3kT}{m}} \tag{4.22}$$

where k is the Boltzmann's constant and m is the mass of an individual molecule. Titov and Levin (Titov & Levin, 2007) found, in a collision-limited DSMC scheme, that 2 collisions per time step per particle are sufficient for the computed non-equilibrium distribution to relax to one differing negligibly from the corresponding Maxwell-Boltzmann equilibrium distribution. In the present analysis, the average time between particle collisions is compared to the computational time step, Δt. The equilibrium assumption may be considered valid for $\Delta t/t_{col,avg} \geq 2$ which indicates there is at least 2 collisions per particle occurs within a computational time step to allow the re-establishment of equilibrium conditions within each computational cell. The speed and accuracy of the QDS scheme will also be discussed in the subsequent chapters.

In the extension of the QDS solver to accommodate injection of liquid droplets as the inlet condition for simulating the flow field in a PP-CVD reactor with liquid reactant delivery system, a few further assumptions have been made. The liquid droplets generated from the ultrasonic atomiser are assumed to be fully atomised and spherical with uniform temperature space-wise. The injected droplets are assumed to be flash evaporated at the droplet surface as discussed in section 4.1.2 above at the droplet surface temperature. The evaporation occurs on the droplet surface where a vapour rich layer adjacent to the liquid surface is formed due to the flash evaporation. The vapour is then transported to the surroundings by diffusion. Each of these assumptions will be discussed in detail and justified in Chapter 7.

5 Quiet Direct Simulation (QDS) Method

5.1 Development of the Quiet Direct Simulation (QDS) method

The QDS method is a relatively new numerical approach for simulating complex fluid flow and transport phenomena. It is a flux-based kinetic theory method which was introduced about a decade ago as an alternative method for fluid dynamics simulations. The QDS method originated with Albright *et al.* in 2002. It was proposed and termed as Quiet Direct Simulation Monte Carlo (QDSMC) method to carry out the direct simulation Monte Carlo (DSMC) computation without involving random sampling of the fluid particles. It was first developed and implemented to first order accuracy as a modelling technique for plasmas (Albright, Daughton, Lemons, Winske, & Jones, 2002) and simple Eulerian flows (Albright, Lemons, Jones, & Winske, 2002). The QDS method was then applied with a random time step to simulate a typical diffusion equation and an improved simulation time was achieved (Peter, 2007).

The QDSMC method was then reformulated to be a conservative, finite volume scheme and was implemented to second order accuracy (Smith, et al., 2009). The reformulated QDSMC scheme was renamed as the QDS scheme due to the lack of stochastic processes. Recently, the QDS method was extended to a second-order axisymmetric solver (Lim, et al., submitted). Some ongoing developments of the QDS method include parallel implementation and multiple species computation (Cave, et al., 2011), application to an arbitrary governing probability distribution function for solving viscous flow (Smith, Kuo, Cave,

Jermy, & Wu, 2010), and investigation of the inherent viscosity of the QDS scheme (Jermy, Lim, & Cave, 2010).

5.2 Maxwell-Boltzmann equilibrium velocity distribution function and Gauss-Hermite quadrature

As described in section 3.4.3, the Maxwell-Boltzmann distribution is an equilibrium distribution function to express the distribution of molecules' thermal velocities when the gas molecules are at the thermal equilibrium condition. The Maxwell-Boltzmann velocity distribution function has the form of a normal probability distribution:

$$p(v) = \frac{1}{\sqrt{2\pi}\sigma} \exp\left(\frac{-(v-u)^2}{2\sigma^2} \right) \tag{5.1}$$

where u is the bulk velocity of the gas and σ^2 is the variance of the velocity distribution in which $\sigma = \sqrt{RT}$ where R is the gas constant and T is the temperature. Hence, $p(v)dv$ is the probability of finding a gas molecule with a velocity in the range $v \rightarrow v + dv$. By using a Gaussian quadrature (or Gauss-Hermite quadrature) , the integration of moments of Equation (5.1) over an infinite velocity range can be represented by the sum of a series of weights, multiplied by the value of $f(v)$ evaluated at N discrete velocities q_j:

$$\int_{-\infty}^{\infty} \frac{e^{-(v-u)^2 / 2\sigma^2}}{\sqrt{2\pi}\sigma} f(v)dv \approx \sum_{j=1}^{N} w_j f(q_j) \tag{5.2}$$

where w_j and q_j are the weights and abscissas of the Gaussian quadrature and are known as the Gauss-Hermite parameters (Zwillinger, 2003). The abscissas are the roots of the Hermite polynomials which can be defined by:

$$H_{n+1}(q) = 2qH_n - 2nH_{n-1} \tag{5.3}$$

where $H_{-1} = 0$ and $H_0 = 1$. The weights can be determined from:

$$w_j = \frac{2^{N-1} N! \sqrt{\pi}}{N^2 \left[H_{N-1}(q_i)\right]^2} \tag{5.4}$$

Equation (5.2) becomes exact when the function $f(v)$ is a linear combination of the $2N$ - 1 polynomials $x^0, x^1, \ldots, x^{2N-1}$.

The QDS method assumes a sufficiently high collision rate in each computational cell such that the velocity distribution relaxes completely to the Maxwell-Boltzmann local equilibrium distribution during the time step. In the QDS method, the Maxwell-Boltzmann equilibrium velocity distribution is discretised into a chosen number of "velocity bins" in each spatial dimension, typically 3 - 4 bins, as shown in Figure 5.1. In general, these "velocity bins" can be visualized as collections of gas molecules that have the same velocity and are spaced evenly across each computational cell. The mass fraction of the computational cell carried in each bin is determined by the weights of the Gauss-Hermite quadrature which is given in Equation (5.5) as:

$$f_{mass} = \frac{w_j}{\sqrt{\pi}} \tag{5.5}$$

The associated velocity of each bin is represented by the corresponding abscissa which is given in Equation (5.6) as:

$$v_j = u + \sqrt{2\sigma^2}\, q_j \tag{5.6}$$

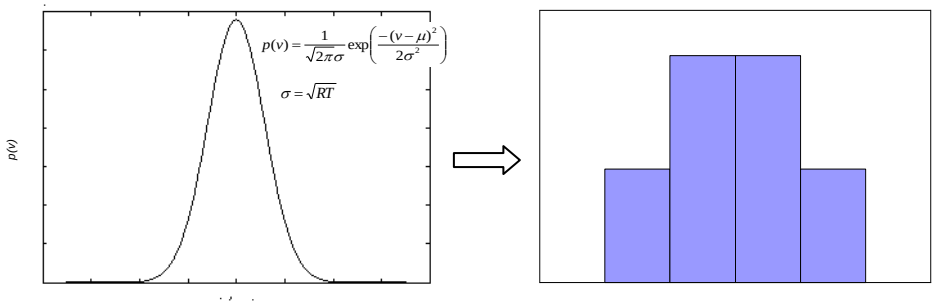

Figure 5.1 Discretisation of Maxwell-Boltzmann velocity distribution into QDS "velocity bins".

These bins are centred on the local mean (bulk) velocity. Choosing either an odd or even number of bins has a certain level of computational limitation. On one hand, if a small odd number of bins (e.g. 3) are used, the majority of the gas molecules velocities are represented by the bulk velocity with zero thermal velocity resulting in an under-prediction of the thermal flux. On the other hand, using an even number of bins will result in over-prediction of thermal flux since no particle with zero thermal velocity is considered.

5.3 First-order QDSMC scheme

The first order QDSMC algorithm proposed is a time marching explicit Eulerian flow solver (Albright, Lemons, et al., 2002). In the first order QDSMC scheme, the concept of "velocity bins" is represented by a chosen amount of fluid particles.

Therefore, the first order QDSMC scheme is a particle-based scheme. For a given computational mesh, the fluid at a grid point x_i is represented by J particles with known fluid properties of quantities of density (ρ_i), velocity (u_i), velocity variance (σ_{vi}^2) and energy (E_i). The particle masses, velocities and internal energies can be represented, respectively, in Equation (5.7) to (5.9) as:

$$m_{ij} = \frac{\rho_i \Delta x w_j}{\sqrt{\pi}} \tag{5.7}$$

$$v_{ij} = u_i + \sqrt{2\sigma_{vi}^2}\, q_j \tag{5.8}$$

$$\varepsilon_{ij} = \frac{(\xi - \Omega)\sigma_{vi}^2}{2\Omega} \tag{5.9}$$

where Δx is the grid size, ξ is the total number of degrees of freedom ($\xi = 2(\gamma - 1)^{-1}$) where γ is the specific heat ratio) and Ω is the number of simulated translational degrees of freedom (i.e. for one-dimensional simulations, $\Omega = 1$). All particles are transported to a new position in the computational mesh over a simulation time step Δt as given in Equation (5.10) at:

$$x_{ij}^{new} = x_i + v_{ij}\Delta t \tag{5.10}$$

The grid properties of mass, momentum and energy at the new time step are then determined by linearly distributing the quantities of mass (m_P), velocity (v_P) and internal energy (ε_P) carried by each particle to the mesh in the form given in Equation (5.11) to (5.13) as:

$$m_i = \sum_P m_P W_{Pi} \tag{5.11}$$

$$p_i = \sum_P m_P v_P W_{Pi} \tag{5.12}$$

$$E_i = \sum_P m_P \left(\frac{1}{2} v_P^2 + \varepsilon_P \right) W_{Pi} \tag{5.13}$$

where the linear weights, W_{Pi}, for each particle are defined by Equation (5.14) as:

$$W_{Pi} = \begin{cases} (x_P - x_{i-1})/(x_i - x_{i-1}) & if \quad x_{i-1} < x_P \le x_i \\ (x_{i+1} - x_P)/(x_{i+1} - x_i) & if \quad x_i < x_P \le x_{i+1} \\ 0 & otherwise \end{cases} \tag{5.14}$$

where x_P is the position of the particle within the cell. The macroscopic equilibrium temperature, T_i, of each cell can be calculated in the manner used by the conventional finite volume solvers and given in Equation (5.15) as:

$$T_i = \frac{1}{C_v} \left[\frac{E_i}{m_i} - \frac{1}{2} \left(\frac{p_i}{m_i} \right)^2 \right] \tag{5.15}$$

where C_v is the gas specific heat at constant volume which can be determined by Equation (5.16) as:

$$C_v = \frac{R}{\gamma - 1} \tag{5.16}$$

5.4 Second order true directional QDS scheme

The first order particle-based QDSMC scheme has been extended to a second order, two-dimensional flux-based scheme (Smith, et al., 2009). This scheme replaces the concept of interpolating particles properties onto a grid point, as in the QDSMC scheme, by a finite volume approach, where fluid properties (density, momentum, temperature) are piecewise linear in the computational cell. Spatial

gradients of the fluid properties are used to calculate the flux from a source cell to any arbitrary destination volume. Mass, momentum and energy are conserved by adding the fluxed quantities to the destination cells.

The 2*N* flux scheme presented by Smith *et al.* (Smith, et al., 2008) is employed to calculate the two-dimensional, true-direction fluxes. In the 2*N* flux scheme, the Maxwell-Boltzmann equilibrium velocity distribution function is discretised to *N* "velocity bins" in *x*- and *y*-directions, respectively, and are used to calculate the QDS flux. *N* true directional fluxes are computed in each coordinate direction in order to produce a total of 2*N* fluxes in the two-dimensional case. These fluxes are then combined to create a total of N^2 fluxes in each computational cell. Hence, for two-dimensional simulations with $j = 1,\ldots,J$ bins generated in the *x*-direction while $k = 1,\ldots,K$ in the *y*-direction, the amount of mass, velocity components and the energy carried in each bin can be calculated, respectively, by Equation (5.17) to (5.20) as:

$$m_{jk} = \frac{\left(\rho + \Delta x_L \frac{d\rho}{dx} + \Delta y_L \frac{d\rho}{dy}\right) V_c w_{xj} w_{yk}}{\pi} \tag{5.17}$$

$$v_{xj} = u_x + \frac{du_x}{dx}\Delta x_L + \sqrt{2\sigma_v^2}\, q_j \tag{5.18}$$

$$v_{yk} = u_y + \frac{du_y}{dy}\Delta y_L + \sqrt{2\sigma_v^2}\, q_k \tag{5.19}$$

$$\varepsilon_{jk} = \frac{(\xi - \Omega)\left(\sigma_v + \Delta x_L \frac{d\sigma_v}{dx} + \Delta y_L \frac{d\sigma_v}{dy}\right)^2}{2} \tag{5.20}$$

where V_c is the volume of the cell, Δx_L and Δy_L represent the locations on the cell in the *x*- and *y*-direction, respectively, from where the flow properties are taken. For example, for a flux moving to the right of the cell centre, $\Delta x_L = 0.5(\Delta x - v_{xj}dt)$ where *dt* is the time step. This is illustrated in Figure 5.2 which shows the addition of a linear variation of density within a computational cell.

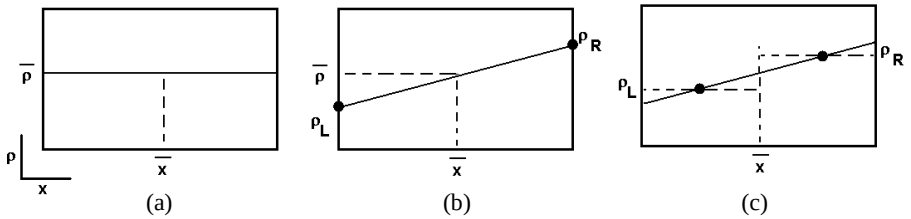

Figure 5.2 Examples of addition of in-cell gradients. (a) No gradient, conventional first order scheme, (b) conventional finite volume implementation where fluxes are calculated at cell interfaces and (c) implementation when calculated fluxes are volume to volume (direction decoupled) as opposed to calculated at flux interfaces (Smith, et al., 2009) .

The true directional QDS scheme is basically a direction coupled volume-to-volume solver. Thus, conditions within a region of space are required such that particles moving to a region right of the source cell are likely to have their properties defined by a region in the right half of the cell. In the present QDS scheme, fluxes moving to the right are assumed to take their quantities from the reconstructed state at Δx_L to the right of the cell center. This corresponds to the displacement of the centre of mass of the flux which moves into the destination cell. Left moving fluxes have properties constructed in a similar manner such that $\Delta x_L = 0.5(-\Delta x - v_{xj}dt)$. The fluxes are then moved in free flight, justifying the use of a linear interpolation routine.

In addition, the property gradients are calculated using a slope limiter in order to prevent unphysical and unstable oscillations in the solution. In the calculation of Equations (5.17) to (5.20), the gradients of the flow properties are determined using the MINMOD (Minimum Modulus) or the MC (Monotonized Central Difference) slope limiter (Van Leer, 1977). As an example, the density gradient in axial flux calculation using the MC slope limiter is given in Equation (5.21) as:

$$\frac{d\rho}{dx} = MINMOD\left[\frac{\rho_{i+1}-\rho_{i-1}}{2\Delta x}, MINMOD\left(2\frac{\rho_{i+1}-\rho_i}{\Delta x}, 2\frac{\rho_i-\rho_{i-1}}{\Delta x}\right)\right] \quad (5.21)$$

where the MINMOD slope limiter is given in Equation (5.22) as:

$$\text{MINMOD}[a,b] = \begin{cases} 0 & \text{if SIGN}(ab) < 0 \\ a & \text{if SIGN}(ab) > 0 \text{ and } |a| < |b| \\ b & \text{if SIGN}(ab) > 0 \text{ and } |b| < |a| \end{cases} \quad (5.22)$$

The fluxes generated in a source cell are then allowed to undergo free flight in true direction to any location determined from the velocity as shown from Figure 5.3 (a) to 5.3 (b). In conserving the flow properties transported from a source cell to a location that may overlap multiple destination cells, the amount of a fluxed property being added to each of the destination cells is computed according to the ratio of the overlap area, A, to the area of the source cell, A_S. The overlap area, A, can be calculated by Equation (5.23) as:

$$A = v_{xj} v_{yk} dt^2 \quad (5.23)$$

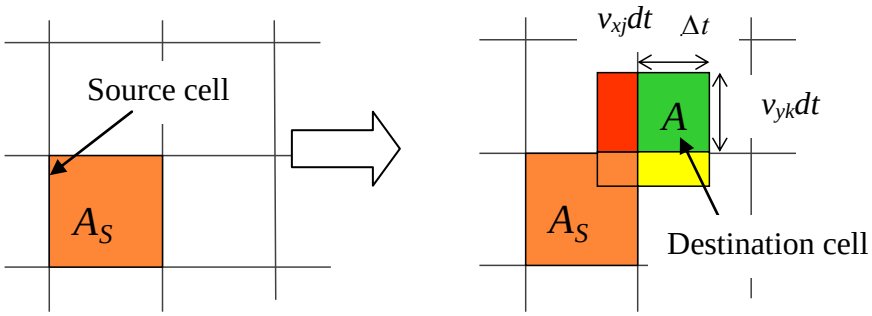

Figure 5.3 Schematic of QDS fluxes of flow properties transported from (a) source to (b) destination cell.

Thus, the mass, $m_{flux,jk}$, components of momentum, $p_{flux,xj}$, and $p_{flux,yk}$, and energy, $E_{flux,jk}$, which are added to each of the destination cells (and subtracted from the source cell) are calculated, respectively, by Equation (5.24) to (5.27) as:

$$m_{flux,jk} = \frac{A}{A_S} m_{jk} \tag{5.24}$$

$$p_{flux,xj} = \frac{A}{A_S} m_{jk} v_{xj} \tag{5.25}$$

$$p_{flux,yk} = \frac{A}{A_S} m_{jk} v_{yk} \tag{5.26}$$

$$E_{flux,jk} = \frac{A}{A_S} m_{jk} \left[\frac{1}{2} \left({v_{xj}}^2 + {v_{yk}}^2 \right) + \varepsilon_{jk} \right] \tag{5.27}$$

5.5 Axisymmetric second order QDS

The simple calculation of the flux being transported to a destination cell in a Cartesian mesh based on the overlap area, which is given in Equations (5.24) to (5.27), becomes more complicated for axisymmetric simulations on a cylindrical

polar mesh. For that, the second-order flux-based QDS scheme has been extended to axisymmetric flow computation (Cave, 2010). Two important corrections must be applied in calculating the mass and momentum fluxes as the volume of the cells vary in the radial direction. The first correction is needed in the calculation of the overlap area due to the fluxes that move away from the axis expanding into a larger cell volume and vice versa. The second correction is applied to the momentum calculation in each cell because of the variation in the force due to static pressure across the top and bottom cell interfaces.

The calculation of the overlap area for the radial component of fluxes shown in Equation (5.23) needs to be corrected to take the change in cell volume into account at different radii. Using the illustration in Figure (5.4) for a flux having radial velocity, v_r, over a time step, Δt, the ratio between the displaced volume, V_d, (which has centroid at radius r and radial width Δr) to the original volume of the mass flux, V_o, can be calculated depending on the direction of the radial velocity given in Equation (5.28) or (5.29) as:

$$\frac{V_d}{V_0} = \frac{v_r \Delta t\left(2r + \Delta r - v_r \Delta t\right)}{2r\Delta r} \quad \text{for } v_r > 0 \qquad (5.28)$$

$$\frac{V_d}{V_0} = \frac{v_r \Delta t\left(-2r + \Delta r + v_r \Delta t\right)}{2r\Delta r} \quad \text{for } v_r < 0 \qquad (5.29)$$

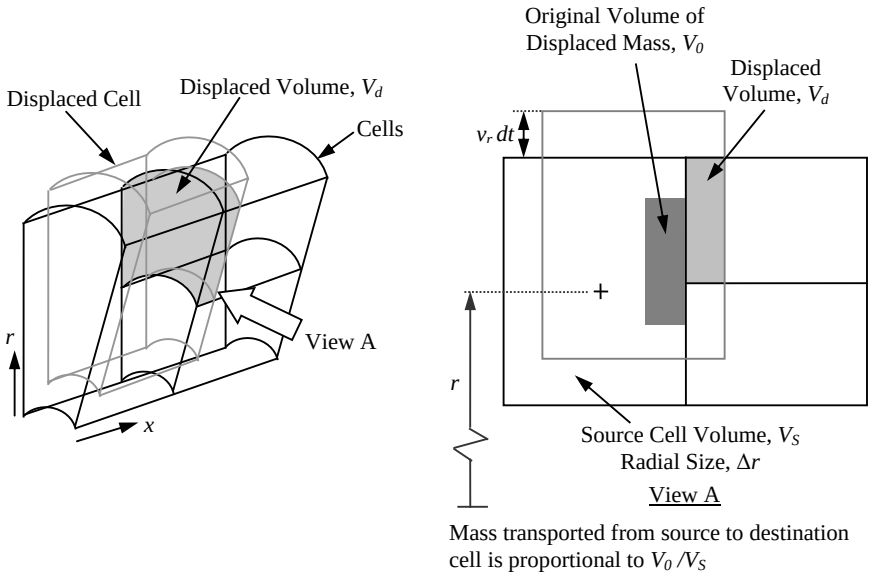

Figure 5.4 Schematic showing the relationship between displaced and original volumes used to calculate the fluxes in axisymmetric QDS (Cave, 2010).

The ratios in Equation (5.28) or (5.29) can be multiplied directly to the radial component of the mass, momentum and energy fluxes to accommodate the variation of volume in the source and destination cells. These ratios, however, are suitable for the first order simulation only. For second order computation, the effect of the property gradients must be considered. The radial flux from a source cell at radius, r_{cell}, (with lower and upper boundaries, r_L, and r_R, respectively) to a cell of greater radius can be demonstrated in Figure 5.5.

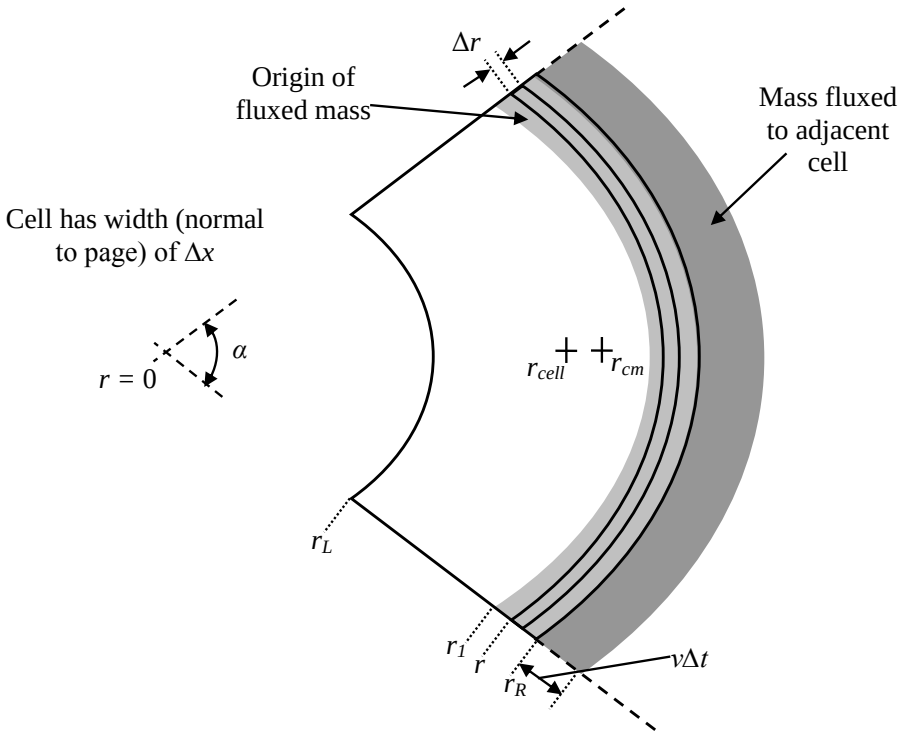

Figure 5.5 Schematic for the derivation of second order expressions of radial fluxes for axisymmetric QDS simulations (Cave, 2010).

Considering that there is a constant density gradient across the cell, $B = d\rho/dr$, the centre of mass of the source cell, r_{cm}, can be determined using Equation (5.30) as:

$$\begin{aligned} r_{cm} &= \frac{1}{m_{cell}} \int_{r_L}^{r_R} \left[\rho_{cell} + B\left(r - r_{cell}\right)\right] \Delta x r \alpha r dr \\ &= \frac{\alpha \Delta x}{m_{cell}} \left[\frac{B\left(r_R^4 - r_L^4\right)}{4} + \frac{\left(\rho_{cell} - B r_{cell}\right)\left(r_R^3 - r_L^3\right)}{3} \right] \end{aligned} \tag{5.30}$$

where m_{cell} is the total mass of the cell, r_R is the upper boundary of the cell, α is the axisymmetric angle (usually π) and $r_1 = r_R - v_{rj}\Delta t$. The mass of the element between r and $r+\Delta r$ can then be expressed by Equation (5.31) as:

$$\begin{aligned} mass\left(r \to r + \Delta r\right) &= \left[\rho_{cm} + B\left(r - r_{cm}\right)\right] \Delta x r \alpha \Delta r \\ &= \alpha \Delta x \left[B r^2 + C r\right] \Delta r \end{aligned} \tag{5.31}$$

where the constant $C = \rho_{cm} - Br_{cm}$. Integrating Equation (5.31) between r_1 and r_R, the net mass flux between the two cells is given in Equation (5.32) as:

$$\begin{aligned} Net \quad mass &= \alpha \Delta x \int_{r_1}^{r_R} \left(Br^2 + Cr \right) dr \\ &= \alpha \Delta x \left[\frac{B}{3} \left(r_R^3 - r_1^3 \right) + \frac{C}{2} \left(r_R^2 - r_1^2 \right) \right] \end{aligned} \tag{5.32}$$

Hence, while the mass carried by the axial fluxes remains the same as in Equation (5.24), the amount of mass carried by the radial fluxes is calculated by Equation (5.33) as:

$$m_{rj} = \frac{\alpha \Delta x \left[\frac{B}{3} \left(r_R^3 - r_1^3 \right) + \frac{C}{2} \left(r_R^2 - r_1^2 \right) \right] w_{yj}}{\sqrt{\pi}} \tag{5.33}$$

A momentum correction is required at each time step to account for the pressure change along the control volume elements in the radial direction for axisymmetric flows. This is because the force due to the static pressure across the top and bottom interfaces of an axisymmetric cell also varies in the radial direction as shown in Figure 5.6. The correction of the amount of momentum to be added to the destination cell can be determined by Equation (5.34):

$$\Delta p = P \alpha \, \Delta r \, \Delta x \Delta t \tag{5.34}$$

where P is the pressure in the cell, α is the axisymmetric angle (usually π), Δr and Δx are the radial and axial size of the cell, respectively, and Δt is the simulation time step.

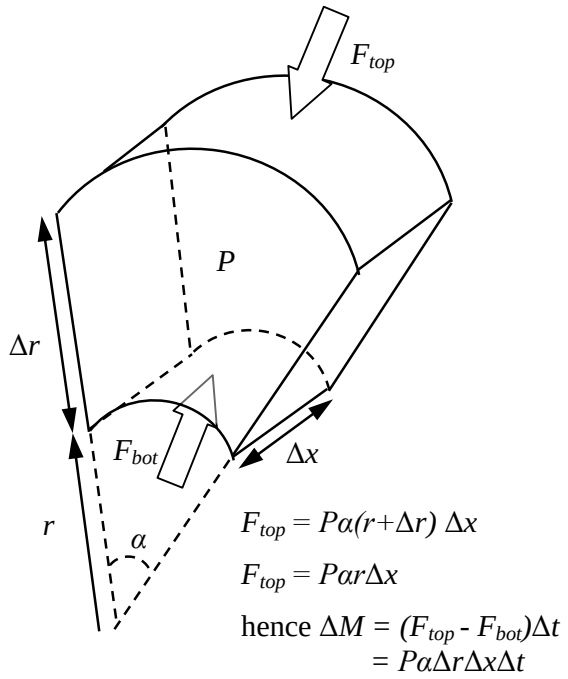

Figure 5.6 Schematic of the forces due to static pressure *P* on an axisymmetric cell (Cave, 2010).

Without the momentum correction, an artificial radial flux appears towards the axis of the symmetry, even when the bulk radial velocity is zero in the flow field.

5.6 Dynamic time step adjustment and boundary conditions

The simulation time step duration Δt is reset at each time step in order to maintain the maximum Courant–Friedrichs–Levy (*CFL*) number in the flow field at a chosen value, always less than 1 and usually 0.5. In the current implementation, the CFL number is determined by Equation (5.35) as:

$$CFL = \frac{\left(\sqrt{\left(u_x^2 + u_y^2\right)} + q_{j(\max)}\sqrt{RT_i}\right)\Delta t}{\sqrt{\left(\Delta x^2 + \Delta y^2\right)}} \qquad (5.35)$$

where $q_{j(max)}$ is the maximum abscissas value of the QDS "velocity bins". This *CFL* restriction is not necessary for the numerical stability of this explicit scheme. It is used to maintain physical realism where a particle is prevented from travelling more than the distance of one cell size before the collision step is carried out and local thermal equilibrium is established.

The boundary conditions are implemented by introducing virtual or 'ghost' cells at all walls, inflow and outflow boundaries (Smith, et al., 2009). Fluxes from flow field cells crossing all of the boundaries are destroyed. The depletion of these fluxes is replaced by the fluxes originating from the ghost cells. The macroscopic properties of the ghost cells are determined accordingly depending on the type of the boundary implemented.

For all wall boundaries, the specular reflection scheme is applied to implement the slip wall boundary condition, since the QDS scheme is essentially an Euler solver. The ghost cells introduced at the wall boundaries have the same flow properties as the adjacent cells within the flow field but a reversed flow direction normal to the wall. Due to the variation in the cell volume in the radial direction of the axisymmetric simulation, the density in a ghost cell at a different radius from the adjacent flow field cell is adjusted to ensure a zero net mass or energy flux and correct momentum flux.

For the inflow boundaries, the ghost cells usually have properties equal to the free stream conditions. For the gas injected PP-CVD flow simulation, choked flow conditions are to be assigned to the ghost cells at the inflow boundary. For

the liquid injected PP-CVD flow simulations, the use of ghost cells at the inlet boundary is turned off. A droplet flash evaporation model is used instead to provide the inflow condition for the gas phase simulation. The droplet flash evaporation model will be described in detail in Chapter 7.

For the outflow boundary, the ghost cells usually have properties extrapolated from values within the adjacent flow field cells to ensure gradients of density, momentum and energy are equal to zero across the outflow boundary. However, for the PP-CVD flow simulation, an outflow rate determined from the vacuum evacuation rate as described in Section 4.2.2 is used to specify the flow properties of the ghost cells.

5.7 Model Validation

5.7.1 Explosion of a Cylindrical Cavity

To validate the axisymmetric second order true directional QDS implementation, a simulation was conducted on the explosion of a cylindrical cavity of high temperature. The simulation was conducted with the axisymmetric QDS codes by using 4 velocity bins per coordinate direction and MINMOD slope limiter in calculating properties gradients. The QDS simulation result was compared to that of the simulation using one-dimensional EFM method discussed in Chapter 3. The EFM simulation of this test case was carried out by Cave (Cave et al., 2009). In the simulation, 200 radial cells are used with a total radius of r =

1.0 m while the 200 axial cells are used for the length of the cylinder of L = 1.0 m. The cylindrical cavity, which has a radius of 0.5r, is initially at temperature T_i = 100 K while the surrounding temperature is at T_s = 1.0 K. The density is initially uniform at ρ = 1.0 kg/m^3 everywhere. The gas constant R = 1.0 J/(kg·K) and the ratio of specific heats is 5/3. The simulation time step was reset after each time step with the condition CFL < 0.5 maintained.

Figure 5.8 shows the comparison of the radial temperature variation for the explosion of the cylinder cavity at a time of 0.025 s between the axisymmetric QDS and the EFM (Pullin, 1980) simulations. From Figure 5.7, the similarity between the results indicates that the second order true directional axisymmetric QDS code is working correctly. The slight difference between the results, in particular near the shock front at about r = 0.6 m indicates that the second order QDS method shows reduced numerical diffusion compared to the first order EFM.

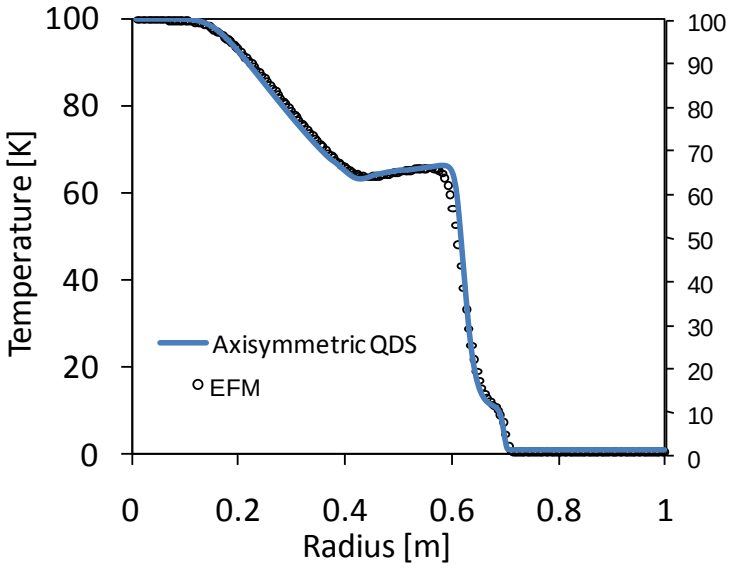

Figure 5.7 Temperature profile comparison for the explosion of a cylindrical cavity problem between the axisymmetric QDS method and the first-order EFM at a flow time of 0.025s.

5.7.2 Shock Wave Flow in a Pipe with a Sudden Expansion

As a further validation for the second order true directional axisymmetric QDS algorithm, the propagation of a Mach 2 shock wave in a circular pipe through a sudden expansion was simulated. This validation simulation was also performed by Cave (Cave, et al., 2009). This problem has been widely studied experimentally and numerically. One of the studies was to investigate the flow of gases at various Mach numbers through tubes of varying ratios of cross sections using both experimental and numerical approaches (Jiang, Takayama, Babinsky, & Meguro, 1997). In the numerical approach, a second-order, dispersion-controlled scheme was employed to solve the axisymmetric Euler equations.

Figure 5.8 show the geometry and boundary conditions of the axisymmetric QDS simulation for a Mach 2 shock through a sudden pipe expansion with R/r = 2.0. The simulation gas was ideal argon with a ratio of specific heats of 5/3 and a gas constant of R = 208.2 J/(kgK). For completeness the undisturbed flow conditions at (2) are ρ_2 = 1.0 kg/m^3 and T_2 = 300 K. The conditions behind the shock can be determined from the Rankine-Hugoniot conditions and are ρ_1/ρ_2 = 2.286, T_1/T_2 =2.078 and the axial velocity is 363 m/s. The variable time step scheme was used so the maximum kinetic *CFL* number in the simulation domain was 0.5 with 100 square cells along the radius r. Four QDS velocity bins were used in each coordinate direction in a 2N flux scheme.

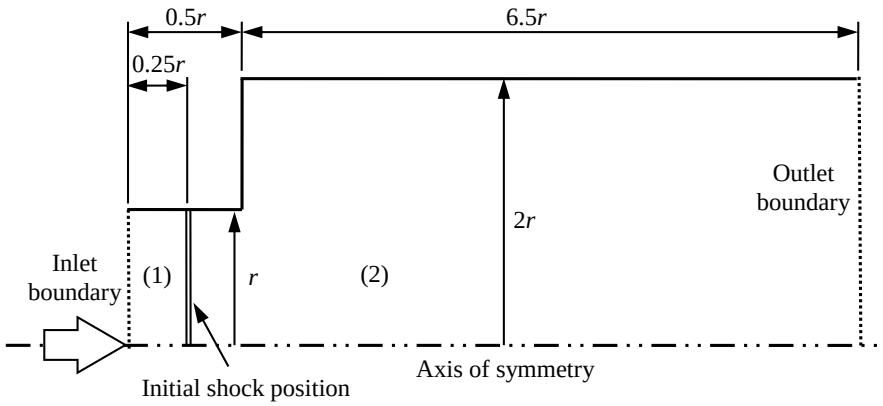

Figure 5.8 Geometry and boundary conditions for the simulation of Mach 2 shock through a sudden pipe expansion.

As a point of comparison, THE QDS METHOD was compared to a direct simulation (DS) based on the PDSC (Wu, et al., 2004). The PDSC algorithm was modified to effectively become equivalent to the Equilibrium Particle Simulation Method (EPSM) solver (Pullin, 1980). Rather than manually setting particle velocities to equilibrium values, each simulation particle was forced to undergo a minimum of four collisions after a free-flight advection stage. Previous investigations have shown that this is sufficient to bring the particles approximately into thermal equilibrium (Sharma & Long, 2004). It has also been studied by Titov and Levin, using a collision-limited DSMC scheme, that two collisions per time step per particle are sufficient to relax the particles into a velocity distribution with negligible difference compared to the corresponding Maxwell-Boltzmann equilibrium distribution (Titov & Levin, 2007). The solver was then further modified to become analogous to the first order QDS solver by randomly redistributing particle locations within the computational cell. It was

necessary to use a direct simulation for comparison since the conventional CFD solvers are direction-coupled and therefore cannot be compared directly to a true direction method like the QDS method. Furthermore, traditional finite volume CFD methods attempt to solve the Euler equations directly, whereas the DS method is based on kinetic theory in the same way as the QDS method. The simulation time step for the DS solver was set to be 5×10^{-6} s which was found to be sufficiently short so that $CFL < 0.5$ for the entire simulation. A large number of particles (a peak of approximately 4.38 million at the sampling time step) were used to reduce the statistical scatter in the simulations. Here 50 square cells along the radius r were used so that the computational expense for the DS was reasonable (the QDS simulation used the same number of cells for this comparison). The DS result required approximately 34.2 hours for 45 ensemble-averaged runs on a PC cluster system of twelve Athlon XP2100s, whereas the QDS simulation took 29 s on a single Intel 3.33GHz Dual Core processor with 4GB of system RAM. Figure 5.9 shows a comparison between the methods at a flow time of 0.01 s. Although the DS results remain scattered, they clearly show the positions of the primary flow features, which can be seen to compare closely to the features in the QDS simulation.

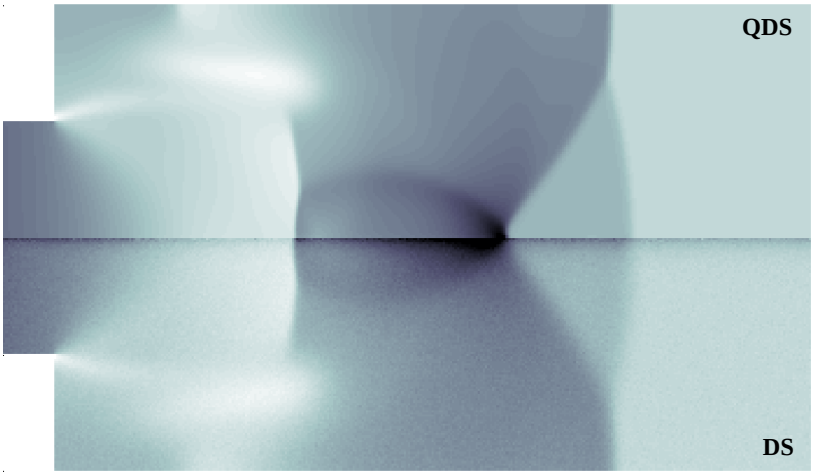

Figure 5.9 Comparisons of density [kg/m^3] contours for a Mach 2 shock through a sudden pipe expansion between QDS (top) and DS (Cave, et al., 2009).

5.8 PP-CVD Simulations by True Directional Axisymmetric QDS

The second order true directional axisymmetric QDS method is applied to simulate the reactor flow field for the gas injected PP-CVD process. Two cases were simulated at two different operating pressure conditions as described in Table 5.1. In both simulations ideal Helium gas, at choked inlet flow conditions, is injected into the reactor through an orifice. The initial reactor flow field is at stationary. Both simulations were carried out on a desktop computer with 3.00GHz Intel Core 2 Duo CPU and 4GB of RAM using 312,744 uniform square cells with 0.25 mm cell size.

Table 5.1 Simulation conditions for PP-CVD flow field simulations using the QDS method.

	Case I	**Case II**
Supply Pressure, P_s	10 kPa	40 kPa
Pulse Range, $P_{min} \rightarrow P_{max}$	1 Pa → ~100 Pa	1 kPa → ~5 kPa
Injection time, t_i	0.1 s	
Supply Temperature, T_s	293 K	
Initial Temperature, T_i	293 K	
QDS velocity bin, N	4 per coordinate direction	
Simulation time step, Δt	variable time step with maximum CFL < 0.5	
Slope limiter	MINMOD	

Figure 5.10 shows the computational domain for both cases.

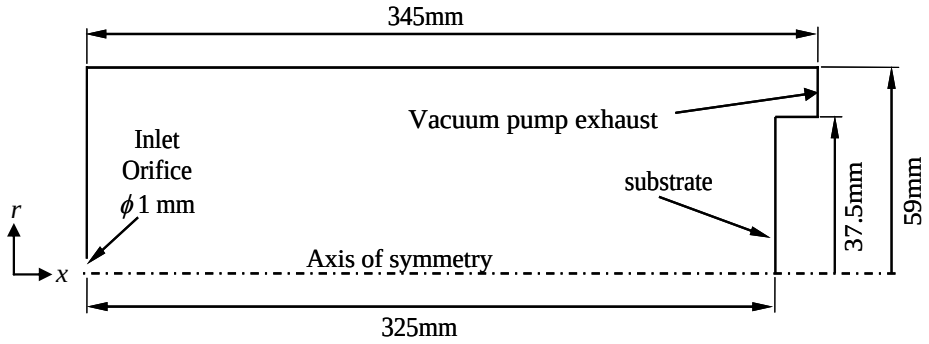

Figure 5.10 Schematic of PP-CVD reactor geometry.

5.8.1 Case I: 1 Pa initial reactor pressure

5.8.1.1 Case I: Injection phase

Figure 5.11 shows, plotted on a natural logarithm scale, the density contours (left) and the pressure contours (right) of Case I conditions during the first 4 ms of the injection phase. It is noted that the under-expanded jet with a wide shock structure develops during the injection phase. These results capture the shock structure and flow development with far higher resolution and computational efficiency than the

DSMC simulations given in the thesis by Cave (Cave, 2008). The contour plots in Figure 5.11 show a wide initial bow shock at the exit of the inlet orifice, followed by the development of a shock wave pattern and the evolution of the shear layer and formation of a Mach disk during the unsteady flow development period. After 4.0 ms, a quasi-steady under-expanded jet structure, which was discussed in section 4.1.1, is seen and impinges onto the substrate region. The formation and evolution of constantly changing expansion and compression waves are captured in clear details by the QDS solver. Similar flow could also be seen in the numerical studies performed using the space-time conservation element solution element (CE/SE) method on unsteady jet flows from a rocket nozzle (Chang, Chang, & Chang, 2005). This demonstrates the capability of the QDS solver in modelling unsteady flow phenomena at low computational cost.

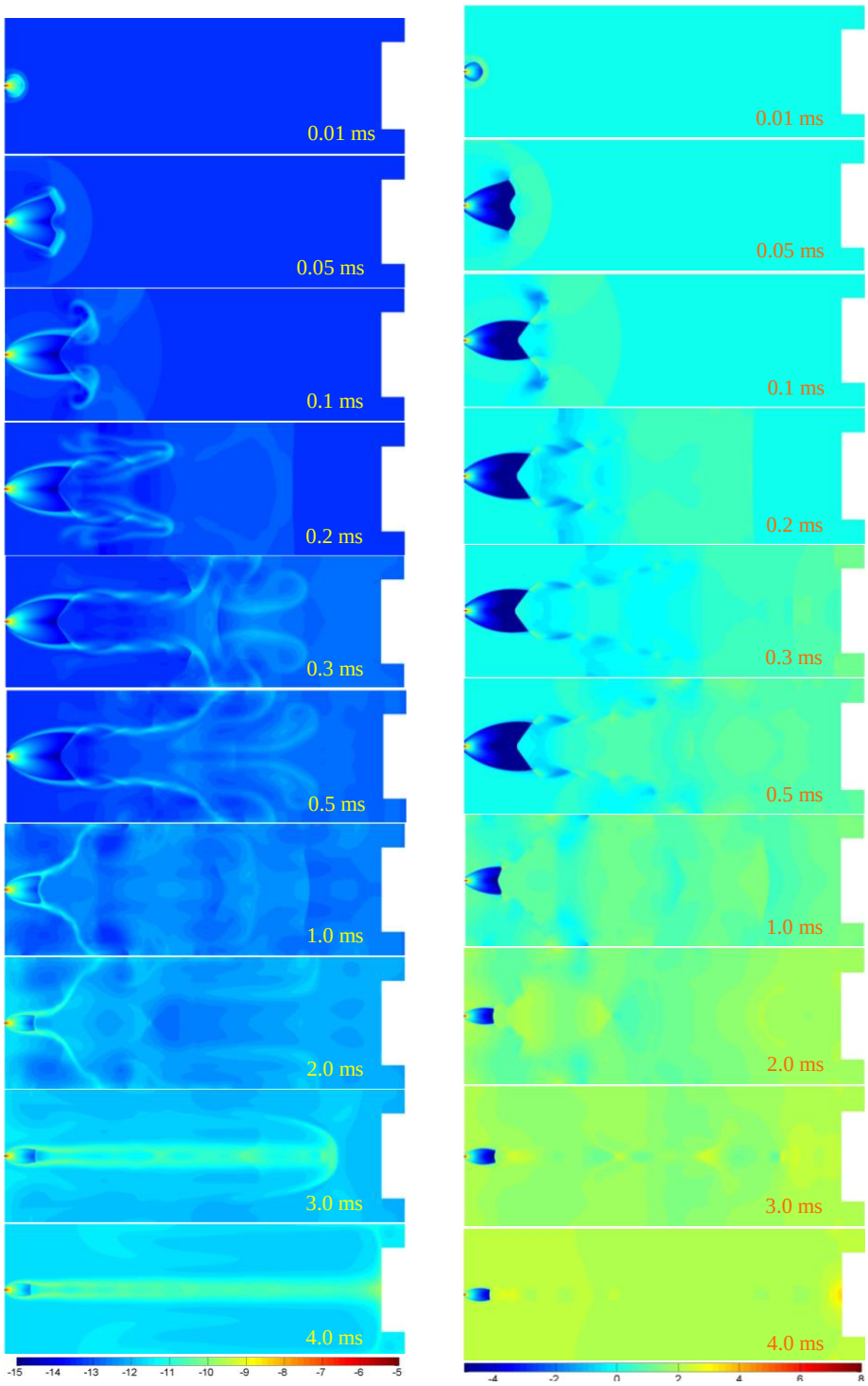

Figure 5.11 Log_e(density) [kg/m^3] contour (left) and Log_e (pressure) [Pa] contour (right) for the unsteady flow development of an under-expanded jet in a PP-CVD reactor at Case I conditions during first 4 ms of the injection phase.

As discussed in section 4.3.5, in the QDS method it is assumed that that thermal equilibrium is established locally within each computational cell by the end of the time step. Based on this assumption, the molecular velocity distribution is approximated with the Maxwell-Boltzmann distribution. In investigating the validity of the local equilibrium assumption, the gradient length local Knudsen number, Kn_{GLL}, discussed in section 4.3.5 was calculated at the simulation times of 0.5 ms and 4 ms. At 0.5 ms, the Mach disc position was stabilised in the flow field while the flow developed into a quasi-steady state at 4ms. The criterion for continuum breakdown occurs is $Kn_{GLL} > 0.05$. Figure 5.12 shows the contours of the gradient length local Knudsen number based on density, $(Kn_{GLL})_\rho$, plotted on natural logarithm scale at the simulation times of 0.5 ms and 4 ms, respectively, for Case I. It is noted that in the most of the shock regions $\log_e(Kn_{GLL}) > \log_e(0.05) \sim -3$ and thus the continuum assumption cannot be considered valid in Case I.

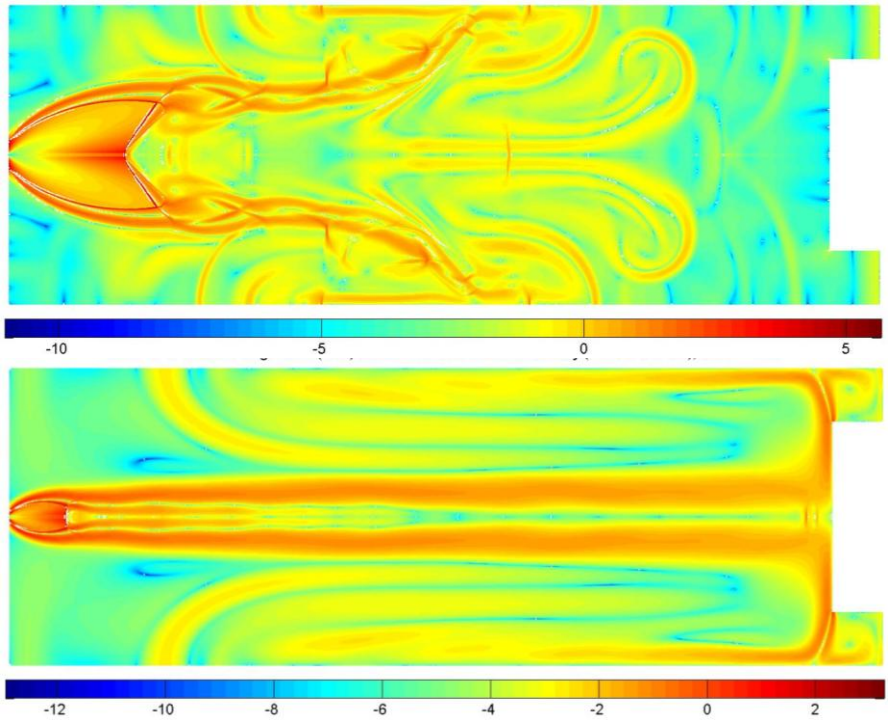

Figure 5.12 $\log_e[(Kn_{GLL})_\rho]$ contours at 0.5ms (top) and 4ms (bottom) at Case I conditions.

The validity of the thermal equilibrium assumption is also tested by calculating the ratio of computational time step to the average time between particle collisions, $\Delta t/t_{col,avg}$, as discussed in section 4.3.5. A criterion of $\Delta t/t_{col,avg} \geq 2$ is used to validate the assumption of the computed non-equilibrium distribution to relax sufficiently close to the corresponding Maxwell-Boltzmann equilibrium distribution. Figure 5.13 shows the contours of the $\Delta t/t_{col,avg}$ plotted on a natural logarithm scale at the simulation times of 0.5 ms and 4 ms, respectively, for Case I. The equilibrium assumption may be considered valid where $\log_e(\Delta t/t_{col,avg}) \geq 0.69$. In Figure 5.13, it is seen that this condition is not satisfied anywhere in Case I either at t = 0.5 s or t = 4 s, except near the orifice exit.

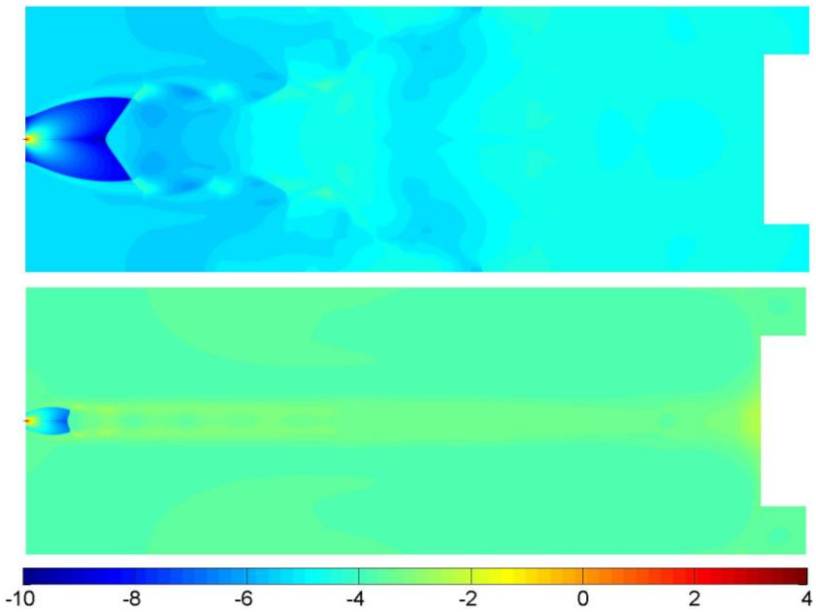

Figure 5.13 $\log_e(\Delta t/t_{col,avg})$ contours at 0.5ms (top) and 4ms (bottom) at Case I conditions.

5.8.1.2 Case I: Pump-down phase

The pump-down phase of the PP-CVD operating cycle at Case I conditions was also simulated. The reactor pressure at the end of the injection phase is estimated to be 100 Pa based on experience with such reactors. Figure 5.14 shows the density contours (left) and the pressure contours (right) plotted on a natural logarithm scale of the unsteady flow development during first millisecond of the pump-down phase at Case I conditions.

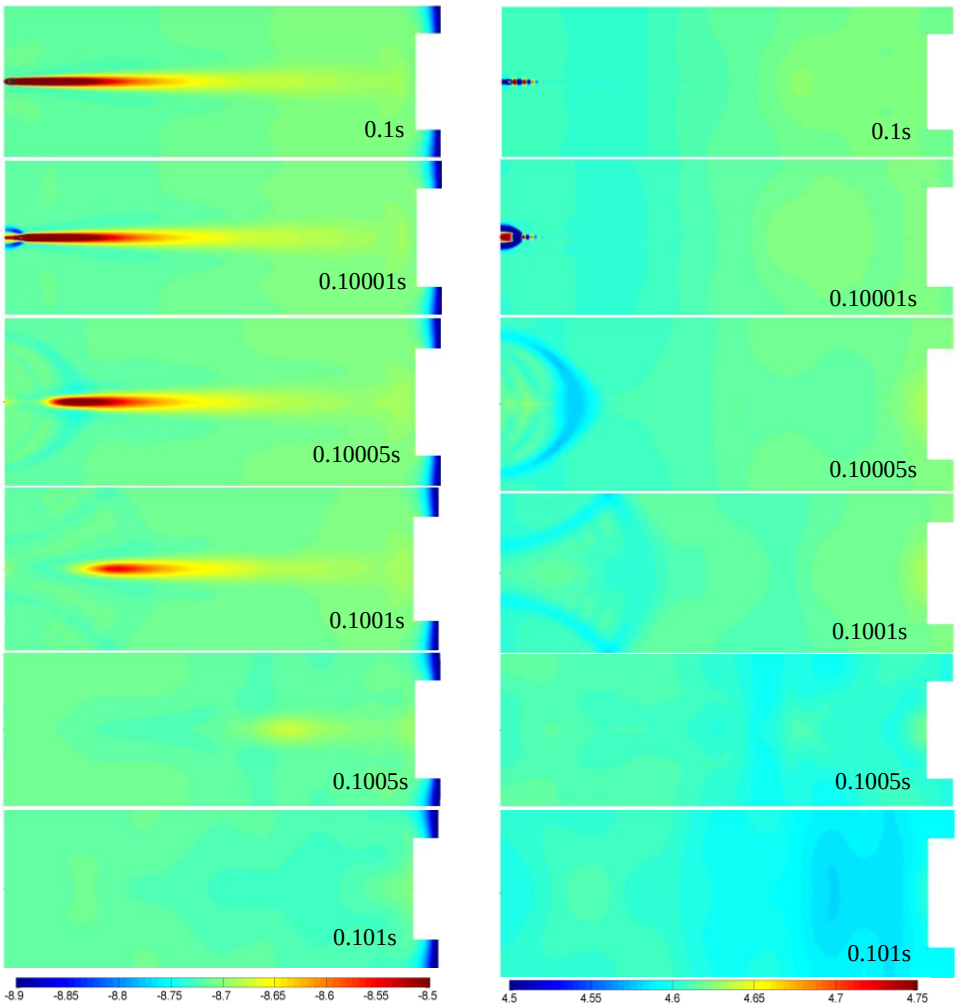

Figure 5.14 $\log_e$(density) [kg/m^3] contour (left) and $\log_e$(pressure) [Pa] contour (right) for the unsteady flow development of an under-expanded jet in a PP-CVD reactor at Case I conditions during first millisecond of the pump down phase.

It is noted that the quasi-steady jet structure developed during the injection phase shortens towards the inlet nozzle and does not impinge on the substrate. The flow is quite uniform near the substrate region, promoting uniform precursor deposition. The inlet nozzle shuts off at 0.1 s and within one further millisecond the jet structure has dissipated. The resulting flow field is rather uniform during the remaining pump-down process. Information on the jet formation and dissipation,

and the structure of the flow field near the substrate, is useful for the design and choice of operating conditions for PP-CVD.

The ratio of the average time between particle collisions to simulation time step was calculated to estimate the number of particle collisions per time step per particle within a computational cell. Figure 5.15 shows the contours of the $\Delta t/t_{col,avg}$ at 0.10001 s (10 μs after the end of injection phase at 0.1 s) and 0.1001 s (after the jet structure has dissipated), respectively, during the pump-down phase for Case I. Figure 5.15 shows that ($\Delta t/t_{col,avg}$) ≥ 0.5, i.e. two collisions per time step per particle, is not achieved during the pump-down phase simulation in Case I.

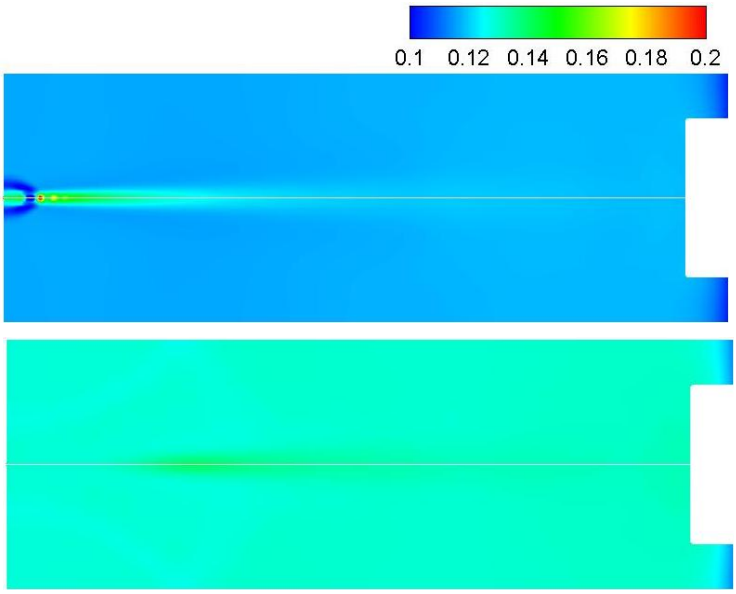

Figure 5.15 ($\Delta t/t_{col,avg}$) contours at 0.10001s (top) and 0.1001s (bottom) at Case I conditions.

Figure 5.16 shows the contours of the gradient length local Knudsen number based on density at the simulation times of 0.10001 s (10 μs after the end of injection) and 0.1001 s, respectively, for Case I.

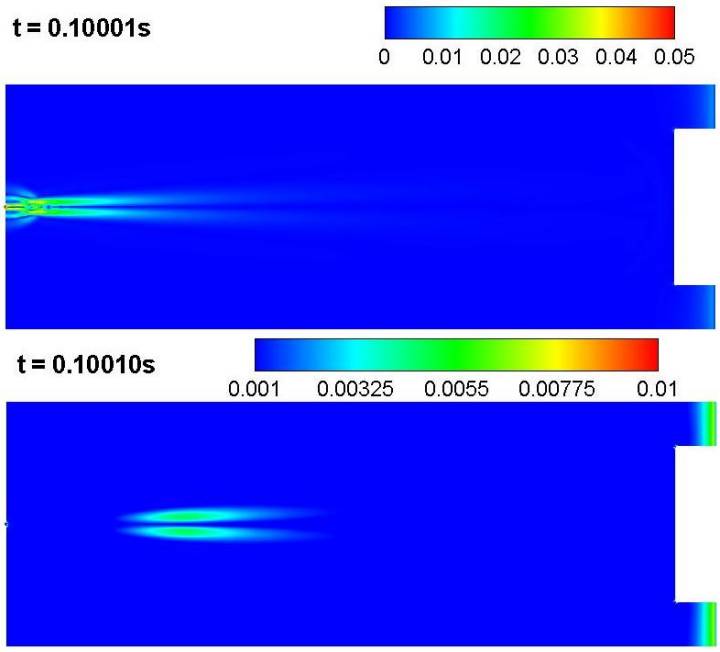

Figure 5.16 $(Kn_{GLL})_\rho$ contours at 0.10001s (top) and 0.1001s (bottom) at Case I conditions.

As discussed above, continuum breakdown occurs when $Kn_{GLL} > 0.05$. The contour plots in Figure 5.16 shows that $(Kn_{GLL})_\rho$ is less than 0.05 everywhere except in a limited region near inlet nozzle with $(Kn_{GLL})_\rho$ close to 0.05 soon after the inlet jet is shut down. However, these regions are unlikely to have a significant effect on the flow field. It is also noted that $(Kn_{GLL})_\rho$ decreases in time during the pump-down phase. Therefore, although the number of collisions was low and the two collisions per time step per particle condition is not satisfied, the local density gradient within the computational cell was not high enough to transport the particles downstream before thermal equilibrium condition was established.

Hence, the assumption that equilibrium is re-established locally in each time step in the current QDS scheme is partially justified for the PP-CVD process during the pump-down phase.

5.8.2 Case II: 1 kPa initial reactor pressure

5.8.2.1 Case II: Injection phase

Figure 5.17 shows, plotted on natural logarithm scale, the density contours (left) and the pressure contours (right) of the simulation results for Case II conditions during the first 4 ms of the injection phase. The pressure ratio between the precursor solution supply and the reactor volume is lower in Case II compared to that in Case I. This results in a lower degree of expansion waves being formed at the exit of the inlet nozzle compared to Case I. Hence, the under-expanded jet has a much narrower shock structure during the injection phase compared to Case I and, consequently, lower rates of mass transport in the radial direction. Again, complicated flow phenomena such as the initial bow shock at the exit of the inlet orifice, the shear layer evolution and eventually Mach disk formation during the unsteady flow development period were captured in clear detail. The flow field eventually becomes quasi-steady at about 1 ms.

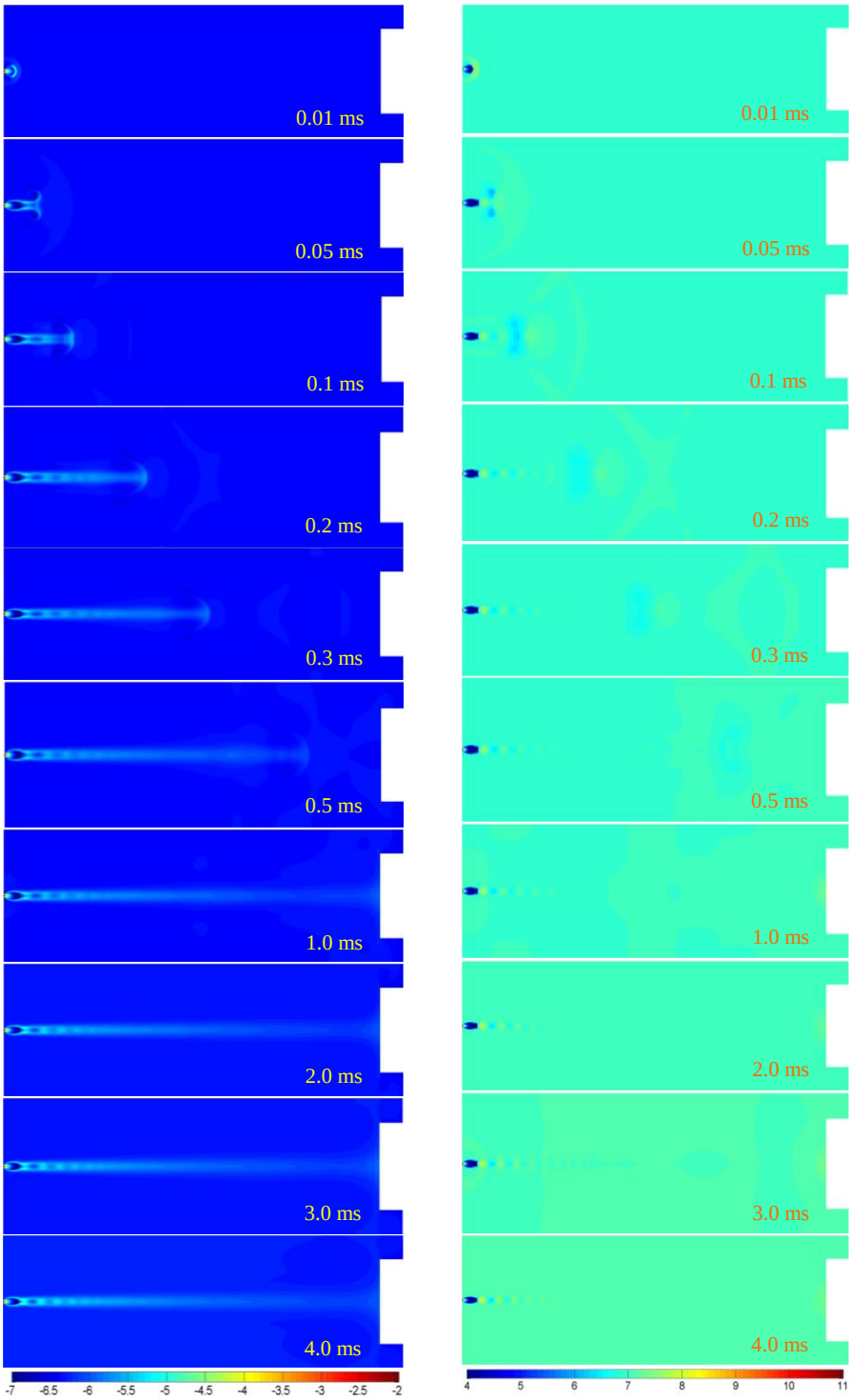

Figure 5.17 $\log_e$(density) [kg/m^3] contour (left) and $\log_e$(pressure) [Pa] contour (right) for the unsteady flow development of an under-expanded jet in a PP-CVD reactor at Case II conditions during first 4 ms of the injection phase.

The thermal equilibrium assumption in the current QDS scheme was also tested for Case II. Figure 5.18 shows the contours of the of the gradient length local Knudsen number based on density plotted on natural logarithm scale at the simulation times of 0.5 ms and 4 ms, respectively, for Case II.

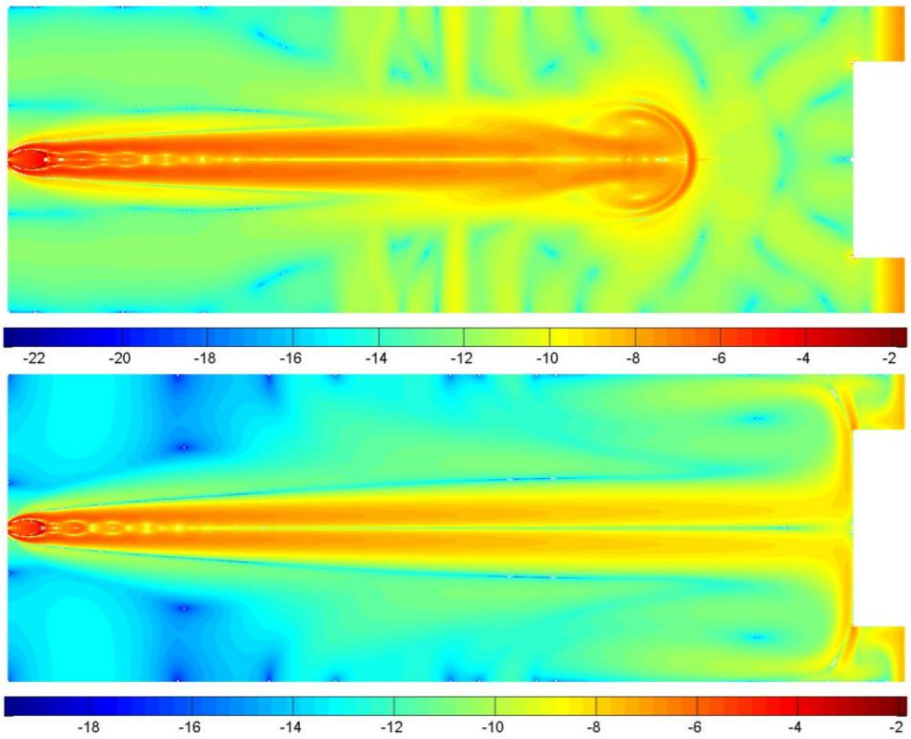

Figure 5.18 $\log_e[(Kn_{GLL})_\rho]$ contours at 0.5 ms (top) and 4 ms (bottom) at Case II conditions.

As shown in Figure 5.18, $(Kn_{GLL})_\rho$ is generally less than 0.05 (i.e. $\mathrm{Ln}(Kn_{GLL})_\rho \leq -3$) except in some limited regions near the Mach disc in the shocks where $(Kn_{GLL})_\rho$ ~ 0.14. However these regions are unlikely to have a significant effect on the flow field. Therefore, it may be assumed that continuum breakdown does not occur in most of the regions of the flow field simulated in Case II. This indicates that the local density gradient within the computational cell was not high

enough to transport the particles downstream before thermal equilibrium condition could be established. Thus, the assumption that equilibrium is re-established locally in each time step in the current QDS scheme is justified at this higher initial reactor pressure.

Furthermore, the ratio of the simulation time step to the average time between particle collisions was also calculated for Case II. Figure 5.19 shows the contours of $\Delta t/t_{col,avg}$ plotted on a natural logarithm scale at the simulation times of 0.5 ms and 4 ms, respectively, for Case II.

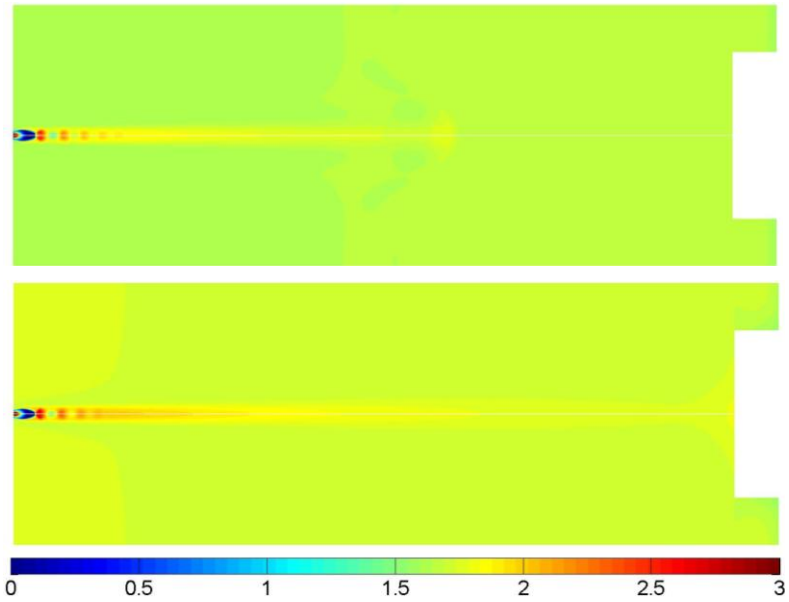

Figure 5.19 $\log_e(\Delta t/t_{col,avg})$ contours at 0.5ms (top) and 4ms (bottom) at Case II conditions.

From Figure 5.19, the ratio of $\Delta t/t_{col,avg} > 2$ or $\log_e(\Delta t/t_{col,avg}) > 0.69$ occurs in most regions except near the Mach disc. This indicates that there are at least two successive particle collisions in most regions of the flow field providing an insignificant difference between the actual physical non-equilibrium distribution

and the Maxwellian equilibrium distribution. Therefore, the equilibrium assumption in the QDS method remains reasonable for the flow field of Case II.

5.8.2.2 Case II: Pump-down phase

The pump-down phase of the PP-CVD operating cycle at Case II conditions was also simulated with the reactor pressure at the end of the injection phase estimated to be 5 kPa. Figure 5.20 shows the density contours (left) and the pressure contours (right), plotted on a natural logarithm scale, of the unsteady flow development during the first millisecond of the pump-down phase at Case II conditions. At 0.1 s, which is the end of the injection phase, the quasi-steady jet structure has the length of about three quarters of the reactor length and not impinging on the substrate, as observed in Case I. This suggests that the mass flux onto the substrate region is reasonably uniform across the substrate, which is the desired condition for uniform film deposition. The jet structure also dissipates rapidly in about 1 ms, after the inlet jet has been shut off at 0.1 s. This is followed by a considerably uniform flow field in the remaining pump-down process.

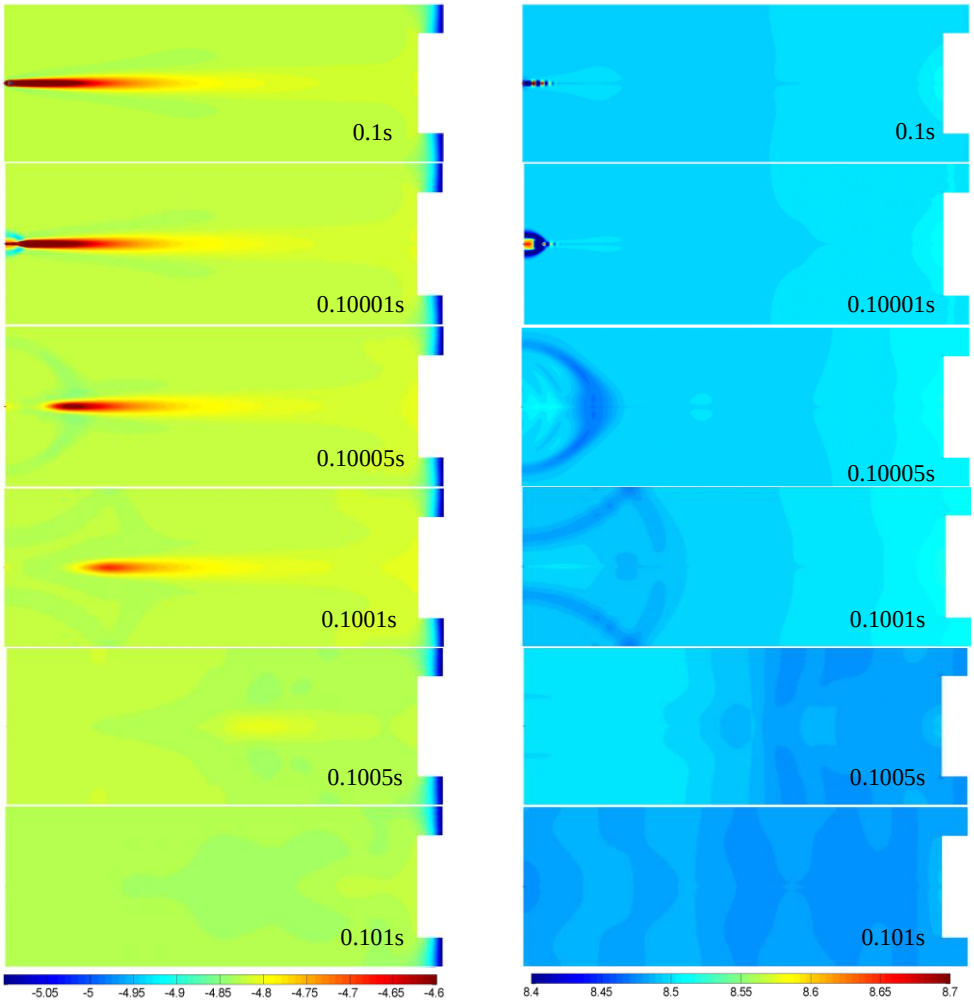

Figure 5.20 $\log_e$(density) [kg/m^3] contour (left) and $\log_e$(pressure) [Pa] contour (right) for the unsteady flow development of an under-expanded jet in a PP-CVD reactor at Case II conditions during first millisecond of the pump down phase.

The validity check on the thermal equilibrium assumption in the current QDS scheme was again performed for the Case II pump-down phase simulation. Figure 5.21 shows the contours of the gradient length local Knudsen number based on density at the simulation times of 0.10001s and 0.1001s, respectively. As discussed above, it can be considered that continuum breakdown does not occur for $(Kn_{GLL})_\rho < 0.05$. The contour plots in Figure 5.21 shows that $(Kn_{GLL})_\rho$ is less

than 0.01 throughout the domain, permitting the continuum assumption to be valid in the flow field based on $(Kn_{GLL})_{\rho}$. The local density gradient within the computational cells is not high enough to transport the particles downstream before thermal equilibrium condition is re-established locally within one time step.

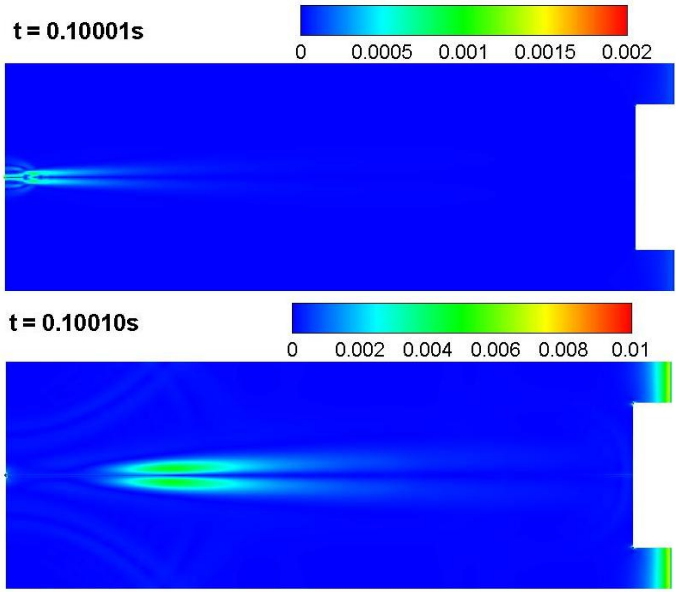

Figure 5.21 $(Kn_{GLL})_{\rho}$ contours at 0.10001s (top) and 0.1001s (bottom) at Case II conditions.

The ratio of the simulation time step to the average time between particle collisions, $(\Delta t/t_{col,avg})$ is shown in Figure 5.22 at 0.10001 s and 0.1001 s, respectively, during the pump-down phase for Case II. Using the condition of $(\Delta t/t_{col,avg}) \geq 2$ for estimating at least two collisions per time step per particle occurs to bring the particles' velocity distribution acceptably close to the Maxwellian equilibrium distribution, Figure 5.22 shows $(\Delta t/t_{col,avg}) > 4$ in the simulation everywhere.

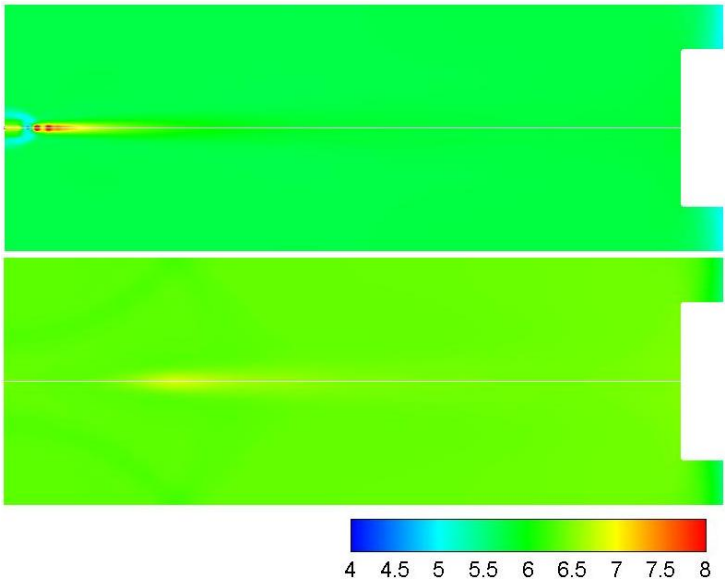

Figure 5.22 ($\Delta t/t_{col,avg}$) contours at 0.10001 s (top) and 0.1001 s (bottom) at Case II conditions.

5.8.3 Discussion

The simulation results in both Case I and II show that the flow field developed into a quasi-steady under-expanded jet structure, which impinges onto the substrate during the injection phase of the PP-CVD process. The impingement of the jet with high density concentration at jet core is undesirable from the CVD perspective due to the formation of a boundary layer on the substrate in this reactor configuration. Consequently, this results in non-uniformity of the mass flux onto the substrate. Such non-uniformity of particles' arrival on the substrate surface, if sustained, would result in non-uniform deposition of the precursor onto the substrate. However, PP-CVD reactors are typically operated with short injection pulses. In fact, the simulation result of the pump-down phase shows that

the quasi-steady jet moves away from the substrate region as the pressure increases during the injection phase. At the end of the injection phase at 0.1s (in both Case I and II), the quasi-steady under-expanded jet does not impinge on the substrate surface. The uniformity of the flow field near the substrate region at the end of the injection phase and throughout the pump-down phase is also noted. Film deposition is thought to continue for some considerably long period after the gas supply is cut off and the jet structure has dissipated. The flow field is more uniform once the jet structure has gone. This encourages uniform film deposition on the substrate surface since the majority of the actual deposition process occurs during the pump down phase. Hence, the non-uniformity of deposition incurred during the injection phase is negligible.

Figures 5.11 and 5.17 have shown that the time required for the quasi-steady structure of the jet to establish is 4 ms in Case I and 1 ms in Case II. The time required for the quasi-steady structure to dissipate is about 1 ms for both cases as noted from Figure 5.14 and 5.20. Knowledge of these times, not previously available, enables judicious choice of the injection pulse length and repetition frequency. Besides, comparing Case I and Case II, it is seen that high density gradient between the inlet and initial condition in the reactor causes higher rates of mass transport in the radial direction, as in Case I. Hence, the lower initial reactor pressure achieves a more uniform distribution of precursor solution before being transported to the substrate region.

These simulation results have also demonstrated some of the problems inherent in using the QDS method throughout the whole PP-CVD flow field. Two features of the QDS scheme limit its accuracy in low Mach number flows. One of the important assumptions in the QDS scheme is the Maxwell-Boltzmann equilibrium distribution of molecular velocities. The validity of this assumption may be checked by calculating the gradient length local Knudsen number and average number of collisions per computational cell per time step as seen in Figures 5.12, 5.13, 5.15, 5.16, 5.18, 5.19, 5.21 and 5.22. The second issue in the QDS scheme is the separation of collision and streaming that leads to excessive numerical diffusion of momentum. Consequently, this results in a very high effective viscosity of the gas when the grid spacing is larger than the mean free path. These two inherent problems in the second order true directional QDS scheme will be addressed in detail in Chapter 6. The problems are improved by recasting the QDS algorithm to approximate the EFM fluxes across the computational cell surfaces by using the moments of the discrete velocity distribution function (the QDS "velocity bins") employed by QDS method. This improvement is termed the directional decoupled QDS (DD-QDS) method and will be discussed in detail in Chapter 6. In addition, although the spatial gradients are evaluated to the second order in the QDS scheme, the temporal gradients (time integration) is to the first order only and this also limits the accuracy of the scheme.

6 Quiet Direct Simulation Method Part II

As mentioned in Chapter 5, there are two features in the basic second order true directional QDS scheme that limit its accuracy in simulating highly rarefied or low Mach number flows. The first issue is related to the moments of the discrete velocity distribution function used to construct QDS fluxes. The second problem in limiting the accuracy of the QDS scheme is the artificial viscosity which is also one of the major concerns in conventional CFD methods.

In QDS scheme, a Maxwell-Boltzmann equilibrium distribution of molecular velocities is assumed. This distribution is valid for a gas in local thermal equilibrium where the gas has undergone an infinite relaxation time and reached a state with no spatial gradients in the macroscopic properties (density, bulk velocity, and temperature) to disturb the equilibrium conditions. The validity of this assumption may be checked by calculating the gradient length local Knudsen number and average number of collisions per time step as discussed in Section 4.3.5. From the results shown in Section 5.8, the assumption of a local thermal equilibrium can be considered valid for low pressure flow up that is greater than 1 kPa.

In the basic true-directional QDS (TD-QDS) scheme discussed in Chapter 5, streaming and collision of the gas molecules are separated. The flow molecules are allowed to transport in free flight from a source cell to any of the neighbouring cells without collision. Then, the gas molecules are assumed to undergo infinite collisions at the destination cells to form a Maxwell-Boltzmann velocity

distribution. This results in an error in thermal transport of the gas molecules which diminishes with increase of Mach number in the flow field making the basic QDS scheme well suited for high speed, inviscid Eulerian flows. However, it leads to excessive artificial viscosity in the scheme which causes inaccuracy in the calculation of low speed viscous flow regions.

Section 6.1 of this chapter aims to investigate and quantify the numerical dissipation in the basic QDS scheme. In Section 6.2, improvements are made to reduce the inaccuracy due to the mentioned inherent problems by recasting the QDS scheme as an approximation to the Equilibrium Flux Method (EFM) which is termed the directional decoupled QDS (DD-QDS) method.

6.1 Analysis of Numerical Dissipation in the Basic QDS Scheme

By considering a control volume element with a defined number of gas molecules, each gas molecule has its individual position, mass m and microscopic (molecular) velocity within the control volume element. In the time evolution of such a control volume element in a flow field, the motion of the molecules is due to the molecules' translation with their original velocity. If a collision occurs between molecules, this will change the molecules' velocities. The molecules' velocities would further change if the molecules are subjected to an external force field.

In the basic QDS scheme, the gas molecules are allowed to stream from a source cell to any of its neighbouring cell, both adjacent and diagonal, in free flight manner without taking the collision between molecules into consideration.

Molecules' collisions are only taken into account within the destination cells. Hence, without collisions during streaming, the changes in the molecules' velocities prior to arrival in the destination cell are under predicted. The collisions between molecules will essentially result in the retardation of the molecular speed of the fastest molecules and increase of the slower i.e. tending towards bulk speed. Overall, it causes the reduction in the amount of QDS fluxes reaching the destination cell and in the speed of those which do reach the destination cell. Thus, collisionless streaming in QDS scheme leads to an excess transport of momentum and energy of the gas molecules compared to that experienced in the real gas. Hence the computed flow field becomes more dissipative than the physical gas flow.

6.1.1 Scheme viscosity of QDS with 3 velocity bins

The numerical dissipation in the basic QDS scheme has been investigated and quantified for a two-dimensional shear flow in which the bulk axial velocity is aligned with the grid (Jermy, et al., 2010) and will be described in detail in this Section. In this study of the numerical dissipation, a basic QDS scheme with 3 molecular speeds (3 moments of the discrete velocity distribution function) is used i.e. $N = 3$ "velocity bins" per coordinate direction are being considered. The molecular speed of the central velocity bin in the *y*-direction will be zero and this group of molecules will not transport any momentum in the *y*-direction. The other two velocity bins have nonzero molecular speeds and hence will transport *y*-

momentum in the *x*-direction. By considering the quantity of momentum transported and the relation between shear stress and viscosity for a real fluid, the effective viscosity of the modelled gas in the QDS scheme may be quantified.

Figure 6.1 shows a schematic of a simple shear flow between two adjacent cells with computed momentum flux in the *y*-direction on a square Cartesian grid. The density and temperature is assumed to be uniform throughout the flow field with the bulk velocity aligned with the *x*-axis. The gas in the top cell (in blue) is moving at an average speed of $\bar{u} = u + \Delta u$ and the gas in the lower cell (in red) at $\bar{u} = u$, in the *x*-direction.

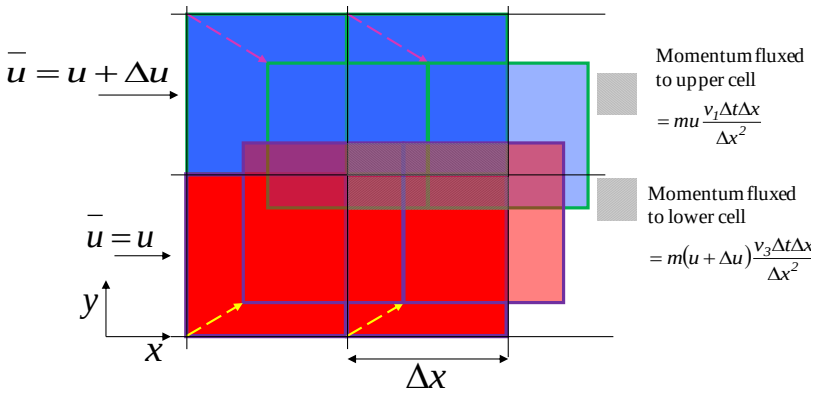

Figure 6.1 Schematic of a simple shear flow showing the computed fluxes (Jermy, et al., 2010).

The subscript 1 and 3 in the *y*-velocity, *v*, denote the two velocity bins which have nonzero thermal speeds in the discrete velocity distribution. The highest of the molecular speeds in the *y*-direction carries a flux of *x*-momentum into the adjacent cell.

The net momentum fluxed to the lower cell Δp can be determined by subtracting the amount of momentum fluxed to the upper cell from the amount of

momentum fluxed to the lower cell of each discrete velocity bin which is illustrated in Equation (6.1) as:

$$\begin{aligned}\Delta p &= \left[m(u+\Delta u)\frac{v_3 \Delta t \Delta x}{\Delta x^2} \right] - \left[mu\frac{v_1 \Delta t \Delta x}{\Delta x^2} \right] \\ &= \sum_{i=1}^{3} \left\{ \left[m_{i3} v_i \frac{|v_3 \Delta t|}{\Delta x} \right] - \left[m_{i1} v_i \frac{|v_1 \Delta t|}{\Delta x} \right] \right\} \\ &= \sum_{i=1}^{3} \left\{ \left[m\frac{w_i}{\sqrt{\pi}}\frac{w_3}{\sqrt{\pi}}\left(u+\Delta u+\sqrt{2RT}\,q_i\right)\frac{|v_3 \Delta t|}{\Delta x} \right] \right. \\ &\quad \left. - \left[m\frac{w_i}{\sqrt{\pi}}\frac{w_1}{\sqrt{\pi}}\left(u+\sqrt{2RT}\,q_i\right)\frac{|v_1 \Delta t|}{\Delta x} \right] \right\}\end{aligned} \tag{6.1}$$

where w_i and q_i are the weights and abscissas of the Gaussian quadrature, respectively, as described in Section 5.2. In the QDS scheme with 3 discretised molecular speeds, the thermal speeds of both outlying velocity bins are the same ($|v_1|$ and $|v_3|$) and have equal weights (w_1 and w_3). Thus, Equation (6.1) can be further simplified to Equation (6.2) as:

$$\begin{aligned}\Delta p &= \sum_{i=1}^{3} \left\{ m\frac{w_i}{\sqrt{\pi}}\frac{w_1}{\sqrt{\pi}}\Delta u\frac{|v_1 \Delta t|}{\Delta x} \right\} \\ &= \rho \cdot \left(\Delta x^2 \cdot 1\right) \cdot \frac{w_1}{\sqrt{\pi}}\Delta u\frac{|v_1 \Delta t|}{\Delta x} = \rho\frac{w_1}{\sqrt{\pi}}\Delta u|v_1 \Delta t|\Delta x\end{aligned} \tag{6.2}$$

The effective shear stress can then be calculated from this net amount of momentum transferred as shown in Equation (6.3):

$$\begin{aligned}\tau_{\text{scheme},N=3} &= \frac{1}{A}\frac{\partial p}{\partial t} = \frac{1}{\Delta x \cdot 1}\rho\frac{w_1}{\sqrt{\pi}}\Delta u|v_1 \Delta t|\Delta x\frac{1}{\Delta t} \\ &= \frac{\rho w_1 \Delta u|v_1|\Delta x}{\sqrt{\pi}\Delta x}\end{aligned} \tag{6.3}$$

The effective shear stress derived in Equation (6.3) may be compared to the physical shear stress given in Equation (6.4) as:

$$\tau = \mu \frac{\partial \mathrm{u}}{\partial \mathrm{y}} \tag{6.4}$$

where μ is the dynamic viscosity of the gas. Hence, an effective dynamic viscosity of the QDS scheme can be expressed in Equation (6.5) as:

$$\mu_{scheme,N=3} = \frac{\rho w_1 |v_1| \Delta x}{\sqrt{\pi}} \tag{6.5}$$

or an effective kinematic viscosity of the QDS scheme can then be expressed in Equation (6.6) as:

$$\nu_{scheme,N=3} = \frac{w_1 |v_1| \Delta x}{\sqrt{\pi}} \tag{6.6}$$

where w_1 = 0.2954 and $|q_1|$ = 1.2247 for the QDS scheme with 3 discretised molecular speeds. Hence, it can be expressed in Equation (6.7) as:

$$\frac{w_1}{\sqrt{\pi}} = \frac{1}{6} \text{ and } |v_1| = \sqrt{\frac{2kT}{m}} |q_1| = 1.2247 \sqrt{\frac{2kT}{m}} \tag{6.7}$$

which allows the expression of the effective kinematic viscosity of the QDS scheme to be given in Equation (6.8) as:

$$\nu_{scheme,N=3} = 0.2887 \sqrt{\frac{kT}{m}} \Delta x = 0.2887 \sqrt{RT}\, \Delta x \tag{6.8}$$

The effective kinematic viscosity in Equation (6.8) may then be compared to the physical kinematic viscosity of a gas which is given in Equation (6.9) (Jeans, 1904):

$$\nu_{physical} = \frac{1}{3}\bar{c}\lambda = \frac{1}{3}\sqrt{\frac{3kT}{m}}\lambda \qquad (6.9)$$

where $\bar{c}$ is the average thermal speed of the gas molecules and λ is the mean free path. Therefore, a ratio of the effective numerical to physical viscosity is given in Equation (6.10) as:

$$\frac{\nu_{scheme,N=3}}{\nu_{physical}} = \frac{0.2887\sqrt{\frac{kT}{m}}\Delta x}{\frac{1}{\sqrt{3}}\sqrt{\frac{kT}{m}}\lambda} \cong 0.5\frac{\Delta x}{\lambda} \qquad (6.10)$$

Equation (6.10) indicates that the basic QDS scheme will only reproduce the correct viscous behaviour if the grid spacing is of the order of the gas molecules' mean free path. In air at standard temperature and pressure, for example, the mean free path of the gas is of order 10^{-8} m. It is not feasible to have such grid spacing with currently available computing speeds and memory.

6.1.2 Scheme viscosity of QDS with 4 velocity bins

The derivation of the scheme viscosity is extended for the QDS scheme with 4 molecular speeds, i.e. N = 4 velocity bins per coordinate direction. The same consideration of a flow with uniform gas density and temperature while the bulk velocity is aligned with the x-axis is assumed, as shown in Figure 6.1. In the

following derivation, the subscripts 1 to 4 in the *y*-velocity, *v*, denote the index of the velocity bins which have nonzero molecular speeds in the discrete velocity distribution. For the QDS scheme with 4 molecular speeds, the discretised *y*-velocities can be expressed in terms of the abscissas, q_j, of the Gauss-Hermite quadrature as $v_j = \bar{v} + \sqrt{2RT}\,q_j$ where $\bar{v}_j$ is the bulk *y*-velocity and q_j = [-1.65068, -0.524648, 0.524648, 1.65068]. Hence, v_1 and v_2 are the *y*-velocity in downward direction while v_3 and v_4 are the *y*-velocities in upward direction. Hence, the total momentum fluxed to the lower cell can be expressed in Equation 6.11 as:

$$\Delta p_{upper\rightarrow lower} = \left[m(u+\Delta u)\frac{v_1 \Delta t \Delta x}{\Delta x^2} + m(u+\Delta u)\frac{v_2 \Delta t \Delta x}{\Delta x^2} \right] \qquad (6.11)$$

and the momentum fluxed to upper cell is expressed in Equation 6.12 as:

$$\Delta p_{lower\rightarrow upper} = \left[m(u)\frac{v_3 \Delta t \Delta x}{\Delta x^2} + m(u)\frac{v_4 \Delta t \Delta x}{\Delta x^2} \right] \qquad (6.12)$$

The net momentum fluxed to the lower cell Δp can then be determined by subtracting the amount of momentum fluxed to the upper cell from the amount of momentum fluxed to the lower cell of each discrete velocity bin which is illustrated in Equation (6.13) as:

$$\Delta p = \left[m(u+\Delta u)(v_1+v_2)\frac{\Delta t \Delta x}{\Delta x^2} \right] - \left[mu(v_3+v_4)\frac{\Delta t \Delta x}{\Delta x^2} \right]$$
$$= \sum_{i=1}^{4} \left\{ \left[\left(m_{i1}u_i \frac{|v_1 \Delta t|}{\Delta x} \right) + \left(m_{i2}u_i \frac{|v_2 \Delta t|}{\Delta x} \right) \right] \right.$$
$$\left. - \left[\left(m_{i3}u_i \frac{|v_3 \Delta t|}{\Delta x} \right) + \left(m_{i4}u_i \frac{|v_4 \Delta t|}{\Delta x} \right) \right] \right\}$$
$$= \sum_{i=1}^{4} \left\{ \left[\left(\rho \Delta x^2 \frac{w_i}{\sqrt{\pi}} \frac{w_1}{\sqrt{\pi}} \left(u + \Delta u + \sqrt{2RT}\, q_i \right) \frac{|v_1 \Delta t|}{\Delta x} \right) \right.\right.$$
$$\left. + \left(\rho \Delta x^2 \frac{w_i}{\sqrt{\pi}} \frac{w_2}{\sqrt{\pi}} \left(u + \Delta u + \sqrt{2RT}\, q_i \right) \frac{|v_2 \Delta t|}{\Delta x} \right) \right]$$
$$- \left[\left(\rho \Delta x^2 \frac{w_i}{\sqrt{\pi}} \frac{w_3}{\sqrt{\pi}} \left(u + \sqrt{2RT}\, q_i \right) \frac{|v_3 \Delta t|}{\Delta x} \right) \right.$$
$$\left.\left. + \left(\rho \Delta x^2 \frac{w_i}{\sqrt{\pi}} \frac{w_4}{\sqrt{\pi}} \left(u + \sqrt{2RT}\, q_i \right) \frac{|v_4 \Delta t|}{\Delta x} \right) \right] \right\} \qquad (6.13)$$

where w_i are the weights of the Gaussian quadrature, respectively. In the QDS scheme with 4 discretised molecular speeds, the thermal speeds of the velocity bins are symmetrical. Thus, $|v_1| = |v_4|$, $|v_2| = |v_3|$. The weights of the Gauss-Hermite quadrature are also symmetrical where $w_1 = w_4$ and $w_2 = w_3$. Thus, net momentum fluxed to the lower cell Δp can be simplified to equation (6.14) as:

$$\Delta p = \sum_{i=1}^{4} \left\{ \left(\rho \Delta x \frac{w_i}{\sqrt{\pi}} \frac{w_1}{\sqrt{\pi}} \Delta u |v_1| \Delta t \right) + \left(\rho \Delta x \frac{w_i}{\sqrt{\pi}} \frac{w_2}{\sqrt{\pi}} \Delta u |v_2| \Delta t \right) \right\} \qquad (6.14)$$

The summation of the weights of the Gauss-Hermite quadrature is equal to $\sqrt{\pi}$. Hence, the summation of weights can be simplified in Equation (6.15) as:

$$\sum_{i=1}^{4} \left(\frac{w_i}{\sqrt{\pi}} \right) = 1 \qquad (6.15)$$

Therefore, the net momentum fluxed to the lower cell Δp can be further simplified to equation (6.16) as;

$$\Delta p = \rho \cdot \Delta x \cdot \left(\frac{w_1}{\sqrt{\pi}} |v_1| + \frac{w_2}{\sqrt{\pi}} |v_2| \right) \Delta u \Delta t \tag{6.16}$$

Using the expression of the net momentum flux in Equation 6.16, the effective shear stress of QDS scheme with 4 velocity bins can be expressed in Equation (6.17) as:

$$\begin{aligned} \tau_{\text{scheme},N=4} &= \frac{1}{A}\frac{\partial p}{\partial t} = \frac{1}{\Delta x \cdot 1} \cdot \rho \Delta x \left(\frac{w_1}{\sqrt{\pi}} |v_1| + \frac{w_2}{\sqrt{\pi}} |v_2| \right) \Delta u \Delta t \cdot \frac{1}{\Delta t} \\ &= \rho \left(\frac{w_1}{\sqrt{\pi}} |v_1| + \frac{w_2}{\sqrt{\pi}} |v_2| \right) \frac{\Delta u \Delta x}{\Delta x} \end{aligned} \tag{6.17}$$

This expression of the scheme's effective shear stress is compared to the physical shear stress given in Equation (6.4). As a result, an effective dynamic viscosity of the QDS scheme with 4 velocity bins is obtained and given in Equation (6.18) as:

$$\mu_{scheme,N=4} = \rho \left(\frac{w_1}{\sqrt{\pi}} |v_1| + \frac{w_2}{\sqrt{\pi}} |v_2| \right) \Delta x \tag{6.18}$$

or the effective kinematic viscosity is given Equation (6.19) as:

$$\nu_{scheme,N=4} = \left(\frac{w_1}{\sqrt{\pi}} |v_1| + \frac{w_2}{\sqrt{\pi}} |v_2| \right) \Delta x \tag{6.19}$$

where w_1 = 0.0813128 and w_2 = 0.804914 for the QDS scheme with 4 discretised molecular speeds while $v_j = \sqrt{2RT}\, q_j$ with $|q_1|$ = 1.65068 and $|q_2|$ = 0.524648. Consequently, the effective kinematic viscosity of the QDS scheme with 4 velocity bin is given in Equation (6.20) as:

$$\nu_{scheme,N=4} = 0.444037 \sqrt{RT}\, \Delta x \tag{6.20}$$

It should be noted that at a high Reynolds number, turbulent flow occurs which introduces eddy viscosity to the flow field. The eddy viscosity will increase the apparent viscosity above the gas physical viscosity. Thus, the value of the apparent viscosity will depend on the local turbulence intensity and eddy spectrum size. As a result, it can be considered that the eddy viscosity would bring the apparent (effective) viscosity of the real gas closer to the simulated (scheme) viscosity.

Besides, from the above derivations, the viscosity in the QDS scheme may be speculated based on the number of "velocity bin", *N*, used, which can be expressed in Equation (6.21) as:

$$\begin{aligned} \nu_{scheme,N} &= \frac{\Delta x}{\sqrt{\pi}} \sum_{i=1}^{N-2} w_i |v_i| \\ &= 0.7979 \left(\sum_{i=1}^{N-2} w_i |q_i| \right) \Delta x \sqrt{RT} \\ &= C_N \Delta x \sqrt{RT} \end{aligned} \tag{6.21}$$

where C_N is a coefficient that relates to the weights and abscissas of the Gaussian quadrature for the corresponding N "velocity bins" used in the scheme. By referring to the values of the weights and abscissas of the Gaussian quadrature for different number of "velocity bin" used as tabulated in Appendix, the value of the scheme viscosity when different numbers of "velocity bins" are used can be estimated as shown in Table 6.1:

Table 6.1 Estimated scheme viscosity for different numbers of "velocity bins" used.

Number of "velocity bin", N	Scheme viscosity, m^2/s Multiplier: × $\Delta x\sqrt{RT}$
3	0.2887
4	0.4440
5	0.3332
6	0.4280
7	0.3520
8	0.4241
9	0.3625

From Table 6.1, it can be seen that when N is an odd number the scheme viscosity increases when the number of "velocity bins" used increases. In reverse, when an even number of "velocity bins" are used, the scheme viscosity decreases when the number of "velocity bins" used increases.

6.2 Directional Decoupled QDS Scheme

In the effort of improving the accuracy of the QDS scheme by reducing the numerical dissipation, the basic QDS scheme is modified to employ split fluxes instead of true directional fluxes. The main difference between the split flux method and the true directional flux method is that the QDS fluxes are computed at the cell centre in the true directional method whereas the split fluxes are computed at the cell interfaces. This is termed as the directional decoupled QDS (DD-QDS). In the true directional QDS (TD-QDS) scheme as described in Section 5.4, fluxes are transported from one cell volume to another and reconstructed at the centre location of the cell. The flux reconstruction location

can be viewed as the average location within the region of gas deemed to travel to the destination region. This means that the fluxes travel from one cell centre to another in the TD-QDS scheme. However, in the DD-QDS scheme, the flux reconstructions occur at the cell interfaces. The net flux across all cell surfaces is calculated in order to determine the average conserved properties, which are stated at the cell centre, within each cell. This effectively implies that the fluxes travel a distance of half the cell length, which reduces the inherent numerical dissipation spanwise.

The DD-QDS is essentially similar to the conventional kinetic-theory approaches such as Pullin's Equilibrium Flux Method (EFM) (Pullin, 1980) and Macrossan's Equilibrium Interface Method (EIM) (Macrossan & Oliver, 1993). However, as mentioned in Section 3.6, the need of evaluating computationally complex functions, which are the error function and exponential function, is avoided in the QDS method. Hence, the DD-QDS method is considered an improved version of the conventional flux calculator by employing the concept of the QDS velocity bins to efficiently approximate the EFM expressions (Lim, et al., submitted).

In the DD-QDS scheme, the assumption of a local thermal equilibrium is used in each computational cell where the molecular velocity is represented by the Maxwell-Boltzmann equilibrium distribution and approximated by a Gauss-Hermite quadrature, as discussed in Section 5.2. However, instead of using Equation (5.2), the integration of moments of the velocity probability distribution

over infinite velocity range within the flow field is evaluated by introducing the Heaviside step function H_s. This permits the fluxes to split to approximate the EFM flux expressions given in Equation (6.22) as:

$$\int_{-\infty}^{\infty} \frac{e^{-(v-u)^2/2\sigma^2}}{\sqrt{2\pi}\sigma} f(v)dv \approx \sum_{j=1}^{N} H_s(-q_j) w_j f(q_j) + \sum_{j=1}^{N} H_s(q_j) w_j f(q_j) \tag{6.22}$$

where $H_s(x) = 1$ if $x > 0$, else $H_s(x) = 0$.

Let the thermal velocity $v' = v - u$. The split fluxes to approximate the EFM fluxes expressions that shown in Equation (3.40) and (3.41) are formed by taking the moments of the conserved macroscopic property, η, around $f(v')$. Hence, the split fluxes in the DD-QDS method are given in Equation (6.23) and (6.24) as:

$$F^{+}_{\eta,QDS} = \int_{0}^{\infty} (v'+u)\eta^{+} f(v')dv' \approx \sum_{j=1}^{N} H_S(v_j) v_j w_j \eta_j^{+} \tag{6.23}$$

$$F^{-}_{\eta,QDS} = \int_{-\infty}^{0} (v'+u)\eta^{-} f(v')dv' \approx \sum_{j=1}^{N} H_S(-v_j) v_j w_j \eta_j^{-} \tag{6.24}$$

where η_j are the conserved macroscopic properties of the j^{th} QDS "velocity bin" given in Equation (6.25) as:

$$\eta_j = \begin{bmatrix} \rho \\ \rho v_j \\ \rho\left(\frac{1}{2}v_j^2 + \varepsilon_j\right) \end{bmatrix} \tag{6.25}$$

where the velocity of the bin is $v_j = v_j = u + \sqrt{2\sigma^2}\, q_j$ and ε_j is the internal energy of the molecular structure in the bin such as the rotational, vibrational, or electronic energy.

Consider a control volume element of the flow field for a computational cell as shown in Figure 6.2. The conserved macroscopic properties of cell *i* updated after one time step *k* + 1 can be computed by applying the divergence theorem and is given in Equation (6.26) as:

$$\eta_i^{k+1} \approx \eta_i^k - \frac{\Delta t}{V}\left(F_R A_R - F_L A_L + \eta_{i,P}^k\right) \tag{6.26}$$

where V is the cell volume, F is the net flux normal to the surface of area A and the subscripts L and R indicate the conditions on the left and right sides of the cell interface (or top and bottom sides of an annular cylindrical cell as shown in Figure 6.2), respectively. $\eta_{i,p}$ is the momentum correction applied to account for the pressure change along the control volume elements in the radial direction for axisymmetric flows as discussed in Section 5.5 and given in Equation (6.27) as:

$$\eta_{i,P} = \begin{bmatrix} 0 \\ P_i \alpha \Delta r \\ 0 \end{bmatrix} \tag{6.27}$$

where P_i is the cell pressure, Δr is the cell width in the radial direction and α is the axisymmetric angle (usually π).

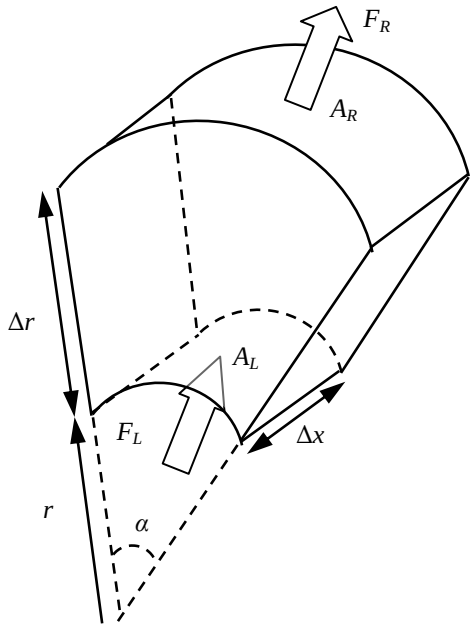

Figure 6.2 Control volume element for a single cell of a cylindrically axisymmetric geometry(Lim, et al., submitted).

In the second order DD-QDS scheme, the split fluxes at the cell interface are reconstructed in a manner similar to the conventional reconstruction method (Zhang & Zhuang, 1991). Hence, by taking a Taylor series expansion of the split fluxes at the cell interface, a second order accurate expression for the net fluxes F_R and F_L are given in Equation (6.28) and (6.29), respectively, as:

$$\begin{aligned} F_R &= F^+_{i+\frac{1}{2}} + F^-_{i+\frac{1}{2}} \\ &= \left[F_i^+ + \frac{\Delta r}{2}\left(\frac{dF^+}{dr} \right)_i \right] + \left[F_{i+1}^- - \frac{\Delta r}{2}\left(\frac{dF^-}{dr} \right)_{i+1} \right] \end{aligned} \tag{6.28}$$

$$\begin{aligned} F_L &= F^-_{i-\frac{1}{2}} + F^+_{i-\frac{1}{2}} \\ &= \left[F_i^- + \frac{\Delta r}{2}\left(\frac{dF^-}{dr} \right)_i \right] + \left[F_{i+1}^+ - \frac{\Delta r}{2}\left(\frac{dF^+}{dr} \right)_{i-1} \right] \end{aligned} \tag{6.29}$$

where the flux gradients dF/dr are calculated from the finite difference approximations of F^+ and F^- using a slope limiter to maintain positivity. As discussed in Section 5.4, the gradients of the fluxes are determined using the MINMOD (Minimum Modulus) or the MC (Monotonized Central Difference) slope limiter (Van Leer, 1977). For example, the gradient in radial flux calculation using the MC slope limiter is given in Equation (6.30) as:

$$\left(\frac{dF^+}{dr}\right)_i = MINMOD\left[\frac{F_{i+1}^+ - F_{i-1}^+}{2\Delta r}, MINMOD\left(2\frac{F_{i+1}^+ - F_i^+}{\Delta r}, 2\frac{F_i^+ - F_{i-1}^+}{\Delta r}\right)\right] \tag{6.30}$$

where the MINMOD slope limiter (Roe, 1986) is given in Equation (6.31) as:

$$\text{MINMOD}[a,b] = \begin{cases} 0 & \text{if SIGN}(ab) < 0 \\ a & \text{if SIGN}(ab) > 0 \text{ and } |a| < |b| \\ b & \text{if SIGN}(ab) > 0 \text{ and } |b| < |a| \end{cases} \tag{6.31}$$

6.3 Dynamic time step adjustment and boundary conditions

Similar to that used in the TD-QDS scheme as discussed in Section 5.6, the simulation time step duration Δt is reset at each time step in order to maintain the maximum Courant–Friedrichs–Levy (*CFL*) number in the flow field at a chosen value, always less than 1 and usually equal to 0.5. In the DD-QDS implementation, the *CFL* number is determined by Equation (6.32) as:

$$CFL = \max\left[\frac{\left(u_x + q_{j(\max)}\sqrt{RT_i}\right)\Delta t}{\Delta x}, \frac{\left(u_r + q_{j(\max)}\sqrt{RT_i}\right)\Delta t}{\Delta r}\right] \tag{6.32}$$

where $q_{j(max)}$ is the maximum abscissas value of the QDS "velocity bins". Ghost cell boundary conditions are also implemented in the DD-QDS scheme at all walls, and inflow and outflow boundaries (Smith, et al., 2009), as discussed in detail in Section 5.6.

6.4 Validation of the Directional Decoupled QDS Scheme

6.4.1 1-D Shock Tube Problem

To validate the DD-QDS code and to compare the performance between DD-QDS and TD-QDS codes, the simulation of a standard 1-D shock tube problem was conducted. In this problem, the gas in a tube is at rest initially and separated into two regions at different pressures and densities by a diaphragm. The initial conditions for left and right side of the diaphragm were chosen as (ρ_l, P_l, U_l) = (10, 10, 0) and (ρ_r, P_r, U_r) = (1, 1, 0) where ρ is the density, P is the pressure, U is the velocity while the subscripts l and r denote the left and right sides of the diaphragm, respectively.

The diaphragm is removed at t = 0, causing a shock to propagate through the tube. Figure 6.1 shows that after the removal of the diaphragm the flow is separated into four different regions by three shock waves that develop: a normal shock that separates region 1 and 2, a contact discontinuity between region 2 and 3, and a rarefaction wave that separates region 3 and 4.

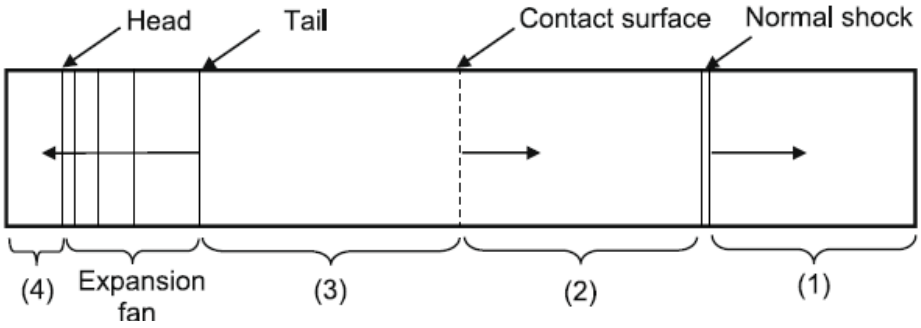

Figure 6.3 Schematic of the flow structure in a shock tube.

The modelled gas has a specific heat ratio of $\gamma = 1.4$ and a gas constant of $R = 1.0$. The length of the tube, $L = 1$ m, was divided into 200 cells. The boundary conditions were implemented as outflow conditions on both sides. The simulation time, t_f, was set to 0.1 s. After this time, no wave reached the boundaries, hence, the choice of the boundary conditions is not critical.

The simulation was conducted with the second order DD-QDS and TD-QDS codes using 4 velocity bins per coordinate direction and MINMOD slope limiter in calculating the property gradients. Dynamic time steps were used in which the simulation time step is adjusted after each time step with the $CFL < 0.5$ condition maintained. The simulation results were compared to the analytical results of the Riemann solver (Toro, 2009). Figure 6.4 shows the normalized density, temperature, velocity and pressure profiles at $t_f = 0.1$ s.

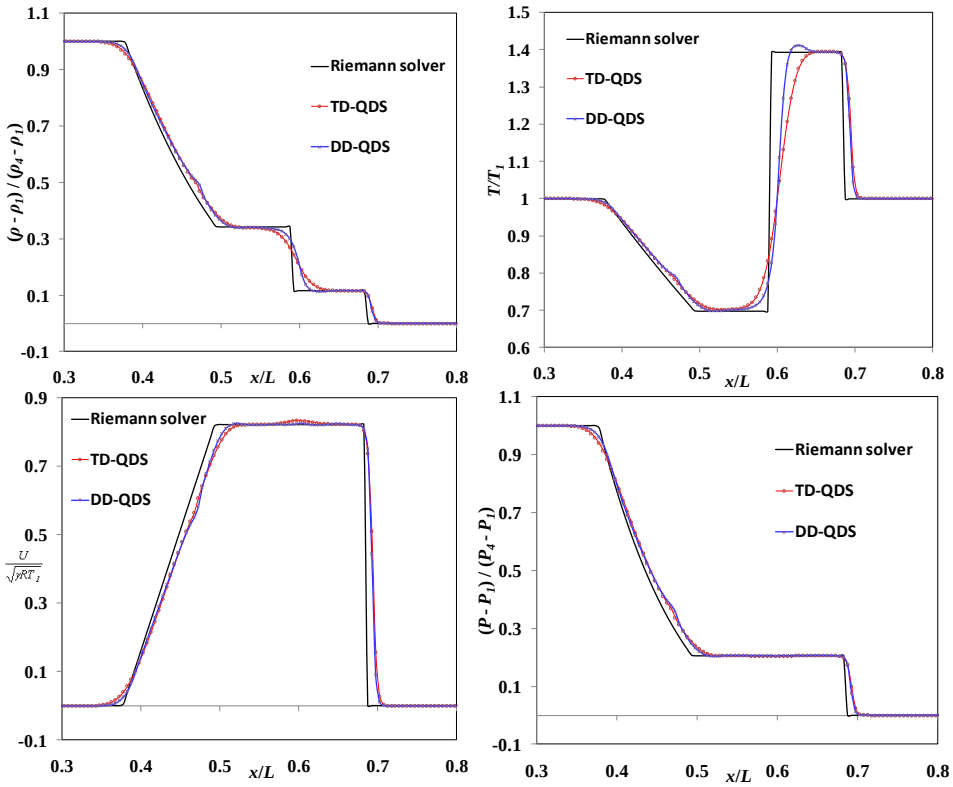

Figure 6.4 Normalised density (top left), temperature (top right), velocity (bottom left) and pressure (bottom right) distribution of the shock tube problem.

From Figure 6.4, both the DD-QDS and the TD-QDS solver are shown to be able to capture the physics of the shock, contact discontinuity and rarefaction waves. It can also be noticed that the DD-QDS solver, in general, produced slightly more accurate results compared to the TD-QDS in this problem. It should also be noted that a slight overshoot of the temperature occurred in the solution from the DD-QDS. This may be due to the low amount of numerical dissipation inherent in the scheme.

As a measure of accuracy of the schemes, the Mean Absolute Percentage Error (*MAPE*) was calculated for both the TD-QDS and the DD-QDS for the

quantities of density, temperature and pressure. By considering the Riemann solution to be the benchmark solution, *MAPE* can be calculated by Equation (6.33) as:

$$MAPE = \frac{1}{n}\sum_{i=1}^{n}\left|\frac{\eta_{i,ref} - \eta_i}{\eta_{i,ref}}\right| \tag{6.33}$$

where n is the number of cell, η_i is the macroscopic quantity at cell i and $\eta_{i,ref}$ is the macroscopic quantity of the Riemann solution at cell i. Table 6.2 show the comparison of *MAPE* for both the TD-QDS and the DD-QDS for this problem.

Table 6.2 *MAPE* between the TD-QDS and the DD-QDS for 1D shock tube problem

Solver	*MAPE*		
	Density, ρ	Temperature, T	Pressure, P
TD-QDS	1.84%	1.35%	8.79%
DD-QDS	1.32%	0.88%	1.01%

From Table 6.2, both the TD-QDS and the DD-QDS produced solutions considerably close to those of the Riemann solver. As noted from Equation (6.33), a perfect match of the solutions would give the value of the *MAPE* to be zero. It can also be clearly seen that the results of the DD-QDS have a closer match to the benchmark solution. Hence, it can be said that the DD-QDS solver produced more highly accurate results than the TD-QDS in this problem.

6.4.2 Shock-Bubble Interaction

As a validation of the accuracy of the DD-QDS code, a test problem for the interaction of shock waves with a spherical bubble was simulated. The problem of

shock-bubble interaction was first studied experimentally by Rudinger and Sommers to understand the fundamental mechanics associated with turbulence generation and mixing (Rudinger & Somers, 1960). Haas and Sturtevant then studied this problem to investigate the nature of shock refraction at low Mach numbers (Haas & Sturtevant, 1987). Numerical simulations on this problem have also been carried out to study the Mach number effects on the shock-bubble interaction (Picone & Boris, 1988; Zabusky & Zeng, 1998). Most of these simulations involve multi-species flow. Figure 6.5 shows the geometry of the problem together with the initial and boundary conditions for the simulation of shock-bubble interaction in a 1.0 unit length cylindrical channel with radius R = 0.5 unit length. The spherical bubble, with radius r = 0.2 unit length, is initially located at 0.4 unit length downstream from the channel inlet. The simulated gas was an ideal gas with a ratio of specific heats of 1.4 and a gas constant of R = 1.0. The inlet boundary was kept at the initial flow condition at all times while the outflow condition was extrapolated from the adjacent flow field cells. Reflecting wall boundary conditions are applied along the walls of the tunnel.

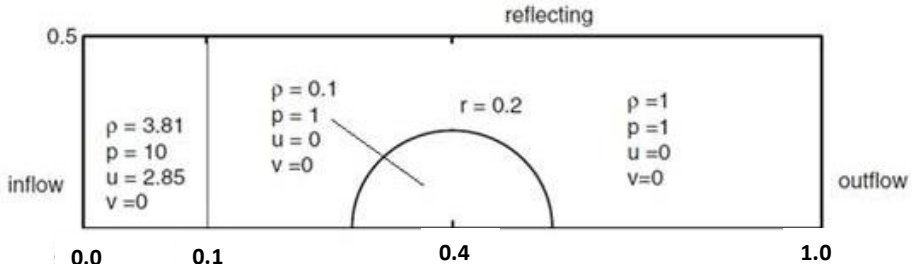

Figure 6.5 Geometry, boundary and initial conditions for the simulation of shock-bubble interaction.

The simulation was conducted with the axisymmetric DD-QDS code by using 3 velocity bins per coordinate direction and MINMOD slope limiter in calculating the property gradients. In the simulation, 200 radial cells and 400 axial cells are used. The computational cells of the bubble were generated at $t = 0$ in a staircase manner with the cells taking the properties of either the bubble or the surroundings, but never values in between. A dynamic time step was used in which the simulation time step was adjusted after each time step to maintain $CFL < 0.25$ everywhere. The simulation was carried out until 0.2 s when the shock wave is just about to reach the outflow boundary.

The DD-QDS simulation result was compared to that of the simulation using EFM (Smith, 2008) as a validation. Figure 6.6 shows the comparison of the density contour between the simulation results of the DD-QDS solver and the EFM solver at the simulation time of 0.2 s. As a consequence of the interaction with a right-moving incident shock, the bubble region, with a lower density than the surroundings, expands radially outward and deforms into a kidney-shape vortex. At the same time a re-entrant jet forms at the upstream interface, as visualised by Haas & Sturtevant (Haas & Sturtevant, 1987) and also predicted by Picone & Boris (Picone & Boris, 1988) and Bagabir *et al.* (Bagabir & Drikakis, 2001). The comparison shows that the DD-QDS solver is able to capture shock-bubble interaction flow field features similar to the EFM. The backward-moving reflected shock and right-moving transmitted shock have an almost exact match in position to that in the EFM result. This shows the DD-QDS scheme's capability to

produce closed, approximated solutions to the problem with simpler formulations and higher computational efficiency. Both simulations, using the DD-QDS and the EFM, were carried out on a single desktop computer with 3.00 GHz Intel Core 2 Duo CPU E6850 processor and 4 GB of RAM. The simulation required 254 s to compute 0.2 s of flow using the DD-QDS solver compared to 369 s by using the EFM solver. Hence, the DD-QDS solver has significantly greater computational efficiency with equivalent accuracy to the EFM for this problem.

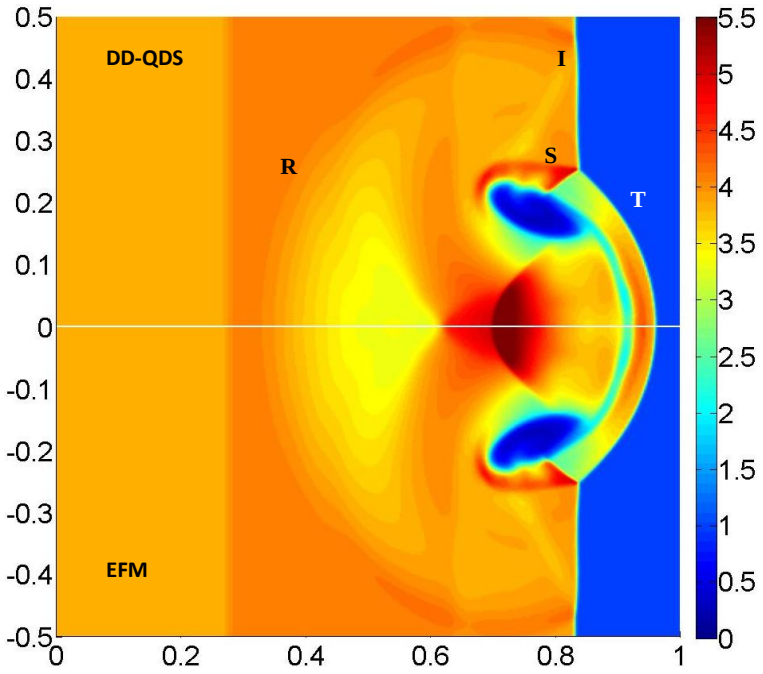

Figure 6.6 Comparison of density [kg/m^3] contour at 0.2 s for shock-bubble interaction simulation between results from present QDS scheme (top) and results from EFM (bottom); I is the incident shock, R is the reflected shock, T is the transmitted shock, S is the contact surface.

The DD-QDS simulation result was also compared to that of the simulation using the TD-QDS solver as discussed in Section 5.4. Figure 6.7 shows the

comparison of the density contour between the simulation results obtained from the DD-QDS solver and the TD-QDS solver at the simulation time of 0.2 s.

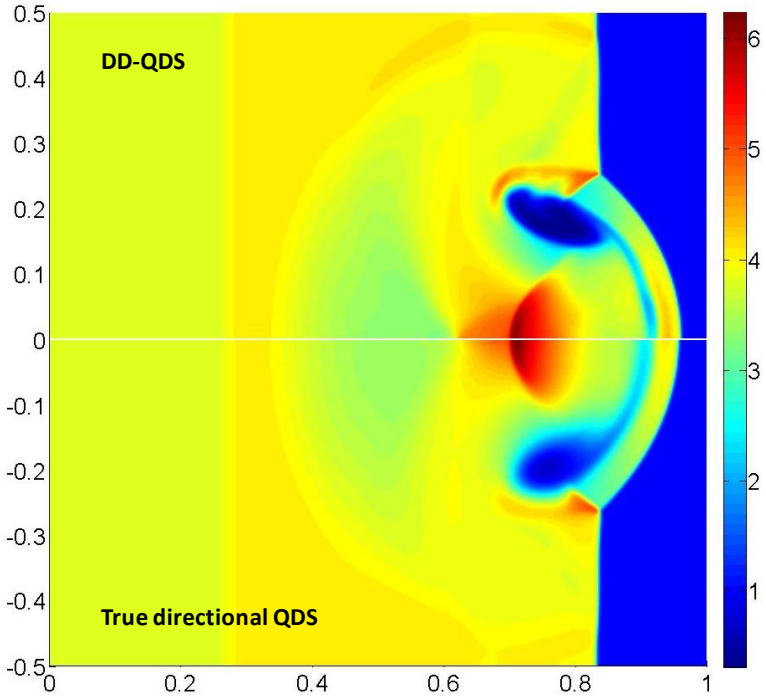

Figure 6.7 Comparison of density [kg/m^3] contour at 0.2s for shock-bubble interaction simulation between results from DD-QDS scheme (top) and results from true directional QDS (bottom).

It is clearly seen in Figure 6.7 that the deformation of the bubble in to a kidney-shaped, vortical structure is more pronounced in the DD-QDS simulation result. This can be ascribed to the lower numerical dissipation in the DD-QDS scheme. The vortical roll-up at the shock-bubble interface has also been captured at higher resolution in the result of the DD-QDS solver compared to that of the TD-QDS code. It is also noted that the transmitted shock (the curved shock front) is travelling slightly faster in the DD-QDS simulation compared to that of the TD-QDS indicating lower effective viscosity in the flow field simulated by the DD-

QDS code. This confirms that improvement is made by using the DD-QDS scheme to reduce the numerical viscosity in the QDS method in order to produce a more accurate simulated solution of the flow field.

6.4.3 Mach 3 Flow over a Forward Facing Step

The second test problem in validating the DD-QDS code is the Mach 3 flow over a forward facing step in a high speed two-dimensional wind tunnel. This test problem was introduced by Emery (Emery, 1968) and has been used in several studies including Woodward & Colella in testing a few numerical schemes (Woodward & Colella, 1984) and Keats & Lien who used a Godunov scheme (Keats & Lien, 2004). Figure 6.8 shows the geometry of the problem with a uniform Mach 3 flow over a step which is located 0.6 unit lengths from the inlet of the tunnel. The simulated gas was an ideal gas with a ratio of specific heats of 1.4 and a gas constant of $R = 1.0$. Initially, the flow is uniform everywhere with density of 1.4, pressure of 1.0, and velocity of 3.0. The inlet boundary was kept as the initial flow condition while the outlet boundary condition was extrapolated from the adjacent flow field cells. Reflecting wall boundary conditions are applied along the walls of the tunnel.

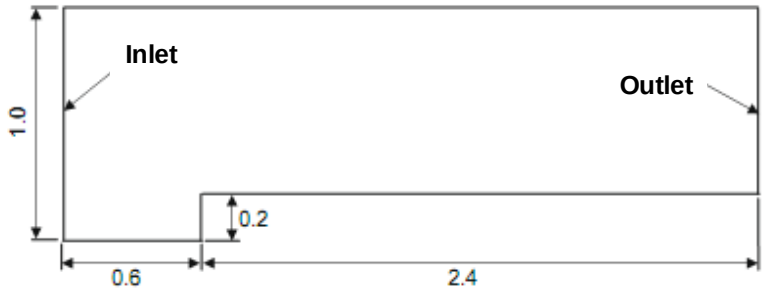

Figure 6.8 Geometry and boundary conditions for the simulation of Mach 3 flow over a forward facing step.

The simulation was conducted with the second order DD-QDS code by using 4 velocity bins per coordinate direction and the MINMOD slope limiter for calculating property gradients. The variable time step scheme was used so that the maximum kinetic *CFL* number in the simulation domain was 0.5. 200 square cells across the inlet wall of the tunnel were used.

The simulation result is compared to that of the second order Godunov method employed by Keats and Lean on an adaptively refined mesh (Keats & Lien, 2004) and to that of the second order TD-QDS method used by Smith *et al*. (Smith, et al., 2009). Figure 6.9 shows a comparison of the density contours at 4 s between the results of Keats and Lien's Godunov scheme and the DD-QDS scheme. Figure 6.10 shows the comparison between the results from the TD-QDS scheme and the DD-QDS scheme. These comparisons show that the DD-QDS code has captured the flow field features such as the Mach stem and rarefaction fan around the corner of the step with results very close to the other two methods. The shock positions on the walls have also shown close matches between the DD-QDS and the two other methods.

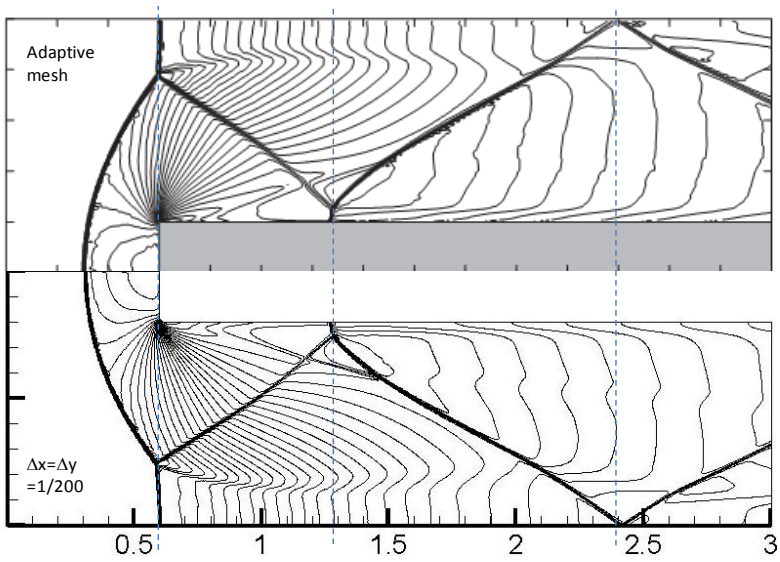

Figure 6.9 Comparison of density [kg/m^3] contour at 4 s for Mach 3 flow over a forward facing step between results from Keats and Lien's Godunov scheme (Top, taken from (Keats & Lien, 2004)) and the DD-QDS scheme (bottom); 30 contours: $0.2568 \leq \rho \leq 6.607$.

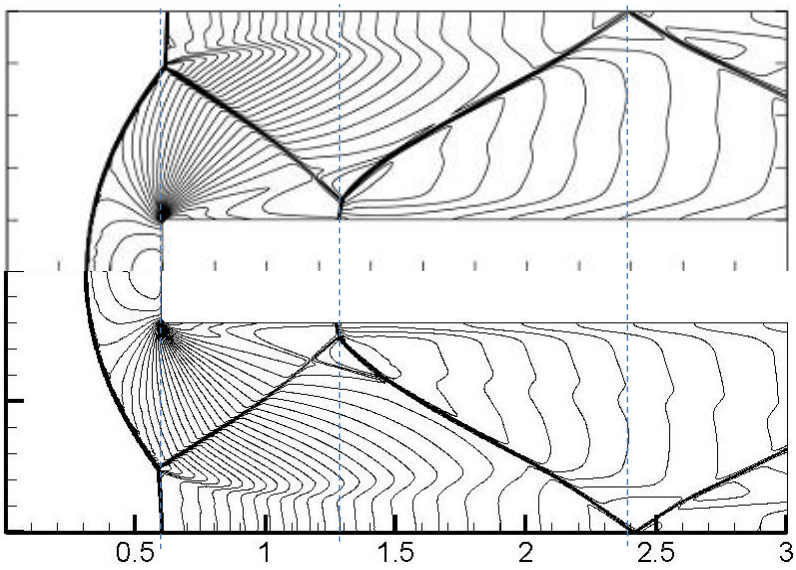

Figure 6.10 Comparison of density [kg/m^3] contour at 4 s for Mach 3 flow over a forward facing step between results from the TD-QDS scheme (Top, taken from (Smith, et al., 2009)) and the DD-QDS scheme (bottom); 30 contours: $0.2568 \leq \rho \leq 6.607$.

The DD-QDS simulation was conducted on a single desktop computer with 3.00 GHz Intel Core 2 Duo CPU E6850 processor and 4 GB of RAM. The simulation consumed 22 min to compute 4.0s of flow using the second order DD-QDS solver. By comparison, the same problem was simulated using a second order True Directional Equilibrium Flux Method (TDEFM) and a Riemann solver on a single laptop computer with 1.73 GHz Intel dual core T2250 processor and 2 GB of RAM (Smith, et al., 2009). The TDEFM required 201 min to compute 4.0 s of flow while the Riemann solver required 77 min. Although the DD-QDS simulation was carried out on a machine with about double the speed, it should be noted that less than half the computational time was taken compared to the other two methods.

6.5 PP-CVD Simulations by Directional Decoupled QDS

The second order true directional axisymmetric DD-QDS solver is used to simulate the reactor flow field for the gas injected PP-CVD process. The same two Cases studied in Section 5.8 with the TD-QDS were simulated as a comparison check on the improvement made by introducing the DD-QDS scheme in the PP-CVD reactor flow field simulations. The simulation conditions for the simulated Cases are described in Table 6.3. Ideal Helium gas at a choked flow condition is used as the inlet conditions with the reactor flow field initially stationary. A constant evacuation volumetric flow rate as discussed in Section 4.2.2 is used as the outflow conditions. Specular reflected wall conditions were

used for all wall and substrate surfaces. Both simulations were carried out on a desktop computer with 3.00GHz Intel Core 2 Duo CPU and 4GB of RAM using 312,744 uniform square cells with 0.25mm cell size.

Table 6.3 Simulation conditions for the PP-CVD flow field simulations using the DD-QDS method.

	Case I	**Case II**
Supply Pressure, P_s	10 kPa	40 kPa
Pulse Range, $P_{min} \rightarrow P_{max}$	1 Pa → ~100 Pa	1 kPa → ~5 kPa
Injection time, t_i	0.1 s	
Supply Temperature, T_s	293 K	
Initial Temperature, T_i	293 K	
QDS velocity bin, N	4 per coordinate direction	
Simulation time step, Δt	variable time step with maximum CFL < 0.5	
Slope limiter	MINMOD	

Figure 6.11 shows the reactor geometry and boundary conditions used for both Cases.

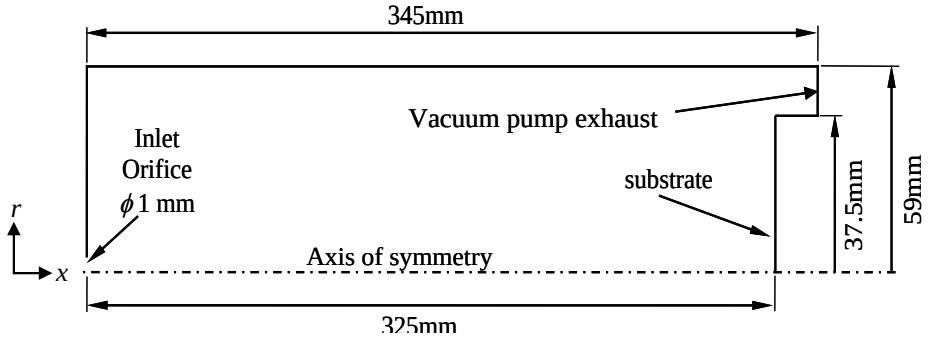

Figure 6.11 Schematic of the PP-CVD reactor geometry.

6.5.1 Case I: 1 Pa initial reactor pressure

6.5.1.1 Case I: Injection phase

Figure 6.12 shows the density contours (left) and the pressure contours (right) plotted on a natural logarithm scale. They show the development of an under-expanded jet during the first 4 ms of the injection phase in Case I conditions. By comparison to Figure 5.11, the development of the under-expanded jet during the injection phase is similar but at much higher resolution. More flow field details have been captured clearly which can be attributed to lower numerical dissipation. Similarly to Figure 5.11, the contour plots in Figure 6.12 show the development of a shock wave pattern at the exit of the inlet orifice, evolution of the shear layer with the vortex roll-up and the formation of a Mach disk and barrel shock during the unsteady flow development period. After 4.0 ms, a quasi-steady under-expanded jet structure is seen and impinges onto the substrate region. This demonstrates the capability of the DD-QDS solver in modelling unsteady flow phenomena and capturing more flow field detail compared to the TD-QDS solver. Therefore, the accuracy in the numerical simulation is improved.

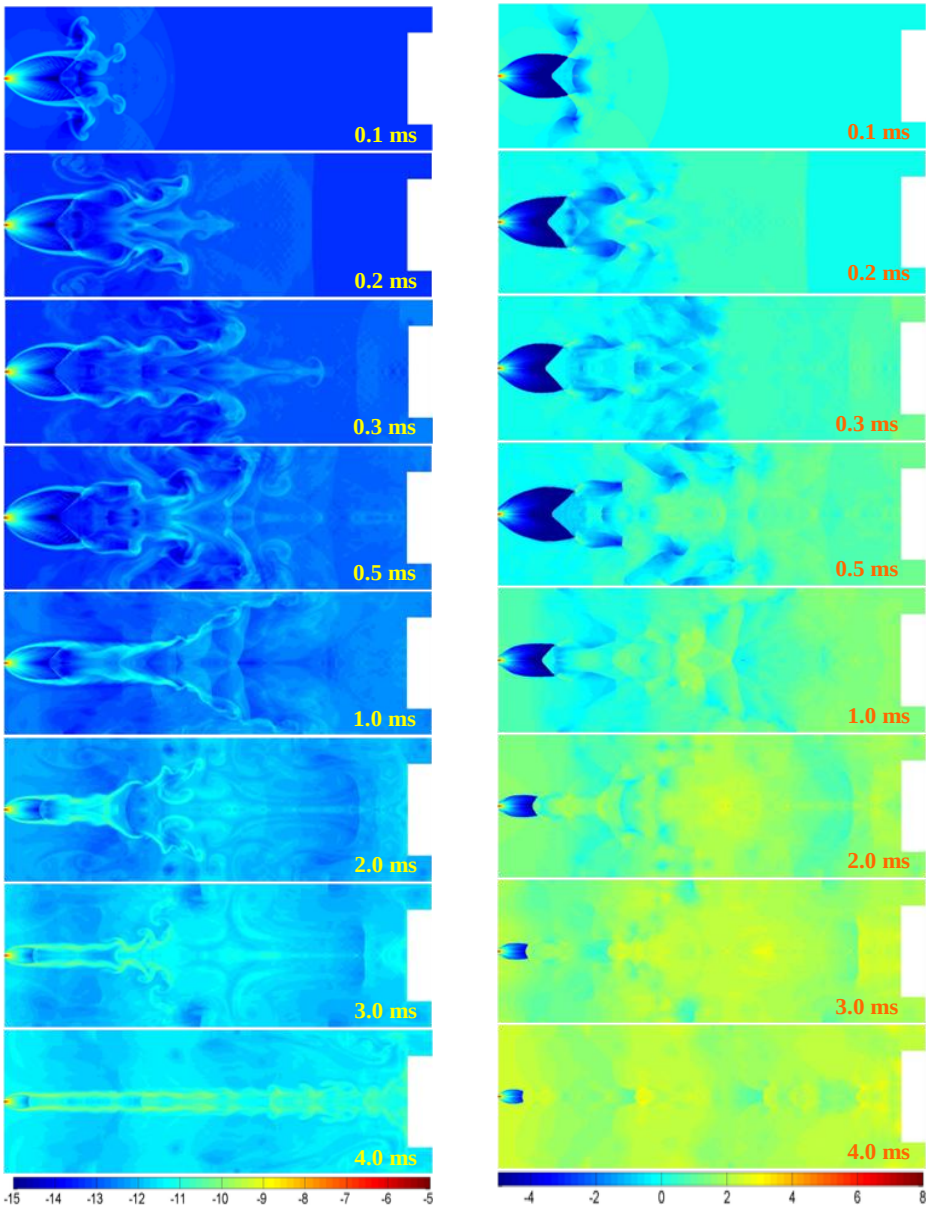

Figure 6.12 DD-QDS results: Log_e(density) [kg/m^3] contour (left) and Log_e(pressure) [Pa] contour (right) for the unsteady flow development of an under-expanded jet in a PP-CVD reactor at Case I conditions during the first 4 ms of the injection phase.

In the DD-QDS scheme, the assumption of thermal equilibrium establishment locally within each computational cell by the end of each time step is also applied in order to allow the molecular velocity distribution to be

approximated with the Maxwell-Boltzmann distribution. Hence, it is necessary to investigate the validity of the local equilibrium assumption. The same procedures of the validity check discussed in Section 5.8 have been carried out on the simulation results of the DD-QDS. First, the gradient length local Knudsen number based on the density $(Kn_{GLL})_\rho$, discussed in Section 4.3.5, was calculated to check whether continuum breakdown occurs in the flow field at the chosen simulation times. The $(Kn_{GLL})_\rho$ also indicates that the potential for the molecule to move due to the local density gradient within the computational cell. When the local density gradient is not high enough, there will be less potential for the physical molecules to transport out of the computational cell before the thermal equilibrium condition is established. In this Case, equilibrium condition being re-established locally in each time step in the current QDS scheme would be justified. As discussed in Section 4.3.5, the criterion for continuum breakdown occurring is $Kn_{GLL} > 0.05$ (Boyd, et al., 1995). Hence, the threshold of $(Kn_{GLL})_\rho < 0.05$, or $\log_e[(Kn_{GLL})_\rho] < -3.0$, is used to ensure that continuum breakdown does not occur and that the local density gradient is not high enough to transport the gas molecules downstream before the thermal equilibrium condition is re-established within the computational cell.

The $(Kn_{GLL})_\rho$ was calculated at the simulation times of 0.5 ms and 4.0 ms. These simulation times were chosen because the Mach disc position was stabilised in the flow field by about 0.5 ms while the flow developed into a quasi-steady state by 4.0 ms. Figure 6.13 shows the contours of $(Kn_{GLL})_\rho$ plotted on a

natural logarithm scale at the simulation times of 0.5 ms and 4.0 ms, respectively, for Case I. It is noted that $\log_e[(Kn_{GLL})_\rho] < -3.0$ occurs throughout the flow field indicating that the continuum assumption is valid in Case I when simulating with the DD-QDS solver.

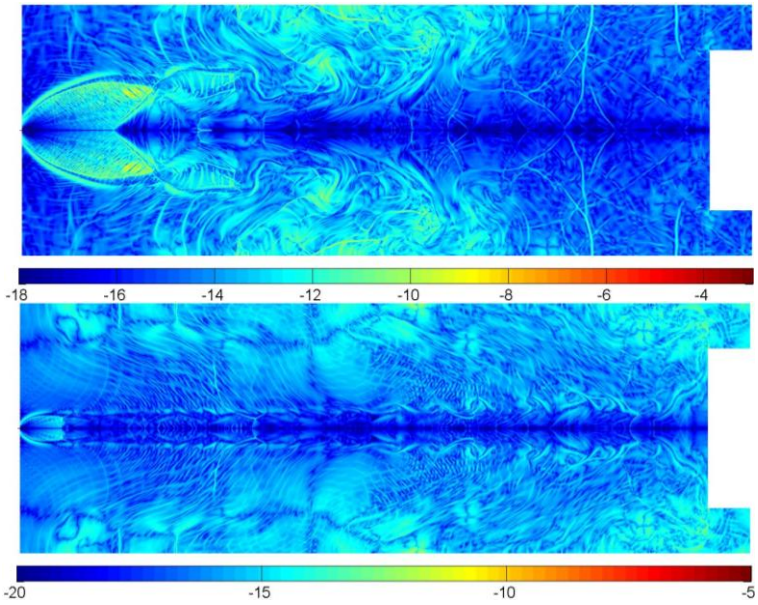

Figure 6.13 DD-QDS results: $\log_e[(Kn_{GLL})_\rho]$ contours at 0.5 ms (top) and 4 ms (bottom) at Case I conditions.

The second parameter used for the validity check of the thermal equilibrium assumption is $\Delta t/t_{col,avg}$. This is determined by calculating the ratio of the computational time step to the average time between particle collisions as discussed in Section 4.3.5. As stated in Section 4.3.5, a criterion of $\Delta t/t_{col,avg} \geq 2$ (Titov & Levin, 2007) , or $\log_e(\Delta t/t_{col,avg}) \geq 0.69$, is used to validate the assumption of the computed non-equilibrium distribution to relax sufficiently close to the corresponding Maxwell-Boltzmann equilibrium distribution. Figure 6.14 shows the contours of the $\Delta t/t_{col,avg}$ plotted on a natural logarithm scale at the

simulation times of 0.5 ms and 4.0 ms, respectively, for Case I. It is noted that the condition of $\log_e(\Delta t/t_{col,avg}) \geq 0.69$ is not satisfied anywhere in Case I either at t = 0.5 ms or t = 4.0 ms, except near the orifice exit. This indicates the computational time step used in the simulation is much smaller than the average molecules' collision time preventing the sufficient relaxation of the molecules. Therefore, the DD-QDS solver may not be able to calculate such non-equilibrium flow accurately. However, it is able to provide a promising qualitative approximation of the flow field at 1 Pa initial pressure condition.

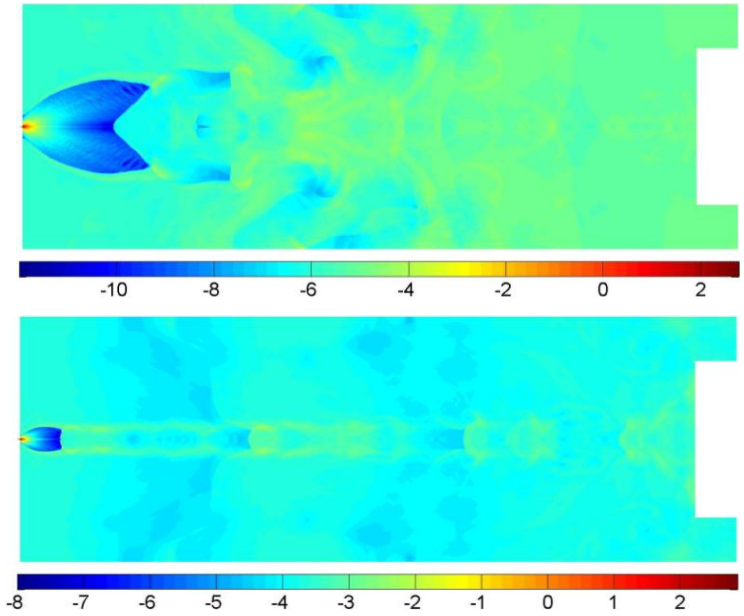

Figure 6.14 DD-QDS results: $\log_e(\Delta t/t_{col,avg})$ contours at 0.5 ms (top) and 4 ms (bottom) at Case I conditions.

6.5.1.2 Case I: Pump-down phase

The pump down phase of the PP-CVD operating cycle at Case I conditions was also simulated using the DD-QDS code. As described in Section 5.8.1.2, the

reactor pressure at the end of the injection phase is estimated to be 100 Pa based on experience with such reactors. Figure 6.15 shows the density contours (left) and the pressure contours (right) plotted on a natural logarithm scale.

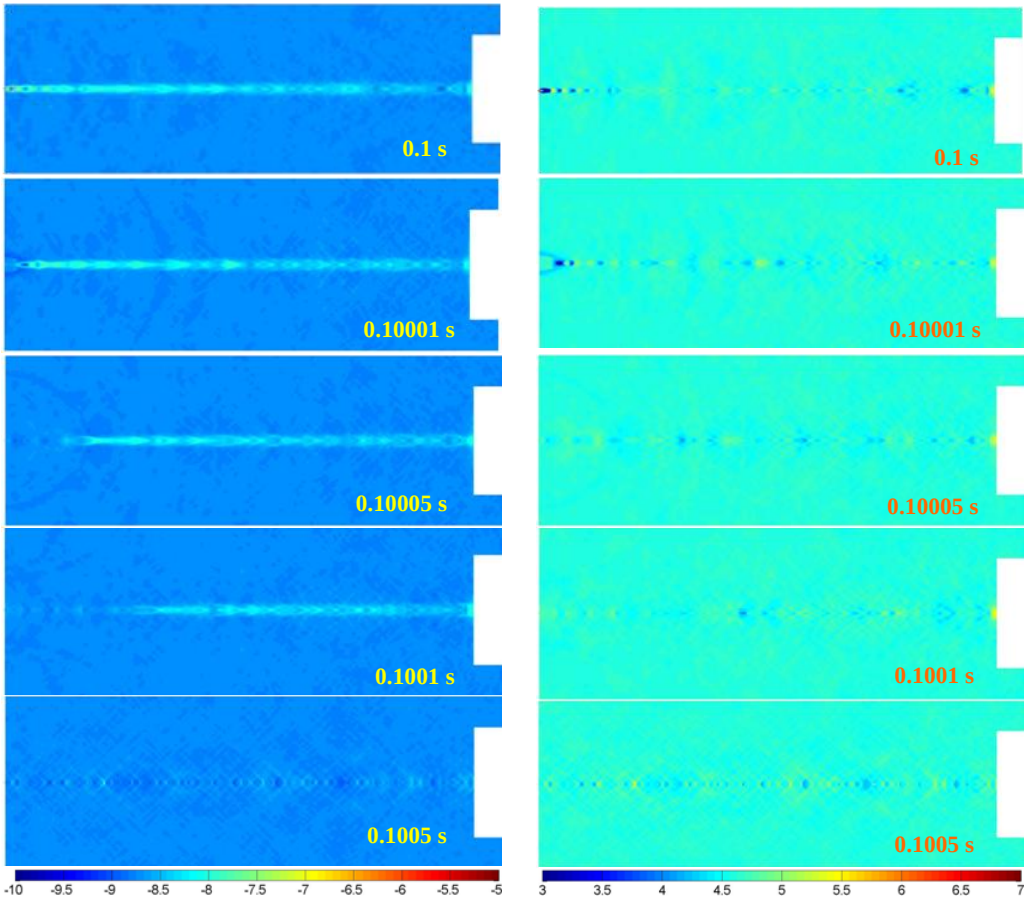

Figure 6.15 DD-QDS results: $\log_e$(density) [kg/m^3] contour (left) and $\log_e$(pressure) [Pa] contour (right) after inlet orifice closes (at 0.1 s) in the PP-CVD reactor at Case I conditions.

The inlet nozzle was shut at 0.1 s. It can be observed that the jet structure has dissipated during the first 0.5 ms of the pump down phase. The resulting flow field is rather uniform for the remaining pump-down process.

To estimate the number of particle collisions per time step per particle within a computational cell, the ratio of the simulation time step to the average

time between particle collisions was calculated. Figure 6.16 shows the contours of the $\log_e(\Delta t/t_{col,avg})$ at 0.10001 s (10 μs after the end of injection) and 0.1001 s (after the jet structure has dissipated), respectively, during the pump-down phase for Case I. Figure 6.16 shows that $(\Delta t/t_{col,avg}) \geq 2$ or $\log_e(\Delta t/t_{col,avg}) \geq 0.69$ i.e. two collisions per time step per particle is not achieved during the pump-down phase simulation in Case I.

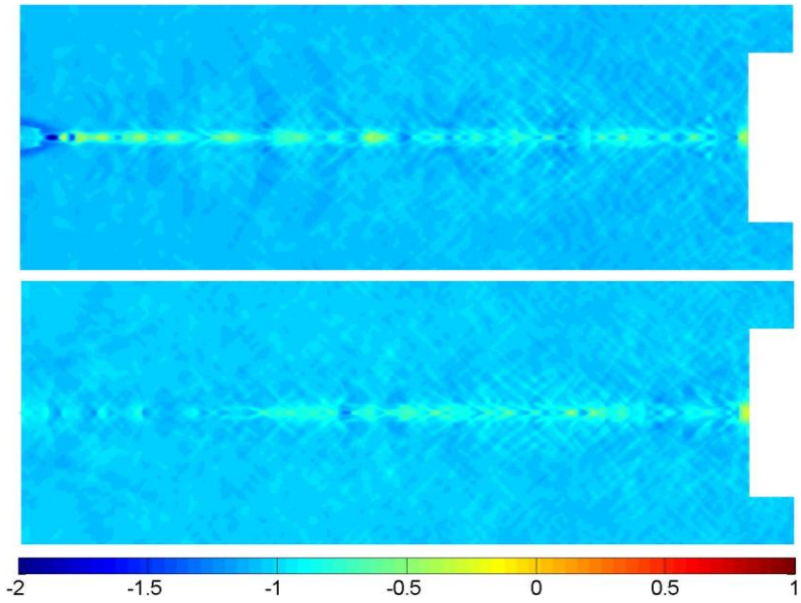

Figure 6.16 DD-QDS results: $\log_e(\Delta t/t_{col,avg})$ contours at 0.10001 s (top) and 0.1001 s (bottom) at Case I conditions.

Figure 6.17 shows the log scaled contours of the gradient length local Knudsen number based on density at the simulation times of 0.10001 s and 0.10010 s, respectively, for Case I. The contour plots in Figure 6.17 show that $(Kn_{GLL})_\rho$ is everywhere less than 0.05, or $\log_e(Kn_{GLL})_\rho < -3$, soon after the inlet jet was shut down. This indicates that although the number of collisions was low and the two collisions per time step per particle condition is not satisfied, the local

density gradient within the computational cell was not high enough to transport the particles downstream before the thermal equilibrium condition was established. Hence, the assumption that equilibrium is re-established locally in each time step in the DD-QDS scheme is partially justified for the PP-CVD process during the pump-down phase.

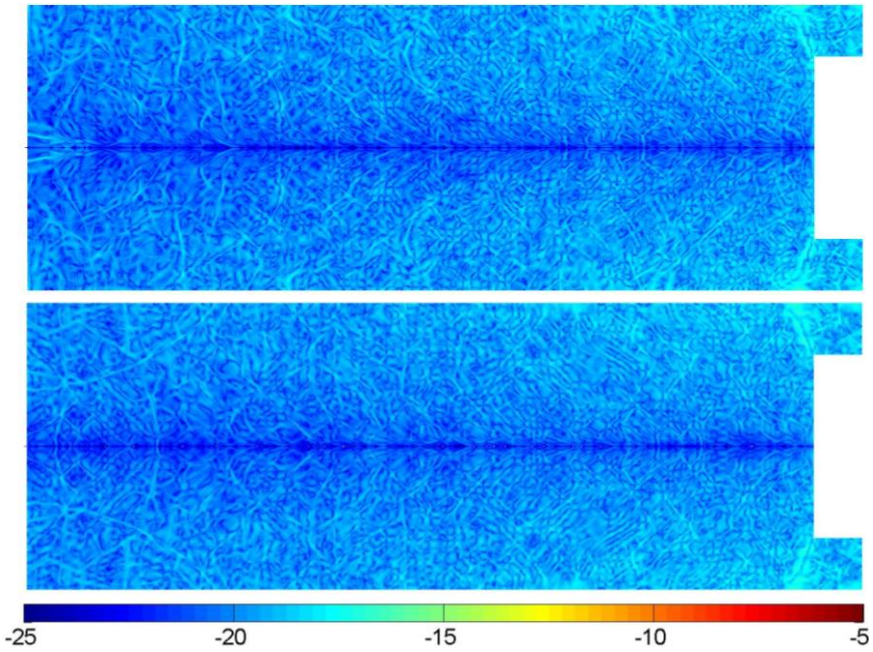

Figure 6.17 DD-QDS results: $\log_e(Kn_{GLL})_\rho$ contours at 0.10001 s (top) and 0.1001 s (bottom) at Case I conditions.

6.5.2 Case II: 1 kPa initial reactor pressure

6.5.2.1 Case II: Injection phase

Figure 6.18 shows the density contours (left) and the pressure contours plotted on a natural logarithm scale (right) of the simulation results using the DD-QDS for Case II conditions during the first 4 ms of the injection phase. Again, the similar

flow phenomena as seen in the TD-QDS simulation in Section 5.8.2 is captured in the simulation using the DD-QDS. However, Figure 6.18 demonstrates the improved accuracy in the DD-QDS computation to acquire enhanced detail of the flow field, especially the evolution of the shear layer and vortex trailing on the jet boundary during the unsteady flow field development. The flow field eventually becomes quasi-steady at about 3.0 ms.

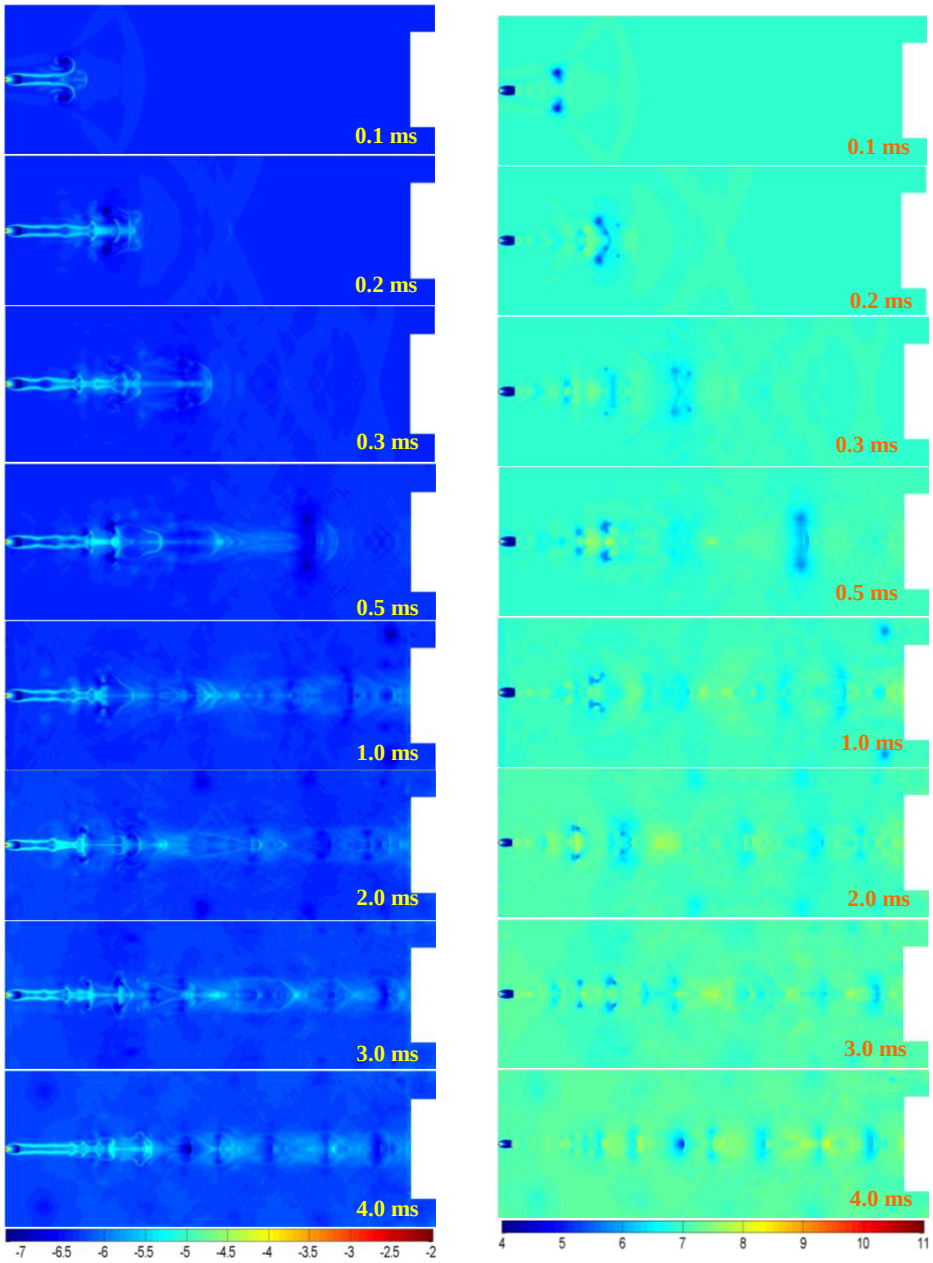

Figure 6.18 DD-QDS results: $\log_e$(density) [kg/m^3] contour (left) and $\log_e$(pressure) [Pa] contour (right) for the flow field in a PP-CVD reactor at Case II conditions during first 4 ms of the injection phase.

Figure 6.19 shows the contours of $(Kn_{GLL})_\rho$ plotted on a natural logarithm scale at the simulation times of 0.5 ms and 4.0 ms, respectively, for simulation results of the DD-QDS for Case II. It is shown that $\log_e[(Kn_{GLL})_\rho] < -3.0$ throughout the flow field at all times. Hence, it may be safely assumed that continuum breakdown does not occur in Case II and the local density gradient within the computational cell was not high enough to transport the particles downstream before the thermal equilibrium condition was re-established after each time step. This justifies the assumption of local thermal equilibrium in the DD-QDS scheme at initial reactor pressure of 1 kPa.

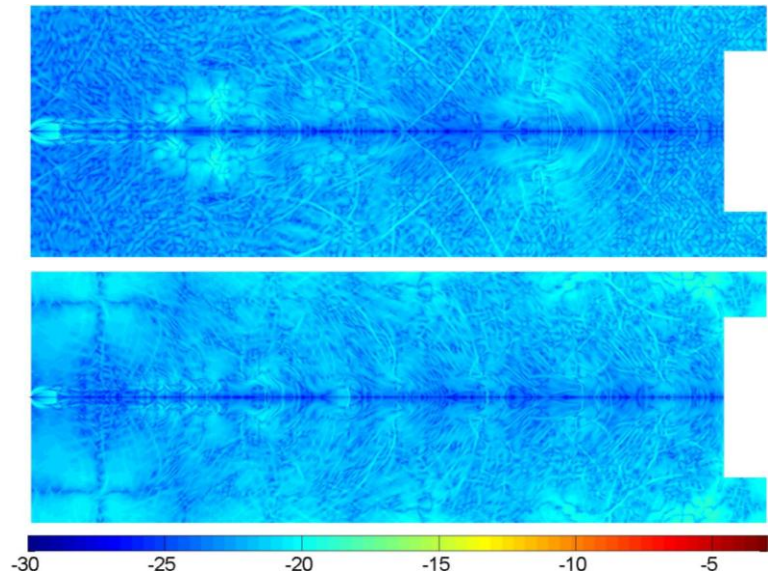

Figure 6.19 DD-QDS results: $\log_e[(Kn_{GLL})_\rho]$ contours at 0.5 ms (top) and 4.0 ms (bottom) at Case II conditions.

The ratio of the simulation time step to the average time between particle collisions was then calculated for Case II for the simulation results of the DD-QDS. Figure 6.20 shows the contours of $\Delta t / t_{col,avg}$ plotted on a natural logarithm

scale at the simulation times of 0.5 ms and 4.0 ms, respectively, for Case II. From Figure 6.20 it is observed that $\log_e(\Delta t/t_{col,avg}) \geq 0.69$ (or $\Delta t/t_{col,avg} \geq 2$) in most regions except a small region near the Mach disc. However, this region is unlikely to have a significant effect on the flow field, especially near the substrate region which is the region of interest in the simulation. Hence, in general, this suggests that there are at least two successive particle collisions in most regions of the flow field providing an insignificant difference between the actual physical non-equilibrium distribution and the Maxwellian equilibrium distribution. This, again, reasonably justifies the equilibrium assumption in the DD-QDS method in simulating the flow field of Case II.

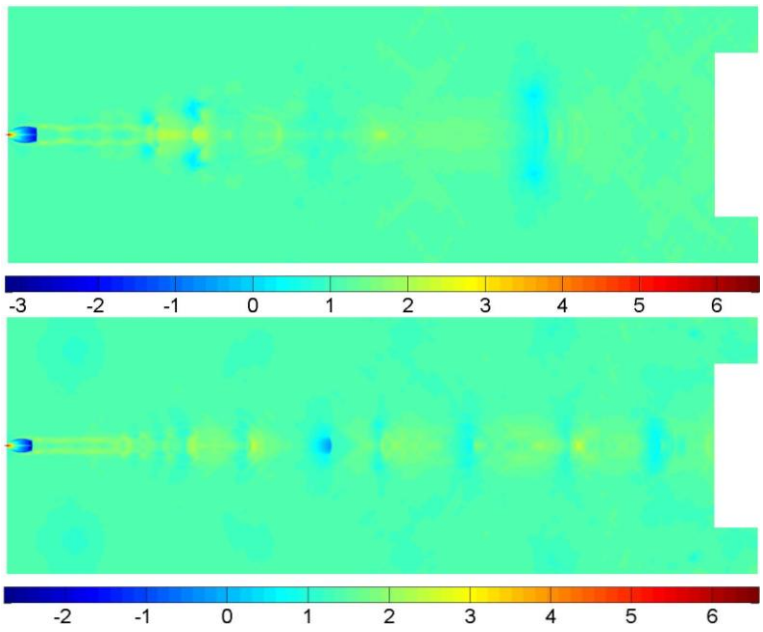

Figure 6.20 DD-QDS results: $\log_e(\Delta t/t_{col,avg})$ contours at 0.5 ms (top) and 4 ms (bottom) at Case II conditions.

6.5.2.2 Case II: Pump-down phase

The pump-down phase of the PP-CVD operating cycle at Case II conditions was also simulated using the DD-QDS code. The reactor pressure at the end of the injection phase is estimated to be 5 kPa. Figure 6.21 shows the density contours (left) and the pressure contours (right) plotted on a natural logarithm scale. Similar to that of Case I, the jet structure also dissipates rapidly in about 0.5 ms, after the inlet jet has been shut off at t = 0.1 s. A considerably uniform flow field is expected in the remaining pump-down process.

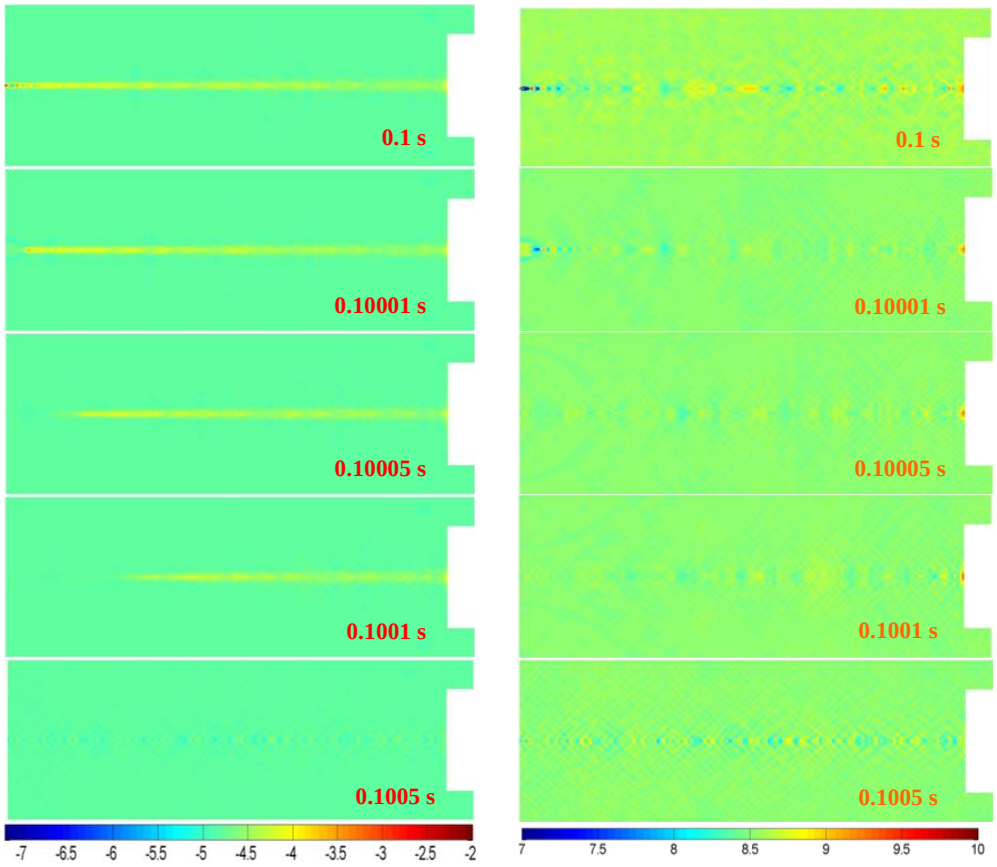

Figure 6.21 DD-QDS results: $\log_e$(density) [kg/m^3] contour (left) and $\log_e$(pressure) [Pa] contour (right) after inlet orifice closes (at 0.1 s) in a PP-CVD reactor at Case II conditions.

The validity of the thermal equilibrium assumption in the DD-QDS scheme was also checked for the Case II pump-down phase simulation. Figure 6.22 shows the log scaled contours of the gradient length local Knudsen number based on density at the simulation times of 0.10001 s and 0.1001 s, respectively. It can be observed that $\log_e(Kn_{GLL})_\rho$ is, overall, less than -5. This means that the local density gradient within the computational cells was not high enough to transport the particles downstream before the thermal equilibrium condition is re-established locally within one time step. Therefore, the continuum assumption can be considered valid in the flow field based on $(Kn_{GLL})_\rho$.

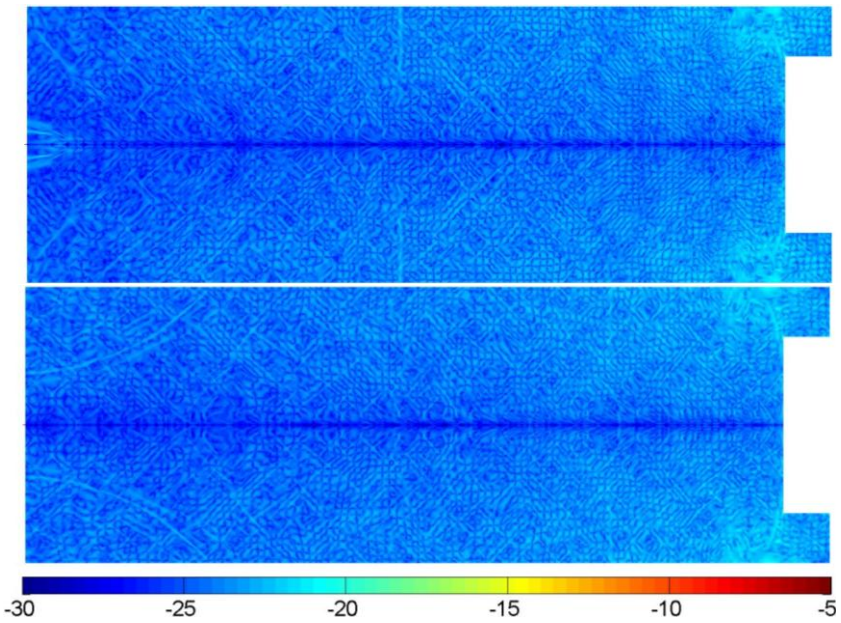

Figure 6.22 DD-QDS results: $\log_e (Kn_{GLL})_\rho$ contours at 0.10001 s (top) and 0.1001 s (bottom) at Case II conditions.

Figure 6.23 shows the ratio of the simulation time step to the average time between particle collisions, ($\Delta t/t_{col,avg}$), at 0.10001 s and 0.1001 s, respectively, during the pump-down phase for Case II. It can be seen in Figure 6.23 that $\log_e(\Delta t/t_{col,avg}) \geq 2.5$ everywhere in the simulation result which is greater than the required criterion of $\log_e(\Delta t/t_{col,avg}) \geq 0.69$.

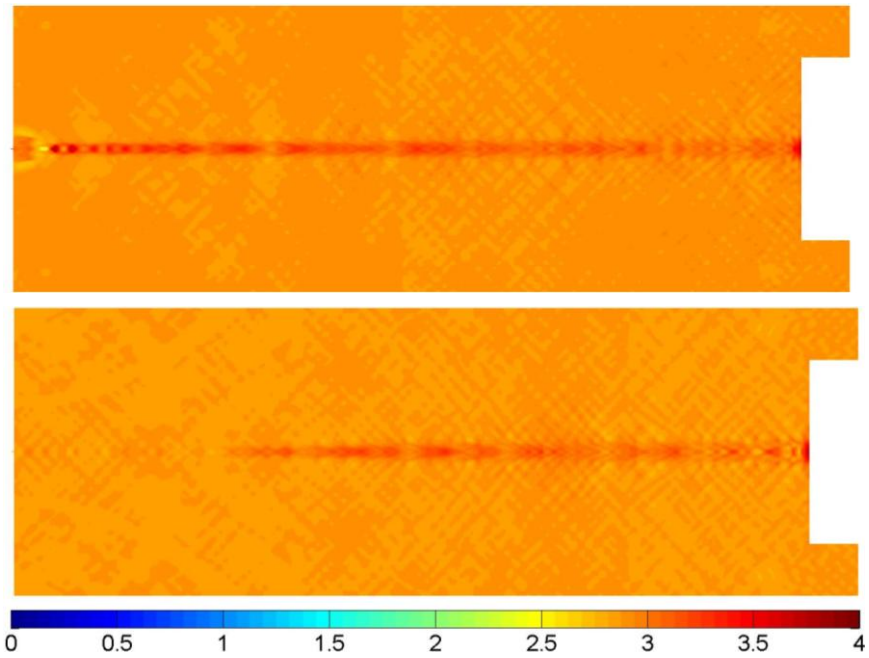

Figure 6.23 DD-QDS results: $\log_e(\Delta t/t_{col,avg})$ contours at 0.10001 s (top) and 0.1001 s (bottom) at Case II conditions.

6.5.3 Discussion

6.5.3.1 Inherent numerical dissipation in QDS scheme

Using the simplified numerical dissipation analysis discussed in Section 6.1.2, the effective kinematic viscosity inherent in QDS scheme with 4 discretised molecular speeds can be estimated using Equation (6.20). It is noted that the

kinematic viscosity is a function of the gas temperature. Table 6.4 shows the estimated effective kinematic viscosity υ_{scheme} for both the DD-QDS and the TD-QDS schemes of the PP-CVD flow field simulations for both Case I and Case II conditions as above. To allow a general characterisation of the flow, the average temperature of the flow field at flow time of 4 ms when the flow reach a quasi-steady state, is used in the calculation of the kinematic viscosity.

Table 6.4 Effective kinematic viscosity for both the DD-QDS and the TD-QDS schemes for PP-CVD flow at 4 ms.

Case	**I** (P_{min} = 1 Pa)		**II** (P_{min} = 1 kPa)	
Scheme (N = 4)	DD-QDS	TD-QDS	DD-QDS	TD-QDS
Average temperature, T_{ave} [K]	368.542	458.540	303.901	304.366
Average velocity, V_{ave} *[m/s]*	610.101	453.695	287.03	112.16
υ_{scheme} [m^2/s]	0.0971	0.1083	0.0882	0.0883

From Table 6.4, it can be noted that both QDS schemes have a similar effective kinematic viscosity overall. However, the DD-QDS shows slightly lower numerical viscosity compared to the TD-QDS at Case I conditions. This is consistent with the finding from the simulation results of the DD-QDS that more detailed flow phenomena have been captured compared to the results of the TD-QDS simulations. For example, the vortical roll-up of the shear layer development in the under-expanded jet. Hence, it can be concluded that the DD-QDS has

slightly lower numerical dissipation in the scheme which promotes accuracy in the solution.

The estimated v_{scheme} is about 2 orders of magnitude (200 times) higher than the physical kinematic viscosity of the gas, which is about 0.0005 m^2/s for Helium gas at standard conditions (Potter and Wiggert, 2002). This is due to the cell size used ($\Delta x = \Delta y = 2.5\times10^{-4}$ m) being a few orders of magnitude higher than the physical mean free path. However, it should be noted that the apparent viscosity in a real fluid will be increased by the eddy viscosity for turbulent flows. The value of the apparent viscosity will depend on local turbulence intensity and eddy spectrum size. Besides, the similarity of the present results of the QDS and that of the DSMC (Cave, 2008; Cave, et al., 2007) suggests that the numerical dissipation does not significantly affect the simulation of high Mach number flows or the low pressure PP-CVD reactor flows simulated here. Both of these flows are inertially dominated. Nevertheless the artificially high viscosity should be borne in mind when interpreting future QDS results.

The numerical diffusion can be minimized by reducing cell size but an increase in computational time will be experienced. The numerical diffusion in the QDS scheme is in proportion to the cell size (Jermy, et al., 2010). For the particular PP-CVD reactor simulation of interest, simulation with cell size of $\Delta x = 2.5\times10^{-4}$ m requires 4 hours for 1 ms of flow time. Reducing the cell size to $\Delta x = 1.25\times10^{-4}$ m halves the viscosity of the simulated gas, and increases the computational time to 72 hours to compute 1 ms of flow time. For the purpose of

exploring PP-CVD reactor design, the speed of simulation is prioritised over the quantitative accuracy of the flow field computed.

Figure 6.24 shows the comparison of $\log_e$(density) contour plots between the simulation results with grid size of $\Delta x = 2.5\times10^{-4}$ m and $\Delta x = 1.25\times10^{-4}$ m. During the injection phase of the PP-CVD process, the flow field develops into a quasi-steady state after the first 4 ms in the 1 s injection phase. The flow remains in quasi-steady state for about 99.6% of the injection time. From Figure 6.24, it shows that halving the grid size, which consequently halves the viscosity, has little effect on the flow field, especially after the quasi-steady jet has developed.

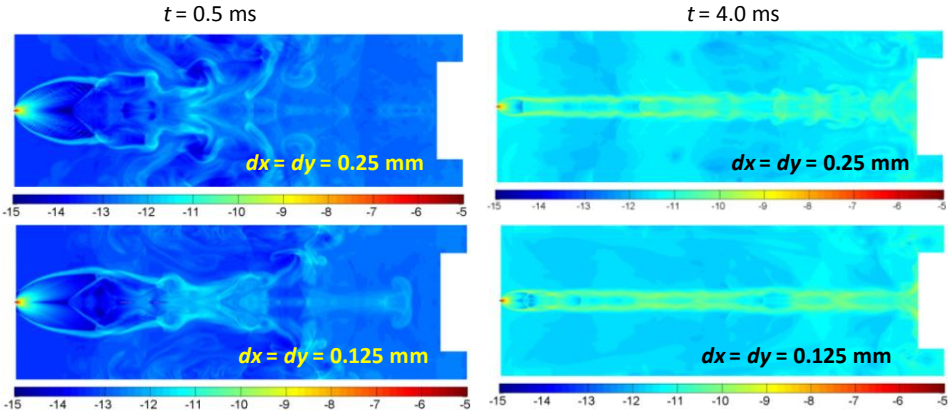

Figure 6.24 Comparison of $\log_e$(density) [kg/m^3] contour plots for PP-CVD simulation with grid sizes of 0.25 mm and 0.125 mm.

Figure 6.25 shows the accumulated number of particles colliding with the substrate face (AMOS) for three different cell sizes used throughout the simulation time of 3 ms. As shown in Figure 6.25, the difference in the amount of particles colliding at the substrate wall between runs with a cell size of $\Delta x = 2.5\times10^{-4}$ m and $\Delta x = 1.25\times10^{-4}$ m is much less compared to that between runs

with a cell size of $\Delta x = 5.0\times10^{-4}$ m and $\Delta x = 2.5\times10^{-4}$ m. From Figure 6.25, it is also noted that AMOS increases linearly with the radius since the annular area of the computational cell normal to the axial direction is linearly proportional to the radius.

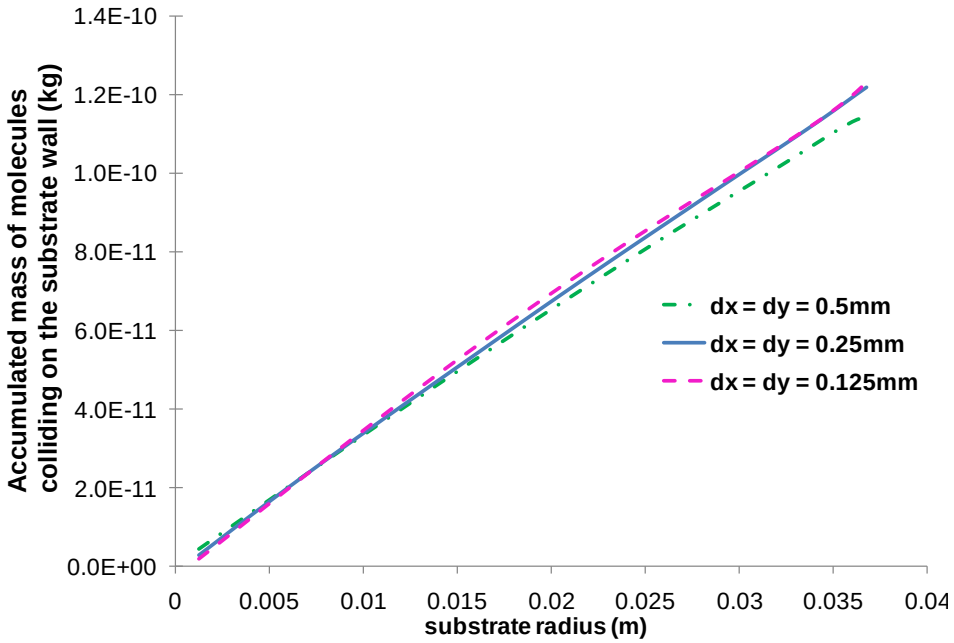

Figure 6.25 Accumulated mass of molecules colliding onto the substrate wall (AMOS) [kg] from simulations of 3 different cell sizes.

To characterise the uniformity of the flow field near the substrate surface, AMOS per unit cell area normal to the axial direction is calculated and plotted as shown in Figure 6.26. It should be noted that non-uniformity in AMOS per area in Figure 6.26 is expected since the results are plotted for only the first 3 ms of the injection phase, which is a very small fraction of the whole deposition cycle. Regardless, the difference in the AMOS per area between runs with a cell size of $\Delta x = 2.5\times10^{-4}$ m and $\Delta x = 1.25\times10^{-4}$ m is less than that between runs with a cell

size of $\Delta x = 5.0\times10^{-4}$ m and $\Delta x = 2.5\times10^{-4}$ m. Hence, a cell size of $\Delta x = 2.5\times10^{-4}$ m is used to allow speedy computation with reasonable quantitative accuracy. Although the quantitative accuracy reduces with the high value of numerical viscosity, the qualitative flow field phenomena, especially the shock position and structure, are not jeopardised. In fact, for the purpose of exploring PP-CVD reactor design and selecting operating conditions, the qualitative simulation result is sufficient.

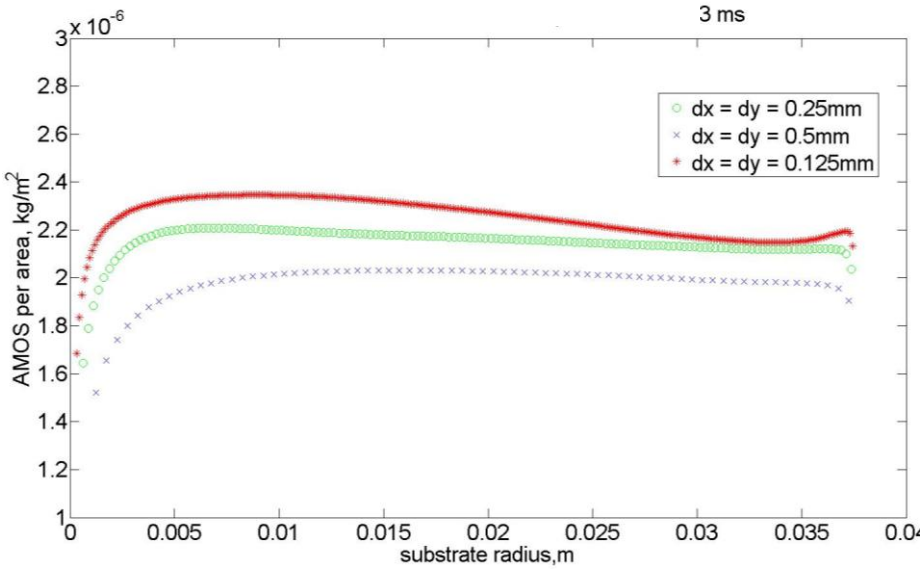

Figure 6.26 Accumulated mass of molecules colliding onto the substrate wall (AMOS) per substrate annular area [kg/m^2] from simulations of 3 different cell sizes.

For the simulation with 0.25 mm cell size, the average Reynolds number based on the physical viscosity of the gas is estimated using the average flow velocity in each simulation and is tabulated in Table 6.5. The average Reynolds number calculated using the physical viscosity ranges from about 2×10^4 to 1×10^5, which indicates that the inertia forces are dominant instead of the viscous forces

in the flow field of the PP-CVD process with gas injection. Hence, it is less likely for the numerical viscosity to have significant erroneous influence on the flow field phenomena. However, the average Reynolds number calculated using the estimated scheme viscosity shows a rather low values indicating high numerical dissipation in the simulation.

Table 6.5 Average Reynolds number calculated using estimated scheme viscosity (Re_{scheme}) and physical viscosity (Re_{real}) of Helium.

Case	**I** (P_{min} = 1 Pa)		**II** (P_{min} = 1 kPa)	
Scheme (N = 4)	DD-QDS	TD-QDS	DD-QDS	TD-QDS
Average velocity, U_{ave} *[m/s]*	610.101	453.695	287.03	112.16
Re_{scheme}	741.22	494.16	384.02	149.95
Re_{real}	143983.89	107072.12	67740.1	26470.05

It should also be noted that at high Reynolds number, turbulent flow occurs which introduces eddy viscosity to the flow field in addition to the gas physical viscosity. To improve the accuracy of the numerical result of such supersonic flow, an appropriate turbulent model is needed which should be considered in the future work.

6.5.3.2 Limitation of DD-QDS scheme in low pressure PP-CVD flow simulation

The local thermal equilibrium assumption excludes the QDS scheme from use in simulating highly rarefied flows. Due to the larger mean free path of the molecules in highly rarefied low pressure flow, the gas may not reach equilibrium

condition during the computational time step used. The limitation of the QDS scheme is investigated by utilising the gradient length local Knudsen number, $(Kn_{GLL})_\rho$, and the ratio of computational time step to the average time between particle collisions, $\Delta t/t_{col,avg}$.

A series of simulations at various minimum reactor pressures have been carried out in order to estimate the limit of the QDS scheme in simulating low pressure flow with a justified assumption of local thermal equilibrium. As seen from Figure 6.13 and 6.19, the threshold of $(Kn_{GLL})_\rho$ is met for the flow pressure as low as 1 Pa, which is the lowest possible reactor pressure in the current experimental PP-CVD reactor. However, the calculation of $\Delta t/t_{col,avg}$ shows that the low frequency of molecular collisions with 1 Pa initial reactor pressure condition hinders the restoration of local thermal equilibrium. Hence, simulations of the same PP-CVD flow condition have been conducted, changing only the reactor initial pressure from 1 Pa to 100 Pa, 200 Pa, 300 Pa and 400 Pa. Figure 6.27 shows the $\log_e(\Delta t/t_{col,avg})$ contours of the PP-CVD reactor flow simulations with initial pressures of 200 Pa, 300 Pa and 400 Pa.

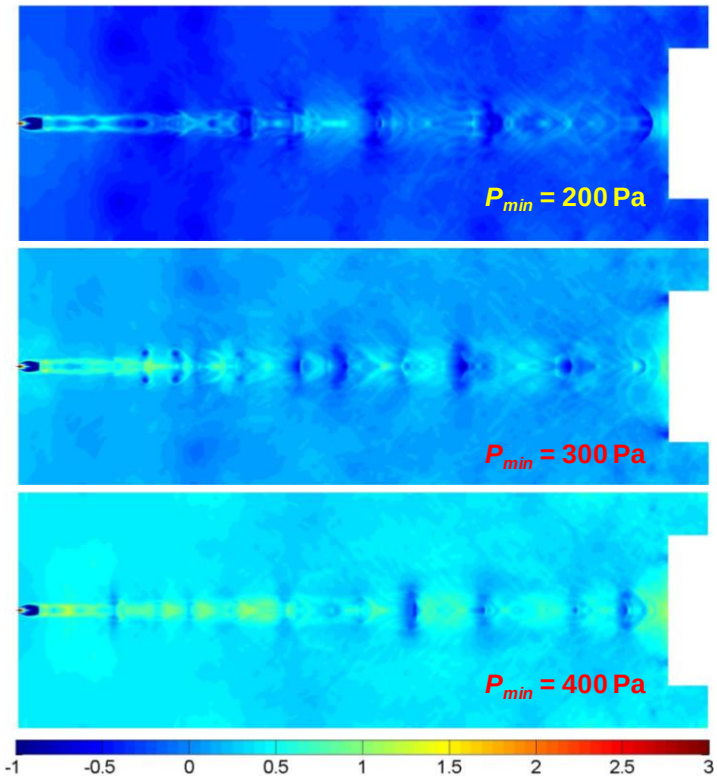

Figure 6.27 DD-QDS results: $\log_e(\Delta t/t_{col,avg})$ contours at 4 ms of the PP-CVD reactor flow simulations with initial pressures of 200 Pa (top), 300 Pa (middle) and 400 Pa (bottom).

Since $(Kn_{GLL})_\rho \leq 0.05$ has been met for runs with P_{min} = 1 Pa as shown in the results from Case I above, it requires only to check if $\Delta t/t_{col,avg} \geq 2$ in order to set a limit for the QDS scheme in simulating PP-CVD flows. From Figure 6.27, it can be seen that $\Delta t/t_{col,avg} \geq 2$, or $\log_e(\Delta t/t_{col,avg}) \geq 0.69$ has been just met in the simulation with P_{min} = 400 Pa in most regions but not for simulations with P_{min} lower than this. Thus, it can be considered that the QDS is able to produce numerical solution with reasonably accuracy to the PP-CVD flow with P_{min} = 400 Pa or greater.

The gradient length local Knudsen number, $(Kn_{GLL})_\rho$, and the Knudsen number, *Kn*, are also calculated for the series of simulations conducted and are tabulated in Table 6.6 below. This is done in order to determine the limit of the QDS that satisfy both $(Kn_{GLL})_\rho$ and $\Delta t/t_{col,avg}$ conditions as mentioned above. The maximum values of $(Kn_{GLL})_\rho$ and the corresponding *Kn* for the simulations with P_{min} = 400 Pa, can be used to set a limit for which the QDS scheme provides simulation results that are considered reasonably valid for low pressure flows. When $(Kn_{GLL})_\rho \leq 1.857\times10^{-7}$ or $Kn \leq 0.00164$ continuum flow assumption can be deemed valid.

Table 6.6 Minimum and maximum values of $(Kn_{GLL})_\rho$ and *Kn* at 4 ms for the series of PP-CVD reactor flow simulation conducted at different P_{min} with diameter of the reactor $D_{reactor}$ = 0.118m.

P_{min} [Pa]	$(Kn_{GLL})_\rho$		Kn $(\lambda/D_{reactor})$	
	min	max	min	max
1	8.892e-17	5.891e-04	2.188e-05	5.61591
100	1.630e-19	9.376e-07	2.188e-06	0.00820
200	4.809e-19	3.487-07	2.188e-06	0.00387
300	1.926e-19	3.694e-07	2.188e-06	0.00213
400	**3.295e-20**	**1.857e-07**	**2.188e-06**	**0.00164**

7 Droplet Flash Evaporation and Transport in PP-CVD

The precursor solution is delivered in a carrier gas from a liquid bubbler in the conventional CVD system. Through the liquid bubbler, the carrier gas becomes saturated with the precursor solution at the pressure and temperature in the bubbler. There are several issues with the conventional liquid bubblers. The liquid precursor solution is usually not fully saturated with the carrier gas and hence the precursor vapour can easily condense on the injection tube walls and fittings before reaching the reactor inlet. This causes cleaning and material wastage problems. Besides, it takes some time for the flow and liquid temperature in the bubbler to stabilize during start-up that causes chemical wastage (Jones & Hitchman, 2009).

As mentioned in Chapter 2, one of the novelties of PP-CVD technique is to allow direct injection of liquid precursor solution into the reactor chamber via an ultrasonic atomiser. This eliminates the problems in the use of bubbler as well as simplifies the reactor design. In the current PP-CVD reactor, an ultrasonic atomiser is used to generate liquid droplet from the injected precursor solution at the reactor inlet. The ultrasonic atomiser used in this study was SONO-TEK 8700-120 cone shape micro spray from SONO-TEK. This model is rated to generate liquid droplet at median diameter of 18 micrometers (Sono-TekCorporation, 1997). The liquid droplet of the precursor solution flows into the PP-CVD reactor by the means of pressure difference between the solution supply pressure and the low pressure of the continuously evacuated reactor. As discussed

in section 4.1.2, the injected liquid droplet evaporates sufficiently quickly due to the sudden pressure drop to below its saturation pressure, which is termed as flash evaporation.

The fast evaporation phenomenon of a liquid droplet in a quiescent low pressure environment seems to be a relatively less studied research. However, the investigation of droplet evaporation in jet flow, at high or atmospheric pressure is well-studied due to the well development in the industrial applications, ranging from fuel injection for combustion system to spray dryers for producing dried powder. Maxwell (Maxwell & Harman, 1890) established the classical diffusion theory to express the mass flux of a single spherical droplet in a medium with given parameters. An empirical correlation was developed for mass transfer number in the case of a sprinkler droplet falling through a moving airstream (Fröessling, 1938). A heat transfer analogy was then proposed that the heat transfer number in the same situation should be correlated in the similar manner with heat transfer data (Ranz & Marshall, 1952). Later, an expression for the growth rate of a droplet in terms of the total local condensation rate in a cloud for continuum region, free molecule regime and the transition regime was proposed (Barrett & Clement, 1988). This was followed by the development of a model for predicting evaporation and temperature changes in water drops travelling through air. The model was evaluated with laboratory data (Kincaid & Longley, 1989). Some rather recent reports on droplet evaporation investigation include a molecular dynamic method was developed to describe the liquid-vapour interface

of argon and water liquid droplet (Minkowycz & Sparrow, 2000), a diffusion model for evaporation of a single spherical droplet in gaseous medium at moderate pressure (Kozyrev & Sitnikov, 2001), and investigation on the problem of non-isothermal droplet evaporation and condensation in the near-continuum regime (Qu, Davis, & Swanson, 2001). An experimental study of droplet evaporation and coalescence in simple jet flow was also conducted to investigate the effect of turbulence on droplet evaporation (Nijdam, Stårner, & Langrish, 2004).

7.1 Concept and Formulations

Based on a molecular approach, the flash evaporation model presented in this study models the evolution of the basic macroscopic properties (mass, momentum and energy) of a liquid droplet exposed to low pressure vapour. A Lagrangian tracking method is used where the quantities of mass, momentum and energy exchanged with the vapour phase are multiplied by a factor during the droplet-gas coupling calculation. This is done to represent the actual quantity of droplets injected over the injection phase of the PP-CVD process. Each representative droplet at high supply pressure enters into the low pressure reactor environment and experiences a sudden drop of pressure to below the saturation pressure at its supply temperature. Hence, the fluid molecules on the droplet surface flash evaporate from liquid to gas phase resulting in the decrease of droplet size and energy, consequently the temperature. The conservation equations of the

macroscopic properties of each representative droplet are used as the droplet flash evaporation model equations. The droplet is assumed to be spherical with uniform temperature. The detail of the assumptions and the corresponding justification will be discussed in section 7.3.

7.1.1 Conservation Equation for Mass

The mass rate of change of a representative droplet is described with the Maxwell's diffusion equation in continuum regime (Pruppacher & Klett, 1997) with some modification for the present simulation conditions as given in Equation (7.1):

$$\frac{dm}{dt} = \frac{4\pi r\, D_{12}\, M}{R}\left(\frac{P_g}{T_g} - \frac{\Delta P}{T}\right) \tag{7.1}$$

where m is the mass of the droplet, r is the droplet radius, M is the molar mass, R is the universal gas constant, P_g and T_g are the pressure and temperature of the surrounding gas respectively, T is the droplet temperature, $\Delta P = 2\sigma_s/r$ is the Young–Laplace equation for pressure inside an equilibrium spherical droplet with a surface tension, σ_s, (Frohn & Roth, 2000), and D_{12} is the effective diffusion coefficient given by Equation (7.2) as (Kimpton & Wall, 1952):

$$D_{12} = \frac{3}{8n\sigma_{12}^2}\left[\frac{kT(m_1 + m_2)}{2\pi m_1 m_2}\right]^{1/2} \tag{7.2}$$

The diffusion coefficient in Equation (7.2) was derived based on the assumption that the gas and liquid phase molecules are rigid elastic spheres of masses, m_1 and

m_2, with molecular diameters, σ_1 and σ_2, respectively. For the current simulations, the hard sphere diameter of Toluene estimated by Rubio *et al.* is used, which is 5.72Å (Lim, et al., submitted). The mean molecular diameter, σ_{12}, is defined as $(\sigma_1 + \sigma_2)/2$ while the total number density, n, is the summation of the number density of the gas and liquid phase molecules. Due to the limited research in measuring the self diffusivity of Toluene in low pressure environment, the calculated diffusion coefficient of Toluene in the present work is compared to the binary diffusion coefficient of Benzene in air. Benzene (C_6H_6) is chosen in this comparison for its closed molecular structure and weight to Toluene (C_7H_8). At the atmospheric pressure, the binary diffusion coefficient of Benzene in air is about 0.88×10^{-5} m^2/s (Incropera & DeWitt, 2001). The calculated diffusion coefficient in the present simulation condition using Equation (7.2) is in the order of 3×10^{-5} m^2/s. The slightly higher diffusion coefficient in present work is within the expectation due to the large density gradient of the evaporated vapour between the droplet surface and the low pressure reactor volume. This causes large concentration difference which results in higher the diffusion coefficient determined.

7.1.2 Conservation Equation for Momentum

The droplets generated from the ultrasonic atomiser are driven away in to the reactor chamber by the pressure gradient between the inlet and the outlet of the reactor as well as the initial momentum of droplets. Thus, convection and

diffusion of moving viscous fluid is needed to be considered. The transport of the representative droplet is modelled by considering the momentum conservation of the droplet. The momentum rate of change of a simulated droplet is calculated from the momentum exchange between the representative spherical droplet and the surrounding gas, utilizing the drag coefficient. The change in droplet momentum, *p*, in a time step is given in Equation (7.3):

$$\frac{\partial p}{\partial t} = F_{gas-drop} = \frac{\vec{V}_g - \vec{V}}{\left|\vec{V}_g - \vec{V}\right|} C_D \frac{\pi d^2}{4} \frac{1}{2} \rho_g \left(\vec{V}_g - \vec{V}\right)^2 \tag{7.3}$$

where $F_{gas\text{-}drop}$ is the drag force exerted by the surrounding gas molecules to the droplet, ρ_g and $\vec{V}_g$ are the density and velocities of the surrounding gas, respectively, d is the droplet diameter, $\vec{V}$ is the droplet velocities, and C_D is the drag coefficient given in Equation (7.4) (Clift, Grace, & Weber, 1978):

$$C_D = \frac{24}{Re}\left[1 + 0.15\,Re^{0.687}\right] + \frac{0.42}{1 + 4.25\times10^4\,Re^{-1.16}} \tag{7.4}$$

which is valid for Reynolds number, $Re < 3\times10^5$. The Reynolds number can be calculated using Equation (7.5):

$$Re = \frac{\rho_g d\left|\vec{V}_g - \vec{V}\right|}{\mu_g} \tag{7.5}$$

where μ_g is the viscosity of the surrounding gas.

7.1.3 Conservation Equation for Energy

As the droplets evaporate, energy is being transferred from liquid to gas phase resulting in the change of the droplet temperature. Hence a non-isothermal droplet evaporation effect needs to be taken into account in the present droplet evaporation model. This can be done by considering the energy conservation of the droplet. The conservation of energy of a representative droplet considers the net change of energy within the droplet, $\Delta\dot{E}$, to be equal to the total energy across the boundary of the spherical droplet which can be expressed in Equation (7.6):

$$\Delta\dot{E} = \dot{E}_{rad} + \dot{E}_{condensate} - \dot{E}_{evaporate} - \dot{E}_{cond} = \rho\frac{4}{3}\pi r^3 c_p \frac{dT}{dt} \qquad (7.6)$$

where ρ is the droplet density and c_p is the specific heat of the droplet.

The radiative energy from surrounding, $\dot{E}_{rad}$, can be calculated by using Equations (7.7):

$$\dot{E}_{rad} = \varepsilon s 4\pi r^2 (T_{sur}^4 - T^4) \qquad (7.7)$$

where ε is the emissivity, s is the Stefan-Boltzmann constant, T_{sur} is taken to be the average surrounding room temperature where the PP-CVD process is conducted and T is the droplet temperature.

The condensation energy due to the re-condensed vapour from the surrounding when colliding with the droplet, $\dot{E}_{condensate}$, is calculated by using Equations (7.8):

$$\dot{E}_{condensate} = \alpha\dot{N}_{coll\ gas-drop} e_g \qquad (7.8)$$

where α is the mass accommodation coefficient, e_g is the molecular energy of the surrounding gas, $\dot{N}_{coll\ gas-drop} = \pi r^2 \bar{V} n$ is the molecular collision rate between the droplet and the surrounding gas at number density of *n*. In the present work, the mass accommodation coefficient is assumed to be 1 for simplicity, which is the same as in the non-isothermal droplet evaporation study conducted by Qu *et al.* (Qu, et al., 2001).

The evaporated energy, $\dot{E}_{evaporate}$, is calculated using Equation (7.9):

$$\dot{E}_{evaporate} = \frac{dm}{dt} c_p T \tag{7.9}$$

Note that the term *dm*/*dt* in Equation (7.9) is the mass rate of change of the droplet. The specific heat value of c_p was a curve-fitted value as a function of temperature based on the saturation data given by Lemmon *et al.* (Lemmon, et al., retrieved July 19, 2011).

Lastly, the conduction energy, $\dot{E}_{cond}$, due to the heat transfer through conduction from the droplet to the surrounding vapour can be determined by using Equation (7.10):

$$\dot{E}_{cond} = k_{cond} 4\pi r^2 \frac{T - T_{sur}}{r} \tag{7.10}$$

where k_{cond} is thermal conductivity. In the present simulation condition, the thermal conductivity of Toluene used is 11.2×10^{-3} W/m·K, which is obtained from the experimental investigation conducted by Vargaftik *et al.* (Vargaftik, Zaitseva, & Yakush, 1968).

7.2 Implementation of Droplet Flash Evaporation Model

The droplet model is coupled to the present QDS algorithm as an inlet condition to the gas phase flow simulation during the injection phase of the PP-CVD process. Figure 7.1 shows the flow chart of the droplet model-QDS solver coupling.

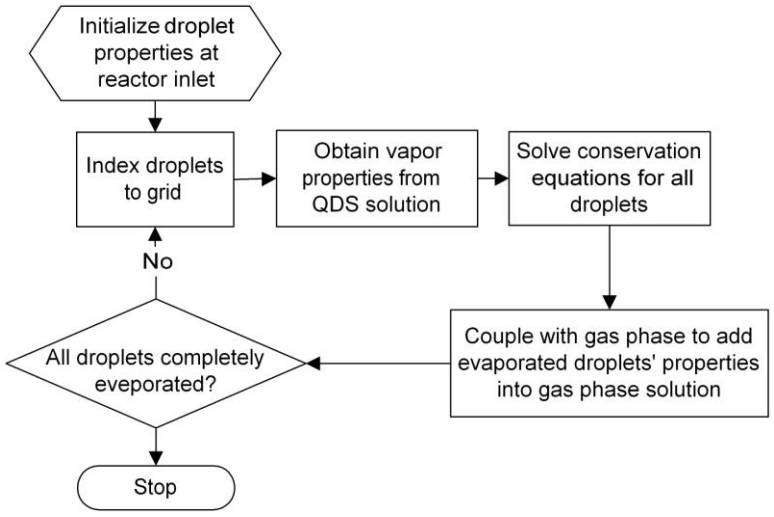

Figure 7.1 Flow chart of coupling the droplet model to gas phase solution by QDS solver.

A representative number of droplets are initialized with droplet size and velocity selected stochastically from the log-normal distribution of those properties for a typical spray. It has been studied experimentally to measure droplet velocity and diameters distribution at the exit of a discharge nozzle during sudden blowdown (Hervieu & Veneau, 1996) and of an ultrasonic atomiser (Nijdam, et al., 2004) by using Phase-Doppler Anemometry (PDA). It has been found that both droplet size and velocity of a typical spray generated have log-normal distribution profile at the nozzle exit. This is in consistency with the

product specification of the Sono-Tek MicroSpray™ nozzles in predicting the spray shape (Sono-TekCorporation, 1997).

In the present droplet evaporation model, a log-normal distribution of droplet diameter, velocity and spray dispersion angle is initialised with median diameter of 18 μm, mean velocity of 8 m/s and spray dispersion angle of 6º, respectively, based on values from the ultrasonic atomiser product specification and experimental investigation. Figure 7.2 below shows a sample plot of the droplet size and velocity distribution profile generated and used in the present simulations. It can be shown in Figure 7.2 that the random number generator employed in the solver is capable of simulating the desired initial droplets' properties profile. The actual median diameter of the droplet generated in the solver is 17.58 μm, while average *x*-velocity and *y*-velocity of the droplet generated is 8.21 m/s and 0.87 m/s, respectively. These agree well to that given by the atomiser manufacturer. It is also noted from the simulation results that all droplets were fully evaporated within a distance of 50 mm from the nozzle inlet, which agrees to the visual observation in the experiment.

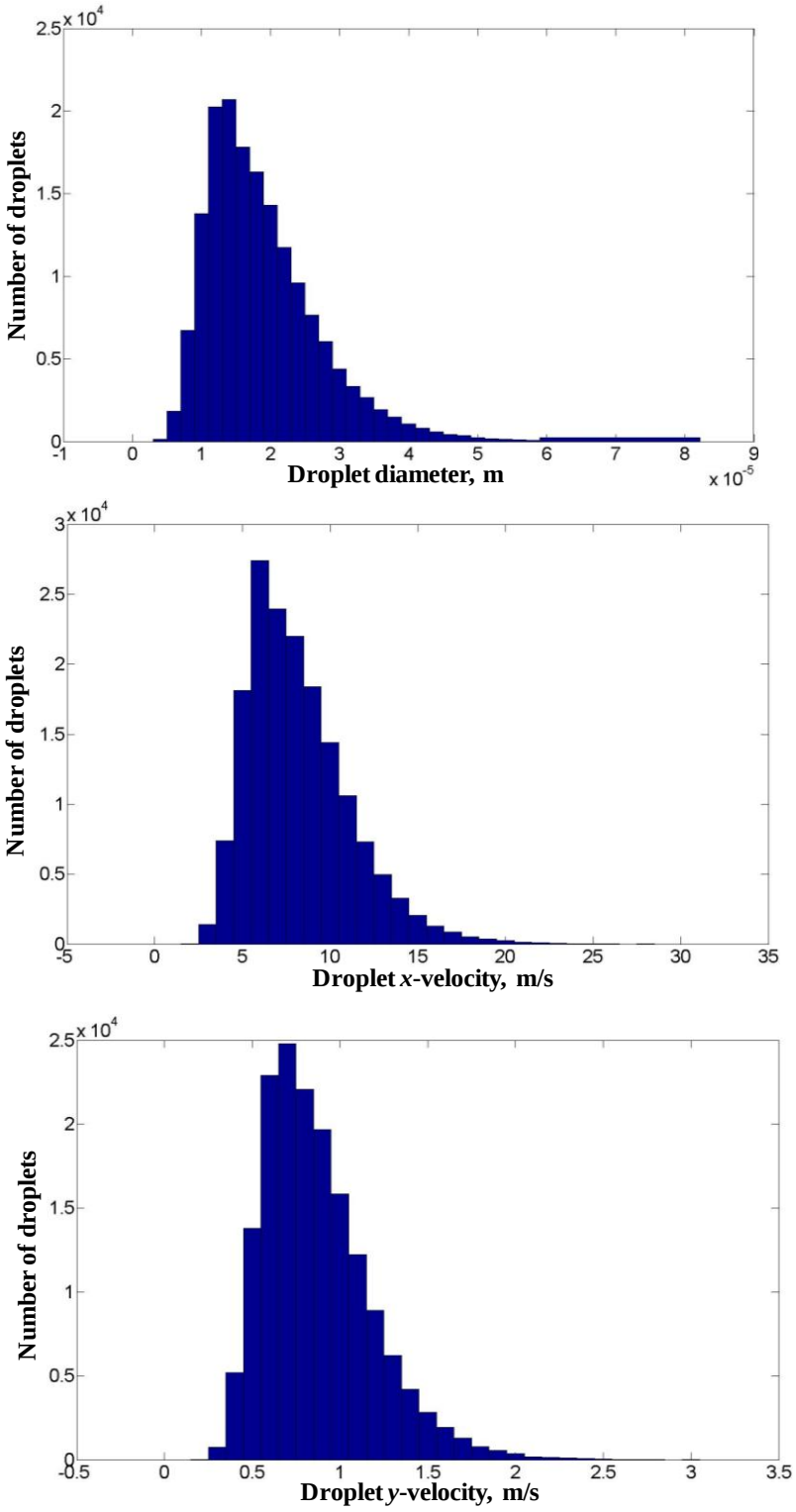

Figure 7.2 Plot of the droplet size (top), *x*-velocity (middle) and *y*-velocity (bottom) distribution profile.

After the droplet properties are initialised, the droplet location within the flow field is identified. This is important to obtain the local gas phase properties needed for calculating the droplet evaporation and evolution. Then, molecular properties of the evaporated droplets are calculated and added to the QDS gas phase solution. Due to gas-droplet collision, the molecular properties of condensed gas molecules are added into the colliding droplet. The state of each droplet is checked at the end of each time step for the completeness of the evaporation.

7.3 Validation of the Droplet Flash Evaporation Model

In PP-CVD process, the rapid injection of precursor solution together with the flash evaporation of the precursor solution droplets cause a high vapour concentration region near the reactor inlet. Hence, the mean free path of the gas molecule is generally small at this region. This allows the assumption of the droplet flash evaporation takes place in a continuum flow regime. Figure 7.3 below shows the plot of the gradient length local Knudsen number based on the density $(Kn_{GLL})_{\rho}$, which is defined in Chapter 4, for a PP-CVD flow field with liquid injection inlet. As noted from Figure 7.3, the $(Kn_{GLL})_{\rho}$ is less than 0.05 (as $\log_e[0.05] \approx -3$) throughout flow field in the reactor that indicates the flow can be treated as continuum condition.

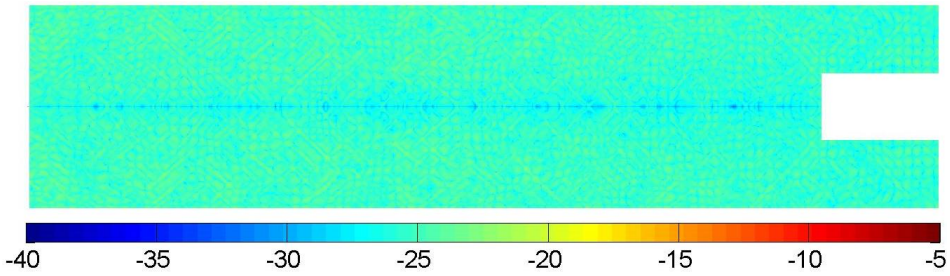

Figure 7.3 Plot of Log Scale $(Kn_{GLL})_{\rho}$ for a PP-CVD flow field with liquid injection inlet at t = 100ms.

The present droplet flash evaporation droplet assumes uniform temperature of the droplet. This can be justified by utilising the Biot number (*Bi*). The Biot number is a dimensionless number used in transient heat transfer analysis which is defined as the ratio of the heat transfer resistances inside of and at the surface of an object when undergoing convective heat transfer as given in Equation (7.11):

$$Bi \equiv \frac{hL_c}{k_{cond,f}} \tag{7.11}$$

where h is the convection heat transfer coefficient, L_c is the characteristic length which is the diameter of the droplet in present study and $k_{cond,f}$ is the thermal conductivity of the droplet. The *Bi* gives an estimated index whether or not the temperatures inside an object will vary significantly in space when convection heat transfer takes place on its surface. As a general guide, the spatial temperature gradient inside the object is negligible if $Bi < 0.1$ (Incropera & DeWitt, 2001). In the present droplet flash evaporation model, the droplet diameter is used as the characteristic length which as a median value of 18×10^{-6} m. The conductivity of the liquid droplet is estimated at the order of 0.1 $W\cdot m^{-1}\cdot K^{-1}$ based on the published

experimental data for Toluene (Ramires, 2000) while the thermal conductivity of the surrounding Toluene vapour in the reactor is about 0.0112 $W \cdot m^{-1} \cdot K^{-1}$ (Vargaftik, et al., 1968). Hence, the convection heat transfer coefficient *h* is estimated using the empirical correlation for external flow over a sphere (Incropera & DeWitt, 2001) and found in the order of 1.5 $W \cdot m^{-2} \cdot K^{-1}$. The *Bi* is then being estimated to be about 2.77×10^{-4} which justifies the uniform temperature assumption within the droplet.

The assumption of spherical droplet is considered in the present droplet evaporation calculation can be justified by examining the Weber number (*We*) of the typical droplet. The Weber number is an important dimensionless parameter that is used in the investigation of liquid droplet deformation breakup. The Weber number that measures the ratio of the dynamic pressure to the pressure due to the surface tension σ can be defined in Equation (7.12):

$$We \equiv \frac{\rho_g U_g^2 d}{\sigma} \tag{7.12}$$

where ρ_g is the density of the environment gas, U_g is the relative velocity of gases and droplet and *d* is the diameter of the droplet. The deformation and breakup of liquid droplet at Weber number near the critical value has been extensively studied. The critical *We* number, which indicates the limit of droplet deformation and breakup, ranges from 2 to 99 depending on the surface tension, regime of flow, turbulence structure of the flow and viscosity of the liquid (Khavkin, 2004). Hence, the droplet is conservatively considered remain in spherical form for *We* <

2. Therefore, in present study, consider a typical droplet generated from the ultrasonic atomiser with mean diameter of 18×10^{-6} m and mean velocity of 20 m/s enters the low pressure reactor where the initial density of the stagnant gas in the reactor is about 3.78×10^{-3} kg/m^3. The surface tension of the droplet is estimated at about 0.024 N/m (Lemmon, et al., retrieved July 19, 2011) for Toluene at 330 K which is used as the precursor solution in the present simulations. The Weber number can then be calculated to be in the order of 0.0011 which is a much smaller value compared threshold value of the Weber number for droplet deformation and breakup. Thus, the assumption of spherical droplet in the present study is justified.

There is very little droplet evaporation and condensation data reported under precisely controlled conditions of pressure and temperature particularly non-isothermal evaporation at low pressure environment. What is more, in the present study of the PP-CVD process, Toluene as the precursor solution is used but most of the droplet evaporation studies were conducted using water droplet. Hence, to validate the present droplet flash evaporation model, flash evaporation of a water droplet is considered. The numerical result is validated against the experimental measurements of the non-isothermal evaporation of a single water droplet (Taflin, Zhang, Allen, & James Davis, 1988). In the experiment conducted, a single water droplet was injected into an electro-dynamically balanced chamber consists of dry air at atmospheric pressure and two different surrounding gas temperatures, T_∞. Slight air was flown through the chamber to maintain the humidity at near zero.

The water droplet is trapped in the chamber where angular light scattering measurements of the droplet size as a function of time was performed. This single droplet evaporation problem was also investigated by Qu *et al.* in their analytical model for non-isothermal droplet evaporation and condensation (Qu, et al., 2001).

Figure 7.4 shows the comparison of the simulation results of the present droplet flash evaporation model to both experimental and simulation results from Taflin *et al*. and Qu *et al.*, respectively. Qu *et al.* used three different numerical models to solve this problem which are non-isothermal droplet evaporation in near-continuum regime, non-isothermal droplet evaporation in continuum regime and isothermal droplet evaporation. Good agreement between the results has been obtained. From Figure 7.4, the results calculated using QDS has close matches to both experimental and numerical model of non-isothermal droplet evaporation in the continuum regime. Therefore, this enables validation of the non-isothermal droplet flash evaporation model developed for the QDS simulation of the flow field in PP-CVD reactor with liquid injection.

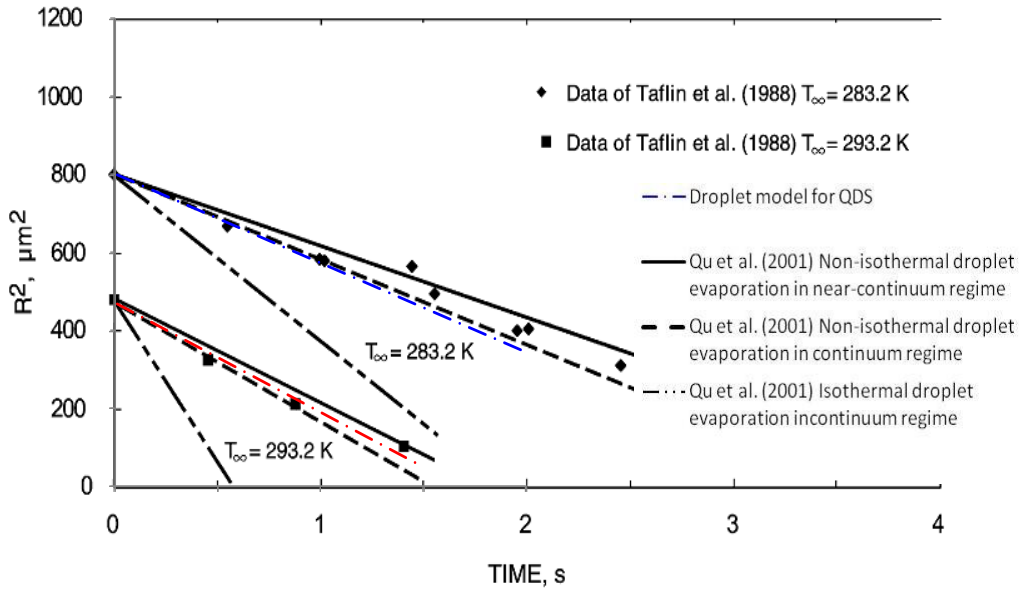

Figure 7.4 Comparisons of water droplet evaporation at atmospheric pressure in dry air.

8 Parametric Simulations of PP-CVD Reactor Flow Field

In both Chapter 5 and 6, the QDS method was developed to simulate the PP-CVD flow field in the reactor volume. Although the numerical viscosity that is inherent in the QDS scheme remains high when a grid size of few orders larger than the gas mean free path is used, the similarity between the results obtained from the QDS solver and the Parallelised DSMC (PDSC) solver (Cave, 2008; Cave, et al., 2007) demonstrates that QDS method as a feasible and simple simulation tool to obtain rapid approximations to the PP-CVD flow field. In fact, the QDS method provides significant improvement to the DSMC method in terms of requirements of the computational resources and reduced statistical scatter in the results. This is important for exploring PP-CVD reactor designs and selecting operating conditions.

In this chapter, together with the liquid droplet flash evaporation model described in chapter 7, the QDS scheme is used to simulate the precursor solvent flow field in different experimental PP-CVD reactor designs and applications. Simulations with varying reactor or substrate geometries, substrate position, the amount of injected precursor solvent and reactor initial conditions were performed.

The simulations conducted in chapter 5 and 6 revealed that the critical part of the PP-CVD process is the injection phase. The injection jet structure has shown to be the limiting factor that leads to the high flow field uniformity required at the start of the pump down phase. During the pump down phase, the

jet structure disperses in a very short period and the reactor flow field remains uniform throughout the rest of the pump down phase.

As described in section 4.2.1, the amount of precursor solution vapour that arrives onto the substrate surface is computed as a measure of surface deposition uniformity. The accumulated mass of gas molecules that strike onto the substrate surface (AMOS) was computed. To justify the uniformity of the total mass onto the circular substrate surface, AMOS over annular segment of the surface area was computed and used as the key parameter to investigate the uniformity of the particles arriving to the substrate surface.

Based on the computed AMOS, two methods are further developed in order to conduct the parametric study for assessing the effect of reactor design or process operating conditions to the flow field uniformity near substrate region in the PP-CVD reactor during the injection phase. First, the increase of the AMOS between chosen injection times is calculated. The increase in AMOS is then normalised to illustrate the relative increase. This allows the estimation of the amount of gas molecules that being transported from inlet to the substrate region. Figure 8.1illustrates the concept of relative increase of AMOS calculation. The difference of AMOS at times t_1 and t_2 is determined to track the amount of gas molecule being transported to the substrate surface. The relative increase of AMOS between time t_1 and t_2 can be calculated using Equation (8.1):

$$relative \quad increase = \frac{(AMOS)_{t_2} - (AMOS)_{t_1}}{(AMOS)_{t_1}} \tag{8.1}$$

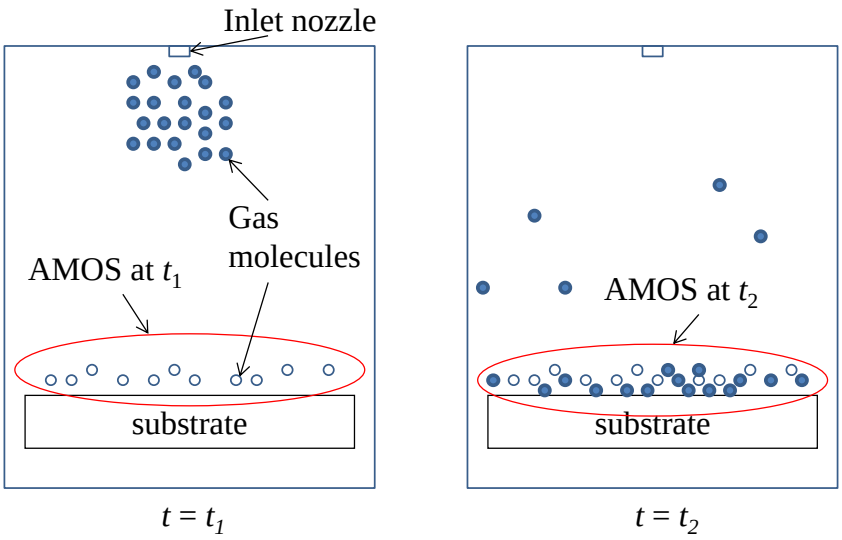

Figure 8.1 Illustrates of the relative increase in AMOS computation.

Second, the AMOS at each computational cell, $(AMOS)_i$, is normalised to the average value, $(AMOS)_{av}$. $(AMOS)_{av}$ can be calculated using Equation (8.2):

$$(AMOS)_{av} = \frac{1}{N_{cell}} \sum_{i=1}^{N_{cell}} (AMOS)_i \qquad (8.2)$$

where N_{cell} is the number of computational cell used across the substrate surface. A non-dimensional parameter U_{AMOS}, which is developed from the PP-CVD flow field uniformity calculation used in the experimental study (Baluti, 2005), is used to quantify the overall uniformity in AMOS and given in Equation (8.3) as:

$$U_{AMOS} = 1 - \frac{1}{N_{cell}} \sum_{i=1}^{N_{cell}} \left| \frac{(AMOS)_i - (AMOS)_{av}}{(AMOS)_{av}} \right| \qquad (8.3)$$

8.1 Parametric Simulations of PP-CVD Reactor Flow Field

8.1.1 Parametric Simulations of PP-CVD Reactor Flow Field

The second order true directional axisymmetric QDS solver described in chapter 5 is used to simulate the PP-CVD injection phase of a cylindrical reactor with a cylindrical pin as the substrate. Figure 8.2 shows the geometries of the reactor and substrate as well as the substrate locations in the reactor used in the simulations. These dimensions are equivalent to the design used in the experimental study conducted by the research group at Advanced Energy and Material Systems (AEMS) laboratory of University of Canterbury for the titanium dioxide (TiO_2) film deposition on a stainless steel pin (Krumdieck, et al., 2010).

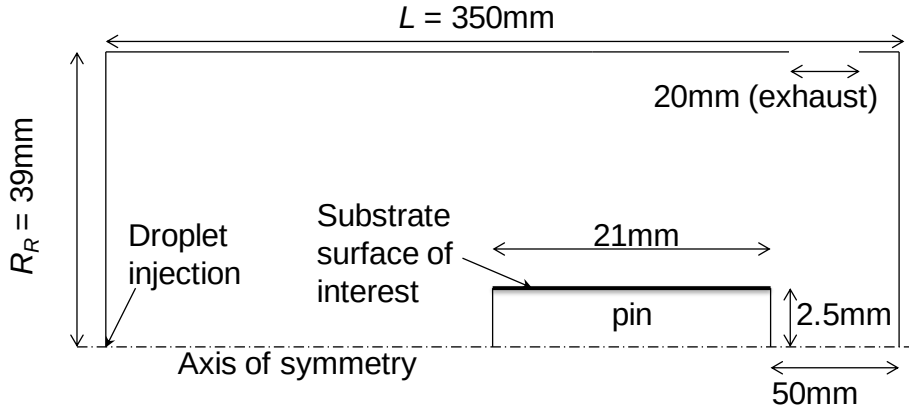

Figure 8.2 Schematic of the geometry for the cylindrical reactor with a circular pin as substrate.

In this study, the precursor solvent, Toluene, with a ratio of specific heats of 1.089 and a gas constant of R = 90.2384 J/(kg·K) is chosen to be the simulation species. A representative droplet at temperature of 333 K with diameter and velocities determined stochastically based on a log-normal distribution of typical

spray as described in chapter 7 is injected into the reactor at each time step during the simulated 1.0 s injection phase. The injected droplets have a median diameter of 18 μm, a mean velocity of 8 m/s and the maximum spray dispersion angle of 6º (Sono-TekCorporation, 1997). A multiplication factor of 20 to the representative droplet is used in order to provide total injected amount of about 43 μg of Toluene throughout the 1 s injection phase simulated, which is the amount used in the experimental deposition.

The initial reactor flow field is at stationary. The simulations were carried out on a desktop computer with 3.00GHz Intel Core 2 Duo CPU and 4GB of RAM using uniform Cartesian cells with 0.5 mm cell size. The cell size was chosen based on the feasible simulation time for the entire injection phase. Table 8.1 describes the simulation conditions used in this study. For all wall boundaries, the specular reflection scheme is applied to implement the slip wall boundary condition.

Table 8.1 Simulation conditions for PP-CVD flow field in the cylindrical reactor with circular pin as substrate.

Initial Pressure, P_{min}	100 Pa
Initial Temperature, T_i	293 K
Injection time, t_i	1.0 s
Spatial accuracy	2nd order
QDS velocity bin, N	4 per coordinate direction
Simulation time step, Δt	variable time step with maximum $CFL < 0.5$
Slope limiter	Monotonized Central Difference
Reactor evacuation rate, Q_P	0.46 L/s
Median droplet diameter	18 μm
Mean droplet velocity	8 m/s
Maximum spray angle	6°

The main goal of this study is to explore the effect of various reactor geometries to the flow field uniformity near the substrate surface. This is done by varying the reactor length L and reactor radius R_R.

8.1.2 Results

Figure 8.3 shows the density contours plotted on a natural logarithm scale as the flow develops throughout the injection phase for the original reactor design as shown in Figure 8.2 above. In Figure 8.3, only the gas phase of the results is plotted.

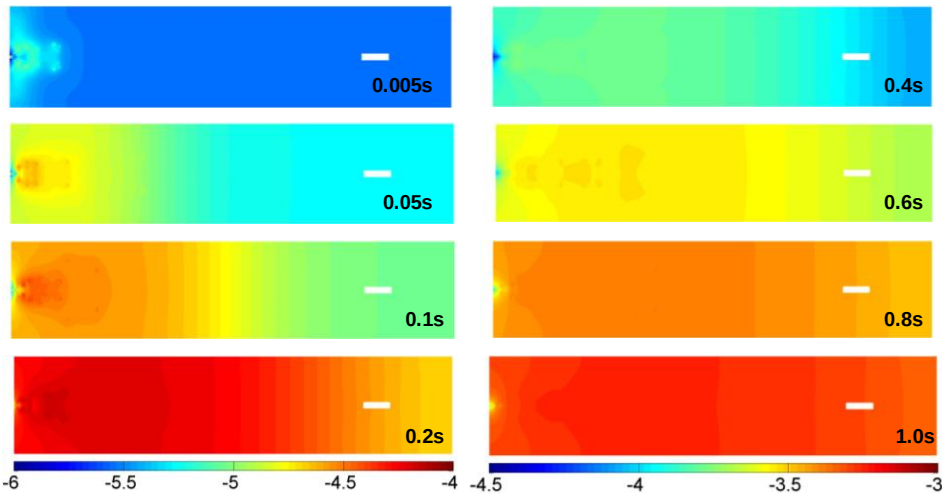

Figure 8.3 $\log_e$(density) [kg/m^3] contour in a cylindrical PP-CVD reactor with a circular pin as substrate during injection phase.

Note that the colour scale changes after 0.2 s to accommodate the overall increase in density of the flow field. The injected liquid Toluene droplets flash evaporate and the evaporated vapour expands and propagates rapidly along the length of the

reactor. From the contours plotted, it can be seen that the flow field in the region near the cylindrical pin where deposition occurs is considerably uniform.

To further investigate the effect of different reactor geometries on the uniformity of the flow field near the pin, two more simulations were conducted by reducing half the reactor length L and radius R_R, respectively, which is summarized in Table 8.2 below. All other conditions in the simulation setup remain unchanged.

Table 8.2 Parametric simulations for PP-CVD flow field in the cylindrical reactor with circular pin as substrate.

	Reactor length, L	Reactor radius, R_R
Initial design	350 mm	39 mm
Case 1	175 mm	39 mm
Case 2	350 mm	20 mm

Figure 8.4 shows the increase of AMOS between 20 ms and 1 s during the injection phase, which was normalised to the value of AMOS at 20 ms to demonstrate the relative increase. The gas vapour is estimated to reach the pin surface at about 20 ms. Hence, Figure 8.4 provides an approximation of the amount of precursor solution that interacts with the substrate surface throughout the injection phase. In Figure 8.4, zero substrate length indicates the front end of the pin, which is at the distance of 279 mm from the inlet of the reactor by referring to Figure 8.2. In this parametric simulation, the circular surfaces at both ends of the pin are not considered in the analysis of uniformity. This is because there are only 5 computational cells used across the radius of the pin with the chosen grid spacing. Hence, it is considered insufficient data on AMOS across the

pin radius to provide a good representative calculation of the average value and uniformity in AMOS.

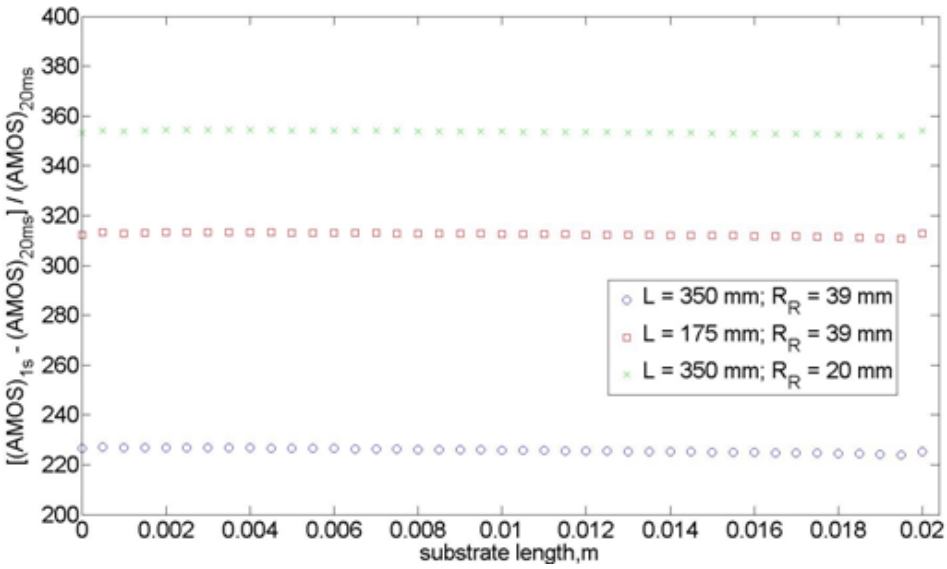

Figure 8.4 Increase in AMOS after 20 ms for the flow field in the cylindrical PP-CVD reactor with a circular pin as substrate during injection phase.

Table 8.3 tabulates the uniformity in AMOS calculated using Equation (8.2).

Table 8.3 Flow field uniformity near substrate region for the cylindrical PP-CVD reactor with circular pin as substrate.

	Uniformity in AMOS, U_{AMOS}
Initial design	0.978514
Case 1	0.969431
Case 2	0.979756

8.1.3 Discussion

In this section, the second order true directional axisymmetric QDS solver was used to simulate the PP-CVD injection phase of a cylindrical reactor with a cylindrical pin as the substrate. When the second order axisymmetric directional decoupled QDS (DD-QDS) scheme as described in Chapter 6 was subsequently

developed, these simulations were not repeated with the DD-QDS solver. This is because the numerical dissipation was not thought to influence the results greatly as demonstrated in Table 6.4.

The initial reactor design with L = 350 mm and R_R = 39 mm has the lowest increase in AMOS. By reducing the reactor length or radius, the volume of the reactor reduces as listed in Table 8.4.

Table 8.4 Volume of the cylindrical reactor at different length or radius.

	Volume, cm^3
Case 1	0.652
Case 2	0.326
Case 3	0.088

Hence, the overall density of the injected precursor solution increases. This allows the increase in the frequency of gas molecules colliding with the substrate wall as shown in Figure 8.4. By reducing the radius of the reactor, the increase in AMOS is the highest among the 3 cases simulated. The uniformity of the increase in AMOS seen in Figure 8.4 also confirms the flow field uniformity as demonstrated in Figure 8.3.

Table 8.3 further illustrates the uniformity of flow field near the substrate surface. All cases have U_{AMOS} above 96%. However, for closer assessment, the uniformity decreases in case 2 which the reactor length is halved. This indicates that a reasonable length is required to allow the accelerated evaporated vapour from the high density inlet region to relax into a uniform flow along the reactor length driven mainly by the pressure gradient.

When comparing the uniformity between case 1 and 3, the uniformity of the flow field increases when the reactor radius is halved. As the substrate is relatively much smaller than the reactor radius, for example the pin radius is only about 12.5% of the reactor radius in case 3, there is sufficient room between the reactor wall and the substrate for the gas molecules to self-diffuse into a "well-mixed" condition. Therefore, in this application, the initial reactor radius could be reduced by half in order to increase the deposition efficiency with more gas molecules strikes on the substrate surface to enhance the film deposition without compromising the uniformity of the deposition.

8.2 Reactor of 2nd Generation PP-CVD System

8.2.1 Simulation Setup

In the effort of improving the ease of use of the PP-CVD reactor relating to the reactor maintenance, substrate placement and reactor outlook, a second generation PP-CVD system has been designed and developed by D. Lee in the University of Canterbury's AEMS laboratory as his master thesis project (details to be published in Lee's master thesis). The initial design of the reactor for the second generation PP-CVD system is shown in Figure 8.5.

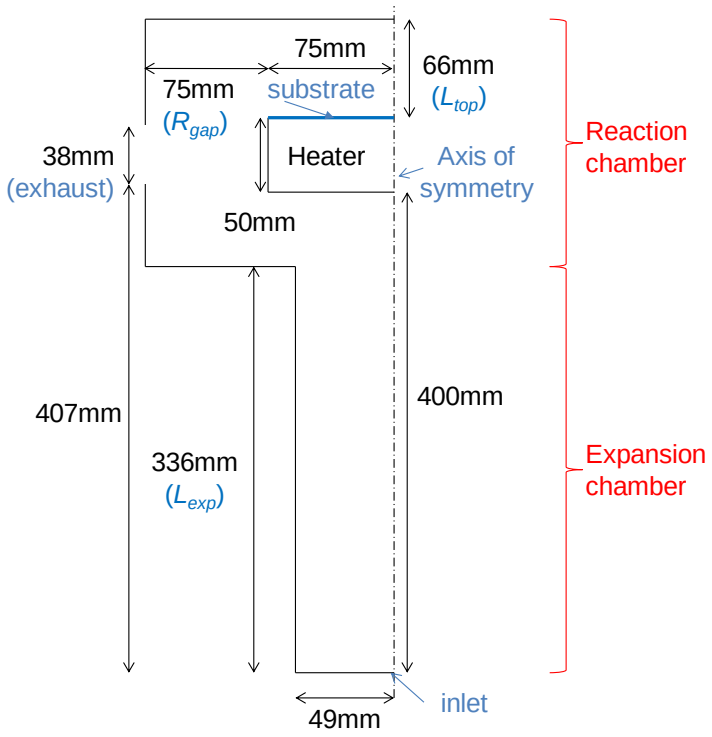

Figure 8.5 Schematic of the reactor geometry for the 2nd generation PP-CVD system.

The second order true directional axisymmetric QDS solver described in chapter 5 is again used to assess a few design parameters of the reactor by simulating the flow field of the PP-CVD process during the injection phase. In this parametric study, Toluene with a ratio of specific heats of 1.089 and a gas constant of R = 90.2384 J/(kg·K) is chosen to be the simulation species. Representative droplets at temperature of 293 K with initial diameter and velocities determined stochastically based on a log-normal distribution of typical spray as described in chapter 7 is injected into the reactor. Each droplet is injected at a chosen frequency together with a multiplication factor of 20 in order to allow a total amount of about 43 μg of Toluene droplets to be supplied throughout the simulated 1.0 s injection phase.

The initial reactor flow field is at stationary. The simulations were carried out on a desktop computer with 3.00GHz Intel Core 2 Duo CPU and 4GB of RAM using uniform Cartesian cells with 1 mm cell size. The cell size was chosen based on the feasible simulation time for the entire injection phase. Table 8.5 describes the simulation conditions used.

Table 8.5 Simulation conditions for flow field in the 2nd generation PP-CVD system.

Initial Pressure, P_{min}	100 Pa
Initial Temperature, T_i	293 K
Injection time, t_i	1.0 s
Spatial accuracy	2nd order
QDS velocity bin, N	4 per coordinate direction
Simulation time step, Δt	variable time step with maximum CFL < 0.5
Slope limiter	Monotonized Central Difference
Reactor evacuation rate, Q_P	0.46 L/s
Median droplet diameter	18 μm
Mean droplet velocity	8 m/s
Maximum spray angle	6°

The objective of this study is to explore the effect of various key parameters for the reactor geometries to the flow field uniformity near the substrate surface. This is done by varying the expansion chamber length L_{exp}, distance between the reactor top wall and the substrate surface L_{top}, and the distance between the reaction chamber wall and the heater R_{gap}. Table 8.6 lists the change in the geometry of each simulation case conducted in this study.

Table 8.6 Parametric simulations for the 2nd generation PP-CVD reactor.

	L_{exp}, mm	L_{top}, mm	R_{gap}, mm
Case 1	336	66	75
Case 2	168	66	75
Case 3	336	33	75
Case 4	336	132	75
Case 5	336	66	37
Case 6	336	66	150

8.2.2 Results

Figure 8.6 shows the density contours plotted on natural logarithm scale as the flow develops throughout the injection phase for the initial reactor design as shown in Figure 8.5.

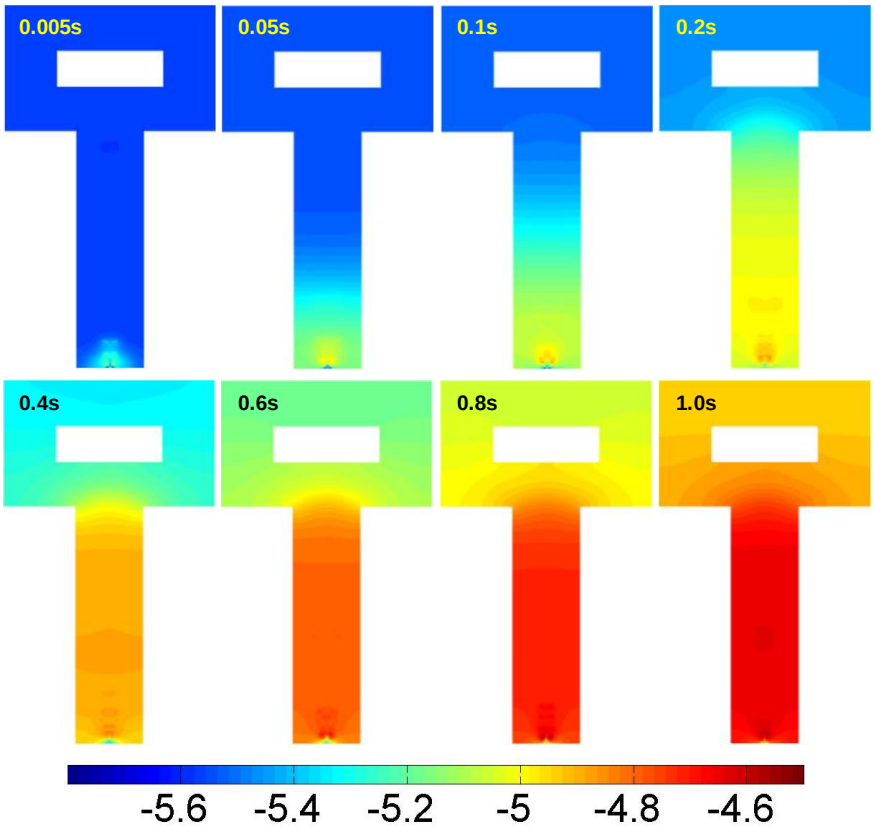

Figure 8.6 $\log_e$(density) [kg/m^3] contour of the flow field in the 2nd generation PP-CVD reactor during injection phase.

Figure 8.7 shows the comparison of the increase in AMOS between 0.2 s and 1 s during the injection phase, which was normalised to the value of AMOS at 0.2 s to demonstrate the factor of increment. As noted from Figure 8.5, the gas vapour is estimated to reach the substrate surface at about 0.2 s.

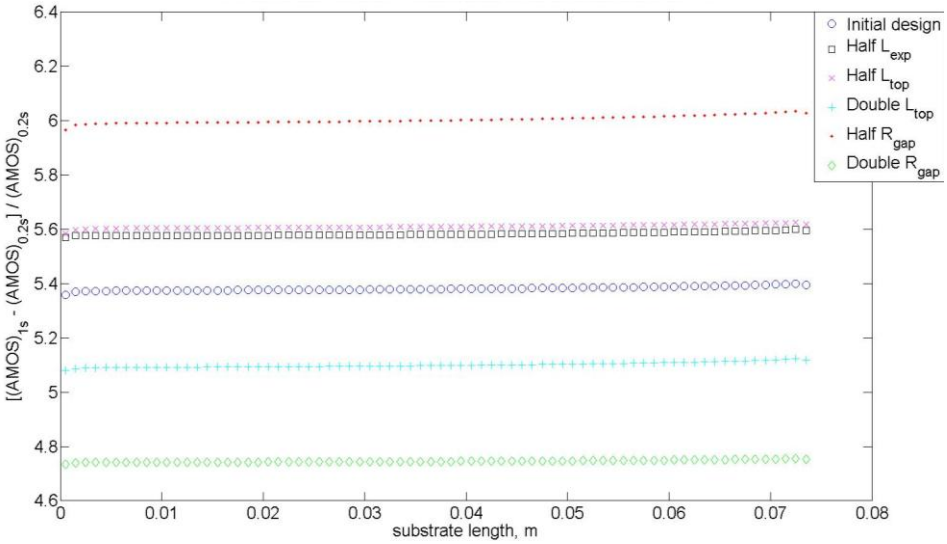

Figure 8.7 Increase in AMOS after 0.2 s for the flow field in the 2nd generation PP-CVD reactor during injection phase.

Table 8.7 shows the uniformity in AMOS calculated using Equation (8.3).

Table 8.7 Flow field uniformity near substrate region for the 2nd generation PP-CVD reactor.

	Uniformity in AMOS, U_{AMOS}
Case 1: Initial design	0.960618
Case 2: Half L_{exp}	0.958104
Case 3: Half L_{top}	0.960730
Case 4: Double L_{top}	0.960483
Case 5: Half R_{gap}	0.960289
Case 6: Double R_{gap}	0.960855

8.2.3 Discussion

One of the main concepts for the design of the 2nd generation PP-CVD reactor is to allow the injected precursor vapour to have sufficient time to fully evaporate, expand and disperse uniformly along the length of the expansion chamber before reaching to the reaction chamber and eventually to the substrate surface. The evaporated vapour propagated into the reaction chamber at about 0.1 s and reaches the substrate surface, which is a circular plate placed on top of the heater, at about 0.2 s. From Figure 8.6, it is shown that uniform flow field was achieved in the reaction chamber, particularly in region near the substrate surface.

The increase in AMOS in the 2nd generation PP-CVD reactor as shown in Figure 8.7 is much less than that in the cylindrical reactor as shown in Figure 8.4. This is due to the much larger volume in the 2nd generation PP-CVD reactor compared to the cylindrical reactor. This suggests that a greater amount of precursor solution supply is required in the 2nd generation reactor in order to maintain or increase the deposition rate of the PP-CVD process conducted in the existing cylindrical reactor.

Besides, the effect of varying a few reactor design parameters to the increase in AMOS can also be interpreted from Figure 8.7. The increase in AMOS reduces when the distance between the top wall of the reactor and the substrate surface L_{top} as well as the distance between the reaction chamber side wall and the heater R_{gap} are doubled. This is due to the larger overall volume of the reactor for

the gas molecules to fill in resulting less gas molecules being transported to and reflected from the substrate surface.

To increase the amount of gas molecules arrival near the substrate region, the reactor volume can be reduced by reducing L_{exp}, L_{top} or R_{gap}. As observed from Figure 8.7, the increase in AMOS after the first 0.2 s of the injection phase was raised when either L_{exp}, L_{top} or R_{gap} was halved. However, when reducing L_{exp}, it should be carefully examined whether there is sufficient distance along the expansion chamber length for the gas molecules to diffuse into a uniform flow field before reaching the reaction chamber. The effect of reducing L_{top} or R_{gap} to the flow field uniformity near the substrate region should also be checked. This is done by estimating the uniformity in AMOS for each simulated case as tabulated in Table 8.7.

By using the uniformity in AMOS for the initial reactor design as reference, the uniformity in AMOS decreases when L_{exp} or R_{gap} was halved. By reducing L_{exp}, there was less time for the gas molecules to develop into a "well-mixed" condition before reaching the reaction chamber. When R_{gap} was reduced, the cross sectional area along the side wall of the heater reduced. This results in greater compression of the flow field along the side wall of the heater compared to that in the initial design of the reactor. Thus, higher flow speed along the height of the heater is encountered in the case of halving R_{gap}. At the outer radius of the substrate, a low density region in the flow may occur due to the flow being diverted by the 90° corner around the edge of the substrate. Hence, a faster speed in the gas flow

before reaching the corner results in lower density in the flow field after the turning which consequently results in lower AMOS near the edge of the substrate compared to other locations on the substrate surface.

The uniformity in the flow field near the substrate surface, however, was increased when L_{top} was halved or R_{gap} was doubled. Reducing L_{top} provides narrower space between the top wall of the reaction chamber and substrate surface which increase the frequency of the gas molecules being reflected between these two surfaces and enhance the flow field uniformity. Increasing R_{gap}, on the other hand, prevents the sudden increase of the flow speed along the side wall of the heater. This allows the gas molecules to diffuse in rather random manner which enhances the uniformity of the flow field.

8.3 Deposition on Concentric Cylinders in the 2nd Generation PP-CVD Reactor

8.3.1 Simulation Setup

The 2nd generation PP-CVD reactor is used to deposit titanium dioxide (TiO_2) film on two concentric cylinders as shown in Figure 8.8. The purpose of this simulation is to study the PP-CVD reactor flow field when a substrate with slightly complex geometrical configuration is considered. In all previous PP-CVD reactor flow field simulations, flow over a flat surface is considered. Those are external flow conditions. In this section, an internal flow along the passage

bounded between the two concentric cylinders is investigated. The second order directional decoupled axisymmetric QDS solver described in chapter 6 was used to simulate the flow field during the injection phase of the PP-CVD process conducted in the 2nd generation PP-CVD reactor with two concentric cylinders as substrate. Figure 8.9 shows the geometries of the computational domain used in the simulations. These dimensions are equivalent to the final design of the 2nd generation PP-CVD reactor of D. Lee at the Advanced Energy and Material Systems (AEMS) laboratory of University of Canterbury.

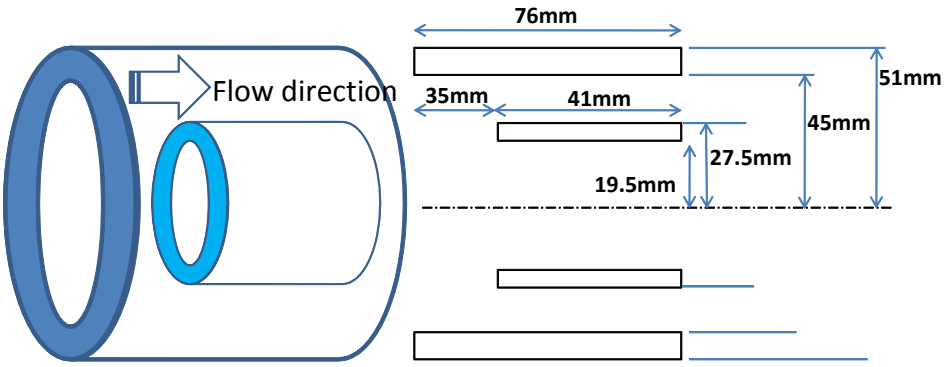

Figure 8.8 Schematic of the geometry for the two concentric cylinders.

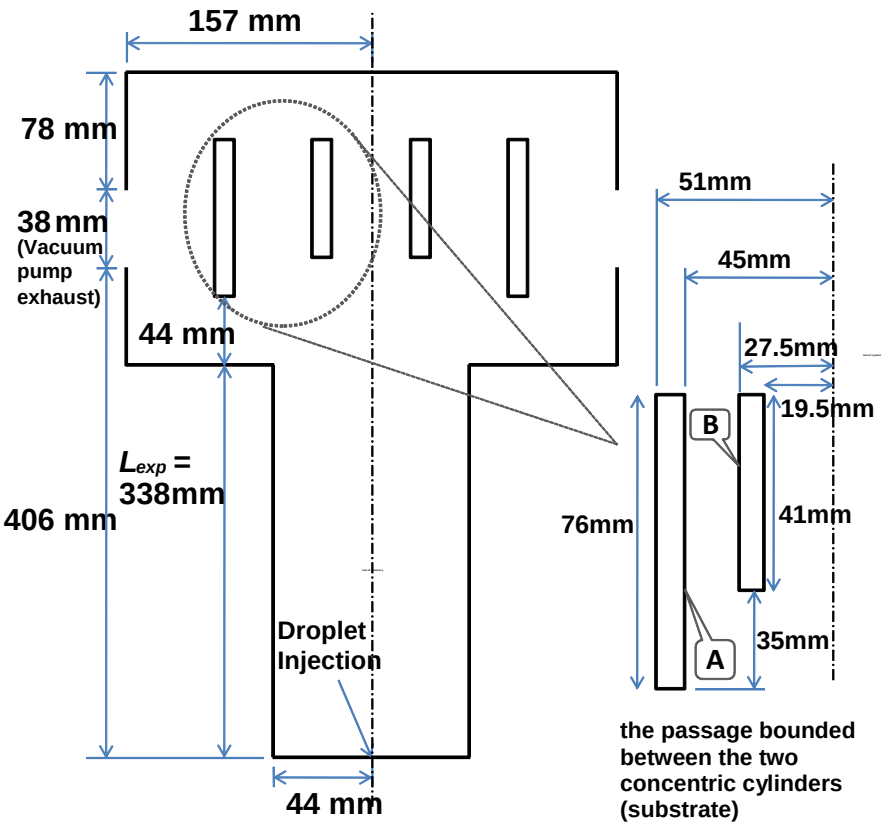

Figure 8.9 Schematic of the geometry of 2nd generation PP-CVD reactor and the position of the two concentric cylinders.

In this parametric study, Toluene with a ratio of specific heats of 1.089 and a gas constant of R = 90.2384 J/(kg·K) was chosen to be the simulation species. Representative droplets at temperature of 333 K with initial diameter and velocities determined stochastically based on a log-normal distribution of typical spray as described in chapter 7 was injected into the reactor. As learned from the study in section 8.2 above, a greater amount of precursor solution is recommended for the 2nd generation PP-CVD reactor to increase the deposition efficiency. However, at the current stage, the actual injection time and the amount of injected

precursor solution for the thin film deposition on the two concentric cylinders in the 2nd generation reactor are yet to be decided in the experimental work. Hence, in this parametric simulation, one droplet was injected at a chosen frequency together with a multiplication factor of 20 in order to allow a total amount of 43 μg of Toluene droplets to be supplied throughout the simulated 0.1 s of the injection phase. Note that for the same amount of injected droplets a shorter simulation time was used compared to that of the simulations in Section 8.2. This enables greater volume of precursor solution being injected throughout the 0.1 s simulation. This simulation time was chosen in order to perform feasible computation with a smaller grid size, which is 0.25 mm, compared to that used in Section 8.2.

The initial reactor flow field was stationary. The simulations were carried out on a desktop computer with 3.00GHz Intel Core 2 Duo CPU and 4GB of RAM using uniform Cartesian cells with 0.25 mm cell size. The smaller cell size was chosen compared to that used in Section 8.2 in order to reduce the numerical dissipation in the simulation results as described in section 6.5.3. Table 8.8 describes the simulation conditions used in this parametric study.

Table 8.8 Simulation conditions for the parametric study of deposition on two concentric cylinders in the 2nd generation PP-CVD reactor.

Initial Pressure, P_{min}	100 Pa
Initial Temperature, T_i	293 K
Injection time, t_i	0.1 s
Spatial accuracy	2nd order
QDS velocity bin, N	4 per coordinate direction
Simulation time step, Δt	variable time step with maximum CFL < 0.5
Slope limiter	MINMOD Difference
Reactor evacuation rate, Q_P	0.46 L/s
Median droplet diameter	18 μm
Mean droplet velocity	8 m/s
Maximum spray angle	6°

The goal of this study is to explore the effect of various operating conditions for the PP-CVD process to the flow field uniformity near the surfaces in the passage bounded between the two concentric cylinders. This was done by varying the amount of injected precursor solution, m_{inj}, and increasing the initial pressure of the reactor, P_{min}. Table 8.9 lists the change in the setup of each simulation case conducted in this study.

Table 8.9 Parametric simulations the parametric study of deposition on two concentric cylinders in the 2nd generation PP-CVD reactor.

	m_{inj}, μg	P_{min}, Pa	L_{exp}, mm	t_{inj}, s
Case 1: Current design	43	100	338	0.1
Case 2: Double m_{inj}	86	100	338	0.1
Case 3: 10x m_{inj}	430	100	338	0.1
Case 4: P_{min} = 1 kPa	43	1000	338	0.1

8.3.2 Results

Figure 8.10 shows the density contours plotted on a natural logarithm scale as the flow develops throughout the injection phase for the current reactor design (Case 1) as shown in Figure 8.9.

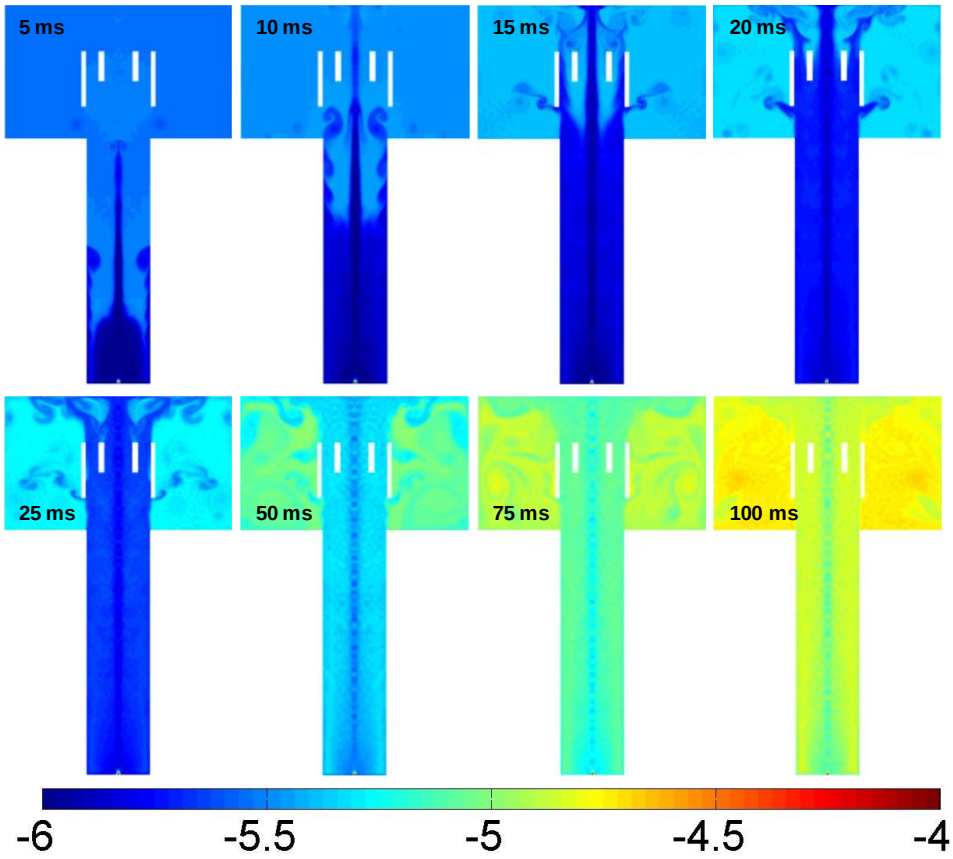

Figure 8.10 $\log_e$(density) [kg/m^3] contour of the flow field in the current design of the 2nd generation PP-CVD reactor with the two concentric cylinders in position during injection phase.

Comparing the results in Figure 8.10 to those of Figure 8.6, the results shown in Figure 8.10 demonstrates a flow field with more detailed flow phenomena. This may due to several reasons:

1. TD-QDS code is used in the simulations in Section 8.2 while DD-QDS code is used in Section 8.3. As discussed in Chapter 6, the numerical dissipation inherent in DD-QDS is slightly lower than that in TD-QDS. Hence, this enables a more detailed flow field dynamics to be captured.
2. The computational cell size used in Section 8.2 is 1 mm which is 4 times larger than the cell size used in Section 8.3. This could also attribute to lower numerical dissipation in the simulations in Section 8.3.
3. The total amount of injected precursor solution is much higher in the simulations in Section 8.3 compared to that of Section 8.2. This causes the concentration gradient between the inlet and outlet of the reactor increases significantly for the simulation in this section. As a result, the net transport of the precursor solution is faster which causes a jet-like flow structure to be seen in Figure 8.10.

Figure 8.11 shows the comparison of the relative increase in AMOS on surface A as indicated in Figure 8.9, between 5 ms and 0.1 s of the injection phase. Figure 8.12 shows the same relative increase in AMOS on surface B. As noted from Figure 8.10, the gas vapour is estimated to reach the substrate surface at about 5 ms.

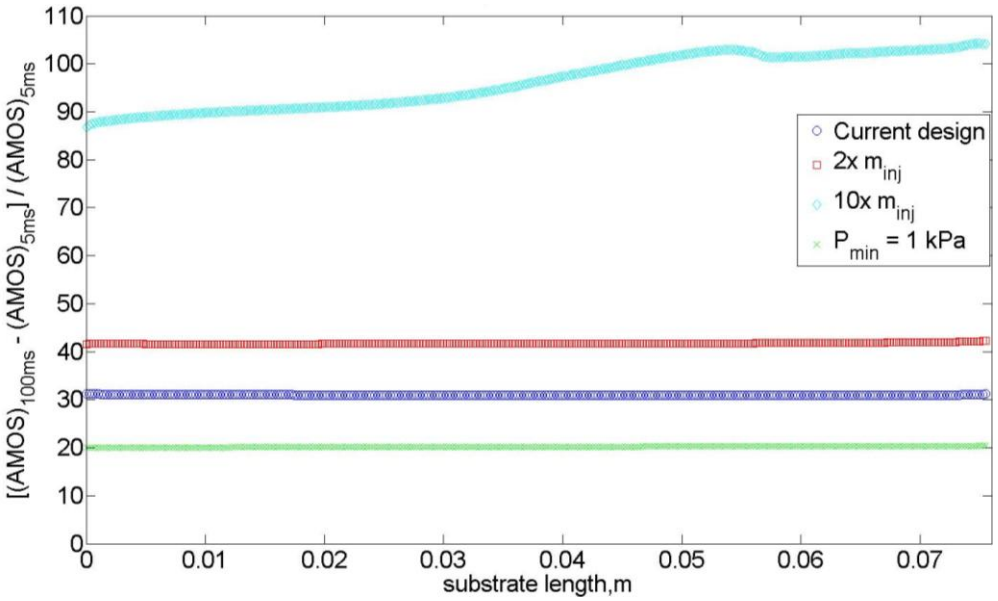

Figure 8.11 Increase in AMOS at surface A after 5 ms for the flow field in the 2nd generation PP-CVD reactor during injection phase.

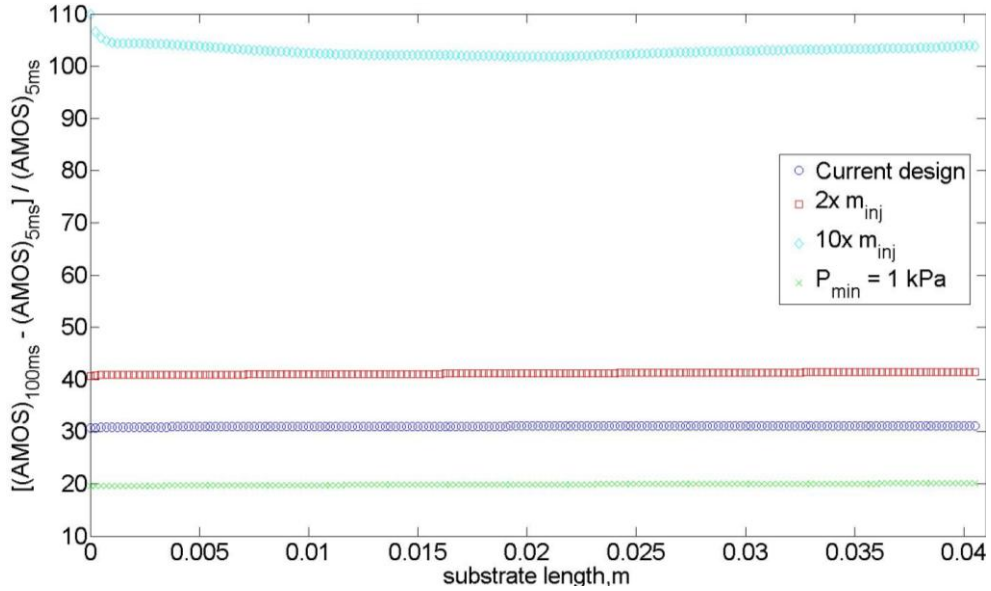

Figure 8.12 Increase in AMOS at surface B after 5 ms for the flow field in the 2nd generation PP-CVD reactor during injection phase.

Table 8.10 shows the uniformity in AMOS near surface A and B of the two concentric cylinders as indicated in Figure 8.8 during the injection phase.

Table 8.10 Flow field uniformity near substrate surface A and B of the two concentric cylinders for the 2nd generation PP-CVD reactor.

	Uniformity in AMOS, U_{AMOS}	
	Surface A	Surface B
Case 1: Current design	0.996944	0.998510
Case 2: Double m_{inj}	0.995214	0.998183
Case 3: 10x m_{inj}	0.989635	0.994720
Case 4: P_{min} = 1 kPa	0.996430	0.994235

8.3.3 Discussion

From Figure 8.10, it can be seen that the evaporated vapour propagates much faster along the length of the reactor compared to that of section 8.2. This can be interpreted from the increase in flow density in the reaction chamber as early as 5 ms, compared to the increase of the flow density in the same region occurs at about 0.1 s in Figure 8.6. This is mainly due to the greater number of droplets injected. Thus, higher flow density occurs near the nozzle inlet leading to higher pressure gradient across the length of the reactor, which consequently allows faster movement of the gas molecules in the direction towards the reaction chamber.

The gas molecules speed up in the expansion chamber upon reaching the reaction chamber where part of the flow expands and disperses into the reaction chamber. However, the main thrust of the flow continues to move along the length of the reaction chamber until reaching and being reflected by the top wall of the

reactor. The flow field near the passage surfaces was rather non-uniform when the flow first propagated to the passage of the two concentric cylinders at about 15 ms. However, the flow field within the passage soon became considerably uniform from 20 ms onwards. Non-uniformity in the flow field remained at the centre axis of the reactor throughout the injection phase due to the jet-like flow structure developed from the high flow field density at the inlet with relatively higher initial momentum. This suggests that substrate placement at the centre of the reaction chamber should be avoided. Despite of such non-uniformity at the centre axis of the reactor, the flow field within the passage of the two concentric cylinders is considered uniform throughout the injection phase.

From Figure 8.11 and 8.12, the increase in AMOS at both surfaces A and B illustrate that flow field uniformity is achievable if the injected mass is doubled but non-uniformity in the flow field increased noticeably if the injected mass was increased tenfold. This has further been shown from the uniformity in AMOS calculated and tabulated in Table 8.10 in which uniformity in AMOS decreases as the amount of injected mass increases. By increasing the injected mass significantly, the concentration gradient between the inlet and outlet of the reactor increases. This results in higher transport rate of the molecules in the direction along the reactor height due to diffusion. This reduces the “mixing” time of the gas in the expansion chamber to diffuse into a uniform flow field. Besides, due to the increase in the injected mass, the overall pressure in the reactor volume increases swiftly. As a result, the pressure gradient between the reactor centre and

the outer radius of the reactor reduces in time. Hence, the degree of flow expansion decreases in time due to the bulk acceleration of the gas in radial direction decreases. Consequently, the gas was unable to expand uniformly before reaching the reaction chamber.

The uniformity in AMOS is also decreases slightly when the initial reactor pressure P_{min} was increased from 100 to 1000 Pa. This is because the pressure gradient between the inlet and outlet of the reactor, which is the main driving force of the flow field, decreases as the initial reactor pressure is being raised. This confirms the observation from the experimental deposition and emphasises the advantage of conducting PP-CVD process at low pressure, usually between 100 to 1000 Pa based on the experience in the experiments.

9 Further Improvement in the Current QDS Scheme

This thesis concentrates on developing an efficient and economical numerical tool for modelling PP-CVD flow field in the reactor. The computational time comparisons for the validation cases in Chapter 5 and 6 demonstrate that QDS could be considered a much faster numerical scheme compared to other solvers such as the Euler equations solver, the kinetic theory based EFM solver and the particle based Parallel Direction Simulation Monte Carlo code (PDSC). The simulation results presented promise that QDS is capable to provide rapid approximation of the PP-CVD flow field. Hence, the main objective of this project has been met.

However, there are two features of the QDS scheme that limits its accuracy in simulating low Mach number flow or highly rarefied flow. As mentioned in Chapter 6, the first issue in QDS is the inherent numerical viscosity in the scheme. The second issue in QDS is related to the assumption of local thermal equilibrium within the computational cell which may cause sizeable inaccuracy in the solution for high Knudsen number flow, as checked in both Chapter 5 and 6. In this chapter, further improvement of the current QDS scheme is discussed focusing mainly on overcoming the two inherent problems in the QDS scheme.

9.1 Collisions en route in QDS flux

In both true directional and directional decoupled QDS scheme discussed in Chapter 5 and 6, respectively, the free movement phase and collision phase of the gas molecules are separated. It is generally known that collision between gas molecules makes their velocity tend towards the average. When the gas molecules traverses between the computational cells without collision, the lack of reduction in the gas molecules' speed enables greater than the physically correct amount of QDS flux to be transported from a source cell to the destination cell. This results in excessive momentum and energy to be transported which leads to high numerical dissipation spanwise which is related to the high value of scheme viscosity.

A simple collision en route (CER) model has been proposed to consider the effect of intermolecular collision during the free movement phase of the gas molecules in QDS (Jermy, et al., 2010). In this model, the movement phase of the molecules in i velocity bin of the QDS scheme is considered. The retardation of the molecular velocity in i velocity bin due to intermolecular collision with molecules in $i \neq j$ velocity bin are computed based on the assumptions below:

1. Each coordinate direction is treated independently.
2. Hard sphere model is considered in collision step.
3. The intermolecular collisions are wholly elastic and one-dimensional.

4. Collisions in the destination cell are neglected since Maxwell-Boltzmann velocity distribution is forced in the destination cell in which infinite collisions are assumed.
5. The number density and bulk velocity do not change during a computational time step, Δt.
6. The speeds of the collision partners after the collision are the same.

Based on these assumptions, the average number of collision, ϕ_{ij}, between molecules in i velocity bin at speed v_i and molecules in j velocity bin at speed v_j, in a time step Δt can be determined by Equation (9.1) give as:

$$\phi_{ij} = n_j \sigma_{ij} \left| v_i - v_j \right| \Delta t \tag{9.1}$$

where n_i is the number density of molecules in i velocity bin and σ_{ij} is the collision cross section given in equation (9.2) as:

$$\sigma_{ij} = \frac{\pi d^2}{4} \tag{9.2}$$

where d is the effective hard sphere molecular diameter. Considering the intermolecular collision of molecules in i velocity bin with molecules in all other N velocity bins used in the QDS scheme, the average intermolecular collisions experienced by molecules in i velocity bin, ϕ_i, can be expressed by Equation (9.3) as:

$$\phi_i = \sum_{j=1}^{N} \left| v_i - v_j \right| n_j \frac{\pi d_2}{4} \Delta t \tag{9.3}$$

In QDS, the number density of molecules in the j velocity bin, n_j, can be expressed in term of the weights of the Gaussian quadrature, w_j, as given in Equation (9.4) as:

$$n_j = n\frac{w_j}{\sqrt{\pi}} \tag{9.4}$$

Hence, Equation (9.3) can be rewritten in Equation (9.5) as:

$$\begin{aligned}\phi_i &= \sum_{j=1}^{N}\left|v_i - v_j\right| n\frac{w_j}{\sqrt{\pi}}\frac{\pi d^2}{4}\Delta t \\ &= n\Delta t\frac{\pi d^2}{4}\left|v_i\sum_{j=1}^{N}\frac{w_j}{\sqrt{\pi}} - \sum_{j=1}^{N}v_j\frac{w_j}{\sqrt{\pi}}\right| \\ &= n\Delta t\frac{\pi d^2}{4}\left|v_i - \bar{u}\right|\end{aligned} \tag{9.5}$$

where $\bar{u}$ is the mean velocity of the cell.

The speed of the molecules in the i velocity bin is then determined. By applying the conservation of momentum of the collision partner during the collision and assumption 6 as above, the post-collision speed of molecules in i velocity bin, $v_{i,post,1}$ after one collision is given in Equation (9.6) as:

$$v_{i,post,1} = \frac{v_{i,pre} + \bar{u}}{2} \tag{9.6}$$

where $v_{i,pre}$ is the speed of molecules in i velocity bin before the collision. By recurring application of Equation (9.6), the speed of molecules in i velocity bin after ϕ_i collisions is given in Equation (9.7) as:

$$v_{i,post,\phi_i} = \frac{v_{i,pre}}{2^{\phi_i}} + \bar{u}\left(1 - \frac{1}{2^{\phi_i}}\right) \tag{9.7}$$

A preliminary implementation of the CER model into QDS code was checked by solving a 2D channel flow (Jermy, et al., 2010). The second order 2D QDS scheme with N = 3 velocity bin in each coordinate direction was used to study the effect of CER model. The MC slope limiter was used for properties gradients calculation. Uniform Cartesian grid was used to model the flow domain in a 1 m × 1 m channel. The gas is ideal with gas constant R = 1.0 J/(kg·K) and the ratio of specific heats is 5/3. The simulation time step was reset after each time step to maintain CFL < 0.1. The bounce-back boundary condition was used to implement non-slip wall boundary condition at the upper and lower wall boundaries by using ghost cells. The inflow and outflow boundaries are periodic. The flow is stationary initially. In each time step, the speed in each velocity bin is incremented by an amount equivalent to the acceleration induced by a pressure gradient of -0.01 Pa/m.

Figure 9.1 shows the comparisons of the simulation results for the basic QDS scheme and QDS schemes with CER model implementation using molecular diameter of 2.5×10^{-12} m and two fixed collision number of ϕ_i = 0.5 and ϕ_i = 2.0. With molecular diameter of 2.5×10^{-12} m, the collision number, ϕ_i, is about 0.2. Two larger collision numbers of ϕ_i = 0.5 and ϕ_i = 2.0 were chosen to test the implementation of the CER model. It can be seen in Figure 9.1 that the numerical viscosity was clearly reduced with the increase of collision number.

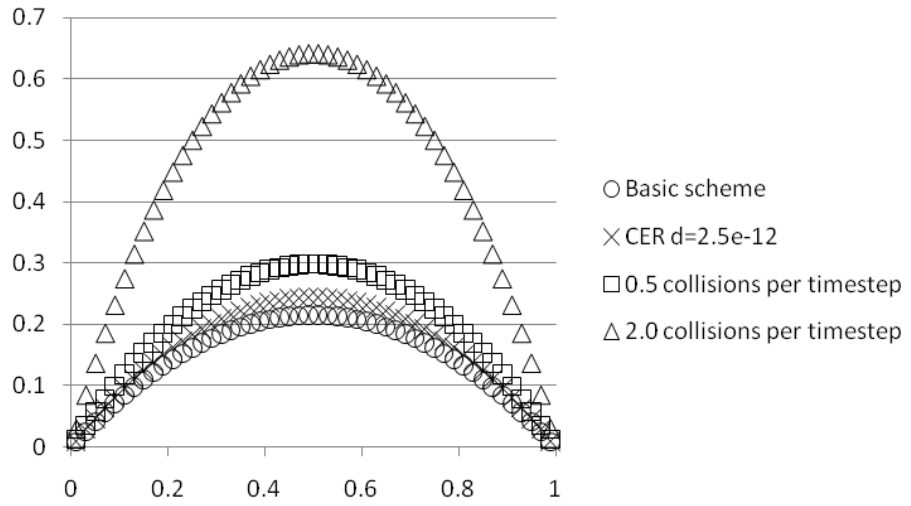

Figure 9.1 2D channel flow simulated by QDS with basic and CER schemes (Jermy, et al., 2010).

The CER model proposed attempts to reduce the numerical dissipation in the current QDS scheme by imposing collision during the flight of the molecules. However, the CER model at its present form is flawed.

First, the assumption of both collision partners will have the same speed after collision is questionable. Consider a single species analysis, the molecular masses of the collision partners are the same. By applying the conservation of momentum and kinetic energy throughout the collision, the two collision partners will exchange velocity after the collision if the intermolecular collisions are assumed to be elastic and one-dimensional. If the collision is in two dimensional, the post-collision velocities depend on the angle of deflection during the collision. Therefore, the post-collision velocities for the molecules are in most cases not the same.

Second, there is a problem in Equation (9.7) when the number of collisions between molecules is large. The denominator of the first and third terms in Equation (9.7) considers taking 2 to the power of ϕ_i. When the number of collision, ϕ_i, is larger, for example $\phi_i > 10$, post-collision speed of molecules in i velocity bin will reach to the value of the bulk velocity. This results in the velocity distribution within the computational cell collapses to a single peak at bulk velocity with zero variance. This is essentially equivalent to the local temperature of 0 K. Such instant cooling in the gas molecules is illogical. Hence the present CER model encounters instability when there are many intermolecular collisions.

Although the proposed CER model is based on several questionable assumptions, the model serves its purpose in demonstrating the principle of collision during the flight of the gas molecules. Further work on addressing the collision en route effect in the QDS scheme is expected to improve the quantitative accuracy of the scheme.

9.2 Hybridisation of QDS-BGK solver

Theoretically, the assumption of local thermal equilibrium is not valid in realistic engineering problem. There is always existence of shear and heat stresses that cause thermal non-equilibrium amongst gas molecules. Thus, the fluxes in QDS scheme obtained by discretising the Maxwell-Boltzmann equilibrium distribution function do not accurately represent the physical fluxes. In the flow region where the molecular mean free path is small, the number of intermolecular collisions is

high enough to promote energy exchange between molecules. This enables the molecules to relax closely to thermal equilibrium condition and hence the gas molecules can be treated in thermal equilibrium with negligible inaccuracy. However, in highly rarefied flow where the mean free path is large, the intermolecular collision is rare. The error of treating a thermal non-equilibrium condition with thermal equilibrium assumption becomes significant. The limit of the thermal equilibrium assumption in simulating PP-CVD flow has been investigated and discussed in Chapter 5 and 6.

To simulate thermal non-equilibrium flow, direct simulation solver such as DSMC which has been discussed in Chapter 3 is one of the excellent methods. However, regardless of recent advances, DSMC is computationally expensive and associated with large amount of statistical scatter in the results.

Another approach to handle thermal non-equilibrium flow is by solving the Boltzmann equation. Due to the complexity in solving the collision term of the Boltzmann equation, the popular BGK collision model as discussed in Chapter 3 is usually used to replace the collision term of the Boltzmann equation by simpler source term. This leads to the gas-kinetic BGK scheme developed by Xu *et al.* (Xu, 1998; Xu, 2000; Xu, 2001; Xu, Kim, Martinelli, & Jameson, 1996; Xu & Prendergast, 1994). The BGK scheme solves the time-dependent gas evolution equation at the cell interfaces and then performing the relaxation within each time step. Unfortunately, such BGK solver requires a significant amount of computational power due to the requirement of solving the complex evolution

equations over the entire range of molecular velocities at each step of the solution. The requirement in calculating the Maxwell-Boltzmann distribution function at cell interfaces which involves evaluation of error functions also incurs expensive computational cost.

In order to preserve the computational speed gained by using QDS method in simulating PP-CVD flow while extending the scheme capability of solving flow field with wide range of Knudsen number, a hybrid QDS-BGK scheme is proposed. The nature of using conserved properties in flux reconstruction in both QDS and BGK allows easy fluxes transfer between both schemes in the hybridisation implementation. In fact, the BGK scheme can be implemented in directional decoupled approach and perform fluxes reconstruction at the cell interfaces. This is well-suited to be hybridised with the directional decoupled QDS scheme in which fluxes reconstruction is conducted at cell interfaces as well.

9.2.1 BGK Model

The detailed description and derivations of the BGK scheme can be found in the report by Xu (Xu, 1998, 2001), only the brief overview of the implementation and key equations are described in this section. The starting point of the BGK scheme is applying the BGK collision model to the Boltzmann equation. The BGK equation is then obtained. The BGK equation in the *x*-direction is given in Equation (9.8) as:

$$\frac{\partial f}{\partial t} + u\frac{\partial f}{\partial x} = \frac{g - f}{\tau} \tag{9.8}$$

where f the gas distribution function and g is the equilibrium state of f which can be represented by the Maxwell-Boltzmann equilibrium distribution as given in Equation (3.19). Both f and g are functions of space, x, time, t, molecular velocities, u and v, and internal variable ξ. The intermolecular collision time, τ, is related to the viscosity and heat conduction coefficients. The relation of the conserved properties, which are the density, ρ, momentum, p_x and p_y, and energy, E, with the distribution function f is given in Equation (9.9) as:

$$\begin{pmatrix} \rho \\ p_x \\ p_y \\ E \end{pmatrix} = \int \psi_\alpha f \, du dv d\xi, \qquad \alpha = 1,2,3,4 \tag{9.9}$$

where ψ_α is the component of the vector of the moments given in Equation (9.10) as:

$$\begin{pmatrix} \psi_1 \\ \psi_2 \\ \psi_3 \\ \psi_4 \end{pmatrix} = \begin{pmatrix} 1 \\ u \\ v \\ \frac{1}{2}\left(u^2 + v^2 + \xi^2\right) \end{pmatrix} \tag{9.10}$$

The general solution of the BGK equation at a cell interface, $x_{j+½}$, and time, t, is given in Equation (9.11) as:

$$\begin{aligned} f\left(x_{j+1/2}, t, u, v, \xi\right) = \frac{1}{\tau}\int_0^t g\left(x', t', u, v, \xi\right) e^{-(t-t')/\tau} dt' \\ + e^{-t/\tau} f_0\left(x_{j+1/2} - ut\right) \end{aligned} \tag{9.11}$$

where $x' = x_{j+½} - u(t - t')$ is the trajectory of a molecule's motion and f_0 is the initial gas distribution function f at the beginning of each time step, which is written in Equation (9.12) as:

$$f_0 = \begin{cases} g_l\left[1 + a_l x - \tau\left(a_l + A_l\right)\right], & x \le 0 \\ g_r\left[1 + a_r x - \tau\left(a_r + A_r\right)\right], & x \ge 0 \end{cases} \tag{9.12}$$

where the subscript l and r denotes the left and right hand side of the cell interface, respectively. The equilibrium state g is given in Equation (9.13) as:

$$\begin{aligned} g = g_0\Bigg[1 + \left(1 - H\left(x - x_{j+1/2}\right)\right)\bar{a}_l\left(x - x_{j+1/2}\right) \\ + H\left(x - x_{j+1/2}\right)\bar{a}_r\left(x - x_{j+1/2}\right) + \bar{A}t\Bigg] \end{aligned} \tag{9.13}$$

where g_0 is the local Maxwell-Boltzmann distribution function at the cell interface and $H(x)$ is the Heaviside function defined in Equation (9.14) as:

$$H(x) = \begin{cases} 0, & x < 0 \\ 1, & x \ge 0 \end{cases} \tag{9.14}$$

All the corresponding spatial (a_l, a_r, $\bar{a}_l$, $\bar{a}_r$) and temporal (A_l, A_r, $\bar{A}$) slopes have the general form given in Equation (9.15) as:

$$a = a_1 + a_2 u + a_3 \frac{1}{2}\left(u^2 + \xi^2\right) \tag{9.15}$$

In Equation (9.12), g_l and g_r are the local Maxwell-Boltzmann distribution functions located to the left and right of the cell interface, respectively. With the definition of the Maxwell-Boltzmann distributions, it can be expressed in Equation (9.16) that:

$$g_l = \rho_l \left(\frac{\lambda_l}{\pi} \right)^{\frac{K+2}{2}} e^{-\lambda_l \left[(u-U_l)^2 + \xi^2 \right]}$$
$$g_r = \rho_r \left(\frac{\lambda_r}{\pi} \right)^{\frac{K+2}{2}} e^{-\lambda_r \left[(u-U_r)^2 + \xi^2 \right]} \qquad (9.16)$$

where K is the total number of degrees of freedom, λ is related to the gas temperature $m/2kT$ and k is the Boltzmann constant. The parameters on the right hand side of Equation (9.16) can be determined from the values of the conserved properties at the cell interface. The parameters corresponding to g_l is evaluated using conserved properties reconstructed from cell j and given in Equation (9.17) as:

$$\rho_j = \overline{\rho}_j (x_{j+1/2})$$
$$U_j = \overline{U}_j (x_{j+1/2}) \qquad (9.17)$$
$$\lambda_j = \frac{(K+1)\overline{\rho}_j (x_{j+1/2})}{4\left[\overline{\rho}_j \overline{\varepsilon}_j (x_{j+1/2}) - \frac{1}{2} \overline{\rho}_j \overline{U}_j^2 (x_{j+1/2}) \right]}$$

while the parameters corresponding to g_r is evaluated using conserved properties reconstructed from cell $j+1$ in similar manner.

The reconstructed conserved properties (density, momentum and energy) are denoted by $\overline{W}_j (x_{j+1/2})$ by for values interpolated from the left side of the interface $x_{j+½}$ while $\overline{W}_{j+1} (x_{j+1/2})$ for values interpolated from the right side of the interface. In second order BGK method, the reconstruction is performed using

flux limiter $L\left(s_j^+, s_j^-\right)$. For example, the van Leer limiter (Van Leer, 1977) is given in Equation (9.18) as:

$$L\left(s_j^+, s_j^-\right) = S\left(s_j^+, s_j^-\right)\frac{2\left|s_j^+\right\|s_j^-\right|}{\left|s_j^+\right| + \left|s_j^-\right|} \tag{9.18}$$

where $S\left(s_j^+, s_j^-\right) = sign\left(s_j^+\right) + sign\left(s_j^-\right)$ and the property gradients are given in Equations (9.19) as:

$$\begin{aligned} s_j^+ &= \left(W_{j+1} - W_j\right)/\Delta x \\ s_j^- &= \left(W_j - W_{j-1}\right)/\Delta x \end{aligned} \tag{9.19}$$

where W_j are the values of conserved properties at cell j and Δx is the grid spacing. Hence, after reconstruction, the interpolated values of conserved properties at the cell interface are given in Equation (9.20) as:

$$\begin{aligned} \overline{W}_j\left(x_{j+1/2}\right) &= W_j + \frac{1}{2}L\left(s_j^+, s_j^-\right)\Delta x \\ \overline{W}_{j+1}\left(x_{j+1/2}\right) &= W_{j+1} - \frac{1}{2}L\left(s_{j+1}^+, s_{j+1}^-\right)\Delta x \end{aligned} \tag{9.20}$$

Next, the spatial slope, a_l, can be determined by using Equation (9.15) and Equation (9.21) given below as:

$$\frac{1}{\rho_l}\begin{pmatrix} \dfrac{\overline{\rho}_j\left(x_{j+1/2}\right) - \overline{\rho}_j\left(x_j\right)}{\Delta x^-} \\ \dfrac{\overline{\rho}_j\overline{U}_j\left(x_{j+1/2}\right) - \overline{\rho}_j\overline{U}_j\left(x_j\right)}{\Delta x^-} \\ \dfrac{\overline{\rho}_j\overline{\varepsilon}_j\left(x_{j+1/2}\right) - \overline{\rho}_j\overline{\varepsilon}_j\left(x_j\right)}{\Delta x^-} \end{pmatrix} = M_{\alpha\beta}^l\begin{pmatrix} a_{1l} \\ a_{2l} \\ a_{3l} \end{pmatrix} \tag{9.21}$$

where the matrix $M^{l}_{\alpha\beta}$ has the form given in Equation (9.22) as:

$$M^{l}_{\alpha\beta} = \begin{pmatrix} 1 & U_l & \frac{1}{2}\left(U_l^2 + \frac{K+1}{2\lambda_l}\right) \\ U_l & U_l^2 + \frac{1}{2\lambda_l} & X \\ U_l^2 + \frac{K+1}{2\lambda_l} & X & Y \end{pmatrix} \tag{9.22}$$

where

$$X = \frac{1}{2}\left(U_l^3 + \frac{(K+3)U_l}{2\lambda_l}\right)$$

$$Y = \frac{1}{4}\left(U_l^4 + \frac{(K+3)U_l^2}{\lambda_l} + \frac{(K^2+4K+3)}{4\lambda_l^2}\right)$$

The slope on the right side of the cell interface, a_r, can also be evaluated in similar manner using properties from cell *j+1*.

In equation (9.12), $\tau(a_l u + A_l)$ and $\tau(a_r u + A_r)$ are the terms that accounts for the deviation of a distribution function away from a Maxwell-Boltzmann distribution in solving thermal non-equilibrium problem. A_l and A_r can be determined from Equation (9.23) given as:

$$\begin{aligned} M^{l}_{\alpha\chi} A_{\beta l} &= -\frac{1}{\rho_l}\int g_l a_l u \psi_\alpha du d\xi \\ M^{r}_{\alpha\chi} A_{\beta r} &= -\frac{1}{\rho_r}\int g_r a_r u \psi_\alpha du d\xi \end{aligned} \tag{9.23}$$

The equilibrium state, g_0, at the cell interface found in Equation (9.13) is given in Equation (9.24) as:

$$g_0 = \rho_0 \left(\frac{\lambda_0}{\pi} \right)^{\frac{K+2}{2}} e^{-\lambda_0 \left[(u-U_0)^2 + \xi^2 \right]} \tag{9.24}$$

where the moments are given in Equation (9.25) as:

$$\begin{aligned}
\rho_0 &= \rho_l \frac{1}{2} erfc\left(-\sqrt{\lambda} U \right) + \rho_r \frac{1}{2} erfc\left(\sqrt{\lambda} U \right) \\
\rho_0 U_0 &= \rho_l \left[U \frac{1}{2} erfc\left(-\sqrt{\lambda} U \right) + \frac{1}{2} \frac{e^{-\lambda U^2}}{\sqrt{\pi \lambda}} \right] \\
&\quad + \rho_r U \left[\frac{1}{2} erfc\left(\sqrt{\lambda} U \right) + \frac{1}{2} \frac{e^{-\lambda U^2}}{\sqrt{\pi \lambda}} \right] \\
\lambda_0 &= \frac{(K+2)\rho_0}{\left[4\left(E_0 - \frac{1}{2} \left((\rho_0 U_0)^2 \right) \Big/ \rho_0 \right) \right]}
\end{aligned} \tag{9.25}$$

The slope, $\bar{a}_l$ and $\bar{a}_r$, of g can then be found using the general form in Equation (9.15) and through the relation in Equation (9.26) as:

$$\frac{1}{\rho_0} \begin{pmatrix} \dfrac{\rho_0 - \bar{\rho}_j(x_j)}{\Delta x^-} \\ \dfrac{\rho_0 U_0 - \bar{\rho}_j \bar{U}_j(x_j)}{\Delta x^-} \\ \dfrac{\rho_0 \varepsilon_0 - \bar{\rho}_j \bar{\varepsilon}_j(x_j)}{\Delta x^-} \end{pmatrix} = M^0_{\alpha\beta} \begin{pmatrix} \bar{a}_{1l} \\ \bar{a}_{2l} \\ \bar{a}_{3l} \end{pmatrix} \tag{9.26}$$

where the matrix $M^0_{\alpha\beta}$ can be determined in similar manner as in Equation (9.22) using U_0 while $\bar{a}_r$ is calculated similarly using conserved properties evaluated at x_{j+1}. Lastly, the temporal slope, $\bar{A}$, is computed using Equation (9.27) as:

$$
\begin{aligned}
M^{0}_{\alpha\beta}\bar{A}_{\beta} = \frac{1}{\rho_0}\int \psi_{\alpha}\big[\ & \gamma_1 g_0 + \gamma_2 u\left(\bar{a}_l H[u] + \bar{a}_r\left(1 - H[u]\right)\right) g_0 \\
& + \gamma_3\left(g_l H[u] + g_r\left(1 - H[u]\right)\right) \\
& + \gamma_4 u\left(a_l H[u] g_l + a_r\left(1 - H[u]\right) g_r\right) \\
& + \gamma_5\left(\left(a_l u + A_l\right) H[u] g_l\right. \\
& \left. + \left(a_r u + A_r\right)\left(1 - H[u]\right) g_r\right)\big] du\, d\xi
\end{aligned}
\tag{9.27}
$$

where

$$
\begin{aligned}
\gamma_0 &= \Delta t - \tau\left(1 - e^{-\Delta t/\tau}\right) \\
\gamma_1 &= -\left(1 - e^{-\Delta t/\tau}\right)\Big/\gamma_0 \\
\gamma_2 &= \left(-\Delta t + 2\tau\left(1 - e^{-\Delta t/\tau}\right) - \Delta t e^{-\Delta t/\tau}\right)\Big/\gamma_0 \\
\gamma_3 &= \left(1 - e^{-\Delta t/\tau}\right)\Big/\gamma_0 \\
\gamma_4 &= \left(\Delta t e^{-\Delta t/\tau} - \tau\left(1 - e^{-\Delta t/\tau}\right)\right)\Big/\gamma_0 \\
\gamma_5 &= \tau\left(1 - e^{-\Delta t/\tau}\right)\Big/\gamma_0
\end{aligned}
$$

The collision time, τ, has the form given in Equation (9.28) as;

$$
\tau = \frac{\mu(W_0)}{P(W_0)} + \frac{\left|\rho_l/\lambda_l - \rho_r/\lambda_r\right|}{\left|\rho_l/\lambda_l + \rho_r/\lambda_r\right|}\Delta t \tag{9.28}
$$

Finally, the time dependent numerical fluxes in *x*-direction across all cell interfaces can be computed using Equation (9.29) as:

$$
\begin{pmatrix} F_{\rho} \\ F_{\rho U} \\ F_{\rho\varepsilon} \end{pmatrix} = \int u \begin{pmatrix} 1 \\ u \\ \frac{1}{2}\left(u^2 + \xi^2\right) \end{pmatrix} f\left(x_{j+1/2}, t, u, \xi\right) du d\xi \tag{9.29}
$$

By integrating Equation (9.29), the total density, momentum and energy transport are computed over a time step.

9.2.2 Hybridisation of QDS-BGK solver

Since the flux reconstruction is carried out at the cell interfaces in both directional decoupled QDS (DD-QDS) and BGK model described above, the hybrid implementation of QDS-BGK solver is straight forward. What is more, both models use the conserved properties to compute the time dependent fluxes. Hence, the flux transfer between both solvers has little problem. The QDS fluxes are employed in regions of thermal equilibrium while the BGK model is employed to compute fluxes in thermal non-equilibrium regions. To distinguish the regions, the gradient length local Knudsen number, Kn_{GLL}, given in Equation (4.4) can be used. Using criterion for continuum breakdown proposed by Boyd (Boyd, *et al.*, 1995) where $Kn_{GLL} > 0.05$, the BGK solver is employed.

The computational efficiency of the hybrid QDS-BGK solver is expected to decrease due to the extensive computation involve in BGK solver. However, the numerical accuracy can be promisingly increased. Hence, an appropriate weight up between the simulation time and improvement in accuracy should be conducted in the hybrid QDS-BGK simulation. This is important to justify the solver feasibility to remain as a rapid simulation tool for PP-CVD reactor design in various industrial applications.

10 Conclusion

In the present work, the axisymmetric, second-order QDS scheme has been tested for its suitability as a numerical tool to provide rapid approximation of the PP-CVD flow field. The simulations of the highly unsteady low pressure flow field encountered in the PP-CVD process demonstrate QDS's capability in producing a good approximation of such complex flow field. The simulations also show excellent computational efficiency of the QDS method compared to the previous attempt using DSMC method. The validity of the local equilibrium assumption used in QDS method has been tested extensively. The time taken to establish and dissipate the quasi-steady jet structure in the PP-CVD reactor has been determined.

From the thorough review of various numerical tools, a selection of the most feasible numerical solver to perform rapid simulation of PP-CVD flow field has been made. A rapid simulation tools is required for the purpose of reactor design in order to meet various industrial applications. A slight modification of the existing reactor design or deposition operating condition is usually required for different substrate or precursor material. In order to comply with the various industrial applications within limited time allowance, a fast approximated solution of the PP-CVD flow field at acceptable accuracy is essential. The current QDS solver has shown its capability of providing acceptable PP-CVD flow field simulation results within days.

The development of QDS method in modelling the gas phase transport phenomena in the PP-CVD reactor volume has been conducted. The basic true-

directional QDS (TD-QDS) algorithm was modified for simulating PP-CVD flow field. Moreover, an algorithm based on the directional decoupled QDS (DD-QDS) method was coded to simulate PP-CVD flow field with the expectation of reducing numerical dissipation in the QDS scheme. Validations of both TD-QDS and DD-QDS solvers to various test cases in both two dimensional and axisymmetric were performed.

From the simulations of the flow field in the PP-CVD reactor with gas precursor solution injection, the flow field develops into a quasi-steady state after the first 4 ms in the 1 s injection phase. The flow stays in quasi-steady state for about 99.6% of the remaining injection time. The quasi-steady jet dissipates within 0.5 ms of the end of injection. This information is essential for the design of PP-CVD reactors and operating cycles. Additionally, the simulation results show that the technique of pulsed injection of precursor solution into a continuously evacuated reactor in the PP-CVD process will produce uniform flow field within the reactor. Such uniform flow field is desired to promote uniform thin film deposition.

A liquid droplet flash evaporation model has been developed to model liquid precursor solution evaporation in the PP-CVD reactor with liquid precursor solution injection. The liquid droplet flash evaporation model serves to provide a rather realistic inlet condition to the QDS solver that simulates the gas phase of the PP-CVD flow field. From the simulations of the flow field in the PP-CVD

reactor with liquid precursor solution injection, the flow field becomes considerably uniform after about 60 mm from the reactor inlet.

The gradient length local Knudsen number based on density, $(Kn_{GLL})_\rho$, and the average number of intermolecular collision per computational cell per time step are used to identify the limit of QDS method in simulating PP-CVD flow. It is found that the simulation results are considered acceptably valid for low pressure flows at 400 Pa or above with $(Kn_{GLL})_\rho \leq 1.857\times10^{-7}$ or $Kn \leq 0.00164$. It is thought that most of the PP-CVD processes operate at base pressure higher that 400 Pa. Hence, the existing QDS solver is concluded to be able to simulate PP-CVD flow field at acceptable accuracy. However, caution should be taken during result interpretation for future simulations with reactor pressure lower than 400 Pa.

The simulation results also show that the flow field uniformities (a percentage variation in AMOS) in the few variants of the PP-CVD reactor geometry are above 96%. Such uniformity in the flow field is deemed acceptable in producing uniform thin film deposition on the substrate. Hence, it is claimed that the flow field uniformity is insensitive to the few variants of the reactor geometry configuration tested. It should also be noted that this conclusion is limited due to the small number of reactor configurations modelled. Provided there is sufficient distance between the substrate location and the reactor inlet, a uniform flow field is achievable on the substrate surface. It is however observed that higher flow field uniformity can be achieved with a lower reactor base pressure.

11 Future Work

In this thesis, the current QDS solver handles wall boundaries which are parallel to the Cartesian grid used only. However, in PP-CVD, depositions on object with complex geometries such as airfoil or synthetic bones for body repairing implants are often required. Therefore, the extension of the present QDS solver to model computational domain with irregular shaped wall boundaries will very much improve the applicability of the solver.

In this chapter, the continued development of QDS is discussed focusing mainly on extending the current QDS scheme to handle flow boundaries with complex geometries. This enhances the QDS solver to be one of the practical simulation tools in facilitating the design of PP-CVD reactor and operational conditions for various industrial deposition applications.

11.1 Modelling of Flow Field with Complex Geometry

One of the advantages in QDS solver is its simplicity in computational mesh generation. The complicated mesh generation using commercial meshing software is not required. Instead, uniform Cartesian grid with wall boundary aligned to the computational grid is used. This feature enables excellent simulation efficiency. In order to maintain such simplicity while extending the solver's capability to model arbitrary complex geometries, a simple yet efficient grid generation technique is desired.

One of the flexible and efficient alternatives to the conventional boundary fitted mesh generation method is the Cartesian cut cell approach (Causon, Ingram, Mingham, Yang, & Pearson, 2000; Ingram, Causon, & Mingham, 2003). In the Cartesian cut cell method, solid regions of the wall boundaries are cut out of the background Cartesian mesh. Special treatment of these cut cells is applied while the remaining flow field cells are simulated as normal. Flux balance along the cut edges of a cut cell is computed using finite volume approach. Hence, this method is well suited for flow solvers that utilise split flux method such as the directional decoupled QDS.

11.1.1 Cartesian cut cell method

In the cut cell method, the wall boundaries are represented by polylines with a set of data points defined in an anti-clockwise direction. The intersections of a polyline with the Cartesian grid are used to determine the location of the cut cells that have the sides coincident with the boundary segment. Consider a line segment as shown in Figure 11.1 with (x_s, y_s) and (x_e, y_e) as the start and end coordinates of the line segment, respectively.

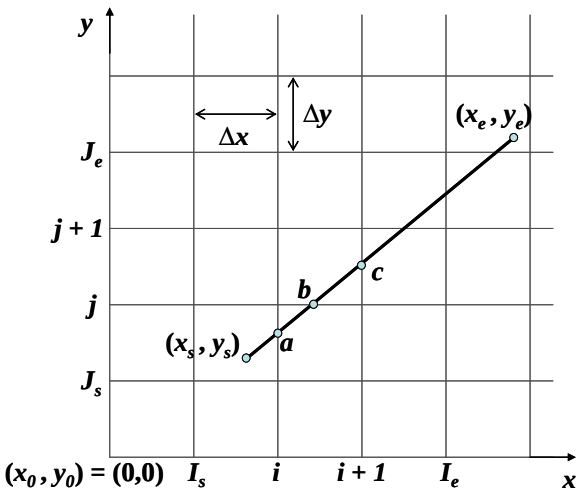

Figure 11.1 Intersection points of a line segment, adapted from (Causon, *et al.*, 2000).

The grid index, (I_s,J_s), of the cell containing the start point of the line can be determined by Equation (11.1) as:

$$I_s = \text{int}\left(\frac{x_s - x_0}{\Delta x}\right)+1; \quad J_s = \text{int}\left(\frac{y_s - y_0}{\Delta y}\right)+1 \qquad (11.1)$$

where int(x) returns the integer part of x and (x_0, y_0) is the origin of the Cartesian mesh. The grid index, (I_e, J_e), of the cell containing the end point of the line can be found in the similar manner. The slope of the line, Q, is also calculated and identified as one of the slope categories as shown in Figure 11.2.

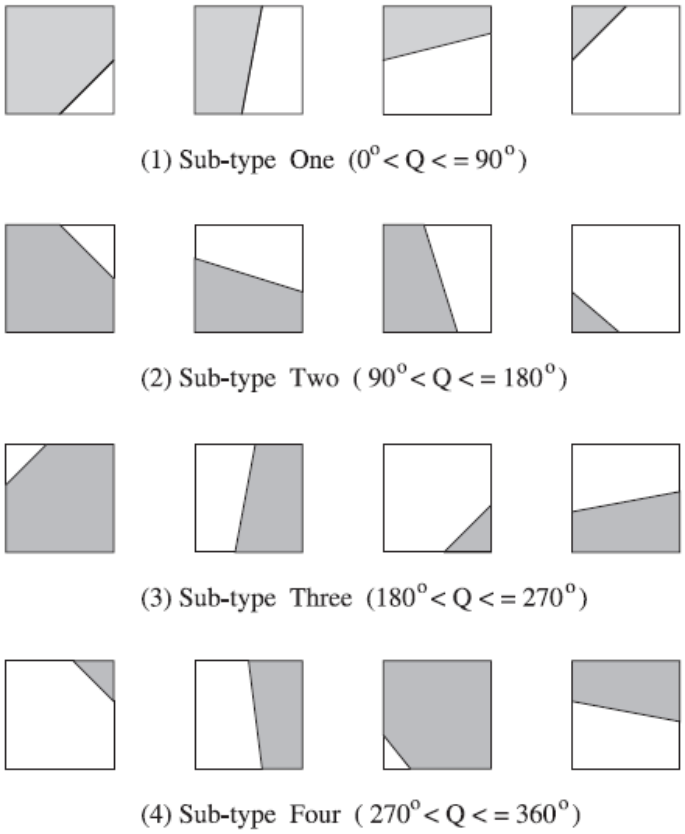

Figure 11.2 Sub-type of cut cell categorized by the slope of the line segment, *Q* (Causon, *et al.*, 2000).

From the grid indexes of the start and end points of the line segment together with its slope, all intersection points of the line segment on the computational grid can be determined in sequential manner along the line from the start point. For example, referring to Figure 11.1, since (x_s, y_s) lies in the cell (I_s, J_s) with Q identified to be sub-type one from Figure 11.2, point a must lie above or on the right side of cell (I_s, J_s). Hence, there are two possible coordinates for point a, which are (x_i, y_a') or (x_a', y_j). $x_i = x_0 + (i + 1)\Delta x$ and $y_j = y_0 + (j + 1)\Delta y$ are known grid coordinates. x_a' and y_a' can be calculated using the line equation

constructed from (x_s, y_s) and (x_e, y_e). In this case, it is found that $x_a' > x_i$, which is not possible. Therefore, the intersection point *a* must lie of the right side of cell (I_s, J_s) with coordinates of $x_a = x_i$ and $y_a = y_a'$. This procedure is repeated to find all subsequent intersection points until (x_e, y_e).

The cases for other sub-type of cut cell with *Q* computed in other three quadrants are deal with analogously. Each grid cells intersected by the line segment together with the intersection points are recorded. Once all the cut cell intersections points have been established, the cells that intersect with wall boundaries are tagged as cut cells. Thus, three primary cell types are formed in the computational domain, which are the flow field cell, cut cell and solid boundary cell.

11.1.2 Reconstruction of fluxes on cut cell

After establishment of the cut cell, QDS fluxes are computed in the spilt flux manner as described in Chapter 6, except proportioned area is used at cut interfaces in the flux calculation. For example, as shown in Figure 11.3, a proportioned L_2 is used to determine the cut interfacial area when calculating the flux on right side of the cell, F_2. Hence, the net fluxes of the cut cell in *x*-direction can be calculated using Equation (11.2) as:

$$\frac{\partial F}{\partial x} = \frac{1}{A}\left(F_1.(L_1.n) + F_2.L_2 - F_3.L_3\right) \qquad (11.2)$$

where A is the area of the cut cell, L_1, L_2 and L_3 are the length of the cut cell interfaces while $\boldsymbol{n}$ is a normal vector.

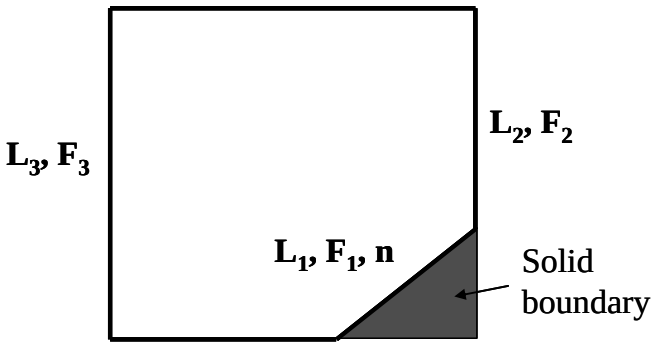

Figure 11.3 Fluxes in *x*-direction of a cut cell.

To calculate the flux across the cut interface, F_1, as shown in Figure 11.3, a ghost cell R inside the solid boundary is used as shown in Figure 11.4. The conserved properties in cell R is obtained by extrapolating from cell (i, j) after applying reflected or bounce back boundary conditions to enforce slip or non-slip wall, respectively.

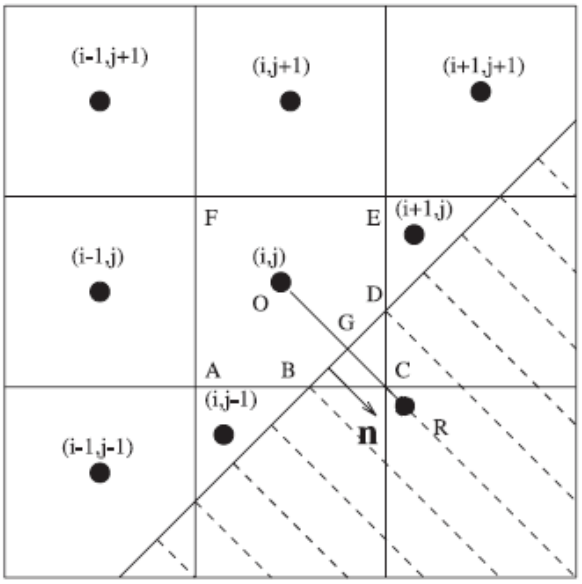

Figure 11.4 Gradient calculation for cut cell (Causon, *et al.*, 2000).

For second order spatial accuracy, a different gradient calculation is needed for cut interface. The property gradients on cut cell (i, j) are divided into fluid gradients and solid gradients. These two types of gradients are calculated separately. The fluid gradients in x- and y-direction can be determined by Equation (11.3) given as:

$$\begin{aligned} U_x^f &= G\left(\frac{U_{i+1,j}-U_{i,j}}{\Delta x_{i+1/2,j}}, \frac{U_{i,j}-U_{i-1,j}}{\Delta x_{i-1/2,j}}\right) \\ U_y^f &= G\left(\frac{U_{i,j+1}-U_{i,j}}{\Delta y_{i,j+1/2}}, \frac{U_{i,j}-U_{i,j-1}}{\Delta y_{i,j-1/2}}\right) \end{aligned} \tag{11.3}$$

where $\Delta x_{i+1/2,j} = x_{i+1,j} - x_{i,j}$, $\Delta y_{i,j+1/2} = y_{i,j+1} - y_{i,j}$, and G is a slope limiter function as given in Equation (5.21) for MC slope limiter or Equation (5.22) for MINMOD slope limiter. The solid gradients in x- and y-direction can be determined by Equation (11.4) given as:

$$\begin{aligned} U_x^s &= G\left(\frac{U_R-U_{i,j}}{\Delta x_{i,R}}, \frac{U_{i,j}-U_{i-1,j}}{\Delta x_{i-1/2,j}}\right) \\ U_y^s &= G\left(\frac{U_{i,j+1}-U_{i,j}}{\Delta y_{i,j+1/2}}, \frac{U_{i,j}-U_R}{\Delta y_{j,R}}\right) \end{aligned} \tag{11.4}$$

where $\Delta x_{i,R} = x_R - x_{i,j}$, $\Delta y_{j,R} = y_{i,j} - y_R$. A length average technique is then used to obtain the unique gradients in the cut cell, which is given in Equation (11.5) as:

$$\begin{aligned} U_x &= \frac{\Delta y_s U_x^s + \Delta y_f U_x^f}{\Delta y} \\ U_y &= \frac{\Delta x_s U_y^s + \Delta x_f U_y^f}{\Delta x} \end{aligned} \tag{11.5}$$

where $\Delta x_f = |AB|$, $\Delta x_s = |BC|$, $\Delta y_s = |CD|$, $\Delta y_f = |DE|$, referring to Figure 11.4. The reconstructed property can be found within the cut cell from Equation (11.6) as:

$$U(x, y) = U_{i,j} + r \cdot \begin{pmatrix} U_x \\ U_y \end{pmatrix} \tag{11.6}$$

where r is the normal distance vector from the cell centroid to the cut interface.

References

Agarwal, R. K., Yun, K.-Y., & Balakrishnan, R. (2001). Beyond Navier-Stokes: Burnett equations for flows in the continuum-transition regime. *Physics of Fluids, 13*(10), 3061-3085.

Albright, B. J., Daughton, W., Lemons, D. S., Winske, D., & Jones, M. E. (2002). Quiet direct simulation of plasmas. *Physics of Plasmas, 9*(5), 1898-1904.

Albright, B. J., Lemons, D. S., Jones, M. E., & Winske, D. (2002). Quiet direct simulation of Eulerian fluids. *Physical Review E, 65*(5), 055302.

Alexander, F. J., Chen, H., Chen, S., & Doolen, G. D. (1992). Lattice Boltzmann model for compressible fluids. *Physical Review A, 46*(4), 1967.

Anderson. (1990). *Modern Compressible Flow : with Historical perspective* (2nd ed.). New York: McGraw-Hill.

Anderson. (1995). *Computational Fluid Dynamics* (International ed.). Singapore: McGraw-Hill, Inc.

Bagabir, A., & Drikakis, D. (2001). Mach number effects on shock-bubble interaction. *Shock Waves, 11*(3), 209-218.

Baluti, S. I. (2005). *Experimental characterization of flow dynamics of Pulsed-Chemical Vapour Deposition.* Master Degree Thesis, University of Canterbury, Christchurch.

Barrett, J. C., & Clement, C. F. (1988). Growth rates for liquid drops. *Journal of Aerosol Science, 19*(2), 223-242.

Bhatnagar, P. L., Gross, E. P., & Krook, M. (1954). A model for collision processes in gases. I. Small amplitude processes in charged and neutral one-component systems. *Physical Review, 94*(3), 511.

Billet, R. (1989). *Evaporation Technology: Principles, Applications, Economics* (J. W. Fullarton, Trans.). Weinheim, Federal Republic of Germany: VCH Verlagsgesellschaft

Bird. (1963). Approach to translational equilibrium in a rigid sphere gas. *Physics of Fluids, 6*(10), 1518-1519.

Bird. (1970a). Breakdown of translational and rotational equilibrium in gaseous expansions. *AIAA Journal, 8*(11), 1998-2003.

Bird. (1970b). Direct simulation and the Boltzmann equation. *Physics of Fluids, 13*(11), 2676-2681.

Bird. (1994). *Molecular Gas Dynamics and the Direct Simulation of Gas Flows*. Oxford: Clarendon Press.

Bird. (2006). *The DS2V Program User's Guide*. Sydney NSW: G.A.B. Consulting Pty Ltd.

Borgnakke, C., & Larsen, P. S. (1975). Statistical collision model for Monte Carlo simulation of polyatomic gas mixture. *Journal of Computational Physics, 18*(4), 405-420.

Boyd, I. D., Chen, G., & Candler, G. V. (1995). Predicting failure of the continuum fluid equations in transitional hypersonic flows. *Physics of Fluids, 7*(1), 210-219.

Causon, D. M., Ingram, D. M., Mingham, C. G., Yang, G., & Pearson, R. V. (2000). Calculation of shallow water flows using a Cartesian cut cell approach. *Advances in Water Resources, 23*(5), 545-562.

Cave. (2008). *Development of Modelling Techniques for Pulsed Pressure Chemical Vapour Deposition (PP-CVD).* PhD Degree Thesis, University of Canterbury, Christchurch.

Cave. (2010). *Raptor QDS Gas Flow Simulation Software User's Manual (version 1.4)*. Software User's Manual. University of Canterbury. Christchurch, New Zealand.

Cave, Krumdieck, & Jermy. (2008). Development of a model for high precursor conversion efficiency pulsed-pressure chemical vapor deposition (PP-CVD) processing. *Chemical Engineering Journal, 135*(1-2), 120-128.

Cave, Lim, Jermy, Krumdieck, Smith, Lin, & Wu. (2011). Multi-species fluxes for the parallel Quiet Direct Simulation (QDS) method. *AIP Conference Proceedings, 1333*(1), 878-883.

Cave, Smith, Wu, Jermy, Krumdieck, Lim, & Tseng. (2009). *Axisymmetric simulations of eulerian gas flows using the Quiet Direct Simulation method*. unpublished manuscript.

Cave, Tseng, Wu, Jermy, Huang, & Krumdieck. (2008). Implementation of unsteady sampling procedures for the parallel direct simulation Monte Carlo method. *Journal of Computational Physics, 227*(12), 6249-6271.

Cave, Tseng, Wu, Jermy, Lian, Krumdieck, . . . Wu. (2007). *Modelling unsteady processes with the Direct Simulation Monte Carlo technique.* Paper presented at the 16th Australasian Fluid Mechanics Conference (AFMC), Gold Coast, Queensland, Australia.

Chang, I.-S., Chang, C.-L., & Chang, S.-C. (2005). *Unsteady Navier-Stokes rocket nozzle flows.* Paper presented at the 41st AIAA Joint Propulsion Conference, Tucson, AZ.

Choy, K. L. (2003). Chemical vapour deposition of coatings. *Progress in Materials Science, 48*(2), 57-170.

Clift, R., Grace, J. R., & Weber, M. E. (1978). *Bubbles, Drops, and Particles*. New York: Academic Press.

Cook, J., G. (1998). *High accuracy capture of curved shock fronts using the method of space-time conservation element and solution element*. Paper presented at the 37th American Institute of Aeronautics and Astronautics Aerospace Sciences Meeting and Exhibit, Reno, NV.

Coronell, D. G., & Jensen, K. F. (1992). Analysis of transition regime flows in Low Pressure Chemical Vapor Deposition reactors using the Direct Simulation Monte Carlo method. *Journal of The Electrochemical Society, 139*(8), 2264-2273.

Crist, S., Sherman, P. M., & Glass, D. R. (1966). Study of the highly underexpanded sonic jet. *AIAA Journal, 4*(1), 68-71.

Dietrich, S., & Boyd, I. D. (1996). Scalar and parallel optimized implementation of the Direct Simulation Monte Carlo method. *Journal of Computational Physics, 126*(2), 328-342.

Emery, A. F. (1968). An evaluation of several differencing methods for inviscid fluid flow problems. *Journal of Computational Physics, 2*(3), 306-331.

Fox, R. W., McDonald, A. T., & Pritchard, P. J. (2003). *Introduction to Fluid Dynamics* (6th ed.). Hoboken, N.J.: John Wiley and Sons.

Fröessling, N. (1938). The evaporation of a falling drops. *Gerlands Beitr Geophys., 52*, 170.

Frohn, A., & Roth, N. (2000). *Dynamics of Droplets*. Berlin Heidelberg: Springer-Verlag.

Gombosi, T. I. (1994). *Gaskinetic Theory*. Cambridge: Cambridge University Press.

Haas, J.-F., & Sturtevant, B. (1987). Interaction of weak shock waves with cylindrical and spherical gas inhomogeneities. *Journal of Fluid Mechanics, 181*, 41-76.

Hervieu, E., & Veneau, T. (1996). Experimental determination of the droplet size and velocity distributions at the exit of the bottom discharge pipe of a liquefied propane storage tank during a sudden blowdown. *Journal of Loss Prevention in the Process Industries, 9*(6), 413-425.

Holway, J. L. H. (1966). New statistical models for kinetic theory: methods of construction. *Physics of Fluids, 9*(9), 1658-1673.

Huang, K. (1987). *Statistical Mechanics* (2nd ed.). New York: John Wiley and Sons.

Incropera, F. P., & DeWitt, D. P. (2001). *Fundamental of Heat and Mass Transfer* (5th ed.). New York: John Wiley & Sons, Inc.

Ingram, D. M., Causon, D. M., & Mingham, C. G. (2003). Developments in Cartesian cut cell methods. *Mathematics and Computers in Simulation, 61*(3-6), 561-572.

Jeans, J. H. (1904). *The Dynamical Theory of Gases*. London: Cambridge: University Press.

Jermy, M. C., Lim, C.-W., & Cave, H. M. (2010). *Validity and inherent viscosity of the Quiet Direct Simulation method.* Paper presented at the 27th Intl Symposium on Rarefied Gas Dynamics 2010, Asilomar, California.

Jiang, Z., Takayama, K., Babinsky, H., & Meguro, T. (1997). Transient shock wave flows in tubes with a sudden change in cross section. *Shock Waves, 7*(3), 151-162.

Jones, A. C., & Hitchman, M. L. (Eds.). (2009). *Chemical Vapour Deposition: Precursors, Processes and Applications*. Cambridge, UK: Royal Society of Chemistry.

Karniadakis, G., & Beşkök, A. (2002). *Micro flows: Fundamentals and Simulation*. New York: Springer.

Karypis, G., Schloegel, K., & Kumar, V. (2011). *ParMeTis*, Parallel Graph Partitioning and Sparse Matrix Ordering Library Version 3.2*. User's Manual. University of Minnesota, Department of Computer Science and Engineering, Minneapolis, MN 55455.

Keats, W. A., & Lien, F. S. (2004). Two-dimensional anisotropic Cartesian mesh adaptation for the compressible Euler equations. *International Journal for Numerical Methods in Fluids, 46*(11), 1099-1125.

Khavkin, Y. I. (2004). *Theory and Practice of Swirl Atomizers*. New York: Taylor & Francis.

Kimpton, D. D., & Wall, F. T. (1952). Determination of diffusion coefficients from rates of evaporation. *The Journal of Physical Chemistry, 56*(6), 715-717.

Kincaid, D. C., & Longley, T. S. (1989). A water droplet evaporation and temperature model. *Transactions of the American Society of Agricultural Engineers, 32*(2), 457-563.

Kotecki, D. E., Conti, R. A., Barbee, S. G., Cacouris, T. D., Chapple, x, . . . Zuhoski, S. P. (1994). Applications of computational fluid dynamics for

improved performance in chemical-vapor-deposition reactors. *Journal of Vacuum Science & Technology B: Microelectronics and Nanometer Structures, 12*(4), 2752-2757.

Koura, K., & Matsumoto, H. (1991). Variable soft sphere molecular model for inverse-power-law or Lennard-Jones potential. *Physics of Fluids A: Fluid Dynamics, 3*(10), 2459-2465.

Koura, K., Matsumoto, H., & Shimada, T. (1991). A test of equivalence of the variable-hard-sphere and inverse-power-law models in the direct-simulation Monte Carlo method. *Physics of Fluids A: Fluid Dynamics, 3*(7), 1835-1837.

Kozyrev, A. V., & Sitnikov, A. G. (2001). Evaporation of a spherical droplet in a moderate-pressure gas. *Physics – Uspekhi, 44*(7), 725-733.

Krumdieck. (2001). Kinetic model of low pressure film deposition from single precursor vapor in a well-mixed, cold-wall reactor. *Acta Materialia, 49*(4), 583-588.

Krumdieck, Baluti, Marcus, & Peled. (2005). *Design investigation for three-dimensional uniformity of the mass transport field.* Paper presented at the Fifteenth European Conference on Chemical Vapor Deposition (EUROCVD-15), 5-9 Sep 2005, Bochum, Germany.

Krumdieck, Cave, Baluti, Jermy, & Peled. (2007). Expansion transport regime in pulsed-pressure chemical vapor deposition. *Chemical Engineering Science, 62*(22), 6121-6128.

Krumdieck, Kristinsdottir, Ramirez, Lebedev, & Long. (2007). Growth rate, microstructure and conformality as a function of vapor exposure for zirconia thin films by pulsed-pressure MOCVD. *Surface and Coatings Technology, 201*(22-23), 8908-8913.

Krumdieck, Lee, & Raatz. (2003). Uniform molecular flux in a vertical reactor with pulsed transition regime gas flow. *Journal of the Electrochemical Society, 2003*(8), 179-185.

Krumdieck, & Raj. (1999). Conversion efficiency of alkoxide precursor to oxide films grown by an ultrasonic-assisted, pulsed liquid injection, Metalorganic Chemical Vapor Deposition (Pulsed-CVD) process. *Journal of the American Ceramic Society, 82*(6), 1605-1607.

Krumdieck, & Raj. (2001a). Experimental characterization and modeling of Pulsed MOCVD with ultrasonic atomization of liquid precursor. *Chemical Vapor Deposition, 7*(2), 85-90.

Krumdieck, & Raj. (2001b). Growth rate and morphology for ceramic films by pulsed-MOCVD. *Surface and Coatings Technology, 141*(1), 7-14.

Krumdieck, Sbaizero, Bullert, & Raj. (2002). Solid yttria-stabilized zirconia films by Pulsed Chemical Vapor Deposition from metal-organic precursors. *Journal of the American Ceramic Society, 85*(11), 2873-2875.

Krumdieck, Sbaizero, Bullert, & Raj. (2003). YSZ layers by pulsed-MOCVD on solid oxide fuel cell electrodes. *Surface and Coatings Technology, 167*(2-3), 226-233.

Krumdieck, Siriwongrungson, Reyngoud, & Barnett. (2010). Bio-integration ceramics on 3D specimens by Pulsed-Pressure Metal-Organic CVD. *Chemical Vapor Deposition, 16*(1-3), 15-18.

LeBeau, G. J. (1999). A parallel implementation of the direct simulation Monte Carlo method. *Computer Methods in Applied Mechanics and Engineering, 174*(3-4), 319-337.

LeBeau, G. J., & Lumpkin III, F. E. (2001). Application highlights of the DSMC Analysis Code (DAC) software for simulating rarefied flows. *Computer Methods in Applied Mechanics and Engineering, 191*(6-7), 595-609.

Lemmon, E. W., McLinden, M. O., & Friend, D. G. (retrieved July 19, 2011). Thermophysical properties of fluid systems. In P.J. Linstrom & W.G. Mallard (Eds.), *NIST Chemistry WebBook, NIST Standard Reference Database Number 69*. Gaithersburg: National Institute of Standards and Technology.

Lilley, C. R. (2005). *A Macroscopic Chemistry Method for the Direct Simulation of Non-equilibrium Gas Flows.* PhD Degree Thesis, The University of Queensland, Brisbane.

Lim, C. W. (2004). *The Development of a Three-Dimensional Lattice Boltzmann Model for Compressible Flows.* Master Degree Thesis, Purdue University, Indianapolis, USA.

Lim, C. W., Smith, M. R., Jermy, M. C., Wu, C.-S., & Krumdieck, S. P. (submitted). The direction decoupled Quiet Direct Simulation method for rapid simulation of axisymmetric inviscid unsteady flow in Pulsed Pressure Chemical Vapour Deposition. *Computers & Fluids*.

Lin. (2008). *Simulation of the Transport Phenomena in a Pulsed Pressure Chemical Vapour Deposition (PP-CVD) Process*. Master Degree Thesis, National Chiao Tung University, Hsinchu, Taiwan.

Lin, Smith, Cave, Huang, & Wu. (2011). General higher order extension to the Quiet Direct Simulation method. *AIP Conference Proceedings, 1333*(1), 1010-1015.

Macrossan, M. N. (1989). The equilibrium flux method for the calculation of flows with non-equilibrium chemical reactions. *Journal of Computational Physics, 80*(1), 204-231.

Macrossan, M. N. (2001). [nu]-DSMC: A fast simulation method for rarefied flow. *Journal of Computational Physics, 173*(2), 600-619.

Macrossan, M. N., & Oliver, R. I. (1993). A kinetic theory solution method for the Navier–Stokes equations. *International Journal for Numerical Methods in Fluids, 17*(3), 177-193.

Maxwell, & Harman (Eds.). (1890). *The Scientific Letters and Papers of James Clerk Maxwell*. Cambridge, UK: Cambridge University Press.

Minkowycz, W. J., & Sparrow, E. M. (Eds.). (2000). *Advances in Numerical Heat Transfer* (Vol. 2). New York: Taylor & Francis.

Morosanu, C. E. (1990). *Thin Films by Chemical Vapour Deposition*. Amsterdam: Elsevier.

Nijdam, J., Stårner, S., & Langrish, T. (2004). An experimental investigation of droplet evaporation and coalescence in a simple jet flow. *Experiments in Fluids, 37*(4), 504-517.

Ohring, M. (2002). *Materials Science of Thin Films: Deposition and Structure* (2nd ed.). San Diego, CA: Academic Press.

Oran, E. S., Oh, C. K., & Cybyk, B. Z. (1998). Direct Simulation Monte Carlo: Recent advances and applications. *Annual Review of Fluid Mechanics, 30*(1), 403-441.

Peter, W. (2007). Quiet direct simulation Monte-Carlo with random timesteps. *Journal of Computational Physics, 221*(1), 1-8.

Picone, J. M., & Boris, J. P. (1988). Vorticity generation by shock propagation through bubbles in a gas. *Journal of Fluid Mechanics, 189*, 23-51.

Potter, M. C., Wiggert, D. C., Hondzo, M., & Shih, T. I.-P. (2002). *Mechanics of Fluids* (3rd ed.). Pacific Grove, CA.: Brooks/Cole.

Pruppacher, H. R., & Klett, J. D. (1997). *Microphysics of Clouds and Precipitation*. Boston: Kluwer Academic Publishers.

Pullin, D. I. (1980). Direct simulation methods for compressible inviscid ideal-gas flow. *Journal of Computational Physics, 34*(2), 231-244.

Qu, X., Davis, E. J., & Swanson, B. D. (2001). Non-isothermal droplet evaporation and condensation in the near-continuum regime. *Journal of Aerosol Science, 32*(11), 1315-1339.

Ramires, M. (2000). Reference data for the thermal conductivity of saturated liquid toluene over a wide range of temperatures. *J. Phys. Chem. Ref. Data, 29*(2), 133.

Ranz, W. E., & Marshall, W. R. J. (1952). Evaporation from drops, Part II. *Chemical Engineering Progress, 48*(4), 173-179.

Risken, H. (1989). *The Fokker-Planck Equation: Methods of Solution and Applications* (2nd ed.). Berlin: Springer-Verlag.

Roe, P. L. (1986). Characteristic-based schemes for the Euler equations. *Annual Review of Fluid Mechanics, 18*(1), 337-365.

Roth, A. (1990). *Vacuum Technology* (3rd ed.). Amsterdam: North Holland.

Rudinger, G., & Somers, L. M. (1960). Behaviour of small regions of different gases carried in accelerated gas flows. *Journal of Fluid Mechanics, 7*(2), 161-176.

Saury, D., Harmand, S., & Siroux, M. (2002). Experimental study of flash evaporation of a water film. *International Journal of Heat and Mass Transfer, 45*(16), 3447-3457.

Schuegraf, K. K. (Ed.). (1988). *Handbook of thin-film deposition processes and techniques : principles, methods, equipment and applications* (Reprint ed.). Westwood, N. J.: Noyes Publications.

Seshan, K. (Ed.). (2002). *Handbook of Thin-Film Deposition Processes and Techniques : Principles, Methods, Equipment and Applications* (2nd ed.). Norwich, N.Y.: Noyes Publications.

Setyawan, H., Shimada, M., Ohtsuka, K., & Okuyama, K. (2002). Visualization and numerical simulation of fine particle transport in a low-pressure parallel plate chemical vapor deposition reactor. *Chemical Engineering Science, 57*(3), 497-506.

Sharma, & Long. (2004). Numerical simulation of the blast impact problem using the Direct Simulation Monte Carlo (DSMC) method. *Journal of Computational Physics, 200*(1), 211-237.

Siriwongrungson, V. (2010). *Characterisation of Step Coverage by Pulsed-Pressure Metalorganic Chemical Vapour Deposition: Titanium Dioxide Thin Films on 3-D Micro- and Nano-Scale Structures.* PhD Degree Thesis, University of Canterbury, Christchurch.

Siriwongrungson, V., Alkaisi, M. M., & Krumdieck, S. P. (2007). Step coverage of thin titania films on patterned silicon substrate by pulsed-pressure MOCVD. *Surface and Coatings Technology, 201*(22-23), 8944-8949.

Smith, M. R. (2008). *The True Direction Equilibrium Flux Method and its Application.* PhD Degree Thesis, The University of Queensland, Brisbane.

Smith, M. R., Cave, H., Wu, J. S., Jermy, M. C., & Chen, Y. S. (2009). An improved quiet direct simulation method for Eulerian fluids using a second-order scheme. *Journal of Computational Physics, 228*, 2213-2224.

Smith, M. R., Kuo, F.-A., Cave, H. M., Jermy, M. C., & Wu, J.-S. (2010). *Quiet Direct Simulation (QDS) of viscous flow using the Chapman-Enskog distribution.* Paper presented at the 27th Intl Symposium on Rarefied Gas Dynamics 2010, Asilomar, California.

Smith, M. R., Macrossan, M. N., & Abdel-jawad, M. M. (2008). Effects of direction decoupling in flux calculation in finite volume solvers. *Journal of Computational Physics, 227*(8), 4142-4161.

Sono-TekCorporation. (1997). Ultrasonic Spray Nozzle Systems. Vienna, Austria: LICO Electronics GmbH.

Sterling, J. D., & Chen, S. (1996). Stability analysis of Lattice Boltzmann Methods. *Journal of Computational Physics, 123*(1), 196-206.

Succi, S. (2001). *The Lattice Boltzmann Equation for Fluid Dynamics and Beyond*. Oxford: Clarendon Press.

Sun. (1998). Lattice-Boltzmann models for high speed flows. *Physical Review E, 58*(6), 7283.

Sun, Boyd, & Candler. (2004). A hybrid continuum/particle approach for modeling subsonic, rarefied gas flows. *Journal of Computational Physics, 194*(1), 256-277.

Sun, & Hsu. (2004). Multi-level lattice Boltzmann model on square lattice for compressible flows. *Computers & Fluids, 33*(10), 1363-1385.

Taflin, D. C., Zhang, S. H., Allen, T., & James Davis, E. (1988). Measurement of droplet interfacial phenomena by light-scattering techniques. *AIChE Journal, 34*(8), 1310-1320.

Taga, Y. (2001). Recent progress of nanotechnologies of thin films for industrial applications. *Materials Science and Engineering: C, 15*(1-2), 231-235.

Teshima, K., & Usami, M. (2001). DSMC simulation of axisymmetric supersonic free jets. *Computational Fluid Dynamics JOURNAL, 10*, 525-530.

Titov, E. V., & Levin, D. A. (2007). Extension of the DSMC method to high pressure flows. *International Journal of Computational Fluid Dynamics, 21*(9), 351 - 368.

Toro, E. F. (2009). *Riemann Solvers and Numerical Methods for Fluid Dynamics* (3rd ed.). Berlin Heidelberg: Springer-Verlag

Van Leer, B. (1977). Towards the ultimate conservative difference scheme III. Upstream-centered finite-difference schemes for ideal compressible flow. *Journal of Computational Physics, 23*(3), 263-275.

van Leer, B. (1982). Flux-vector splitting for the Euler equations. *Lecture Notes in Physics, 170*, 507-512.

Vanka, S. P., Luo, G., & Glumac, N. G. (2004). Numerical study of mixed convection flow in an impinging jet CVD reactor for atmospheric pressure deposition of thin films. *Journal of Heat Transfer – Transactions of the ASME, 126*, 764-775.

Vargaftik, N. B., Zaitseva, L. S., & Yakush, L. V. (1968). Experimental investigation of the thermal conductivity of toluene, biphenyl, and carbon tetrachloride vapor. *Journal of Engineering Physics and Thermophysics, 14*(5), 466-470.

Versteeg, Avedisian, & Raj. (1995a). Metalorganic Chemical Vapor Deposition by pulsed liquid injection using an ultrasonic nozzle: titanium dioxide on sapphire from titanium(IV) isopropoxide. *Journal of the American Ceramic Society, 78*(10), 2763-2768.

Versteeg, Avedisian, & Raj. (1995b). US Patent No. 5451260.

Wagner, W. (1992). A convergence proof for Bird's direct simulation Monte Carlo method for the Boltzmann equation. *Journal of Statistical Physics, 66*(3), 1011-1044.

Wang, W. L., & Boyd, I. D. (2003). Predicting continuum breakdown in hypersonic viscous flows. *Physics of Fluids, 15*(1), 91-100.

Welander, P. (1954). On the temperature jump in a rarefied gas. *Arkiv for Fysik, 7*, 507-553.

White, F. M. (1991). *Viscous Fluid Flow* (International ed.). Singapore: McGraw-Hill, Inc.

Woodmansee, M. A., Iyer, V., Dutton, J. C., & Lucht, R. P. (2004). Nonintrusive pressure and temperature measurements in an underexpanded sonic jet flowfield. *AIAA Journal, 42*(6), 1170-1180.

Woodward, P., & Colella, P. (1984). The numerical simulation of two-dimensional fluid flow with strong shocks. *Journal of Computational Physics, 54*(1), 115-173.

Wu, Chou, Lee, Shao, & Lian. (2005). Parallel DSMC simulation of a single under-expanded free orifice jet from transition to near-continuum regime. *Journal of Fluids Engineering, 127*(6), 1161-1170.

Wu, Hsiao, Lian, & Tseng. (2003). Assessment of conservative weighting scheme in simulating chemical vapour deposition with trace species. *International Journal for Numerical Methods in Fluids, 43*(1), 93-114.

Wu, & Lian. (2003). Parallel three-dimensional direct simulation Monte Carlo method and its applications. *Computers & Fluids, 32*(8), 1133-1160.

Wu, Lian, Cheng, Koomullil, & Tseng. (2006). Development and verification of a coupled DSMC-NS scheme using unstructured mesh. *Journal of Computational Physics, 219*(2), 579-607.

Wu, & Tseng. (2005). Parallel DSMC method using dynamic domain decomposition. *International Journal for Numerical Methods in Engineering, 63*(1), 37-76.

Wu, Tseng, & Wu. (2004). Parallel three-dimensional DSMC method using mesh refinement and variable time-step scheme. *Comput. Phys. Comm., 162*, 166.

Xie, & Raj. (1993). Epitaxial LiTaO3 thin film by pulsed metalorganic chemical vapor deposition from a single precursor. *Applied Physics Letters, 63*(23), 3146-3148.

Xu, K. (1998). Gas-Kinetic Schemes for Unsteady Compressible Flow Simulations *von Karman Institute for Fluid Dynamics Lecture Series 1998-03*.

Xu, K. (2000). A gas-kinetic BGK Scheme for the compressible Navier-Stokes equations *ICASE Report 00-38*: NASA Langley Research Center.

Xu, K. (2001). A gas-kinetic BGK scheme for the Navier-Stokes equations and its connection with artificial dissipation and Godunov method. *Journal of Computational Physics, 171*(1), 289-335.

Xu, K., Kim, C., Martinelli, L., & Jameson, A. (1996). BGK-based schemes for the simulation of compressible flow. *International Journal of Computational Fluid Dynamics, 7*(3), 213-235.

Xu, K., & Luo, L.-S. (1998). Connection between Lattice-Boltzmann equation and Beam scheme. *International Journal of Modern Physics C, 9*(8), 1177-1187.

Xu, K., & Prendergast, K. H. (1994). Numerical Navier-Stokes solutions from gas kinetic theory. *Journal of Computational Physics, 114*(1), 9-17.

Zabusky, N. J., & Zeng, S. M. (1998). Shock cavity implosion morphologies and vortical projectile generation in axisymmetric shock-spherical fast/slow bubble interactions. *Journal of Fluid Mechanics, 362*, 327-346.

Zhang, H., & Zhuang, F. (1991). NND schemes and their applications to numerical simulation of two- and three-dimensional flows. *Advances in Applied Mechanics, 29*, 193-256.

Zwillinger, D. (Ed.). (2003). *CRC Standard Mathematical Tables and Formulae* (31st ed.). Boca Raton, FL: CRC Press.

Appendix

Gauss-Hermite Quadrature (Zwillinger, 2003)

n	Nodes $\{\pm x_i\}$	Weights $\{w_i\}$
2	0.7071067811	0.8862269254
3	0	1.1816359006
	1.2247448713	0.2954089751
4	0.5246476232	0.8049140900
	1.6506801238	0.0813128354
5	0	0.9453087204
	0.9585724646	0.3936193231
	2.0201828704	0.0199532420
6	0.4360774119	0.7246295952
	1.3358490740	0.1570673203
	2.3506049736	0.0045300099

n	Nodes $\{\pm x_i\}$	Weights $\{w_i\}$
7	0	0.8102646175
	0.8162878828	0.4256072526
	1.6735516287	0.0545155828
	2.6519613568	0.0009717812
8	0.3811869902	0.6611470125
	1.1571937124	0.2078023258
	1.9816567566	0.0170779830
	2.9306374202	0.0001996040
9	0	0.7202352156
	0.7235510187	0.4326515590
	1.4685532892	0.0884745273
	2.2665805845	0.0049436242
	3.1909932017	0.0000396069